ZEOLITE CATALYSTS FOR NITRIC OXIDE PRODUCTION

Samantha Russell

A Thesis Submitted for the Degree of PhD
at the
University of St Andrews

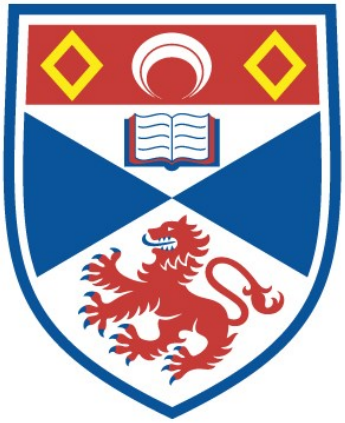

2019

Zeolite Catalysts for Nitric Oxide Production

Samantha Russell

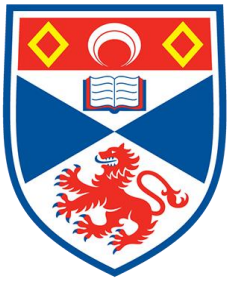

University of
St Andrews

This thesis is submitted in partial fulfilment for the degree of

Doctor of Philosophy (PhD)

at the University of St Andrews

September 2018

Candidate's declaration

I, Samantha Russell, do hereby certify that this thesis, submitted for the degree of PhD, which is approximately 48,000 words in length, has been written by me, and that it is the record of work carried out by me, or principally by myself in collaboration with others as acknowledged, and that it has not been submitted in any previous application for any degree.

I was admitted as a research student at the University of St Andrews in September 2014.

I received funding from an organisation or institution and have acknowledged the funder(s) in the full text of my thesis.

Date Signature of candidate

Supervisor's declaration

I hereby certify that the candidate has fulfilled the conditions of the Resolution and Regulations appropriate for the degree of PhD in the University of St Andrews and that the candidate is qualified to submit this thesis in application for that degree.

Date Signature of supervisor

Permission for publication

In submitting this thesis to the University of St Andrews we understand that we are giving permission for it to be made available for use in accordance with the regulations of the University Library for the time being in force, subject to any copyright vested in the work not being affected thereby. We also understand, unless exempt by an award of an embargo as requested below, that the title and the abstract will be published, and that a copy of the work may be made and supplied to any bona fide library or research worker, that this thesis will be electronically accessible for personal or research use and that the library has the right to migrate this thesis into new electronic forms as required to ensure continued access to the thesis.

I, Samantha Russell, confirm that my thesis does not contain any third-party material that requires copyright clearance.

The following is an agreed request by candidate and supervisor regarding the publication of this thesis:

Printed copy

No embargo on print copy.

Electronic copy

No embargo on electronic copy.

Date Signature of candidate

Date Signature of supervisor

Underpinning Research Data or Digital Outputs

Candidate's declaration

I, Samantha Russell, understand that by declaring that I have original research data or digital outputs, I should make every effort in meeting the University's and research funders' requirements on the deposit and sharing of research data or research digital outputs.

Date Signature of candidate

Permission for publication of underpinning research data or digital outputs

We understand that for any original research data or digital outputs which are deposited, we are giving permission for them to be made available for use in accordance with the requirements of the University and research funders, for the time being in force.

We also understand that the title and the description will be published, and that the underpinning research data or digital outputs will be electronically accessible for use in accordance with the license specified at the point of deposit, unless exempt by award of an embargo as requested below.

The following is an agreed request by candidate and supervisor regarding the publication of underpinning research data or digital outputs:

Embargo on all of electronic files for a period of 1 year on the following ground(s):

- Publication would preclude future publication

Supporting statement for embargo request

Further publications may follow, therefore the raw data will be required.

Date Signature of candidate

Date Signature of supervisor

Acknowledgements

Firstly, thank you to Russell for the opportunity to work on such an enjoyable project. Thank you for your ideas and input over the past four years, as well as your reassurance when things didn't go as planned. I have thoroughly enjoyed working with you.

A massive thank you to the Morris group members, past and present, for making my PhD experience so enjoyable. One of the greatest parts of my PhD has been the many wonderful people I have met, and I know many of which have become life-long friends. I adore all of you and can't imagine having had better company for the past four years. The plentiful baking and gin drinking has also been wonderful.

The CRITICAT Centre for Doctoral Training provided me with the opportunity to undertake my PhD, and for that I am very thankful. A special thank you to Kevin Jones for all his help and the many chats over the years. I would also like to thank the Engineering and Physical Sciences Research Council, University of St Andrews, and CRITICAT CDT for financial support [Grant code: EP/L016419/1].

I have been lucky enough to be surrounded by such incredible friends, both near and far, during my time in St Andrews. To my "chickens", thank you for the many dinner dates and wine drinking. I consider myself lucky to have shared this experience with you. To Fee, you have been the most supportive friend I could ever ask for. Thank you for your constant reassurance and pep-talks, they have helped me when I needed it most.

The continuous love and support I have received from my family has been incredible. Mum, Dad and Amy; thank you for always believing in me and being the best support system I could ever ask for. I hope I have made you proud.

Lastly, thank you to my fellow thesis writer, Ross. I couldn't be more thankful to be completing this journey with you by my side. Thank you for always being there for me.

Abstract

This thesis considers the nitric oxide production from a range of zeolite catalysts with either acid or copper active sites. The aim of the research was to find potential candidates for stent coatings that could help to prevent stent thrombosis.

Acid site mordenite, ferrierite, SSZ-13 and ZSM-5 are studied in chapter 4 for the catalytic conversion of sodium nitrite to nitric oxide. All zeolites successfully produced nitric oxide, with ranging levels of conversion from 14 – 24 %. Recycled samples revealed the consumption of the acid site, rendering the acid site zeolites non-catalytic.

Copper site zeolites were considered in chapters 5 and 6, with copper mordenite, ferrierite, SSZ-13, ZSM-5 and UZM-4 being studied. All zeolites successfully converted sodium nitrite to nitric oxide, with SSZ-13, ZSM-5 and UZM-4 producing around 100 % conversion. The use of cysteine as a sacrificial reductant to activate the copper sites allowed catalytic nitric oxide production. The promising catalytic tests led to further studies of the materials, including copper leaching and toxicology.

Chapter 6 looked further into the catalytic copper zeolites with nitric oxide flow studies and polymer incorporation. Flow studies showed sustained levels of nitric oxide production. Incorporation of the zeolite powders into the polymer of intrinsic microporosity, EATB(Me), showed good nitric oxide production from the initial studies. Recycled samples, however, showed a drop in production.

Lastly, chapter 7 explored the use of the ADOR (Assembly-Disassembly-Organisation-Reassembly) process to generate a series of zeolites for catalysis. Aluminium was incorporated into zeolites IPC-2, 4 and 6 through the organisation step to create aluminated zeolites. The aforementioned zeolites, as well as Al-UTL, were assessed for nitric oxide production with acid active sites. The results showed an interesting relation between ring size and nitric oxide production, with the largest rings of Al-UTL having the highest production and the smallest rings of Al-IPC-4 having the lowest.

Publications

Publications Arising from this Thesis

"A comparison of copper and acid site zeolites for the production of nitric oxide for biomedical applications" Russell, S. E.; González Carballo, J. M.; Orellana-Tavra, C.; Fairen-Jimenez, D; Morris, R. E., *Dalton Trans*., 2017, **46**, 3915-3920.

Publications Outside the Scope of this Thesis

"Expansion of the ADOR strategy for the synthesis of zeolites: The synthesis of IPC-12 from zeolite UOV" Kasneryk, V., Shamzhy, M., Opanasenko, M., Wheatley, P. S., Morris, S. A., Russell, S. E., Mayoral, A., Trachta, M., Cejka, J., Morris, R. E., *Angew. Chem. Int. Ed*., 2017, **56**, 4324 –4327.

"Assembly-disassembly-organisation-reassembly synthesis of zeolites based on cfi-type layers" Firth, D. S., Morris, S. A., Wheatley, P. S., Russell, S. E., Slawin, A. M. Z., Dawson, D. M., Mayoral, A., Opanasenko, M., Položij, M., Čejka, J., Nachtigall, P., Morris, R. E., *Chem. Mater*., 2017, **29**, 5605 – 5611.

"Cost-effective ^{17}O enrichment and NMR spectroscopy of mixed-metal terephthalate metal-organic frameworks" Bignami, G. P. M., Davis, Z. H., Dawson, D. M., Morris, S. A., Russell, S. E., McKay, D., Parke, R. E., Iuga, D., Morris, R. E. & Ashbrook, S. E., *Chem. Sci.*, 2018, **9**, 850–859.

Table of Contents

Chapter 1: Introduction

1.1. Zeolites

1.1.1. Zeolite Overview

As defined by the International Zeolite Association (IZA), zeolites are aluminosilicates with open 3-dimensional framework structures, that have pore diameters of less than 2 nm.[1] Zeolite frameworks are generated by a series of connected TO_4 tetrahedra, where the T-atoms are most commonly silicon or aluminium, but can also be elements such as phosphorous, germanium, tin or boron. The tetrahedra are often known as primary building units (PBUs) and are connected through corner-sharing oxygen atoms, figure 1.1.

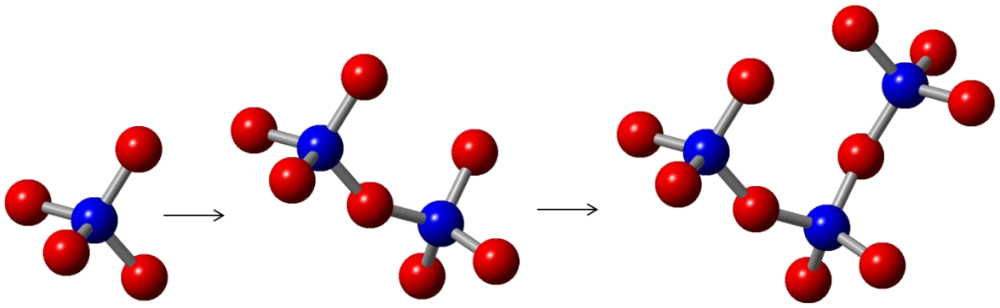

Figure 1.1: Zeolite tetrahedra connecting through corner-sharing oxygen atoms, where the blue atoms are silicon and the red are oxygen.

The connection of the PBUs can generate diverse shapes that can be a common feature in a range of zeolites, these are known as secondary building units (SBUs). There are 23 SBUs, figure 1.2, with varying frequencies in zeolite structures. They are key components in the building of zeolite frameworks, where the assembly of these building units determines the size and porosity of the zeolite structure.

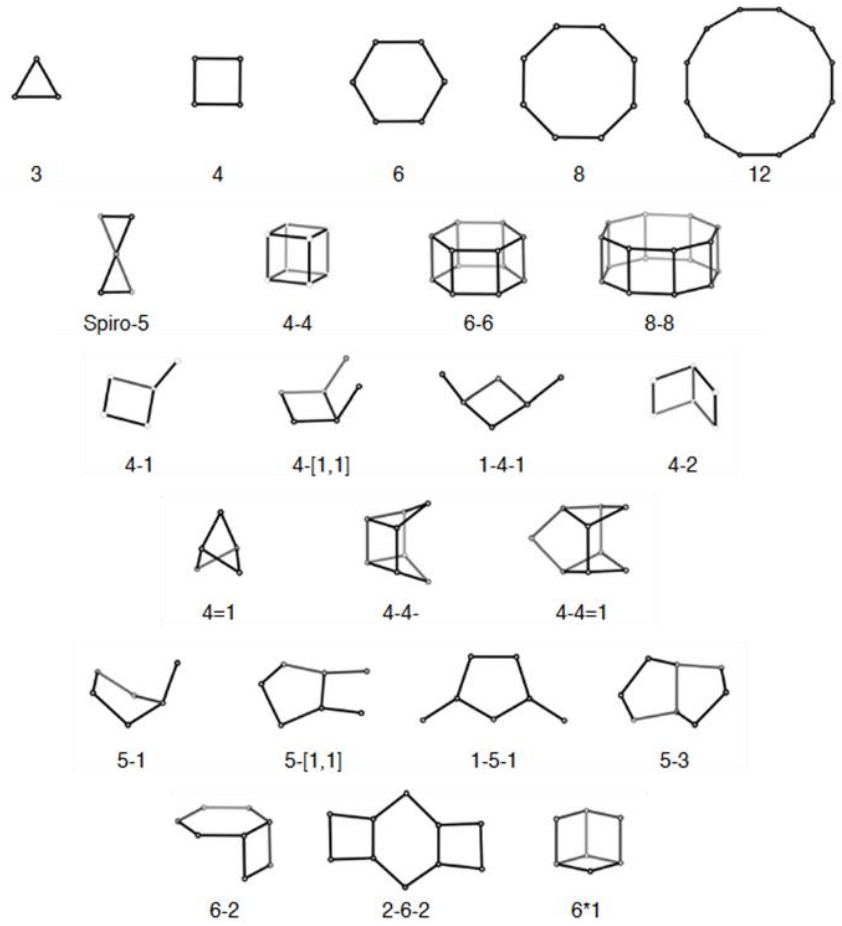

Figure 1.2: The 23 SBUs formed from connected tetrahedra (PBUs), where the nodes represent T atoms.[2]

As zeolite synthesis progresses, there are more complex zeolite frameworks being discovered. A system that is more advanced than SBUs was required to consider common structural features present in more than one zeolite. Composite building units (CBUs) are generally larger sections of common structural features, such as cages, channels, chains and layers.[3] The majority of CBUs are named after one of the zeolite frameworks that they are featured in and are only named when they are present in more than one framework. An example of four CBUs are shown in figure 1.3, named after the zeolites gmelinite, sodalite, chabazite and Linde Type A respectively.

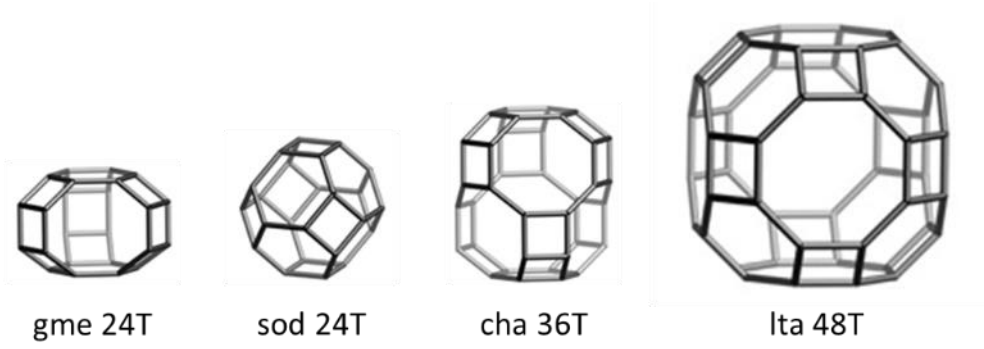

Figure 1.3: An example of some of the CBU units, with the unit name and the number of T atoms.[1]

There are currently 235 recognised zeolite structures in the IZA database, all with a unique assembly of building units. Each structure is assigned a three-letter code by the IZA, this allows zeolites of the same framework type to be grouped together. These frameworks can then be sub-divided into materials with differing compositions.

The material names are often associated with the company or institution where the zeolite was first discovered, such as zeolite ZSM-5 named from Zeolite Socony Mobile – five. Since ZSM-5 was the first zeolite of this framework type, the company name is incorporated into the framework three-letter code MFI coming from **M**obile **Fi**ve. There are now around 30 related materials under the MFI three-letter code, all with the same framework as ZSM-5 but with differing compositions, such as a variation of T-atoms or countercations within the pore. A second example is the zeolite SSZ-13, which has the three-letter code CHA, coming from the naturally occurring zeolite **cha**bazite. There are around 30 materials classed under the CHA framework.

Zeolites exist both naturally and synthetically, with the first natural zeolite, stilbite discovered in 1756 by Cronstedt, a Swedish mineralogist. Naturally occurring zeolites are formed under geological conditions of high temperature (T > 200 °C) and pressure (P > 100 bar); conditions which were transferred into research labs in an attempt to form zeolites synthetically.[4] Therefore, zeolites are now most commonly synthesised under hydrothermal conditions of high pressure and temperature in an autoclave.

The incorporation of cations or organic molecules into the synthesis gel can help to organise the zeolite and provide the desired structure, these are known as structure directing agents (SDAs). For some structures, such as mordenite, a simple cation such as

sodium can be used as an SDA. Other zeolites however, such as SSZ-13, require more complex organic SDAs.[5] These cations or organic SDAs remain within the pores post-synthesis until ion-exchange or calcination is completed to remove them.

Zeolites are net neutral structures. Pure silica zeolites satisfy this neutrality due to the SiO_2 units with Si (4+) and O (2-) charges. The incorporation of other elements, such as aluminium for example, can create a net negative charge due to the 4+ charge of silicon and 3+ charge of aluminium, creating an overall 1- charge for every aluminium atom within the structure. The use of countercations balance this charge, where extra-framework species residing in the pores provide an overall neutral framework.

One stipulation that comes with the incorporation of aluminium into zeolites, is that there cannot be any Al-O-Al bonds, this is known as Loewenstein's Rule.[6] The reasoning behind this, is that the oxygen bridge between two aluminium ions only has stability when at least one of them has the enhanced coordination of five or six, to counteract the coordination of three from the other aluminium. Therefore, in an aluminosilicate framework, the maximum level of aluminium T-atoms is 50 %, this can alternatively be considered as a maximum possible Si/Al ratio of 1.

The combined high porosity and cation inclusion capability of zeolites, as well as a high stability, makes them extremely useful for a range of applications. These range from catalysis and gas storage to water softening and impurity removal from waste water.

1.1.1. Zeolite Applications

Gas storage is an important application for porous materials, with roles in energy, nature, medicine and biology.[7] One of the main features that determine the potential of a porous material for gas storage, is the amount of gas released compared to what can be stored, a factor affected by the bonding of the gas to the material.

The high energy content of hydrogen, along with the clean, non-toxic nature, makes it an extremely desirable source of energy. Many methods of storing and releasing hydrogen on demand have recently been considered.[8] The use of zeolites as hydrogen storage materials found that elevated temperatures and pressures drove the hydrogen molecules within the pores of the zeolite. A return to ambient conditions trapped the hydrogen within the pores. The release of the hydrogen was performed by a return to increased

temperatures, indicating a useful storage and release mechanism.[9–11] The studies found that small cages, such as sodalite, were particularly good at hydrogen uptake.

Zeolites also have medical applications, an area of interest within this thesis. QuikClot Combat Gauze® (QCG) is a zeolite-containing gauze that stops bleeding significantly faster than standard gauze dressings. This is due to the zeolite presence accelerating the body's natural blood clotting cascade.[12] Thanks to the rapid blood clotting, QCG is used by all branches of the US military to limit blood loss from trauma wounds. Secondly, Gadolite Oral Suspension is a gadolinium containing zeolite that has shown promise as a magnetic resonance imaging (MRI) contrast agent. MRI contrast agents help to improve the visibility of internal agents, with oral agents commonly used to image the gastrointestinal (GI) tract. Early studies showed Gadolite Oral Suspension to be a promising candidate with the desired lack of absorption from the GI tract and no adverse side effects.[13]

1.1.2. Catalysis

The inclusion of countercations in aluminosilicate structures can be exploited for catalysis, where the cation can act as an active site. In this thesis, two different active sites have been considered. The first are Brønsted acid sites and the second are copper sites.

1.1.3.1. Acid Sites

There are two types of acidity that can be present in zeolites, Lewis or Brønsted. The difference between the two is that a Brønsted acid site can donate a proton whereas a Lewis acid site can accept an electron pair. Brønsted acid sites are formed by hydroxyl protons that are weakly bound to oxygen bridges between silicon and aluminium atoms, figure 1.4, to balance the framework charge. The higher the aluminium content of the framework, the more acid sites are present. Lewis acid sites are generally formed by surface defects, most of which arise from heat treatments to the zeolite.[14] The thermal treatments can result in extra-framework aluminium species or the presence of trigonal aluminium, both of which have been considered to act as Lewis acid sites.[15,16]

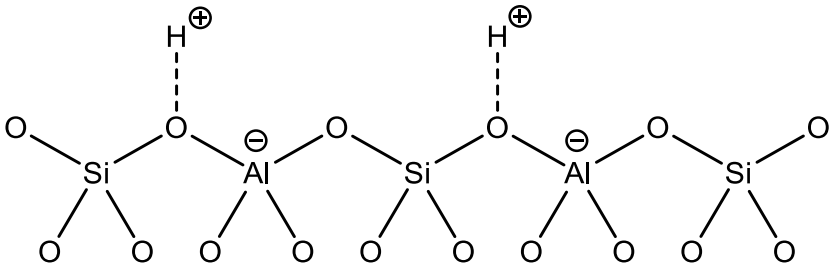

Figure 1.4: Brønsted acid sites in a zeolite, where a proton is weakly bound to a bridging oxygen to balance the overall framework charge.

Fluid catalytic cracking (FCC) is deemed one of the most important catalytic processes in the world.[14] The process converts high molecular weight hydrocarbons to more useful lower weight products, with FCC producing the majority of the world's gasoline. The introduction of acid zeolites to commercial FCC catalysts in the early 1960s was one of the most significant advances in the history of catalytic cracking.[17] The zeolite most commonly used in this process is zeolite Y, this is partly due to the easily tuned acidity, high thermal stability and 3D channel system.[18]

A similar catalytic application that Brønsted acid zeolites are employed for is the cracking of biomass products into smaller more useful products. Isomerisations, such as the formation of mono-branched-chain saturated fatty acids, have been demonstrated with a range of zeolites.[19,20] Furthermore, high temperature reactions of used sunflower oil with H-ZSM-5 resulted in the formation of a range of gaseous and liquid hydrocarbons.[21] These examples indicate the potential of acid zeolites to break down waste biomass products into useful compounds.

Acid zeolites have also been used in other heterogeneous catalysis reactions, including Friedel-Crafts alkylations of benzene and toluene and Beckmann rearrangements of cyclohexanone oxime.[22,23] A further application exploits the shape-selective catalysis of acid zeolites to convert lactic acid into lactide, a precursor of bioplastics.[24]

1.1.3.2. Copper Sites

One of the main applications that use copper zeolites is deNO_x catalysis, the reduction of NO_x emissions from cars. NO_x gases from car exhausts are considered pollutants and therefore a limit on their emission is required.[25] A catalytic converter is required to turn harmful and toxic exhaust gases, such as nitrogen oxides (NO_x) and carbon monoxide into safer gases, such as nitrogen, oxygen and carbon dioxide. This process generally takes place at high temperatures, an example of such is the maximal deNO_x activity of Cu-ZSM-5 that is observed between 823 and 873 K.[26] There are many examples of zeolite catalysts within deNOx reactions, with copper active sites the most predominant.[5,26,27]

In an alternative manner, copper zeolites have been shown to produce nitric oxide at low temperatures, as opposed to the decomposition at high temperatures.[28] Despite being a toxic gas molecule, at lowered concentrations NO has extremely important biological properties. These are discussed further in section 1.2.1. Therefore, the controlled production of NO at lower temperatures is of great interest. Cu-MCM-41 was capable of simultaneously releasing stored NO gas and catalytically producing it from a source of nitrite. A source of cysteine was used as a sacrificial reductant to activate the copper sites and allow the generation of a catalytic cycle. This increased the NO delivery lifetime of the NO-stored zeolite due to the catalytic addition. A second study found similar results with Cu-ZSM-5 and zeolite X.[29] Considering this surprising finding that some deNO_x catalysts can be used for NO production, a selection of zeolites were chosen for the attempted production of nitric oxide.

1.1.4. Zeolites Within this Thesis

Five hydrothermally synthesised zeolites were studied for their catalytic activity. The framework information presented here was obtained from the IZA structural database.[1] The pore size classifications are determined by the largest ring size within the framework, with 8, 10 and 12 rings corresponding to small, medium and large pore zeolites respectively. The dimensionality of the zeolites are considered by the pore openings that are greater than 6 T-atoms. The pore openings are assessed in all three dimensions, providing channel systems of 0, 1, 2 or 3 dimensionalities, figure 1.5.

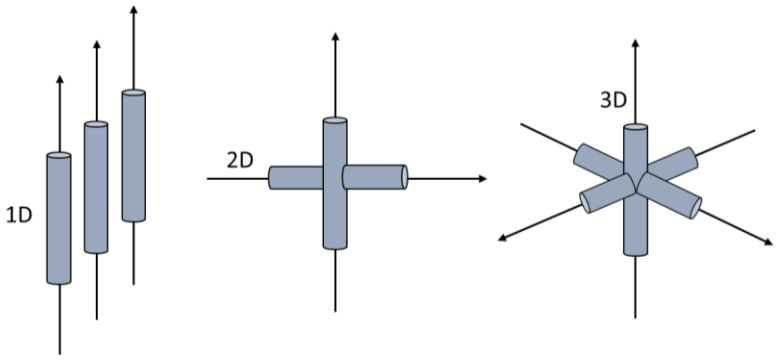

Figure 1.5: An illustrative example of 1D, 2D and 3D channel systems in zeolites. The pore openings and channel connectivity determine the dimensionality of the zeolites.

Determining the locations of the active sites in each zeolite is beneficial when studying the different properties of the zeolites, including catalytic activity. The copper locations within many zeolites are relatively well studied due to the use of the zeolites as catalysts for different reactions, as discussed in section 1.1.3.2.

The general method of copper insertion involves a copper solution. The aqueous ion exchange conditions promote fully hydrated octahedral copper species that are capable of accessing the larger pores but not the 6-membered rings.[30] Once the copper enters the pores and the water is removed, the copper then coordinates to the framework oxygen. This coordination is related to the aluminium distribution that provides the stabilising negative charge for the copper cation.

Dependant on the number of copper atoms present within the pores, copper clustering can occur, this is most common in over-exchanged zeolites where the Cu/Al ratio exceeds 0.5. Certain conditions can also reduce the Cu^{2+} to Cu^{+}, such as high temperature or inert atmosphere; this can result in binuclear copper species.[31] Furthermore, it has been proposed that the copper reduction can result in the expulsion of aluminium from the framework and into the pores as extra-framework aluminium species.[16]

The variety of factors affecting the copper species and locations has led to the use of a range of techniques to further understand the copper ion exchange of zeolites. Some of the most useful techniques to detect Cu^{2+} species include ultraviolet-visible (UV-vis) spectroscopy and electron paramagnetic resonance spectroscopy (EPR), this is due to the characteristic blue colour and unpaired electron respectively.[32] Computational quantum

mechanical modelling, such as density functional theory (DFT), has also proved to be very important at predicting the copper coordination within a zeolite.[33]

General trends observed for zeolites place the preferred Cu^{2+} location in 6-membered rings that contain 1, 2 or 3 aluminium atoms. The copper has preferential coordination with the oxygen atoms from the tetrahedral aluminium due to their higher basicity from the shared aluminium negative charge.[32] Although this general trend has been observed, further literature information is available for a number of the zeolites within this thesis.

1.1.4.1. Mordenite

Mordenite has ring sizes of 12, 8, 5 and 4, classing it as a large pore structure. It is a naturally-occurring zeolite and has the MOR framework. The all-silica framework is shown in figure 1.6 in the a, b and c direction. The c-direction contains all ring sizes, with a compressed 8-membered ring "side-pocket" running alongside the 12-membered channel with the 4 and 5-membered rings connecting the two larger rings. The b-direction contains a series of 8 rings that zig-zag through the structure, creating a smaller channel of 6 T-atoms running through the framework. The a-direction contains smaller ring sizes, creating a restricted channel entrance.

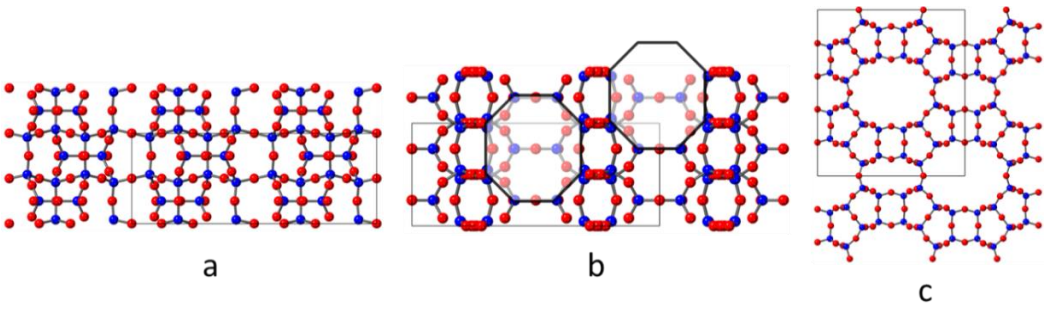

Figure 1.6: The ball and stick model of pure-silica MOR in the a, b and c directions, where blue is silicon, red is oxygen and the grey box represents the unit cell. The 8-membered rings in the b-direction are highlighted by the black octagon, due to the appearance of 6-membered rings created from zig-zagging 8 rings.

Mordenite is classified as a 2D channel system on the IZA, but the overlapping 8 rings limit the space in the b direction, limiting larger molecules from accessing the zeolite. Figure 1.7 shows the channel system voids in all directions, obtained from the IZA. The lack of channels in a, the limited channels in b and the open channels in c can all be observed.

The maximum diameter of a sphere that can diffuse along the a, b and c direction is 1.57 Å, 2.95 Å and 6.45 Å respectively.

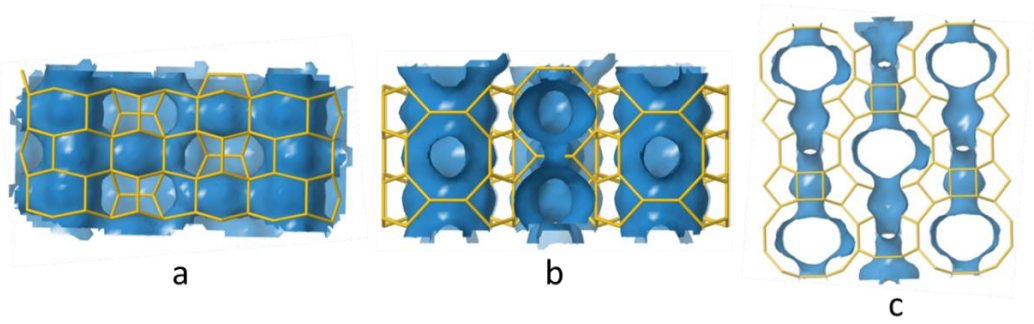

Figure 1.7: The channel systems of MOR where the blue represents the channels.

The copper location of Cu-MOR has been determined by *in situ* X-ray absorption spectroscopy (XAS). The results found the copper as trinuclear Cu-oxo clusters located at the entrance to the 8-membered pocket.[34] Ultraviolet-visible (UV-vis) and Raman spectroscopy also studied the copper location and were in agreeance with sites at the entrance of the side pockets.[35]

The amount of copper in the zeolites can influence the preferred copper locations, with the copper levels related to both the Si/Al ratio and the copper loading. One study found that high copper loadings, corresponding to a Cu/Al ratio of 0.43 in mordenite with a Si/Al ratio of 5, resulted in the presence of mononuclear Cu^{2+} sites.[31] It was found that in this sample of copper mordenite, 30 % of the copper occupied these mononuclear sites, which were determined to have square planar and distorted square pyramidal coordination.

1.1.4.2. Ferrierite

Ferrierite has ring sizes of 10, 8, 6 and 5, classing it as a medium pore structure. Ferrierite is a naturally-occurring zeolite and has the FER framework. The all-silica FER framework is shown in figure 1.8 in the a, b and c direction, where the 10, 6 and 5 rings can be seen in the c-direction. The 8-rings running in the b-direction create a second open channel. Finally, the a-direction contains 5, 6 and 10 rings that are blocked further into the zeolite with interconnecting pores.

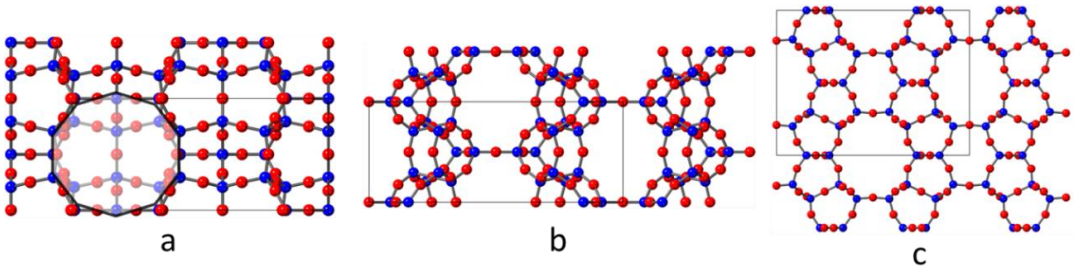

Figure 1.8: The ball and stick model of pure-silica FER in the a, b and c directions, where blue is silicon, red is oxygen and the grey box represents the unit cell. The 10-membered ring in the a-direction has been highlighted by the black decagon.

Ferrierite is classed as a 2D zeolite with channels running in the b and c-direction, as shown in figure 1.9. The maximum diameter of a sphere that can diffuse along the a, b and c direction is 1.56 Å, 3.40 Å and 4.69 Å respectively.

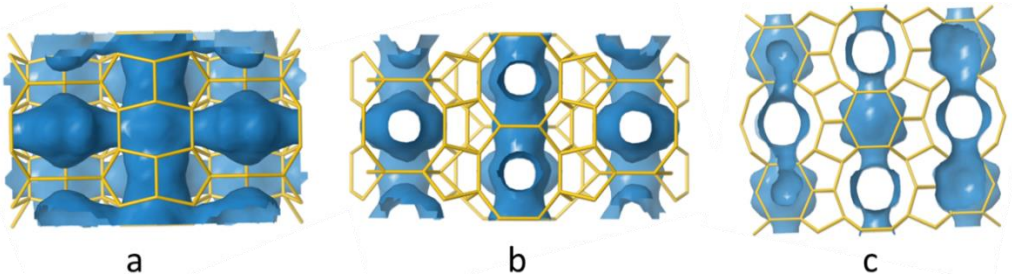

Figure 1.9: The channel systems of FER where the blue represents the channels.

Density functional theory (DFT) and Fourier-transform infrared (FTIR) measurements predicted two main locations for the Cu^{2+} ions.[36] The first is located in an elongated 6-membered ring, formed by two adjacent 5-membered rings, present on the wall of the main channel. The second site is another 6-membered ring, this time within an 8-membered channel. This DFT/FTIR ferrierite sample had a Si/Al ratio of 8.6 and a Cu/Al ratio of 0.35.

A second study predicted a different copper location using synchrotron X-ray diffraction (XRD) and electron spin resonance (ESR).[37] The location of Cu^{2+} was determined to reside at the intersection between the 8 and 10-membered channels. The difference in findings may be due to the different copper loadings from the two studies. The ferrierite in this study had a Si/Al ratio of 14.4 and a Cu/Al ratio of 0.09, substantially less copper than the previous DFT/FTIR study. It may be that preferential sites are occupied with different levels of copper within the pores.

1.1.4.3. ZSM-5

ZSM-5 has ring sizes of 10, 6, 5 and 4, classing it as a medium pore structure. ZSM-5 has the MFI framework, with the name derivation previously discussed in section 1.1.1. The all-silica MFI framework is shown in figure 1.10 in the a, b and c direction. Both the a and c-directions have 10-membered rings that are slightly intersected throughout the structure. The b-direction shows 10 rings that are open throughout the structure, creating a large channel.

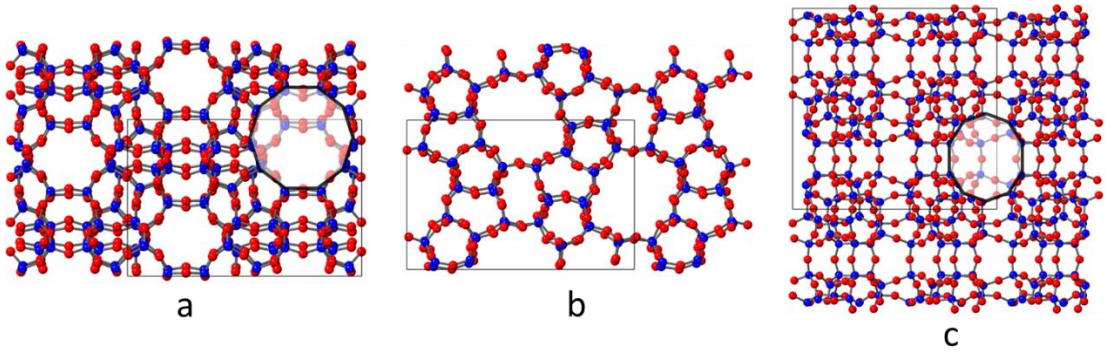

Figure 1.10: The ball and stick model of pure-silica MFI in the a, b and c directions, where blue is silicon, red is oxygen and the grey box represents the unit cell. The 10-membered rings in the a and c-directions have been highlighted by the black decagon.

The IZA defines ZSM-5 as a 3D channel system, with the maximum diameter of a sphere that can diffuse along the a, b and c direction as 4.70 Å, 4.46 Å and 4.46 Å respectively. The 3D channel system is shown in figure 1.11.

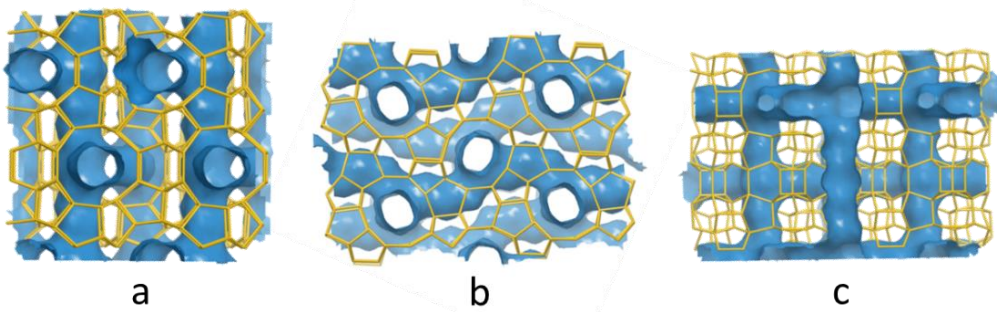

Figure 1.11: The channel systems of MFI where the blue represents the channels.

Cu-ZSM-5 is extremely well studied due to the high catalytic activity for deNO_x catalysis.[26] Early studies determined Cu^{2+} to exist as Cu-oxo clusters in small cages as well as in open channels.[38,39] This was determined from the fact that small cages with 5- or 6-membered ring apertures are accessible to Cu^{2+} ions but inaccessible to hydrated Cu ions. More

recent studies utilised Raman spectroscopy and DFT calculations to locate the copper as Cu_2O species located in the 10-membered ring.[40] This has also been confirmed by powder X-ray diffraction (PXRD) measurements.[41]

1.1.4.4. SSZ-13

SSZ-13 has ring sizes of 8, 6 and 4, classing it as a small pore structure. It has a CHA type framework, named after the zeolite chabazite. The all-silica CHA framework is shown in figure 1.12 in the a, b and c direction. The a and b-directions are extremely similar, consisting of 8 and 4-membered rings. The c-direction consists of 6-membered rings connected through 4-membered rings.

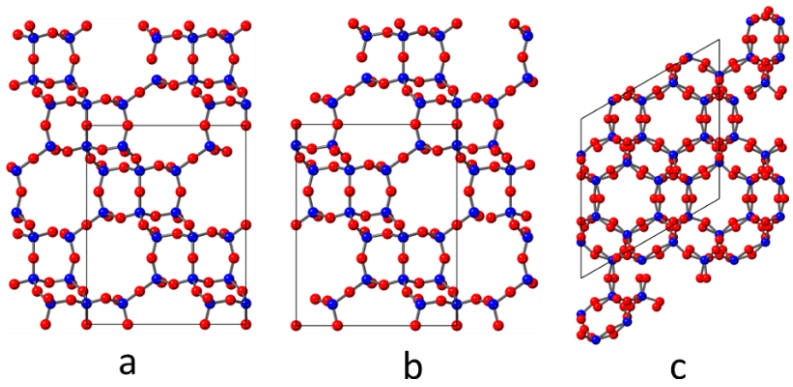

Figure 1.12: The ball and stick model of pure-silica CHA in the a, b and c directions, where blue is silicon, red is oxygen and the grey box represents the unit cell.

SSZ-13 has a 3D channel system due to the 8 rings in the a and b directions and the 6 rings in the c direction, figure 1.13. The c-direction channels appear slightly confined, most likely due to the compact 6-membered ring. The maximum diameter of a sphere that can diffuse along the a, b and c direction is 3.72 Å, 3.72 Å and 3.72 Å respectively.

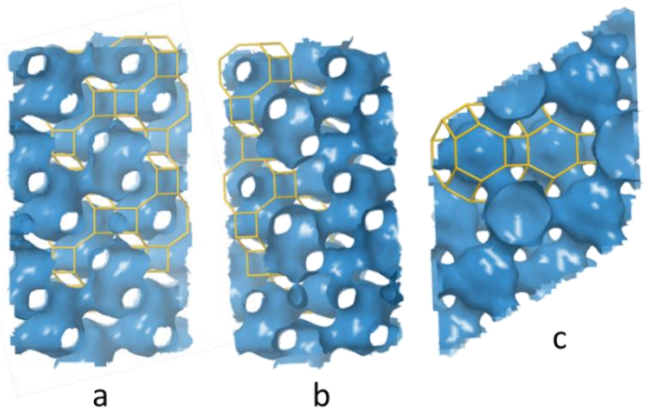

Figure 1.13: The channel systems of CHA where the blue represents the channels.

The location of the copper sites in Cu-SSZ-13 have been determined to be located just outside the plane of the 6-membered ring, using Rietveld refinement of variable-temperature XRD synchrotron data.[5] This was supported by data collected by *in situ* UV-vis spectroscopy and XAS, however this was with SSZ-13 with a Cu/Al ratio of 0.18.[42]

It has been reported, that Cu-SSZ-13 structures with a higher Cu/Al ratio, first fill the 6-membered ring and then occupy space by the 8-membered ring. This has been confirmed initially by FTIR and hydrogen temperature-programmed desorption (H_2-TPD) and supported by electron paramagnetic resonance spectroscopy (EPR). Due to the optimal exchange level of Cu/Al of 0.5 used throughout this thesis, it can be assumed that the copper ions would reside both in the 6 and 8-membered rings.[43,44]

1.1.4.5. UZM-4

UZM-4 has ring sizes of 12, 8, 6 and 4, classing it as a large pore structure. UZM-4 has the BPH framework type, named after the structure of zeolite **b**eryllo**p**hosphate-**H**. The all-silica BPH framework is shown in figure 1.14 in the a, b and c direction. The a and b-directions are similar with a mixture of 8, 6 and 4-membered rings. Some of the 8 rings are open, while others are partially blocked by deeper intersecting rings. The c-direction is composed of the large 12-membered rings connected by 4-membered rings.

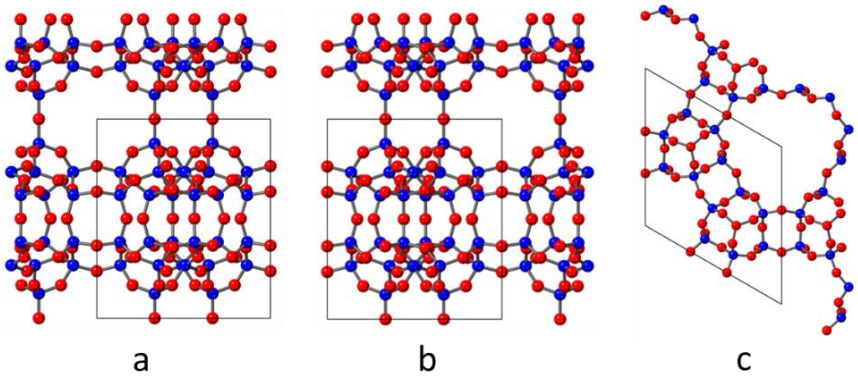

Figure 1.14: The ball and stick model of pure-silica BPH in the a, b and c directions, where blue is silicon, red is oxygen and the grey box represents the unit cell.

UZM-4 has a 3D channel system due to the large open pores in all three directions, as shown in figure 1.15. The maximum diameter of a sphere that can diffuse along the a, b and c direction is 3.51 Å, 3.51 Å and 6.01 Å respectively.

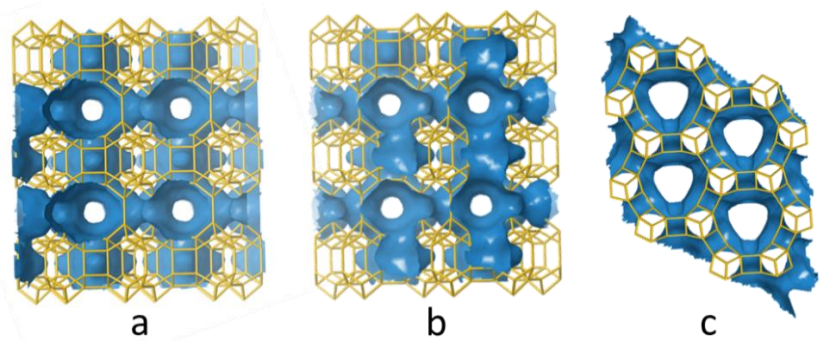

Figure 1.15: The channel systems of BPH where the blue represents the channels.

Unfortunately, there is currently no literature that studies the cation siting of Cu-UZM-4. Literature sources reveal the high aluminium content in UZM-4, with Si/Al ratios ranging between 1.78 and 2.66.[45–47] This indicates that there would be a high level of copper if the sample was exchanged to the copper form.

1.1.5. The ADOR Process

The ADOR process is a method of producing zeolites that may not have been possible to synthesise through typical hydrothermal methods. ADOR stands for Assembly-Disassembly-Organisation-Reassembly and forms new zeolite frameworks through the break-down of a parent zeolite. A schematic of this process is shown in figure 1.16.

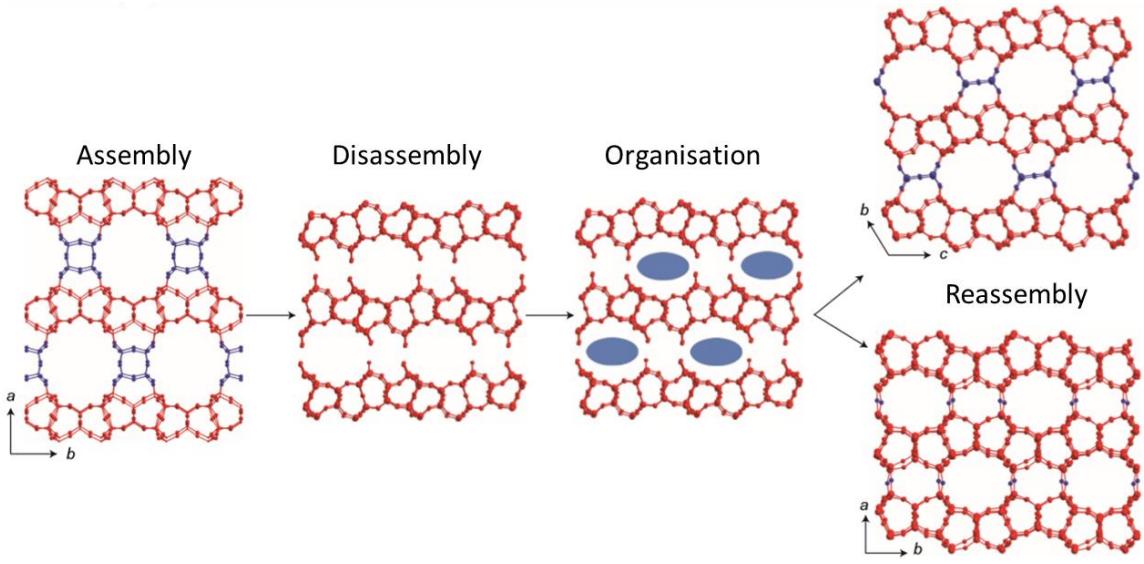

Figure 1.16: An adapted schematic of the ADOR process where red is the layer topology that is consistent throughout, the blue structures highlight the area undergoing change and the blue ovals correspond to organic molecules that help to organise the layers.[48] The parent zeolite is Ge-UTL and the resulting zeolite products are IPC-2 (top) and IPC-4 (bottom).

The process takes advantage of chemical weakness in the parent zeolite structure; namely hydrolytic Ge-O bonds that are susceptible to hydrolysis. The original parent zeolite of the ADOR process was UTL, although the process has since been expanded to UOV and the newly synthesised SAZ-1.[48–50] The synthesis of this initial parent zeolite is known as the assembly stage of the ADOR process.

The Ge-O bonds of UTL are situated in double-4-rings (d4r) due to the larger size of the germanium atoms than the silicon.[51] Hydrolytic removal of these units produces a material with UTL-like layers connected only by hydrogen bonding through silanol groups. The layered material is known as IPC-1P and represents the disassembly step.[52]

The next stage in the process is the organisation of the IPC-1P layered material. The conditions of the organisation step depend upon the desired end product. Up until now, there have been six different end products from the UTL ADOR process reported.[48,53,54] IPC-2 and IPC-4 were the first two ADOR products formed. The IPC-2 connections contain single-4-rings (s4r) between the layers that are formed from the incorporation of diethoxydimethylsilane. IPC-4 contains a single oxygen linkage between the layers, in this case no further silica sources were required, but octylamine was used to order the layers.

It was found that hydrolysis under near-neutral conditions removes all the d4r units from between the UTL layers, while hydrolysis using 12 M hydrochloric acid (HCl) removes only half the d4r units.[53] This finding was exploited to synthesise IPC-6 and IPC-7, two zeolites with alternating connections between the layers. IPC-6 has a mixture of oxygen linkages and s4r whereas IPC-7 has a mixture of s4r and d4r.

Lastly, IPC-9 and IPC-10 were formed from a new mechanism within the ADOR process, a shift of layers. With the use of choline cations, it is possible to shift the IPC-1P layers. The effect of the choline intercalation on the arrangement of multiple layers is dependent on the amount of choline included. With a choline:silanol ratio of 1:4, the most favourable layer shift is along the crystallographic b axis, a choline:silanol ratio of 1:2 shows a favourable shift along the crystallographic c axis.[54] The shifted layers were again connected through both a direct oxygen linkage, IPC-9, and through a s4r, IPC-10. One of the most interesting properties of these zeolites is the inclusion of odd-numbered rings within the structure, with IPC-9 containing 7-membered rings and IPC-10 containing

9-membered rings. These odd-numbered rings are not very common in zeolite frameworks, with only five containing 7-membered rings and eleven containing 9-membered rings.[1,55]

The final stage of the ADOR process is the reassembly. This is generally performed by a calcination to remove the organics and condense the silanol groups. The resulting family of zeolites produced are known as "isoreticular", meaning that they have the same overall topological features but different pore sizes. A summary of the isoreticular zeolites produced from UTL so far are discussed in table 1.1. The new family of zeolites formed from this process are also often known as "daughter zeolites".

Table 1.1: The new zeolites formed from the ADOR process of UTL, including the layer connections and the ring sizes of the newly formed rings. The ring sizes of UTL correspond to the two rings that are altered during the ADOR process.

Zeolite	Layer Connection	Ring Sizes
UTL	d4r	14 and 12
IPC-2	s4r	12 and 10
IPC-4	direct oxygen	10 and 8
IPC-6	s4r and oxygen	12, 10 and 10, 8
IPC-7	d4r and s4r	14, 12 and 12, 10
IPC-9	**shifted**, direct oxygen	7 and 10
IPC-10	**shifted**, s4r	9 and 12

One paper of interest looked to aluminate a series of zeolites from the ADOR family to be able to use them as catalysts for the alkylation of toluene with isopropyl alcohol.[56] Traditional Ge-UTL was synthesised along with aluminium UTL.[57] The Ge-UTL was hydrolysed in the presence of aluminium nitrate, resulting in aluminated IPC-1P that was then used to form aluminated IPC-2 and IPC-4. Aluminated IPC-6 and IPC-7 were also prepared with altered hydrolysis steps. The Al-UTL and the Al-IPC-2, 4, 6 and 7 were used as acid site catalysts for toluene alkylation. The results of the toluene conversion were assessed by gas chromatography, with increased conversion corresponding to increasing size of zeolite rings, in the order IPC-4<IPC-6<IPC-2<IPC-7<UTL.

1.2. Nitric Oxide

The zeolites described previously (section 1.1.4) are the catalysts discussed throughout this thesis. The target molecule of the catalysis is nitric oxide. NO is a very reactive, colourless, free radical gas. NO is well known as a toxic gas present in cigarette smoke and smog as well as a contributor to ozone damage and a precursor to acid rain.[58] In the late 80's, biological activity from NO was determined as the endothelial-derived relaxing factor (EDRF).[59,60] EDRF was an unknown chemical produced from arteries that caused muscle relaxation, resulting in vasodilation. The discovery of the essential biological properties of NO led to the gas being awarded "Molecule of the Year" in 1992.[58] Further to this, in 1998, the Nobel Prize in physiology or medicine was awarded to Robert F Furchgott, Louis J Ignarro and Ferid Murad for their work identifying nitric oxide (NO) as a signalling molecule in the cardiovascular system.[61] The signalling properties of NO means that the production of NO by one cell can trigger a response in another.

1.2.1. Biological Importance

NO plays an important role in many areas of the body, including antimicrobial action in the immune system, neuronal signalling in the nervous system and vasodilation in the cardiovascular system.[62] Focussing on the cardiovascular system, blood arteries are lined by a layer of endothelial cells, known as the endothelium. The endothelium is responsible for the production of NO, the EDRF. The NO diffuses to the vascular smooth muscle cells and activates guanylate cyclase, which leads to cGMP-mediated vasodilation, the relaxation and widening of blood arteries.[63] This is an important function as it can help to control blood pressure by altering the flow.

A further example of the signalling shown by NO is in the inhibition of platelet formation. Platelets are anucleated cells present in the blood which often aggregate together upon endothelial cell damage.[64] The clotting mechanism is one which is extremely important within the body to limit blood loss. The formation of blood clots when not required however, can cause serious health conditions, such as angina and myocardial infarction, which can be fatal. The inhibition of platelet aggregation by nitric oxide has been shown in work with a nitric oxide releasing zeolite (NO-Z), where NO was stored within the zeolite.[65] Figure 1.17 below shows the effect of NO on platelet cells shown by scanning

electron microscopy (SEM) imaging. The left-hand image shows the aggregation of platelet cells in the absence of NO, the right-hand image however shows the inhibition of aggregation due to the release of NO. Further action of NO signalling includes inhibition of vascular smooth muscle cell proliferation.[62]

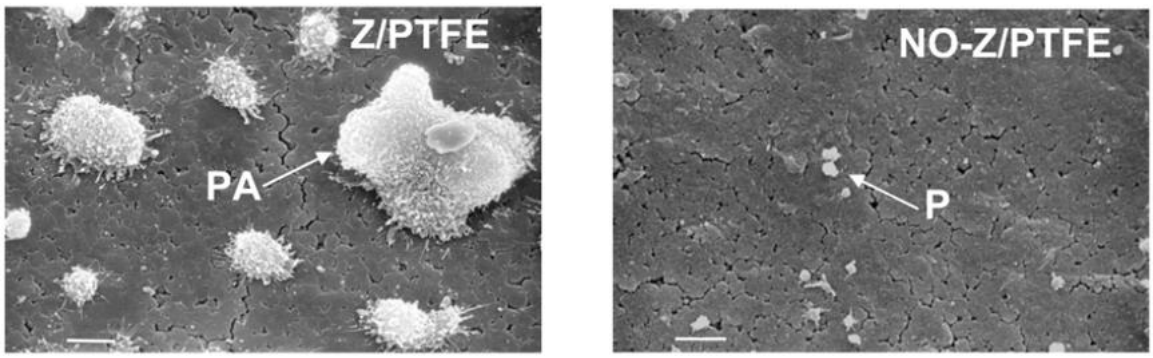

Figure 1.17: SEM images showing the difference in platelet aggregation with and without NO present. The gas-free zeolite (left) shows white clumps where platelet aggregation (PA) has occurred. The NO-loaded zeolite (right) shows single platelet cells (P) where aggregation has been prevented by NO.[65]

Biologically, NO is produced from the amino acid L-arginine by the enzyme nitric oxide synthase (NOS). The substrate, L-arginine, undergoes a two-step oxidation to L-citrulline via hydroxy-L-arginine, with molecular oxygen and reduced nicotinamide-adenine-dinucleotide phosphate (NADPH) as co-substrates, as shown in figure 1.18. The resulting products are one molecule of NO and one of L-citrulline, along with two molecules of water.

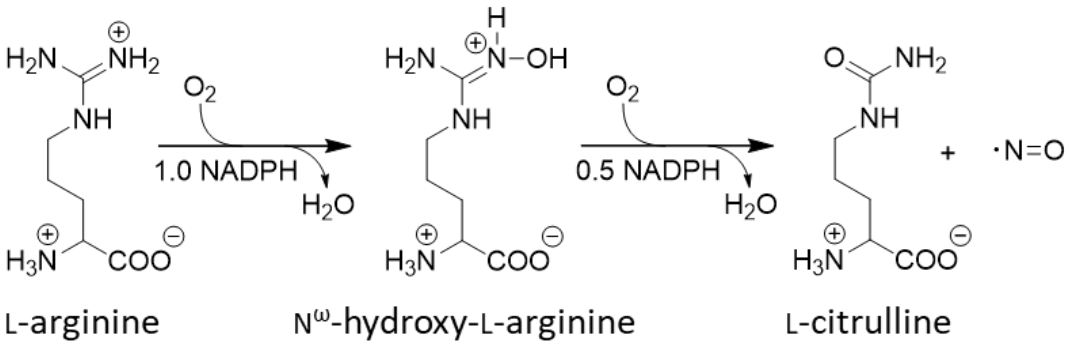

Figure 1.18: The biological production of nitric oxide from L-arginine by NOS enzymes.

NOS exists in three different isoforms; endothelial (eNOS), neuronal (nNOS) and inducible (iNOS), with each isoform acting in different locations in the body and performing

different functions. eNOS is expressed by the endothelial cells, nNOS by neurons in the brain and iNOS in the immune system.[62]

When oxygen is present, the NOS pathway is the main formation of biological NO. In hypoxic conditions however, a second pathway contributes to NO production, the nitrate-nitrite-NO pathway.[66] The nitrate-nitrite-NO pathway can work complementarily next to the NOS pathway in situations where the oxygen-dependent NOS enzyme activities are compromised. Nitrate and nitrite are present in the body from two main routes; firstly from NO that has been oxidised in the blood and tissues and secondly through the diet.[67] There are a number of pathways that can further reduce nitrite to NO.

$$\begin{aligned} NO_2^- + H^+ &\rightarrow HNO_2 \\ 2HNO_2 &\rightarrow 2N_2O_3 + H_2O \\ N_2O_3 &\rightarrow NO^\bullet + NO_2 \end{aligned} \qquad (1.1)$$

One of these pathways is through a reaction with protons, the reaction of which can be seen in equation 1.1.[68] Other reactions include interactions with metals present within the body, including Fe^{2+} from deoxyhaemoglobin or myoglobin and Mo^{4+} from xanthine oxidoreductase.[66]

1.2.2. Nitric Oxide Delivery Systems

Nitric oxide is delivered as a therapeutic agent for a range of disorders, including cardiovascular disease, erectile dysfunction and cancer.[37,69,70] The delivery of NO can be troublesome due to the negative implications of concentrations that are too high or too low. A lack of NO can result in heart attacks or strokes due to blocked arteries or infection due to a limit of the antithrombotic and antimicrobial properties. On the other hand, an increase in NO concentrations may lead to toxic responses. Toxic levels of NO can interfere with cell proliferation, cause DNA strand break or react with a superoxide anion to form peroxynitrite, a cytotoxic oxidant which can interact with lipids, DNA and proteins, often resulting in cell apoptosis.[71,72]

There are a number of methods for delivering NO, with ranging modes of action. One of the first methods was the use of NO donor materials, chemicals that decompose within the body to release NO. The most common examples are sodium nitroprusside (SNP) and glyceryl trinitrate (GTN), figure 1.19, which have been used clinically for years.[73] SNP is

commonly required to provide a rapid lowering of blood pressure in hospitals when high blood pressure becomes a serious issue. GTN is often used as a pain relief for angina, the condition where there is a restriction of blood to the heart causing chest pain.[74] In both cases, the vasodilatory properties of NO are employed. SNP has also been used on a stent coating to provide NO to the artery.[75]

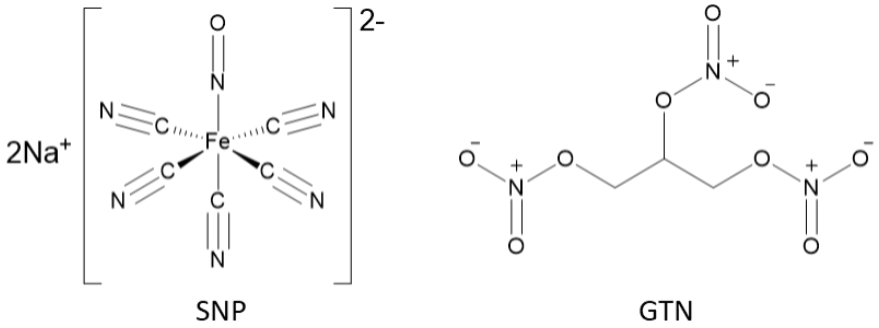

Figure 1.19: The chemical structures of sodium nitroprusside (SNP) and glyceryl trinitrate (GTN), two NO donors that decompose to release NO.

Other methods have looked into storage and release mechanisms, where the NO gas is stored within a structure and released upon exposure to moisture. The adsorption of NO onto the pores of Co-exchanged zeolite A can be desorbed through the displacement of the NO molecules by water molecules.[65] These properties were suggested for use in medical coatings, such as catheters, to prevent thrombosis formation.[76] A further application is wound healing, where the antimicrobial action of NO can help to prevent infection of the wound. The same mechanism can also be applied to metal-organic frameworks (MOFs), with the activation-loading-delivery NO cycle within a MOF shown in figure 1.20.[77] The MOF is initially dehydrated to remove water from the pores, known as the activation. The loading is performed by exposing the MOF to NO under pressure to load the gas into the pores. The gas can then be released upon exposure to moisture, where the water displaces the bound NO molecules.

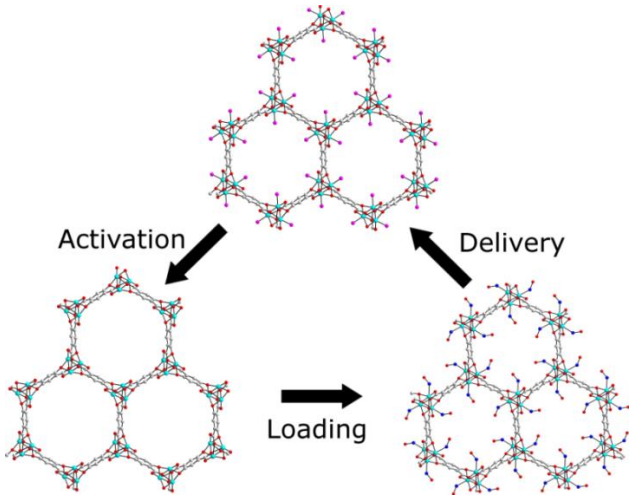

Figure 1.20: The activation, loading and delivery of NO from a porous material. The sample is dehydrated to activate the sample (bottom left), this can then be loaded with NO (bottom right); exposure to moisture then delivers the NO when required (top).

While these delivery mechanisms are a great way of controlling NO release, a limitation that arises is the lifetime of the NO production. The main issue is the restriction of the amount of NO released is directly related to the mass of NO donor that can be delivered and the maximum volume of NO gas that can be stored in a material.

A catalytic production of NO would allow for long-term NO production. This could both enhance some of the current methods of delivering NO and also open up new opportunities for NO production. One such example is NO production from the coating of a stent, a medical device that once inserted can remain in place for years.

1.3. Stents

A stent is a medical device that is required to widen an artery that has been narrowed or blocked, to allow blood flow to return to normal. They are small mesh metal tubes that are inserted around a balloon that is fed to the narrowed section of the artery along an inserted catheter. The balloon is inflated when it has reached the desired location, simultaneously expanding the stent against the walls of the artery. The balloon is then deflated and removed, leaving the stent behind to hold open the artery. This procedure of stent insertion is known as angioplasty.

Although the insertion of a stent can help to avoid major medical issues, such as cardiac arrest, there are still some concerns that follow after stent insertion.[78] The insertion of a stent can damage the surrounding endothelial cells of the artery. As mentioned previously, endothelial cells produce NO that helps to prevent platelet aggregation and encourages healthy cell growth. Therefore, this endothelial cell damage can prevent the release of NO. This results in both scar tissue growth within the damaged artery and platelet aggregation onto the surface of the stent.[79] This combination of effects can result in a build-up of tissue and platelet cells around the stent that can begin to block the artery once again. In some cases, the initial artery narrowing that the stent was employed to overcome can actually result in the recurrence of the narrowing, known as restenosis. The specific term for restenosis caused by stent insertion is known as stent thrombosis. Although advances in medicine have reduced the number of incidences of stent thrombosis over the years, there is still a mortality rate of around 7 % for those who have a stent inserted.[80]

The first angioplasty procedures deployed bare metal stents (BMS) to the affected area. A problem of restenosis became apparent after insertion of these stents due to the body's natural defence mechanism to the unknown material. Attention then turned to drug-eluting stents (DES) which release compounds that target inflammation and vascular smooth muscle cell proliferation.[81] Anti-proliferation compounds such as sirolimus and paclitaxel showed a reduction in the number of cases of restenosis compared with bare metal stents as there was a decreased growth of scar tissue.[82] A risk with using these drugs however is the slow regrowth of the endothelial cells, which are damaged upon insertion

of a stent, increasing the risk of thrombosis formation. Therefore, antiplatelet therapy (APT) is commonly used after DES insertion, where anticoagulants are taken for a period of time to thin the blood and decrease the chances of stent thrombosis occurring.[83]

One of the problems with the use of anticoagulants is selectivity, as it is not possible to localise the blood thinning and therefore other health risks can occur. A second issue is the length of time that the anticoagulants should be taken for, as stopping too early may result in the formation of stent thrombosis, continuing for too long however could lead to further medical issues. A resultant increase in late stent thrombosis in DES has been observed once APT has been stopped, highlighting the issue of time.[84]

A nitric oxide producing stent coating could be a viable solution for overcoming the issue of stent thrombosis, where the zeolite could provide local NO production, as opposed to systemic. One factor that would need to be considered, is the connection of the zeolite to the metal stent.

1.4. Polymers

A polymer coating was deemed the best option for connecting the zeolite powder to a metal stent. Polymers are molecules that are formed from a number of repeating building blocks, known as monomers, usually connected by covalent bonds.[85] The terms are coined from the Greek language, where *poly*, *mono* and *meros* translate to many, one and part respectively, providing definitions of polymer as “many parts” and monomer as “one part”.[86] The properties of different polymers vary depending upon a number of factors, including the monomer units and the bonds that connect them together. Three polymer properties that are useful for the desired stent coating application are robustness, flexibility and porosity. This is to provide a coating that would survive for a long time within the body, be able to move with the expansion and contraction of a stent and have enough space for the substrates to access the zeolite and for any NO produced to be able to escape to the surrounding cells.

A total of five polymers were considered during this work, with three of them belonging to the family of polymers known as polymers of intrinsic microporosity (PIMs). The other two polymers were polyurethane and polyvinylchloride.

1.4.1. Polyurethane

Polyurethanes are polymers that contain multiple urethane bonds, they are usually synthesised from the reaction between isocyanates and polyols.[87] These polymers are generally rubber-like with good physical properties, making them good candidates for applications that require flexibility and durability.[88] The polyurethane used in this work is MDI-polyester/polyether polyurethane, where MDI is methylene diphenyl diisocyanate, the varying polymer composition is shown in figure 1.21.

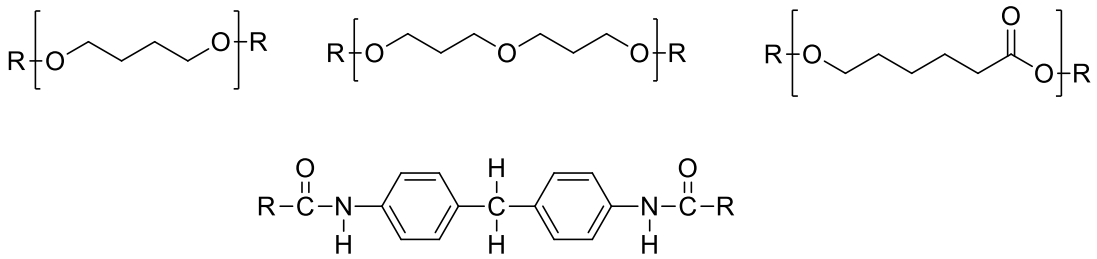

Figure 1.21: The structure of MDI-polyester/polyether polyurethane with the various monomer units (top) that connect the urethane linkages (bottom).

Zeolite incorporation into polyurethane has been used for a wide range of applications, mainly focussed on separation or storage and release mechanisms.[89–91] Regarding NO, there are a range of applications that look at NO release directly from polyurethane. A couple of examples considered the incorporation of the NO donor diazeniumdiolate, also known as NONOate, into the polymer, which slowly decomposes upon exposure to water, with NO released as a consequence.[92,93] The results showed promising biological effects, with a reduction in platelet adhesion and an increase in endothelial cell growth. A further technique incorporated active S-nitrosothiol functionalities onto the polyurethane backbone.[94] NO was released from the nitrosothiol upon exposure to both light and physiological conditions.

1.4.2. Polyvinylchloride

Polyvinylchloride (PVC) is composed of vinyl chloride monomer units, figure 1.22. PVC is frequently mixed with heat stabilisers, lubricants, plasticisers and other additives to help polymer processing, this however can have an influence on the physical properties.[95]

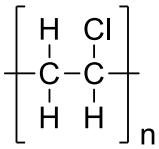

Figure 1.22: The structure of polyvinylchloride (PVC).

PVC was considered a plausible polymer option due to previous work within the literature using NO-releasing MOF/PVC polymer composites.[96] The MOF $H_3[(Cu_4Cl)_3–(BTTri)_8]$ (BTTri = 1,3,5-tris(1H-1,2,3-triazol-5-yl)benzene), known as CuBTTri, was incorporated into polymer films prepared from PVC plasticised with dioctyl sebacate (DOS). The MOF/polymer film was then used to study the decomposition of S-nitroso-N-acetylpenicillamine (SNAP), an S-nitrosothiol. The results showed an enhanced SNAP decomposition for the Cu-MOF/PVC film in phosphate buffered saline (PBS) compared to the decomposition in PBS only.

1.4.3. Polymers of Intrinsic Microporosity

Polymers of intrinsic microporosity (PIMs) are polymer materials that exhibit microporosity, free volume consisting of interconnected pores of a diameter less than 2 nm.[97] The microporosity is obtained by the use of bulky, rigid monomer units that cannot efficiently pack together. PIMs are generally formed by the reaction of fluorinated or chlorinated monomer units with molecules containing multiple catechol units, figure 1.23, this is the case for the first of the PIMs studied in this work, PIM-1.[98]

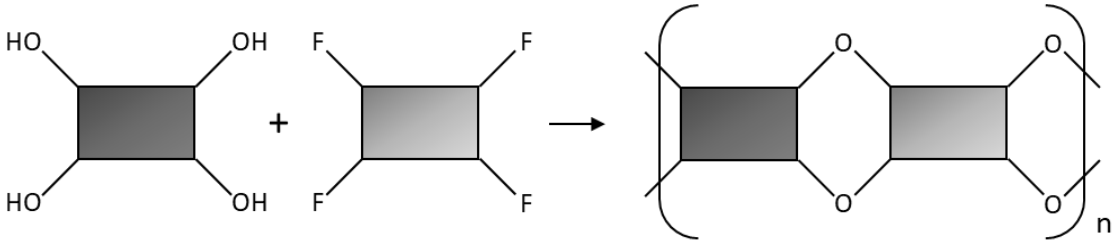

Figure 1.23: The standard formation of PIMs from the reaction of a fluorinated or chlorinated molecule with a catechol-containing molecule.

The structure of PIM-1, figure 1.24, is synthesised from 3,3,3,3-tetramethyl-1,1-spirobi-sindane-5,5,6,6-tetrol and 2,3,5,6-tetrafluoro-phthalonitrile. It was one of the first PIMs prepared and has a high surface area of 760 – 850 m^2g^{-1}.[99,100] PIM-1 has a high solubility in THF and chloroform, allowing for easy handling to form membrane films.

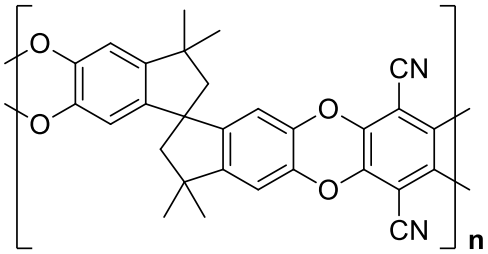

Figure 1.24: The structure of PIM-1.

The other two PIMs studied in this work are from the PIM-EA-TB (ethanoanthracene Tröger's base) family. These PIMs are not formed in the same as way as PIM-1, they are instead formed by the polymerisation of the *in situ* Tröger's base (2,8-dimethyl-6H,12H-5,11-methanodibenzo[b,f][1,5]diazocine) formation reacting with the ethanoanthracene monomer.[101] The hydrogen and methyl form of EA-TB were used in this work, figure 1.25, with the presence of the methyl groups or hydrogens governed by the monomer unit. The PIM-EA-TB structures show a greater surface area than PIM-1 with a value of 1028 m^2g^{-1}.[101] This family of PIMs also have a high solubility in THF and chloroform.

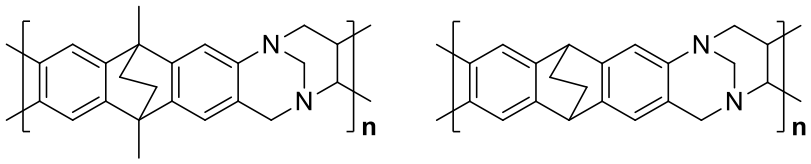

Figure 1.25: The structure of PIM-EA-TB(Me) (left) and PIM-EA-TB(H_2) (right).

The microporosity of PIMs has been exploited for many applications, including membranes and sensors. One membrane application has shown the separation potential of PIM-1 by transporting organics, such as phenol and aliphatic alcohols, from water.[100,102] This separation capability indicates a hydrophobic nature of PIM-1. A second application considered PIM-1 as a visual indicator of trace organic vapours, where the PIM-1 thin film changed colour upon exposure to a wide range of volatile organic compounds.[103] The high surface area of PIM-EA-TB has made it an excellent candidate for gas separation applications. A study considering the permeation of nitrogen, oxygen, carbon dioxide, methane, hydrogen and helium found that PIM-EA-TB shows promise for separations involving hydrogen, as well as the potential to separate oxygen from nitrogen.[101] Further applications using PIM-1 and PIM-EA-TB include hydrogen storage and heterogeneous catalysis, highlighting the impact of PIMs across ranging applications.[104,105]

1.5. References

1 www.iza-online.org, September 2018.

2 C. Baerlocher, W. M. Meier and D. H. Olson, *Atlas of Zeolite Framework Types*, Elsevier, 2007.

3 J. Cejka, R. E. Morris and P. Nachtigall, *Zeolites in Catalysis*, Royal Society of Chemistry, 2017.

4 M. E. Davis and R. F. Lobo, *Chem. Mater.*, 1992, **4**, 756–768.

5 D. W. Fickel and R. F. Lobo, *J. Phys. Chem. C*, 2010, **114**, 1633–1640.

6 W. Loewenstein, *Am. Miner.*, 1954, **39**, 92–96.

7 R. E. Morris and P. S. Wheatley, *Angew. Chemie Int. Ed.*, **47**, 4966–4981.

8 S. Niaz, T. Manzoor and A. H. Pandith, *Renew. Sustain. Energy Rev.*, 2015, **50**, 457–469.

9 H. W. Langmi and G. S. McGrady, *Coord. Chem. Rev.*, 2007, **251**, 925–935.

10 J. Weitkamp, M. Fritz and S. Ernst, *Int. J. Hydrogen Energy*, 1995, **20**, 967–970.

11 D. Fraenkel and J. Shabtai, *J. Am. Chem. Soc.*, 1977, **99**, 7074–7076.

12 K. M. Lamb, H. T. Pitcher, N. C. Cavarocchi and H. Hirose, *Open Cardiovasc. Thorac. Surg. J.*, 2012, **5**, 8–10.

13 D. L. Rubin, K. L. Falk, M. J. Sperling, M. Ross, S. Saini, B. Rothman, F. Shellock, E. Zerhouni, D. Stark, E. K. Outwater, U. Schmiedl, L. C. Kirby, J. Chezmar, T. Coates, M. Chang, J. M. Silverman, N. Rofsky, K. Burnett, J. Engel and S. W. Young, *J. Magn. Reson. Imaging*, 1997, **7**, 865–872.

14 J. Weitkamp and M. Hunger, in *Studies in Surface Science and Catalysis*, Elsevier, 2007, vol. 168, pp. 787–835.

15 L. Damjanović and A. Auroux, in *Zeolite Chemistry and Catalysis*, Springer Netherlands, Dordrecht, 2009, pp. 107–167.

16 P. A. Jacobs and H. K. Beyer, *J. Phys. Chem.*, 1979, **83**, 1174–1177.

17 R. Sadeghbeigi, in *Fluid Catalytic Cracking Handbook (Third Edition)*, Butterworth-Heinemann, Oxford, 2012, pp. 87–115.

18 V. Komvokis, L. X. L. Tan, M. Clough, S. S. Pan and B. Yilmaz, in *Zeolites in Sustainable Chemistry: Synthesis, Characterization and Catalytic Applications*, Springer Berlin Heidelberg, 2016, pp. 271–297.

19 H. L. Ngo, A. Nuñez, W. Lin and T. A. Foglia, *Eur. J. Lipid Sci. Technol.*, 2007, **109**, 214–224.

20 Z. C. Zhang, M. Dery, S. Zhang and D. Steichen, *J. Surfactants Deterg.*, 2004, **7**, 211–215.

21 L. Dandik, H. A. Aksoy and A. Erdem-Senatalar, *Energy & Fuels*, 1998, **12**, 1148–1152.

22 E. Armengol, A. Corma, H. Garcia and J. Primo, *Appl. Catal. A, Gen.*, 1995, **126**, 391–399.

23 A. Corma, H. Garcia, J. Primo and E. Sastre, *Zeolites*, 1991, **11**, 593–597.

24 M. Dusselier, P. Van Wouwe, A. Dewaele, P. A. Jacobs and B. F. Sels, *Science*, 2015, **349**, 78–80.

25 M. Koebel, M. Elsener and M. Kleemann, *Catal. Today*, 2000, **59**, 335–345.

26 H. Yahiro and M. Iwamoto, *Appl. Catal. A Gen.*, 2001, **222**, 163–181.

27 F. Göltl, R. E. Bulo, J. Hafner and P. Sautet, *J. Phys. Chem. Lett.*, 2013, **4**, 2244–2249.

28 A. K. Boës, B. Xiao, I. L. Megson and R. E. Morris, *Top. Catal.*, 2009, **52**, 35–41.

29 A. K. Boës, P. S. Wheatley, B. Xiao, I. L. Megson and R. E. Morris, *Chem. Commun.*, 2008, **0**, 6146–6148.

30 B. E. R. Snyder, M. L. Bols, R. A. Schoonheydt, B. F. Sels and E. I. Solomon, *Chem. Rev.*, 2018, **118**, 2718–2768.

31 P. Vanelderen, J. Vancauwenbergh, M.-L. Tsai, R. G. Hadt, E. I. Solomon, R. A. Schoonheydt and B. F. Sels, *ChemPhysChem*, 2014, **15**, 91–99.

32 P. Vanelderen, J. Vancauwenbergh, B. F. Sels and R. a. Schoonheydt, *Coord. Chem. Rev.*, 2013, **257**, 483–494.

33 A. Delabie, K. Pierloot, M. H. Groothaert, R. A. Schoonheydt and L. G. Vanquickenborne, *Eur. J. Inorg. Chem.*, 2002, **2002**, 515–530.

34 S. Grundner, M. A. C. Markovits, G. Li, M. Tromp, E. A. Pidko, E. J. M. Hensen, A. Jentys, M. Sanchez-Sanchez and J. A. Lercher, *Nat. Commun.*, 2015, **6**, 7546.

35 P. Vanelderen, B. E. R. Snyder, M.-L. Tsai, R. G. Hadt, J. Vancauwenbergh, O. Coussens, R. A. Schoonheydt, B. F. Sels and E. I. Solomon, *J. Am. Chem. Soc.*, 2015, **137**, 6383–6392.

36 S. Sklenak, P. C. Andrikopoulos, S. R. Whittleton, H. Jirglova, P. Sazama, L. Benco, T. Bucko, J. Hafner and Z. Sobalik, *J. Phys. Chem. C*, 2013, **117**, 3958–3968.

37 M. P. Attfield, S. J. Weigel and A. K. Cheetham, *J. Catal.*, 1997, **170**, 227–235.

38 W. Gruenert, N. W. Hayes, R. W. Joyner, E. S. Shpiro, M. R. H. Siddiqui and G. N. Baeva, *J. Phys. Chem.*, 1994, **98**, 10832–10846.

39 H. Y. Chen, L. Chen, J. Lin, K. L. Tan and J. Li, *Inorg. Chem.*, 1997, **36**, 1417–1423.

40 J. S. Woertink, P. J. Smeets, M. H. Groothaert, M. A. Vance, B. F. Sels, R. A. Schoonheydt and E. I. Solomon, *Proc. Natl. Acad. Sci.*, 2009, **106**, 18908–18913.

41 B. F. Mentzen and G. Bergeret, *J. Phys. Chem. C*, 2007, **111**, 12512–12516.

42 S. T. Korhonen, D. W. Fickel, R. F. Lobo, B. M. Weckhuysen and A. M. Beale, *Chem. Commun.*, 2011, **47**, 800–802.

43 J. Hun Kwak, H. Zhu, J. H. Lee, C. H. F. Peden and J. Szanyi, *Chem. Commun.*, 2012, **48**, 4758–4760.

44 F. Gao, E. D. Walter, E. M. Karp, J. Luo, R. G. Tonkyn, J. H. Kwak, J. Szanyi and C. H. F. Peden, *J. Catal.*, 2013, **300**, 20–29.

45 C. S. Blackwell, R. W. Broach, M. G. Gatter, J. S. Holmgren, D.-Y. Jan, G. J. Lewis, B. J. Mezza, T. M. Mezza, M. a. Miller, J. G. Moscoso, R. L. Patton, L. M. Rohde, M. W. Schoonover, W. Sinkler, B. A. Wilson and S. T. Wilson, *Angew. Chemie Int. Ed.*, 2003,

42, 1737–1740.

46 G. J. Lewis, D. Y. Jan, B. J. Mezza, J. G. Moscoso, M. A. Miller, B. A. Wilson and S. T. Wilson, in *Recent Advances in the Science and Technology of Zeolites and Related Materials*, Elsevier, 2004, vol. 154, pp. 118–125.

47 M. A. Miller, J. G. Moscoso, S. C. Koster, M. G. Gatter and G. J. Lewis, in *From Zeolites to Porous MOF Materials - The 40th Anniversary of International Zeolite Conference*, Elsevier, 2007, vol. 170, pp. 347–354.

48 W. J. Roth, P. Nachtigall, R. E. Morris, P. S. Wheatley, V. R. Seymour, S. E. Ashbrook, P. Chlubná, L. Grajciar, M. Položij, A. Zukal, O. Shvets and J. Cejka, *Nat. Chem.*, 2013, **5**, 628–33.

49 V. Kasneryk, M. Shamzhy, M. Opanasenko, P. S. Wheatley, S. A. Morris, S. E. Russell, A. Mayoral, M. Trachta, J. Čejka and R. E. Morris, *Angew. Chemie Int. Ed.*, **56**, 4324–4327.

50 D. S. Firth, S. A. Morris, P. S. Wheatley, S. E. Russell, A. M. Z. Slawin, D. M. Dawson, A. Mayoral, M. Opanasenko, M. Položij, J. Čejka, P. Nachtigall and R. E. Morris, *Chem. Mater.*, 2017, **29**, 5605–5611.

51 T. Blasco, A. Corma, M. J. Díaz-Cabañas, F. Rey, J. A. Vidal-Moya and C. M. Zicovich-Wilson, *J. Phys. Chem. B*, 2002, **106**, 2634–2642.

52 W. J. Roth, O. V Shvets, M. Shamzhy, P. Chlubná, M. Kubů, P. Nachtigall and J. Čejka, *J. Am. Chem. Soc.*, 2011, **133**, 6130–6133.

53 P. S. Wheatley, P. Chlubná-Eliášová, H. Greer, W. Zhou, V. R. Seymour, D. M. Dawson, S. E. Ashbrook, A. B. Pinar, L. B. McCusker, M. Opanasenko, J. Čejka and R. E. Morris, *Angew. Chemie*, 2014, **126**, 13426–13430.

54 M. Mazur, P. S. Wheatley, M. Navarro, W. J. Roth, M. Položij, A. Mayoral, P. Eliášová, P. Nachtigall, J. Čejka and R. E. Morris, *Nat. Chem.*, 2016, **8**, 58–62.

55 X. Li and M. W. Deem, *J. Phys. Chem. C*, 2014, **118**, 15835–15839.

56 N. Žilková, P. Eliášová, S. Al-Khattaf, R. E. Morris, M. Mazur and J. Čejka, *Catal. Today*, 2016, **277**, 55–60.

57 M. V. Shamzhy, O. V. Shvets, M. V. Opanasenko, P. S. Yaremov, L. G. Sarkisyan, P. Chlubná, A. Zukal, V. R. Marthala, M. Hartmann and J. Čejka, *J. Mater. Chem.*, 2012, **22**, 15793–15803.

58 E. Culotta and D. Koshland, *Science*, 1992, **258**, 1862–1865.

59 R. M. J. Palmer, A. G. Ferrige and S. Moncada, *Nature*, 1987, **327**, 524–526.

60 L. J. Ignarro, G. M. Buga, K. S. Wood, R. E. Byrns and G. Chaudhuri, *Proc. Natl. Acad. Sci.*, 1987, **84**, 9265–9269.

61 *http://www.nobel.se/medicine/laureates/1998/index.html*, 1998.

62 U. Forstermann and W. C. Sessa, *Eur. Heart J.*, 2012, **33**, 829–837.

63 J. E. Deanfield, J. P. Halcox and T. J. Rabelink, *Circulation*, 2007, **115**, 1285–1295.

64 Z. M. Ruggeri and G. L. Mendolicchio, *Circ. Res.*, 2007, **100**, 1673–1685.

65 P. S. Wheatley, A. R. Butler, M. S. Crane, S. Fox, B. Xiao, A. G. Rossi, I. L. Megson and R. E. Morris, *J. Am. Chem. Soc.*, 2006, **128**, 502–509.

66 J. O. Lundberg, E. Weitzberg and M. T. Gladwin, *Nat. Rev. Drug Discov.*, 2008, **7**, 156–67.

67 N. G. Hord, Y. Tang and N. S. Bryan, *Am. J. Clin. Nutr.*, 2009, **90**, 1–10.

68 M. Mowbray, X. Tan, P. S. Wheatley, R. E. Morris and R. B. Weller, *J. Invest. Dermatol.*, 2008, **128**, 352–360.

69 A. L. Burnett, *J. Clin. Hypertens.*, 2006, **8**, 53–62.

70 W. Xu, L. Z. Liu, M. Loizidou, M. Ahmed and I. G. Charles, *Cell Res.*, 2002, **12**, 311–320.

71 B. Weinberger, D. L. Laskin, D. E. Heck and J. D. Laskin, *Toxicol. Sci.*, 2001, **59**, 5–16.

72 P. Pacher, J. S. Beckman and L. Liaudet, *Physiol. Rev.*, 2007, **87**, 315–424.

73 L. J. Ignarro, C. Napoli and J. Loscalzo, *Circ. Res.*, 2002, **90**, 21–28.

74 M. R. Miller and I. L. Megson, *Br. J. Pharmacol.*, 2007, **151**, 305–321.

75 D. Hou, H. Narcisco, K. Kamdar, P. Zhang, B. Barclay and K. L. March, *Cardiovasc. Intervent. Radiol.*, 2005, **28**, 60–65.

76 M. L. Linenberger, *J. Natl. Compr. Cancer Netw.*, 2006, **4**, 889–901.

77 A. C. McKinlay, R. E. Morris, P. Horcajada, G. Férey, R. Gref, P. Couvreur and C. Serre, *Angew. Chemie - Int. Ed.*, 2010, **49**, 6260–6266.

78 G. Lemesle, C. Delhaye, L. Bonello, A. de Labriolle, R. Waksman and A. Pichard, *Arch. Cardiovasc. Dis.*, 2008, **101**, 769–777.

79 G. Dangas and F. Kuepper, *Circulation*, 2002, **105**, 2586–2587.

80 G. W. Stone, J. W. Moses, S. G. Ellis, J. Schofer, K. D. Dawkins, M.-C. Morice, A. Colombo, E. Schampaert, E. Grube, A. J. Kirtane, D. E. Cutlip, M. Fahy, S. J. Pocock, R. Mehran and M. B. Leon, *N. Engl. J. Med.*, 2007, **356**, 998–1008.

81 J. Iqbal, J. Gunn and P. W. Serruys, *Br. Med. Bull.*, 2013, **106**, 193–211.

82 D. R. Holmes, C. O. Shaughnessy, R. P. Caputo, D. J. Kereiakes, D. O. Williams, P. S. Teirstein, J. L. Jaeger and R. E. Kuntz, *N. Engl. J. Med.*, 2003, **349**, 1315–1323.

83 L. Mauri, D. J. Kereiakes, R. W. Yeh, P. Driscoll-Shempp, D. E. Cutlip, P. G. Steg, S.-L. T. Normand, E. Braunwald, S. D. Wiviott, D. J. Cohen, D. R. Holmes, M. W. Krucoff, J. Hermiller, H. L. Dauerman, D. I. Simon, D. E. Kandzari, K. N. Garratt, D. P. Lee, T. K. Pow, P. Ver Lee, M. J. Rinaldi and J. M. Massaro, *N. Engl. J. Med.*, 2014, **371**, 2155–66.

84 E. P. McFadden, E. Stabile, E. Regar, E. Cheneau, A. T. L. Ong, T. Kinnaird, W. O. Suddath, N. J. Weissman, R. Torguson, K. M. Kent, A. D. Pichard, L. F. Satler, R. Waksman and P. W. Serruys, *Lancet*, 2004, **364**, 1519–1521.

85 S. Koltzenburg, M. Maskos and O. Nuyken, *Polymer Chemistry*, Springer-Verlag Berlin Heidelberg, 2017.

86 A. Rudin and P. Choi, in *The Elements of Polymer Science & Engineering (Third Edition)*, Academic Press, Boston, 2013, pp. 1–62.

87 Y. Li, X. Luo and S. Hu, in *Bio-based Polyols and Polyurethanes*, Springer

International Publishing, Cham, 2015, pp. 1–13.

88 D. Rosu, N. Tudorachi and L. Rosu, *J. Anal. Appl. Pyrolysis*, 2010, **89**, 152–158.

89 H. Shehu, E. Okon and E. Gobina, *Matériaux Tech.*, 2017, **105**, 205–212.

90 H. T. Afarani, M. Sadeghi and A. Moheb, *Adv. Polym. Technol.*, 2018, **37**, 339–348.

91 L. Li, H. Song, B. Cao, Q. Xiao, W. Yi and X. Ni, *Polym. Plast. Technol. Eng.*, 2017, **56**, 866–872.

92 H.-W. Jun, L. J. Taite and J. L. West, *Biomacromolecules*, 2005, **6**, 838–844.

93 M. M. Reynolds, J. A. Hrabie, B. K. Oh, J. K. Politis, M. L. Citro, L. K. Keefer and M. E. Meyerhoff, *Biomacromolecules*, 2006, **7**, 987–994.

94 P. N. Coneski and M. H. Schoenfisch, *Polym. Chem.*, 2011, **2**, 906.

95 I. Fischer, W. F. Schmitt, H.-C. Porth, M. W. Allsopp and G. Vianello, in *Ullmann's Encyclopedia of Industrial Chemistry*, American Cancer Society, 2014, pp. 1–30.

96 M. J. Neufeld, B. R. Ware, A. Lutzke, S. R. Khetani and M. M. Reynolds, *ACS Appl. Mater. Interfaces*, 2016, **8**, 19343–19352.

97 N. B. McKeown, *Sci. China Chem.*, 2017, **60**, 1023–1032.

98 N. B. McKeown, *ISRN Mater. Sci.*, 2012, **2012**, 1–16.

99 P. M. Budd, B. S. Ghanem, S. Makhseed, N. B. McKeown, K. J. Msayib and C. E. Tattershall, *Chem. Commun.*, 2004, **0**, 230.

100 P. M. Budd, E. S. Elabas, B. S. Ghanem, S. Makhseed, N. B. McKeown, K. J. Msayib, C. E. Tattershall and D. Wang, *Adv. Mater.*, 2004, **16**, 456–459.

101 M. Carta, R. Malpass-Evans, M. Croad, Y. Rogan, J. C. Jansen, P. Bernardo, F. Bazzarelli and N. B. McKeown, *Science*, 2013, **339**, 303–307.

102 S. V Adymkanov, Y. P. Yampol'skii, A. M. Polyakov, P. M. Budd, K. J. Reynolds, N. B. McKeown and K. J. Msayib, *Polym. Sci. Ser. A*, 2008, **50**, 444–450.

103 N. A. Rakow, M. S. Wendland, J. E. Trend, R. J. Poirier, D. M. Paolucci, S. P. Maki, C. S. Lyons and M. J. Swierczek, *Langmuir*, 2010, **26**, 3767–3770.

104 N. B. McKeown, B. Gahnem, K. J. Msayib, P. M. Budd, C. E. Tattershall, K. Mahmood, S. Tan, D. Book, H. W. Langmi and A. Walton, *Angew. Chemie Int. Ed.*, 2006, **45**, 1804–1807.

105 S. D. Ahn, A. Kolodziej, R. Malpass-Evans, M. Carta, N. B. McKeown, S. D. Bull, A. Buchard and F. Marken, *Electrocatalysis*, 2016, **7**, 70–78.

Chapter 2: Aims

The overriding aim of this thesis is to assess the potential of zeolite catalysts to be used within biomedical applications for nitric oxide production. The main application that was considered throughout was a stent coating, where the nitric oxide produced from the zeolite catalysts could help to decrease the risk of stent thrombosis.

A range of aluminosilicate zeolites will be synthesised and characterised. They will then be prepared for catalysis by ion-exchange procedures to form either acid sites or copper sites. The zeolite catalysts will be assessed for nitric oxide production from biologically available substrates. These initial studies will provide an insight into any structure-activity relationships between the zeolites and the nitric oxide production.

The feasibility of copper zeolite inclusion within the body will be probed by leaching and toxicology studies. This will provide information on the levels of copper that may leach from the zeolites and any detrimental impact of the zeolite on cell viability.

Further steps towards the proposed biomedical application will be taken, with catalytic flow studies that mimic the biological setting and polymer incorporation to determine a method of connecting the zeolite catalyst powders to the biomedical devices.

Lastly, a different range of zeolites will be considered. The ADOR process will be probed as a method to study the affect of ring size on catalytic activity. A range of four isoreticular zeolites will be synthesised, characterised and assessed for catalytic NO production.

Chapter 3: Experimental Techniques

3.1. Nitric Oxide Analyser

A Sievers 280i Nitric Oxide Analyser (NOA) was used to determine the catalytic activity of the acid and copper site zeolites in chapters 4 and 5, as well as the polymer films in chapter 6. The concentration of the nitric oxide (NO) produced is calculated by a reaction between ozone and NO. Ozone is generated within the analyser from an oxygen supply which then reacts with the NO produced from the sample inside a reaction cell. The below reaction, equation 3.1, takes place, where the relaxation of the excited nitrogen dioxide species releases a photon, this release is measured by a photomultiplier that allows for quantification of the NO production.

$$NO^{\bullet} + O_3 \rightarrow NO_2^{*} + O_2$$
$$NO_2^{*} \rightarrow NO_2 + h\nu \text{ (photon)} \qquad (3.1)$$

NOA calibrations were performed frequently by use of “zero gas” and a calibration gas. A supply of “zero gas” was passed through the analyser, which is a stream of air taken from the lab that is drawn through a scrubber to remove any NO present and a calibration performed to set the measurement to 0 ppm. Secondly, a flow of NO calibration gas of a known concentration was passed through the system to the analyser with the reading measurement set as the concentration of the gas. Calibrations were performed on a weekly basis.

To convert the NO concentration to the number of moles, a “constant” was generated that corresponds to the number of moles of NO in 1 ppm/s. The calibration gas with a known concentration (~90 ppm, specific values vary slightly with different gas cylinders) was passed to the analyser at a set rate, 200 mL/min, for 3 minutes. The total volume of gas to enter the analyser was calculated from the rate and the time, with the final two minutes of data used within the calculation, corresponding to 400 mL of gas. The knowledge of the volume of gas entering the reaction cell, allowed use of the rearranged ideal gas law, equation 3.2, to calculate the number of moles of gas in the set time period.

$$pV = nRT$$

$$n = \frac{pV}{RT} \tag{3.2}$$

p = pressure (101325 Pa)

R = ideal gas constant (8.314 J K^{-1} mol^{-1})

T = temperature (293 K)

V = volume of gas (0.0004 m^3)

Using the known calibration gas concentration, it is possible to multiply the number of moles of gas by the concentration to obtain the number of moles of NO in the 120 second period. The area under the curve for the two minute section was also calculated, determining the ppm of NO in 120 seconds. The number of moles was divided by the area under the curve to produce the number of moles of NO in ppm/s. This was the value of the constant.

The constant was applied to the results by using it to multiply the sum concentration (in ppm), thus providing the total number of moles produced at each 1 second measurement. The sum concentration was determined by summing the concentrations (in ppm) at each 1 second time point.

The experimental set-up of the NOA is shown in figure 3.1, where the sample to be analysed was placed inside the sample vial with water. The samples were degassed for 10 minutes prior to that start of a run. The desired substrate was injected into the vial through a septum. A supply of nitrogen was used as the carrier gas for any NO produced, to prevent oxidation to further NO_x species before it reached the NOA. The nitrogen bubbled through the sealed reaction vial to carry any NO produced to the NOA. The gas also passed through a series of traps and a filter to prevent any solid or liquid from passing to the NOA.

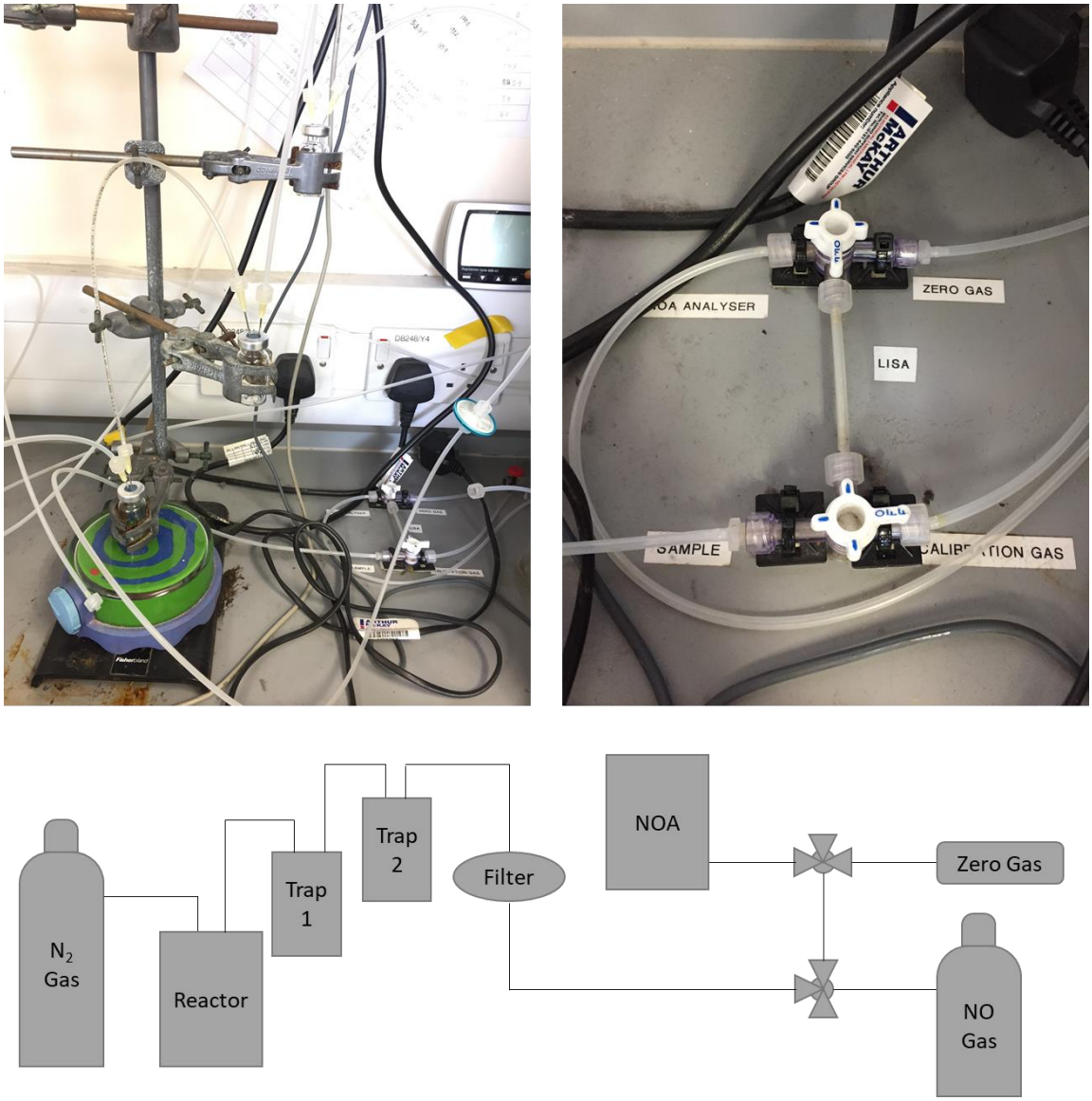

Figure 3.1: The NOA set-up for catalysis. The sample is placed in a sealed sample vial (left) with a nitrogen gas inlet and an outlet needle to transport any NO produced. A series of traps and a filter are present to prevent any liquid or solid travelling to the NOA. The stopcock section (right) allows control over the paths of the gas. It is shown flowing zero gas to the NOA, but moving the "off" position to the zero gas would allow the system to be used for NO production measurements by carrying the sample gas to the NOA. The diagram below indicates the order of the processes in the NOA set-up.

3.2. APOLLO Nitric Oxide Electrode System

An APOLLO 4000 nitric oxide electrode system was set-up to allow NO production to be monitored in a flow set-up. Two NO-sensitive electrodes, ISO-NOP (2 mm), were used to monitor NO concentrations before and after the zeolite catalyst. The NO concentration produced by the zeolite catalyst was determined by the difference in measurements of the two electrodes.

The electrode membranes are fragile and required replacement on a number of occasions during the studies. Once the old membrane was removed, the electrode tip was washed with distilled water and dried with tissue paper. Electrolyte (ISO-NOP filling solution, 100 µL) was injected inside the new membrane sleeve and the dried electrode tip dipped into the electrolyte solution bottle. The membrane was slowly placed over the electrode and secured with the locking cap. The new membrane tip was placed in water to settle the current, a process that could take a couple of days.

The flow set-up was calibrated weekly by the chemical generation of NO, this was performed by combining a mixture of sulfuric acid and potassium iodide (solution 1) with sodium nitrite (solution 2). The proposed reaction is shown in equation 3.3. The 1:1 ratio of $NaNO_2$ and NO means that the number of moles of NO generated will be equal to the number of moles of $NaNO_2$ in solution.

$$2NaNO_2 + 2KI + 2H_2SO_4 \rightarrow 2NO + I_2 + 2H_2O + 2Na_2SO_4 \quad (3.3)$$

500 mL of solution 1 was prepared by slowly adding concentrated sulfuric acid (2.7 mL) to Milli-Q water (~400 mL) with stirring, followed by the addition of potassium iodide (8.3 g). The remaining Milli-Q water was then added to provide a 500 mL solution. A solution of 50 µM sodium nitrite (solution 2) was prepared by dilution from a 0.05 M solution.

To perform the calibration, 10 mL of solution 1 was placed in a large sample vial with a stirrer bar. The tip of the electrode was placed in the solution and the stirrer bar set to a gentle stir rate. The $NaNO_2$ was added in 50 µL portions, starting with 50 µL and reaching 200 µL, with each addition resulting in an increase in electrode current, an example of calibration data can be found in table 3.1. The next portion of $NaNO_2$ was only added once the current had plateaued from the previous addition.

Table 3.1: APOLLO flow set-up calibration data. The NO concentration values are calculated from the volume of $NaNO_2$ added and the response is produced by the electrode.			
Volume of $NaNO_2$ added (µL)	Total Volume of $NaNO_2$ added (µL)	NO Concentration (nM) (Calculated)	Response (pA) (Experimental)
0	0	0	0
50	50	249	273
100	150	493	544
150	300	728	814
200	500	952	1059

The electrode response from each $NaNO_2$ addition is plotted against the NO concentration to determine a calibration curve. The data from table 3.1 is shown in figure 3.2, where the four data points generate a straight line with the equation of y = 1.1123x.

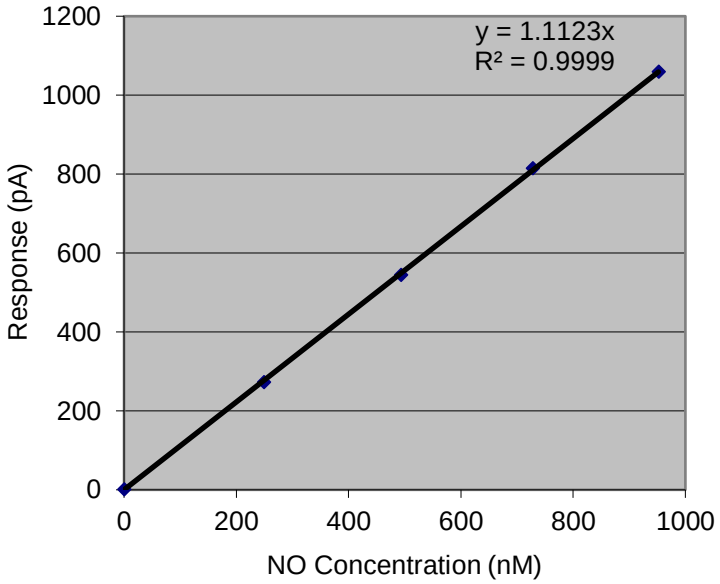

Figure 3.2: The plotted calibration data from table 3.1. The calculated NO concentrations are plotted against the electrode response from the $NaNO_2$ additions, providing a straight line.

To apply this calibration to recorded data, the currents (in pA) obtained from samples within this calibration period were divided by 1.1123 to provide the NO concentrations (in nM). When working with two electrodes, two separate calibrations were performed for each electrode. The data collected during the runs was converted into NO concentrations for each electrode before a subtraction was completed to determine the difference in NO concentration between the two electrodes.

The set-up, shown in figure 3.3, is composed of a large round bottom flask (3 L) for the stock solution, connected to tubing that carries the solution to the flow meter. The flow meter could be adjusted to set the rate of the flow to the desired value. The stock solution then reached the first electrode, where a current was recorded, before reaching the first stopcock. The stopcock has two paths, one which leads to the zeolite-containing syringe filter and the other which acts as a by-pass, connecting the tubing to a second stopcock the other side of the syringe filter. The second electrode was placed after the second stopcock, to monitor the NO concentration once the substrate had passed over the zeolite catalyst. The substrate was then collected in a beaker for disposal.

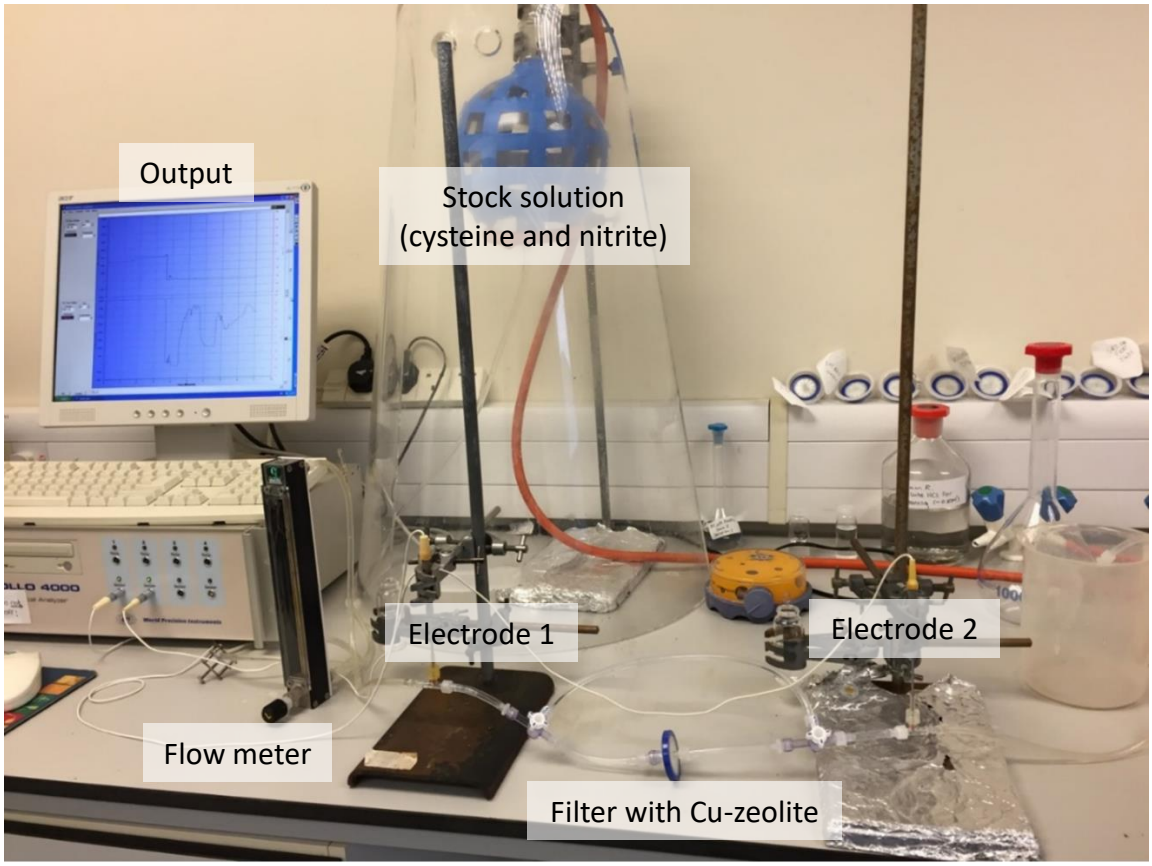

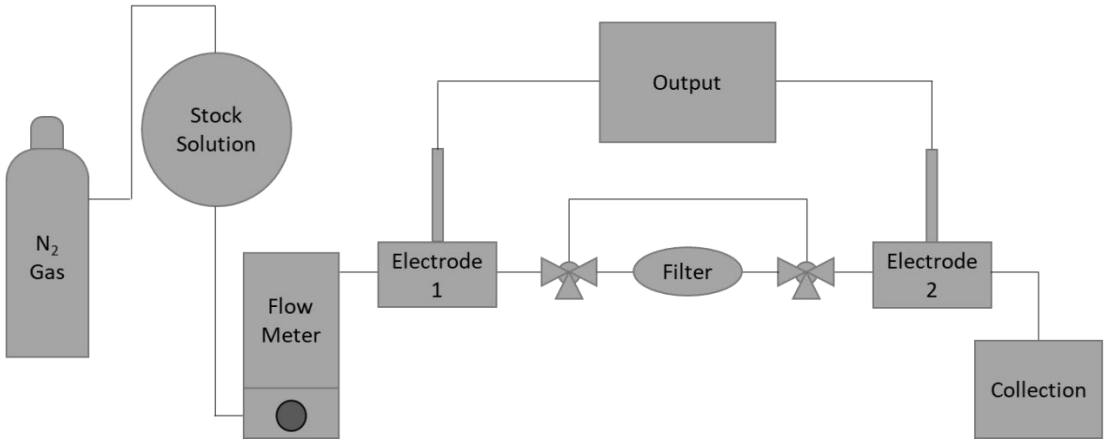

Figure 3.3: The electrode flow set-up used in chapter 6 to monitor the NO production from the constant flow of substrates over the copper zeolites. The diagram below indicates the order of the processes in the flow set-up.

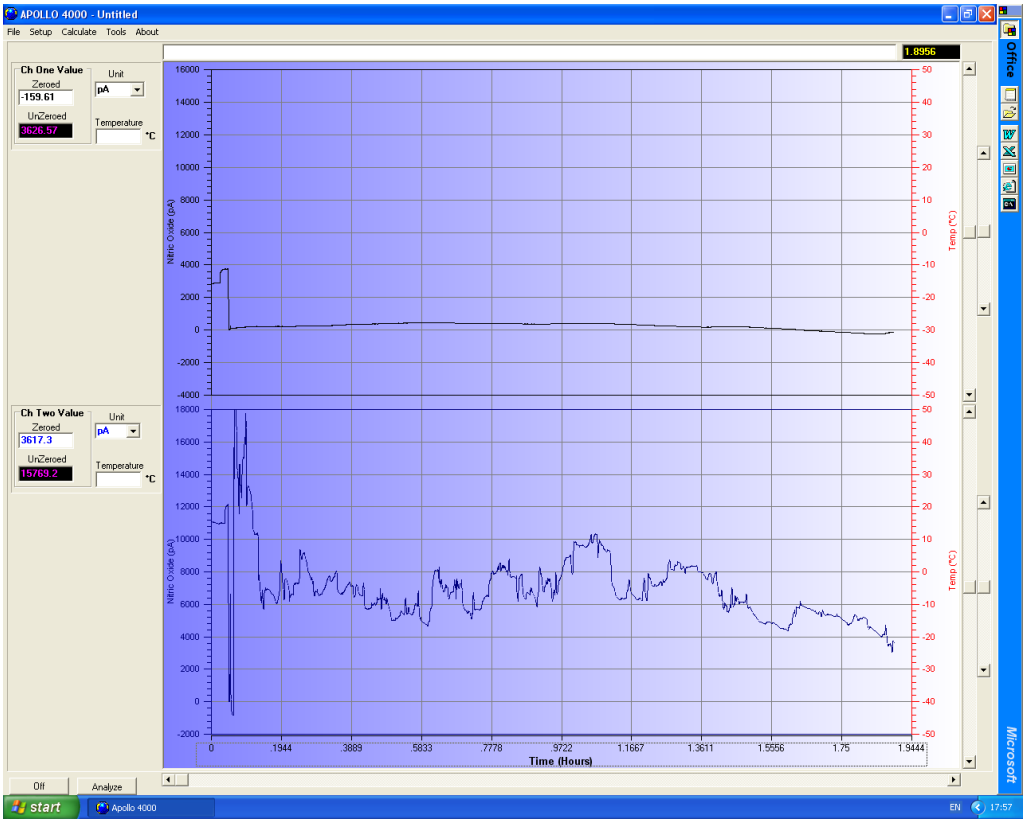

Figure 3.4: The current of the two electrodes during a run, with the top channel corresponding to the electrode located before the zeolite and the bottom channel the electrode after the zeolite.

The current of the electrodes was monitored by the output, where the current correlated to the NO concentration. The current of the electrodes was zeroed prior to exposure of the stock solution to the zeolite, to allow any change in current to be assigned to NO production. An example of the observed electrode currents is shown in figure 3.4, where the top channel corresponds to the electrode placed before the zeolite and the bottom channel corresponds to the electrode after the zeolite. The drop of the current to 0 pA at the beginning of the runs corresponds to the electrode zeroing before exposing the zeolite to the stock solution. Once all stock solution had passed through the system, the two sets of current data were converted to NO concentrations. The difference in NO concentration between the two channels was considered as the NO produced from the zeolite catalyst.

3.3. X-Ray Diffraction

A crystalline material is one that contains a series of repeating units that expand in all dimensions, providing a highly ordered structure. Lattice points are points of the structure that are repeated throughout to generate the crystal lattice. The smallest repeating unit is known as the unit cell, figure 3.5, which can be defined in terms of the cell lengths (a, b and c) and the angles connecting them (α, β and γ).[1,2] The unit cell is a parallelepiped connected through lattice points that describe the structure and symmetry of the crystal.

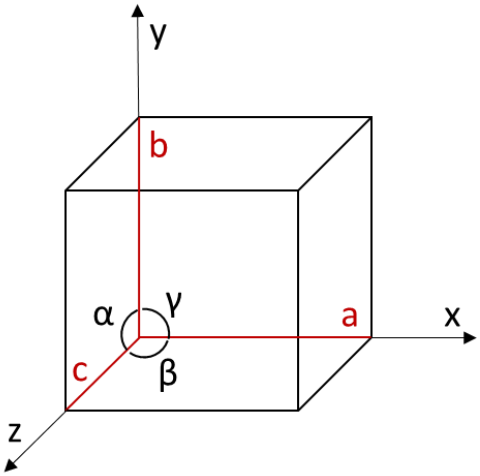

Figure 3.5: A unit cell schematic, defining the a, b and c edges and the α, β and γ angles connecting them.

Unit cells are defined by the positions of the lattice points within them. Symmetry operations, namely rotation and reflection, limit the number of ways that these lattice points can be arranged within the unit cell. The three main types of lattice point distributions are shown in figure 3.6 with primitive (P), body-centred (I) and face-centred (F) systems shown in a cubic unit cell.

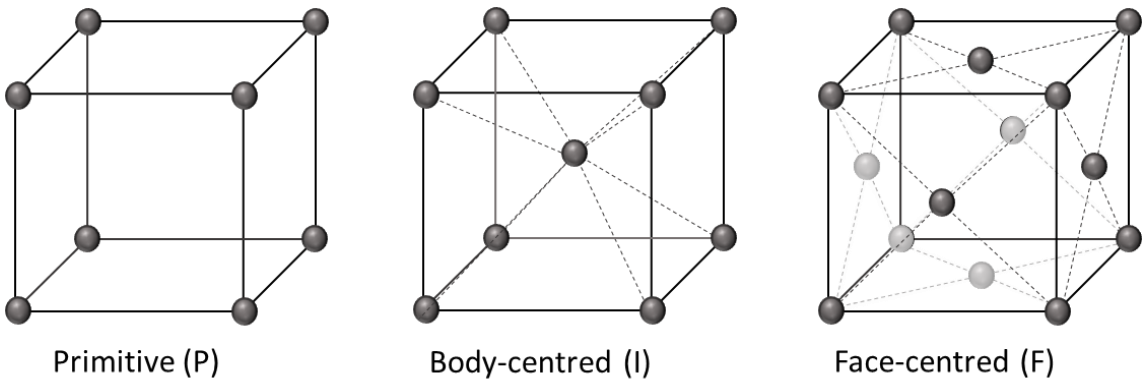

Figure 3.6: Three lattice point distributions within a cubic unit cell.

Primitive unit cells, also known as non-centred, contain only one lattice point that is contributed from an eighth of each corner lattice point. Body-centred cells contain two lattice points due to the addition of a lattice point in the centre of the cell. Face-centred cells contain lattice points on each face, as well as the corners, resulting in a total of four lattice points per unit cell. The last type of cell is known as base-centred, which is similar to face-centred but with lattice points only on one set of parallel faces, resulting in in a total of two lattice points. The base-centred code can be A, B or C, depending on the parallel faces that the lattice points reside.[3]

Besides the four types of lattice point distributions, there are also ranging values of a, b and c and the α, β and γ angles for each unit cell. The ranging geometric arrangement produces a total of seven crystal systems.[4] Paired with the four types of lattice system, there are a total of 14 Bravais lattices available, table 3.2. The Bravais lattices describe all types of unit cell lattice points possible in three-dimensional crystals.

Table 3.2: The fourteen possible Bravais lattices generated from seven crystal systems.

Crystal System	**Unit Cell Parameters**	**Lattice Type**
Cubic	a=b=c, α=β=γ=90°	P, I and F
Orthorhombic	a≠b≠c, α=β=γ=90°	P, I, F and C
Tetragonal	a=b≠c, α=β=γ=90°	P and I
Monoclinic	a≠b≠c, α=γ=90° β≠90°	P and C
Rhombohedral	a=b=c, α=β=γ≠90°	P
Triclinic	a≠b≠c, α≠β≠γ≠90°	P
Hexagonal	a=b≠c, α=β=90° γ=120°	P

Point groups are a set of symmetry operations that describe the symmetry elements of a molecule while keeping one point unmoved. The operations include reflection, rotation and inversion. There are a total of 32 point groups. Point groups can be expanded further to space groups by considering translational symmetry also. This includes operations such as screw axes and glide planes.[1] There are a total of 230 space groups, providing the most detailed description of the spatial symmetry of a crystal.[5]

X-ray diffraction (XRD) provides structural information on a crystalline solid, such as the atomic positions and unit cell dimensions. Miller planes are parallel planes within a unit cell that intersect at different points along the a, b and c axes, three examples of this are shown in figure 3.7.[6] The numbers within the brackets correspond to (abc) and relate to how many times the plane intersects the axis.

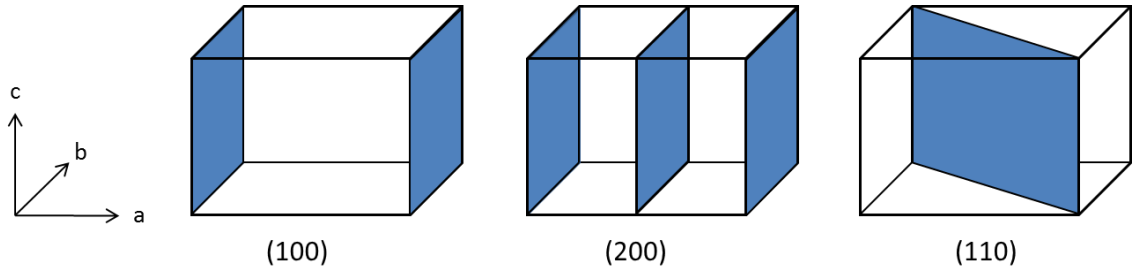

Figure 3.7: Three different Miller planes within a crystal structure. Left: (100), centre: (200) and right: (110).

X-rays are diffracted from different miller planes within the crystal sample as shown in figure 3.8. The difference in length that the X-ray beam travels to the different planes (AB+BC) can be calculated using Braggs Law, equation 3.4 below.

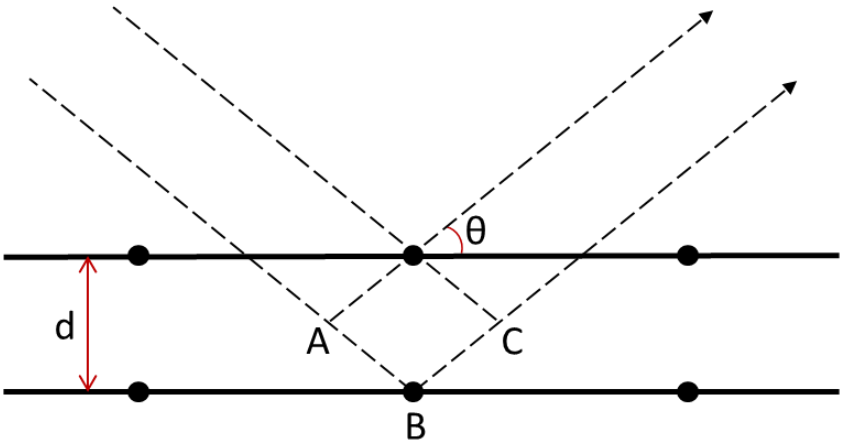

Figure 3.8: X-ray beam diffraction from two Miller planes within a crystal. The distance of AB+BC is the extra distance travelled by the X-ray beam to the lower plane.

$$n\lambda = 2d\sin\theta \qquad (3.4)$$

λ = the wavelength of the X-ray beam

d = the distance between the planes

θ = the scattering angle

n = an integer

Waves must interfere constructively to produce a diffraction peak. When n is an integer, the waves will remain in phase until they reach the detector, this will produce a spot in the diffraction pattern, satisfying Braggs Law.[3] The final diffraction pattern will contain intense peaks where Braggs condition has been satisfied for many planes in the crystalline material.

3.3.1. Powder X-Ray Diffraction

Powder X-ray diffraction (PXRD) was used to determine the purity of the synthesised zeolites. XRD patterns are unique to zeolite frameworks due to d-spacing corresponding to unit cell size and peak intensity relating to atom positions. Therefore, it is possible to confirm the phase purity of the zeolites with this technique. The sample is either packed into a disk to ensure a flat, even surface, producing many layers of zeolite crystals in various orientations for the X-ray beam to interact with, or packed into a capillary and spun to encounter a wide selection of crystals. The X-ray beam is fired at the sample at ranging 2θ values to ensure diffraction from all angles of the crystals. The X-ray detector collects the diffracted waves and measures the wave intensity of the peaks to create a peak pattern over a range of 2θ, which is the resulting powder pattern observed. The cones of the powder diffraction, figure 3.9, correspond to different miller planes within the crystal.

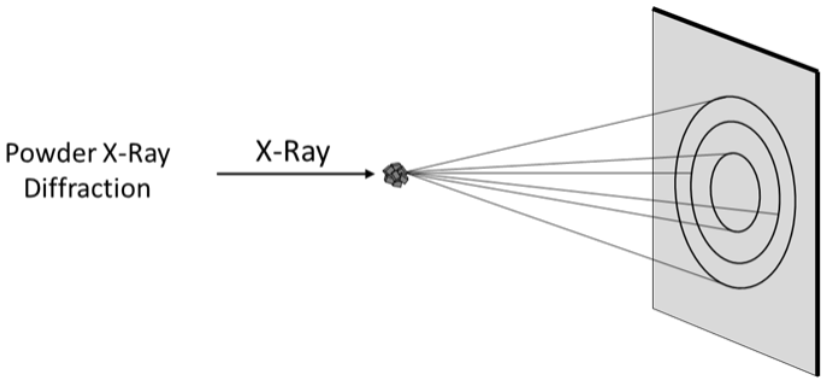

Figure 3.9: An illustrative example of the diffraction cones generated by powder X-ray diffraction.

The powder X-ray diffraction was recorded between 3 and 50° on a PANalytical Empyrean diffractometer operating monochromated Cu Kα1 radiation (1.54 Å) for the disks. The capillaries were run on a STOE STADIP with Cu Kα1 radiation at the same range as the disks. The recorded patterns were compared with simulated patterns that were obtained from zeolite cif files on the IZA database. A peak comparison was used to indicate the phase purity of the sample.

3.3.2. Single Crystal X-Ray Diffraction

Single crystal X-ray diffraction was used in the study of the single crystal ferrierite in chapter 5. The diffraction is performed by rotating the crystal in the X-ray beam and collecting the diffraction peaks, resulting in a pattern of spots, figure 3.10.

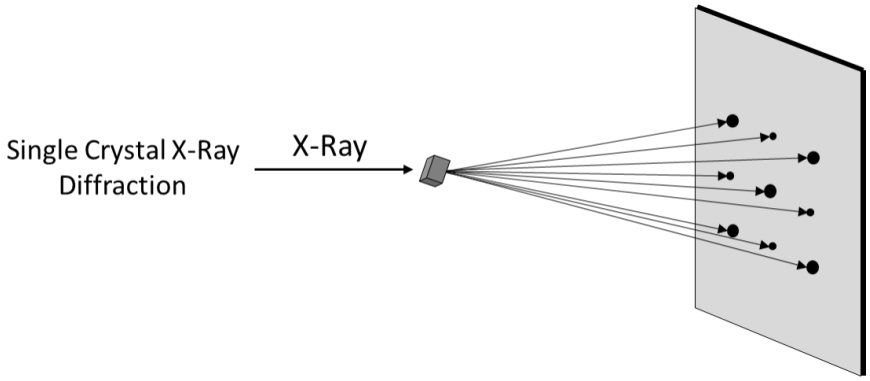

Figure 3.10: An illustrative example of the single crystal diffraction spots of varying intensities.

The single crystal diffraction spots have three properties of interest that relate to different properties of the crystal structure.[4] Firstly, the pattern has a specific geometry that is related to the crystal unit cell, providing information on the distances between the repeating units. Secondly, the pattern has symmetry that is related to the symmetry operations of the crystal, corresponding to space groups. Lastly, the intensities of the spots provide information on the positions of the atoms in the unit cell, since it is the combination of individual atom interactions that generate different amplitudes of the X-rays.

One of the main issues that faces X-ray diffraction is known as “the phase problem”, where the phase of the X-ray is lost, therefore preventing the Fourier transformation. There are a range of techniques that help to overcome this issue including multi-wavelength anomalous diffraction (MAD) and multiple isomorphous replacement (MIR).

The single crystal measurements were either collected at 173 K using a Rigaku MM-007HF High brilliance RA generator/confocal optics with XtaLAB P100 diffractometer or at 125 K using a Rigaku MM-007HF High brilliance RA generator/confocal optics with XtaLAB P200 diffractometer. Both datasets were collected using Cu Kα radiation (λ = 1.54187 Å).

3.3.3. Synchrotron X-Ray Diffraction

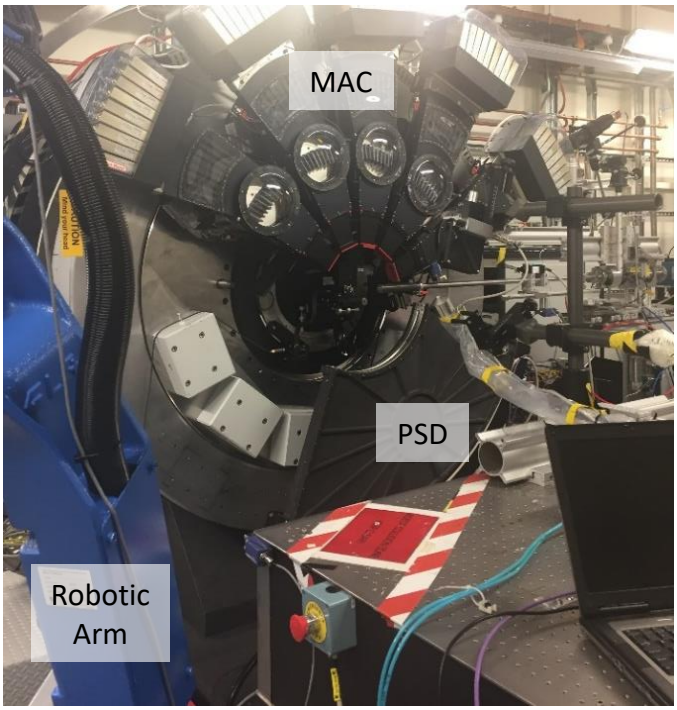

Figure 3.11: Beamline I11 at the Diamond Light Source with the MAC and PSD detectors.

Lastly, the synchrotron measurements in section 5.4.3 were performed on beamline I11 at the Diamond Light Source. The beam line consists of a robotic arm and automatic sample rack for sample changes and both multi-analyser crystal (MAC) and position sensitive (PSD) detectors, figure 3.11. The samples were run as capillaries at room temperature using both detectors.

3.4. Scanning Electron Microscopy

The morphology and crystal size of zeolites can be studied using scanning electron microscopy (SEM). SEM is used to provide information on surface topology and the chemical composition on the surface of the sample. An electron beam is generated from a tungsten filament under the influence of an intense electric field.[7] The electrons are then scanned as a single beam over the surface of the sample and the reflections are collected by a detector, providing an image of the zeolite surface.

There are two types of reflections from the sample; secondary electrons (SE) and back-scattered electrons (BSE). If the energy of the electron beam is high enough, the valence electrons of the surface atoms can be released, known as a secondary electron.[8] Back

scattering is when the original electron is reflected by the sample, where the intensity of the reflected signal is proportional to the atomic number of the atom.[9]

Figure 3.12 shows the basic components of a scanning electron microscope, showing the path of the electron beam from the gun through to the sample. The electron beam is focussed using multiple lenses to form a small electron beam spot projected onto the sample. The typical diameter of an electron beam is around 1 – 10 nm, with the condenser lens used to alter this diameter as required.[7] The objective lens focusses the small electron beam on the surface of the sample. The scan coils are used to deflect the beam to scan across the sample in a raster motion, providing a complete image of the rectangular section of sample.

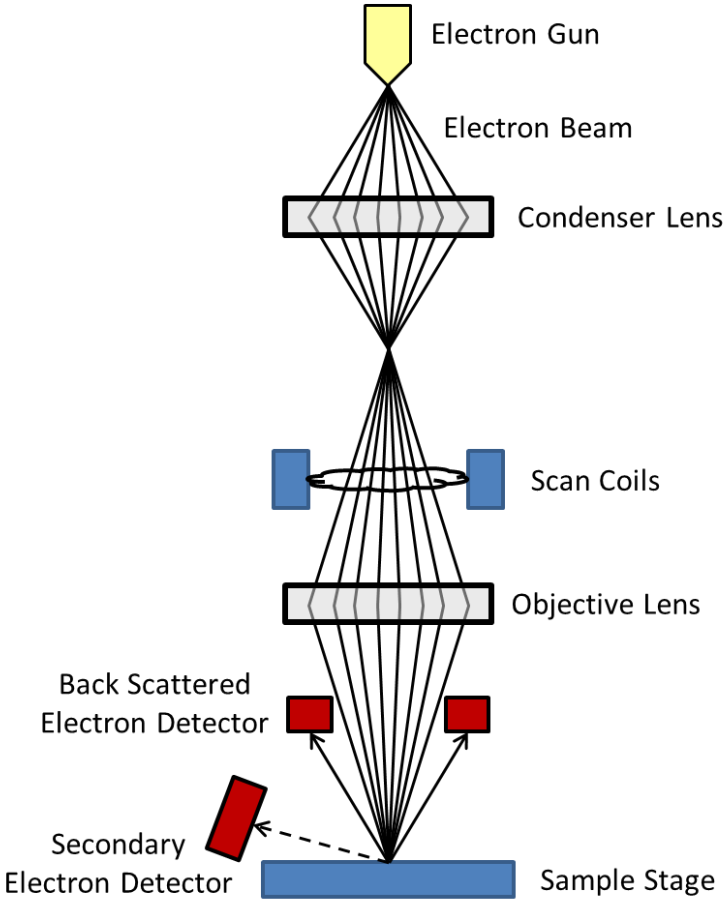

Figure 3.12: The setup of a scanning electron microscope showing the electron beam pathway.

The morphology and the crystal size of the zeolite samples were studied on a Jeol JSM-5600 Scanning Electron Microscope with a tungsten filament and a secondary electron detector. The working conditions included a working distance of 20 mm, a spot

size around 40 and an electron voltage of 5 kV. The samples were gold coated to provide a conductive surface that prevents charge build up on the sample. The gold sputter-coating was completed using a Quorum Q150R ES with a setting of 15 mA/40 s.

The SEM images of the polymer films (section 6.4.3.1) were performed by Simon Vornholt on a FEI Scios Dualbeam SEM, equipped with an electron beam and a focused ion beam (FIB) column, powered by a Ga-source. Samples were placed on a carbon-based conducting adhesive, brushed with Ag-paste and coated with a conducting gold layer. The sputter coating was carried out on a Quorum Q150R ES with a setting of 15 mA/30 s. The acceleration voltage for imaging was 5 kV, to ensure a sensitive mapping of the surface.

A cross-section removal was conducted for the polymer films in chapter 6. Prior to the removal of the cross-section, the sample was first protected by a 20x2x0.1 µm Pt-layer that was deposited with the electron beam at 3 kV and 0.2 nA. The sample was then further protected by a thicker Pt-layer of 20x2x0.5 µm that was deposited with the FIB at 30 kV and 0.2 nA. Once protected, a 20x10x8 µm area below the Pt-layer was cut with the FIB at 30 kV and 3 nA, a cleaning cross section was then conducted at 30 kV and 1 nA.

3.5. Energy Dispersive X-Ray Spectroscopy

Energy dispersive X-ray spectroscopy (EDX) was used to determine the chemical composition of the synthesised zeolites, as well as the copper content of the exchanged samples. The EDX is connected to the SEM equipment and provides a spectrum from the characteristic X-rays emitted by elements in the sample. X-rays are produced when the electron beam ejects inner shell electrons from atoms within the sample. This results in an electron from a higher energy shell filling the electron gap, with the difference in energy produced as an X-ray. The energies of the atomic shells of an element are sharply defined, with the shell difference also a well-defined quantity, therefore the resulting X-ray photon has an energy that is characteristic of the particular atom species and the shells involved, known as a “characteristic X-ray.” A high energy electron beam is required to produce the X-rays since the energy of the electron beam must be greater than the electron binding energy.[9]

The EDX consists of two main components; firstly, an X-ray detector receives the X-rays and convert them to electronic signals. These signals then go through a pulse processor

to determine the energy within each X-ray which is then displayed on a monitor. The characteristic X-rays and the counts recorded provide information on the presence and the ratios of the elements in the sample. A typical EDX spectrum can be seen in figure 3.13 with a sample of Cu-SSZ-13.

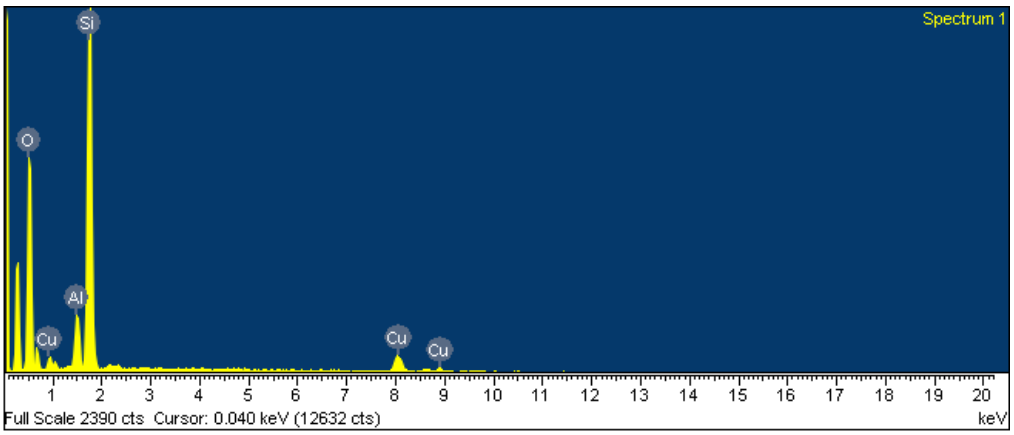

Figure 3.13: A typical EDX spectrum showing the Si, Al, O and Cu composition of Cu-SSZ-13.

An electron voltage of 25 kV was applied for the EDX measurements, with a standard data collection time of 90 seconds. A range of crystals and surface points were analysed with a combination of both single-point and area data collection. The average values of the composition were calculated from the range of measurements, along with the standard deviation to calculate the degree of error in the final value. The EDX data for the majority of the zeolites considered silicon and oxygen as well as copper and/or aluminium. Although oxygen is present within the zeolite frameworks, the atmospheric presence and the low atomic number can often provide high levels of error with the EDX measurements. Even if oxygen has been recorded, often in this thesis it has been excluded from the data presented, therefore the percentage compositions quoted do not always total 100 %.

3.6. Ammonia Temperature Programmed Desorption

Ammonia temperature-programmed desorption (NH_3-TPD) was used to study the quantity and strength of the acid sites in the zeolites. Ammonia can be used as a probe molecule due to its affinity to acid sites and also due to the small size allowing access into the pores. The zeolite samples were dehydrated, exposed to ammonia and then heated to remove the adsorbed ammonia. The mass of ammonia and the temperature at which it was desorbed provide information on the quantity and strength of acid sites

respectively. Mass spectrometry was used to monitor the amount of ammonia desorbed from each zeolite. The equipment used was a Micromeritics AutoChem 2950 coupled to a Balzers Thermostar quadrupole Mass Spectrometer.

The NH_3-TPD was calibrated using the breakdown of hexaammine cobalt (III) chloride by the reaction shown in equation 3.5.[10] Three different masses were run on the same protocol as the zeolite samples to provide a calibration curve. Due to the known starting masses it was possible to calculate how many moles of ammonia were released and plot this against the area under the curves of each mass.

$$6\ Co(NH_3)_6Cl_3 \rightarrow 3\ CoCl_2 + 3\ (NH_4)_2[CoCl_4] + N_2 + 28\ NH_3 \qquad (3.5)$$

Quartz wool was inserted into the glass reactor as a support for the zeolite. 80 mg of zeolite was loaded onto the wool and the reactor was then connected to the TPD equipment. The sample was dehydrated under argon by a two stage process. Firstly, it was heated at 120 °C for 30 minutes, this was followed by heating up to 500 °C for 20 minutes with a heating ramp of 10 °C/min. The system was then cooled down to 100 °C and the sample loaded with ammonia by exposure to 15 volume % NH_3 with He for 60 minutes. The reactor was then purged with argon gas for 60 minutes to remove any free and unbound ammonia molecules. The ammonia was finally desorbed with a gradual temperature increase from 100 °C up to 500 °C with a heating ramp of 10 °C/min. The temperature remained around 500 °C for the final few minutes of data collection, before cooling down to room temperature.

3.7. Inductively Coupled Plasma Atomic Emission Spectroscopy

Inductively coupled plasma atomic emission spectroscopy (ICP-AES) was used to determine the copper concentrations of the leached copper in section 5.4.5. The terms “atomic emission spectroscopy” (AES) and “optical emission spectroscopy” (OES) are used interchangeably, but are effectively the same technique. The ICP works by delivering the aqueous sample to the plasma flame as a mist, by the use of a nebuliser. The plasma flame is formed from an argon supply and is used to turn the solution into free atoms.[11] Once the sample enters the plasma flame, a multistep process occurs, consisting of desolvation, volatilisation and atomisation.[12]

The high temperature of the sample atoms, as well as the high potential of collisions with other atoms, results in the formation of excited species. The relaxation of these species to a lower energy level produce a spontaneous emission of radiation.[13] The wavelengths of the emission lines are characteristic of different elements and therefore provide information of the elements present. The lines of the elements of interest can be selected for data recording to limit the possible interference from other elements.

All samples were run on a Thermo Scientific iCAP 6000 Series ICP Emission Spectrometer with a CETAC Autosampler and copper emission lines of Cu2043, Cu2218, Cu2247 and Cu3247. The lines correspond to emission wavelengths of 204.3 nm, 221.8 nm, 224.7 nm and 324.7 nm respectively. The Cu3247 line produced the greatest number of counts and was therefore the line chosen when determining the concentrations of copper. The tubing was washed with 2% HNO_3 between samples to remove any metal traces from previous samples. Further to this, the samples were run in predicted increasing concentration values to limit any contamination from one sample to the next. Frequent calibrations were performed, at the beginning of the run and after every 20 samples, these confirmed the accuracy of the machine, as well as confirmation of sufficient washing of the tubing between samples.

A range of standards were prepared for the calibrations, they were; 0.01, 0.025, 0.05, 0.10, 0.25, 0.5, 1.0, 2.5, 5 and 10 ppm. All solutions were prepared in 5 % nitric acid with Milli-Q water. A copper standard of 1000 mg/L (VWR, 2 % nitric acid) was diluted by a factor of 100 to provide a 10 ppm solution that was used for further dilutions to reach the target concentrations. All glassware for the dilutions was soaked in 5 % nitric acid and rinsed with Milli-Q water prior to use.

3.8. Nuclear Magnetic Resonance

The basis of nuclear magnetic resonance (NMR) relies on the nuclei and the nuclei spin within a sample. When an external magnetic field is applied to a sample, energy transfers can occur between energy levels. The frequency of these transfers can be observed, providing an NMR spectrum. If the applied magnetic field was the only magnetic field experienced by the nuclei then a single line would be observed on the spectrum.[14] The electrons of the molecules, however, produce additional magnetic fields, resulting in

shielding of the nucleus. Whether the nucleus is shielded or deshielded results in different frequencies of the NMR lines. The molecular arrangement affects the level of shielding of each nucleus, with each chemically different nucleus experiencing a different shift, this is known as chemical shielding. It is this shift observed from the different chemical surroundings that allows identification of the molecules present within an NMR sample.

3.8.1. Solution State NMR

Solution state NMR is possible by dissolving a molecule of interest in a deuterated solvent. Molecules in solution tend to have a rapid tumbling that result in the magnetic field being applied to the molecules in all orientations. This tumbling allows the averaging of many line broadening interactions, including anisotropic interaction, to zero.[14] The resulting NMR spectrum is of high resolution with sharp lines that allow for easy data extraction.

Solution-state ^{1}H NMR measurements were performed on a Bruker Avance AVII 400 or Bruker AV 400. A small mass of material was dissolved in D_2O to prepare the sample.

3.8.2. Solid State NMR

Solid state NMR is an extremely useful tool for materials that cannot be dissolved in deuterated solvents for solution state NMR. The rapid tumbling with solids does not reduce line broadening, as it does with solution state NMR, since the molecules are fixed within a lattice. Instead, extremely broad peaks are observed from the tumbling of the solids, which provide minimal chemical and structural information.[14]

A solution to this problem lies within magic angle spinning (MAS). Many nuclear interactions, such as chemical shift anisotropy and dipolar interactions, depend on the mathematical function shown in equation 3.6.

$$\frac{1}{2}(3cos^2\theta - 1) \tag{3.6}$$

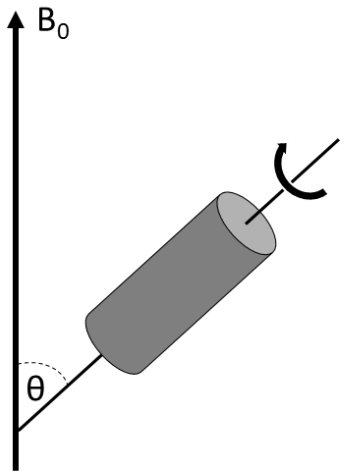

Figure 3.14: Spinning angle of the sample (θ) in relation to the magnetic field (B_0). An angle (θ) of 54.74 ° corresponds to magic angle spinning where all anisotropic affects are removed.

By setting θ to 54.44 °, figure 3.14, the anisotropic effects disappear since the mathematical term is now equal to zero.[15] Assuming that the spinning rate is greater than the anisotropic interactions, then narrow lines should be obtained thanks to MAS.

The solid-state NMR data was recorded by Dr Daniel Dawson on a Bruker Avance III spectrometer equipped with a 14.1 T wide-bore superconducting magnet (Larmor frequencies of 119.2 and 156.4 MHs for ^{29}Si and ^{27}Al, respectively). Samples were packed into 1.9 mm ZrO_2 rotors and rotated at the magic angle at a rate of 37.5 kHz. ^{29}Si NMR spectra were recorded using a rotor-synchronised spin-echo experiment with an echo delay of one rotor period (26.7 μs), with signal averaging carried out for 49152 (before synthesis) or 24576 (after synthesis) transients with a recycle interval of 0.1 s. ^{27}Al NMR spectra were recorded using a rotor-synchronised spin-echo experiment with pulse durations of 0.5 and 1 μs to ensure quantitative spectra. An echo delay of one rotor period (26.7 μs) was used with signal averaging carried out for 4098 (before synthesis) or 12288 (after synthesis) transients with a recycle interval of 0.1 s. Spectra are referenced to $(CH_3)_4Si$ and 0.1 M aqueous $Al(NO_3)_3$ using forsterite (δ= –62 ppm) and $Al(acac)_3$ (δ_{iso} = 0.0 ppm) as secondary solid references.

3.9. References

1 M. Ladd and R. Palmer, *Structure Determination by X-ray Crystallography*, Springer US, Boston, MA, 2013.

2 C. Hammond, *The Basics of Crystallography and Diffraction*, Oxford University Press, Third Edit., 2002.

3 Y. Waseda, E. Matsubara and K. Shinoda, *X-Ray Diffraction Crystallography; Introduction, examples and solved problems*, Springer Berlin Heidelberg, 2011.

4 W. Clegg, *Crystal Structure Determination*, Oxford University Press, 1998.

5 G. Burns and A. M. Glazer, in *Space Groups for Solid State Scientists (Third Edition)*, Academic Press, Oxford, Third Edit., 2013, pp. 85–151.

6 J. Cejka, R. E. Morris and P. Nachtigall, *Zeolites in Catalysis*, Royal Society of Chemistry, 2017.

7 R. F. Egerton, *Physical Principles of Electron Microscopy*, Springer International Publishing, Cham, 2016.

8 G. Michler, *Electron Microscopy of Polymers*, Springer-Verlag Berlin Heidelberg, 2008.

9 J. I. Goldstein, D. E. Newbury, J. R. Michael, N. W. M. Ritchie, J. H. J. Scott and D. C. Joy, *Scanning Electron Microscopy and X-Ray Microanalysis*, Springer-Verlag New York, 2018.

10 E. I. Stocka and A. Bogacz, *J. Therm. Anal.*, 1989, **35**, 1373–1386.

11 V. A. Fassel and R. N. Kniseley, *Anal. Chem.*, 1974, **46**, 1110–1120.

12 J. L. Todoli and J. M. Mermet, in *Liquid Sample Introduction in ICP Spectrometry*, Elsevier, 2008, pp. 3–15.

13 E. Talanta, in *Spectrochemical Analysis by Atomic Absorption and Emission*, Royal Society of Chemistry, Cambridge, 2004, vol. 44, pp. 202–256.

14 J. Iggo, *NMR Spectroscopy in Inorganic Chemistry*, Oxford University Press, 2011.

15 D. Apperley, R. Harris and P. Hodgkinson, *Solid State NMR Basic Principles & Practice*, Momentum Press, 2012.

Chapter 4: Acid Site Zeolite Catalysts

4.1. Aim

This chapter will assess the potential of acid site zeolites to be used as catalysts for the production of nitric oxide (NO) for biomedical applications. Four zeolites will be examined, they are mordenite, ferrierite, ZSM-5 and SSZ-13. The acid sites of the zeolites will be characterised by ammonia temperature programmed desorption (NH_3-TPD) and the NO production studied by the nitric oxide analyser (NOA). This work will indicate the viability of these materials for long term NO production.

4.2. Introduction

As discussed in section 1.1.3.1, acid site zeolites have many applications. The main application this chapter will focus on is the production of NO from acidified nitrite. While previously studied with citric, hydrochloric and ascorbic acid, there does not appear to be any examples where a zeolite has been used as the acid.[1–3]

One main advantage of using zeolites for this reaction, would be the solid support of the acid. The positioning of the zeolite could provide directed NO production, allowing for local NO effects as opposed to systemic. Furthermore, due to the low toxicity of zeolites, it is hoped that the acid zeolites would be safe for use in biomedical applications.[4] Furthermore, the U.S. Food and Drug Administration (FDA) has classified zeolites as a Generally Regarded as Safe (GRAS) substance.

One issue that is general to the acidified nitrite route, however, is the possible lack of regeneration of the active acid site. The proposed mechanism of NO production by acidified nitrite, equation 1.1 in section 1.2.1, suggests the consumption of the acid site during the reaction. Therefore, there was a risk that the acid site zeolites would not provide a catalytic NO production, limiting them to short-term NO production.

4.3. Experimental

4.3.1. Materials

Materials used in the zeolite syntheses: Sodium hydroxide (pellets, Fisher Scientific), sodium aluminate (technical, anhydrous, Al (Al_2O_3): 50 – 56 %, Na (Na_2O): 37 – 45 %, Sigma Aldrich), Ludox AS-30 colloidal silica (30 wt. % suspension in water, Sigma Aldrich), ethylenediamine (99 %, Sigma Aldrich), fumed silica (Sigma Aldrich).

4.3.2. Zeolite Synthesis

ZSM-5 was obtained from Zeolyst (CBV 3024E) in the ammonium form (NH_4-ZSM-5) and SSZ-13 was obtained from Chevron in the acid form (H-SSZ-13).

Ferrierite was synthesised hydrothermally using a literature procedure.[5] Distilled water (25.8 mL), sodium hydroxide (0.14 g, 3.5 mmol) and sodium aluminate (0.66 g, 8.0 mmol) were stirred together in a beaker until dissolved. In a separate beaker, Ludox AS-30 colloidal silica (9.29 g, 0.046 mol) and ethylenediamine (3.66 g, 0.061 mol) were mixed until homogeneous. The two solutions were combined in a 50 mL autoclave providing a molar composition of 1.85 Na_2O : Al_2O_3 : 15.2 SiO_2 : 592 H_2O : 19.7 ethylenediamine. The gel was placed in the oven at 175 °C for 10 days. The resulting crystals were recovered by vacuum filtration, washed with water and allowed to dry at room temperature.

Mordenite was also synthesised hydrothermally from a literature source.[6] Distilled water (6.6 mL), sodium hydroxide (0.76 g, 0.019 mol) and sodium aluminate (0.37 g, 4.5 mmol) were stirred in a Teflon liner until dissolved. Distilled water (20.5 mL) was added and stirred followed by the addition of silica solution (3.93 g). The silica solution was prepared with fumed silica (3.62 g, 0.060 mol) and distilled water (0.31 mL). The resulting molar composition was 6 Na_2O : 30 SiO_2 : Al_2O_3 : 780 H_2O. A small sample of mordenite (0.25 g) was added as a seed to encourage the crystallisation of the synthesis gel. The autoclave was placed into the oven at 175 °C for 2 days. The resulting crystals were recovered by vacuum filtration, washed with water and allowed to dry at room temperature.

4.3.3. Acid Site Formation

The first step in the acid site formation, was an ammonium ion exchange to insert ammonium cations within the pores. The ZSM-5 sample did not require ammonium exchange as it was purchased in the ammonium form. Mordenite and ferrierite were calcined prior to ion exchange to remove any SDAs or adsorbed molecules from within the pores. The calcinations were performed at 550 °C for 6 hours with a heating rate of 2 °C/min. The calcined zeolites were ion-exchanged with ammonium chloride solution (0.3 M, Fisher Scientific) using a ratio of 10 mL of solution to 50 mg of zeolite. The samples were stirred overnight at room temperature before the zeolites were filtered and washed; this procedure was repeated three times. The sample was washed thoroughly with water after the final ion exchange and then dried on top of the oven. The SSZ-13 sample was provided in the acid form from Chevron, therefore did not require any treatment.

The final step in the formation of the acid sites, was a calcination to remove ammonia, creating an acidic proton within the zeolite pores. The ammonium ZSM-5, ferrierite and mordenite were calcined under the same conditions as the SDA removal to remove ammonia gas and form the acid site. The strength and number of acid sites were then determined by ammonia temperature-programmed desorption (NH_3-TPD).

4.3.4. Catalytic Testing

The zeolite catalytic activities were studied by the conversion of sodium nitrite to NO. The concentration of NO produced after an injection of sodium nitrite was recorded by the NOA. Zeolite (5 mg), Milli-Q water (2.6 mL) and a stirrer bar were placed into a vial and sealed with a cap. The substrate, sodium nitrite (Alfa Aesar, 0.05 M, 250 µL, 1.25×10^{-5} mols) was injected into the sample vial 5 minutes into the NOA run and the sample run until the NO concentration returned to background levels. A control run of the acid site catalysis can be found in figure A1 of the Appendix.

4.4 Results and Discussion

To aid the results and discussion section, a table summarising the previously discussed key features of the four zeolites is shown in table 4.1.

Table 4.1: Framework summaries of the four zeolites applied for acid catalysis.

Zeolite	Ring Sizes	Channel System	Diffusion Along the a, b and c Axes
ZSM-5	10, 6, 5 and 4	3D	4.70 Å, 4.46 Å, 4.46 Å
SSZ-13	8, 6 and 4	3D	3.72 Å, 3.72 Å, 3.72 Å
Mordenite	12, 8, 5 and 4	2D	1.57 Å, 2.95 Å, 6.45 Å
Ferrierite	10, 8, 6 and 5	2D	1.56 Å, 3.40 Å, 4.69 Å

4.4.1. Zeolite Characterisation

4.4.1.1 Powder X-Ray Diffraction

All zeolites were first characterised by PXRD, with the phase purity determined by comparison against a simulated pattern that was calculated from the IZA cif files. The resulting patterns from all zeolites are shown in figures 4.1 – 4.4. The simulated PXRD patterns are derived from pure silica samples with no preferential orientation, occasionally resulting in minor differences between the simulated and experimental patterns.

Although purchased from Zeolyst, the phase purity of NH_4-ZSM-5 was still determined by PXRD. The resulting powder pattern is shown in figure 4.1. The experimental peaks match well with the simulated pattern, but with some extra peaks. These peaks are most likely due to the presence of ammonium within the pores of the experimental sample of ZSM-5.

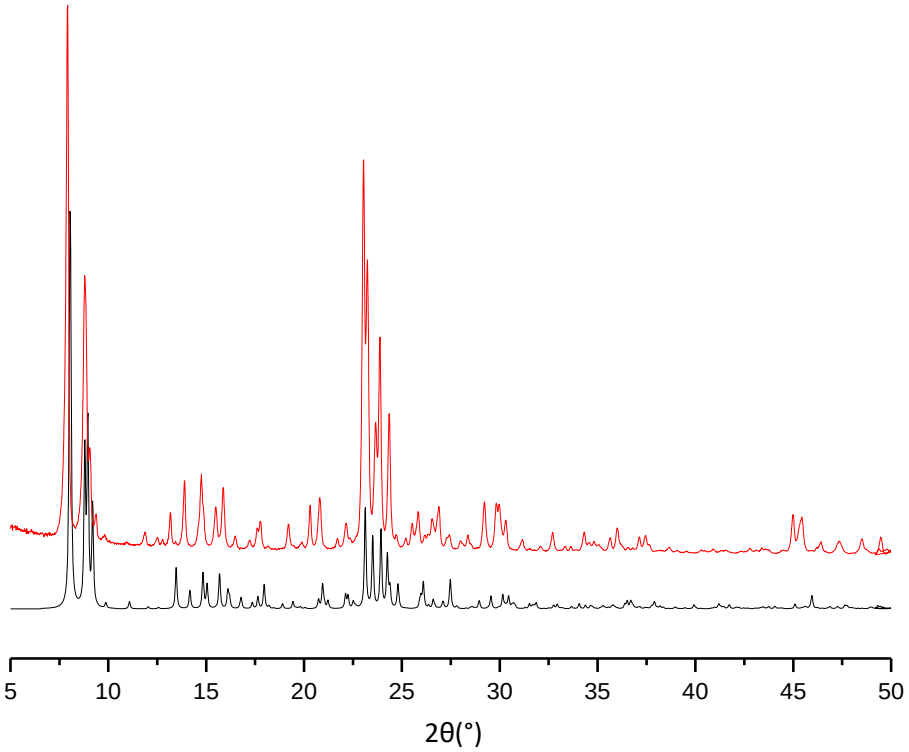

Figure 4.1: PXRD patterns of Zeolyst NH_4-ZSM-5 (red) and simulated (black).

Similarly, the diffraction pattern for the Chevron H-SSZ-13 sample was recorded, figure 4.2. Besides some small differences in the peak intensities, the results match well with the simulated pattern, confirming a phase pure sample.

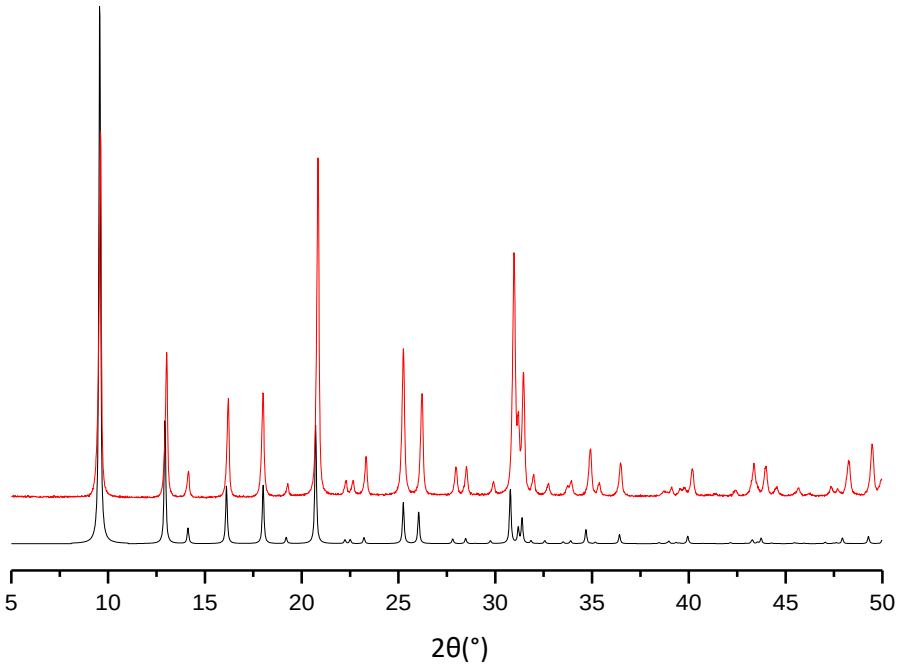

Figure 4.2: PXRD patterns of Chevron H-SSZ-13 (red) and simulated (black).

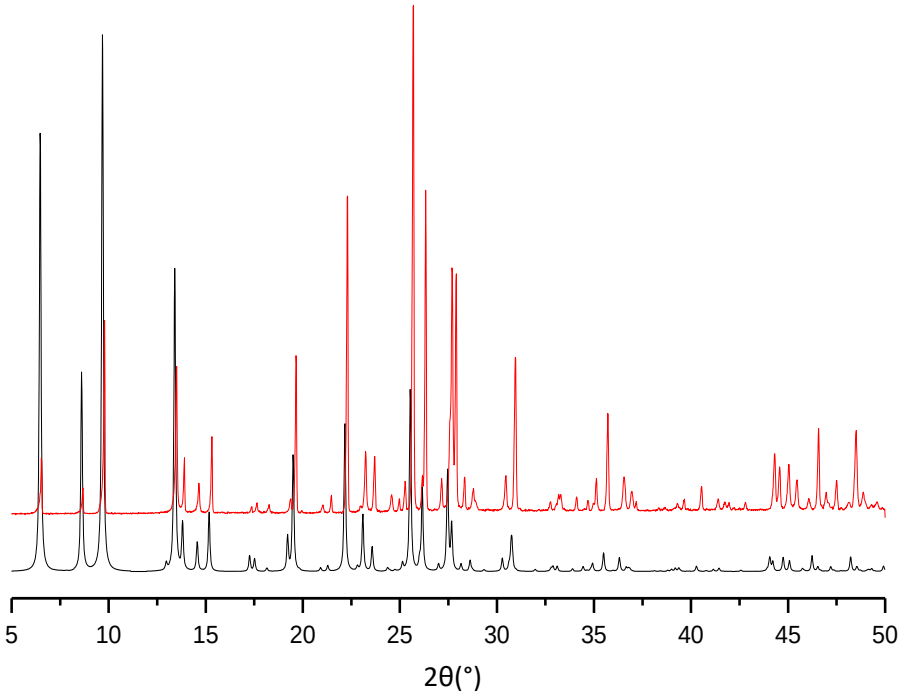

Figure 4.3: PXRD patterns of as-synthesised mordenite experimental (red) and simulated (black).

As a synthesised zeolite, the determination of the as-synthesised mordenite phase purity was important. On comparison to the simulated pattern, figure 4.3, the peaks matched well, indicating that pure mordenite had been synthesised.

The diffraction pattern of the as-synthesised ferrierite proved to be troublesome. On initial inspection, there appeared to be impurities, represented by extra diffraction peaks. Some of the main peaks of concern are highlighted by an asterisk in figure 4.4.

On comparison to data from the Verified Syntheses of Zeolitic Materials, however, the peaks matched well, as shown in figure 4.5.[5] Further characterisation by SEM, shown later in this chapter, helped to confirm only one phase was present.

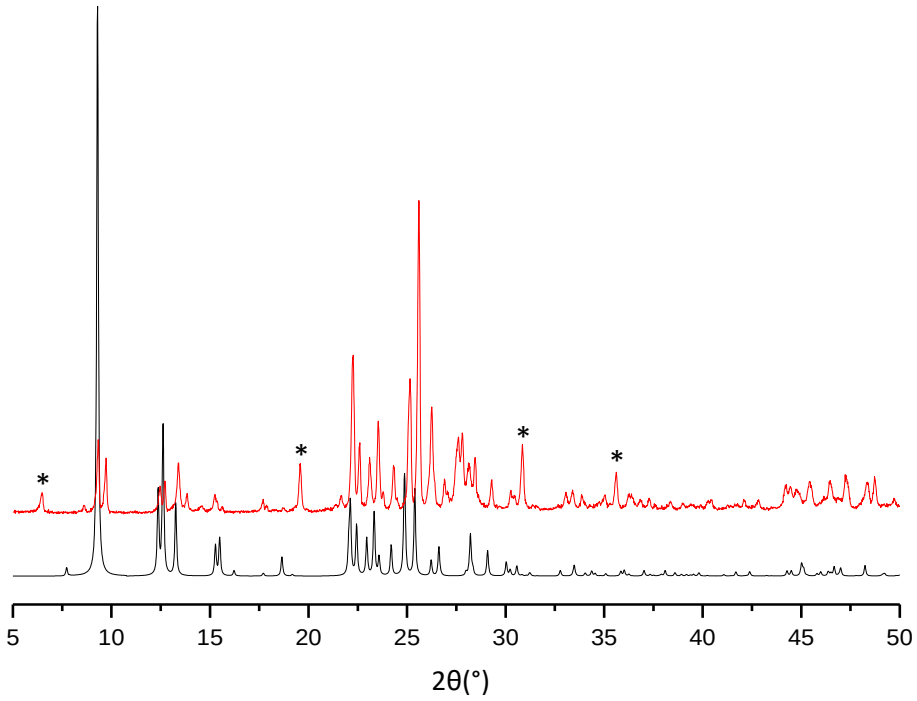

Figure 4.4: PXRD patterns of as-synthesised ferrierite experimental (red) and simulated (black), where additional experimental peaks are highlighted by an asterisk (*).

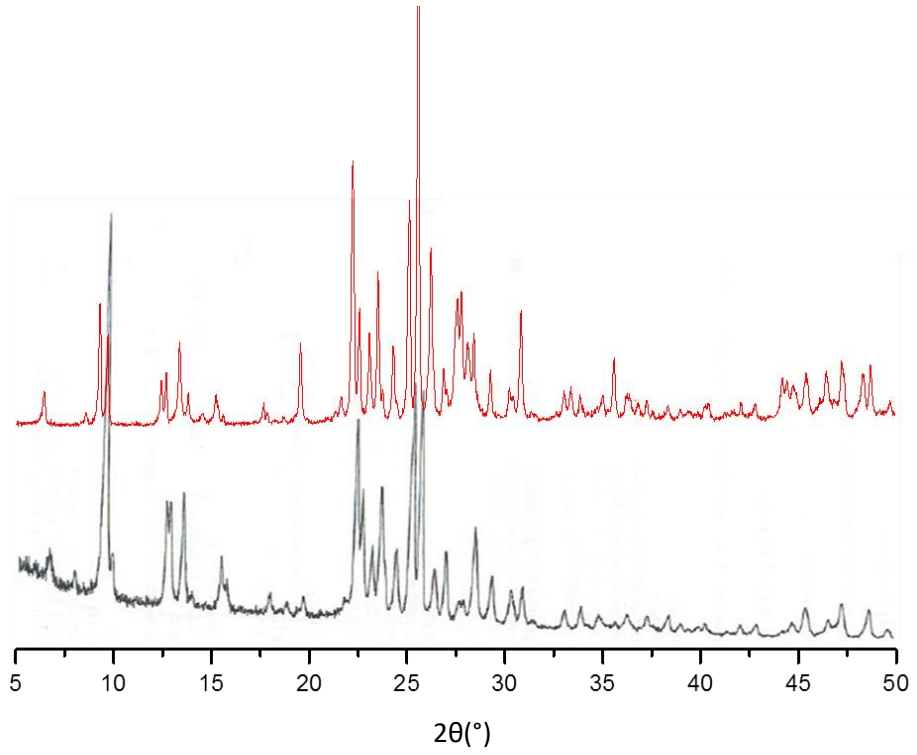

Figure 4.5: PXRD patterns of as-synthesised ferrierite experimental (red) and the Verified Syntheses of Zeolitic Materials reference (black).

4.4.1.2. Scanning Electron Microscopy – Energy Dispersive X-Ray Spectroscopy

Once the purity had been determined by PXRD, a combination of SEM and EDX was used to study the morphology and size of the as-synthesised crystals and the Si/Al ratios of the zeolites.

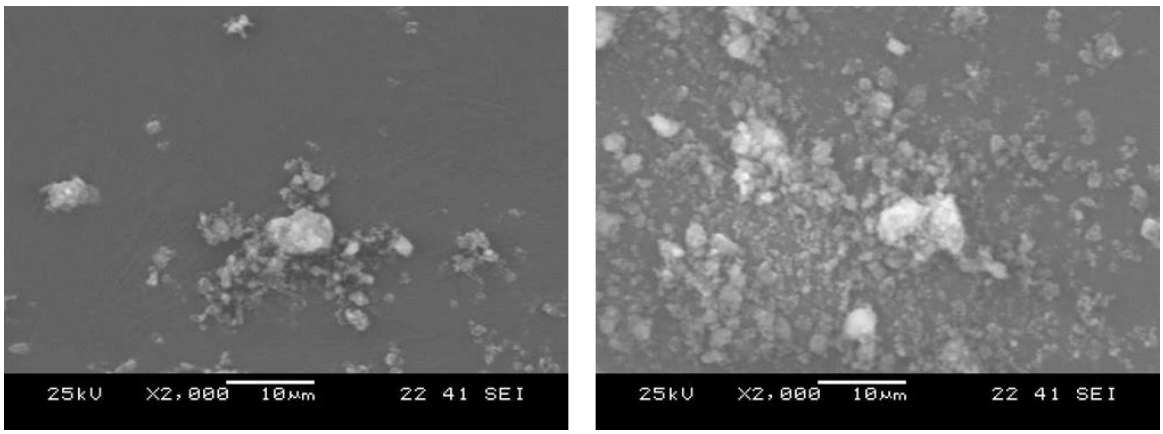

Figure 4.6: Zeolyst NH_4-ZSM-5 SEM images.

The SEM images of the NH_4-ZSM-5 and H-SSZ-13 samples, figures 4.6 and 4.7 respectively, showed relatively small crystal size, both around 2 – 3 µm in diameter. Both samples, especially the ZSM-5, showed some damage, most likely from the calcination and ion-exchange procedures to obtain the ammonium and acid forms of the zeolites. The SSZ-13 sample showed rather clear spherical crystals.

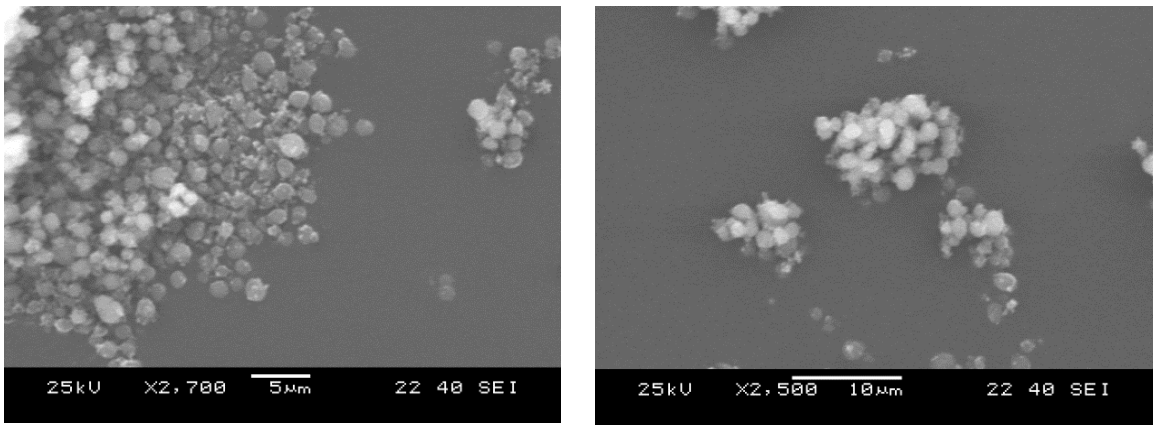

Figure 4.7: Chevron H-SSZ-13 SEM images.

The SEM images of as-synthesised mordenite showed thin platelet-like crystals around 10 µm in diameter, figure 4.8. The homogeneity of the crystals further confirms a pure mordenite sample, with only one phase present.

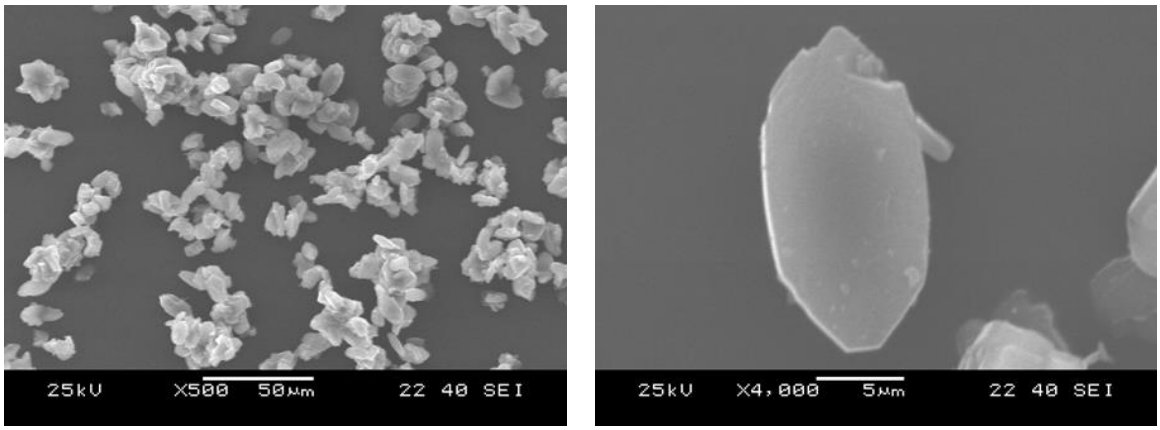

Figure 4.8: As-synthesised mordenite SEM images.

The SEM images of as-synthesised ferrierite show spherical crystals around 40 µm in diameter. The consistency of spherical crystals, along with possible fragments from damaged crystals, confirms that only one phase is present in the sample, removing the doubt from the PXRD pattern that a competing phase may be present.

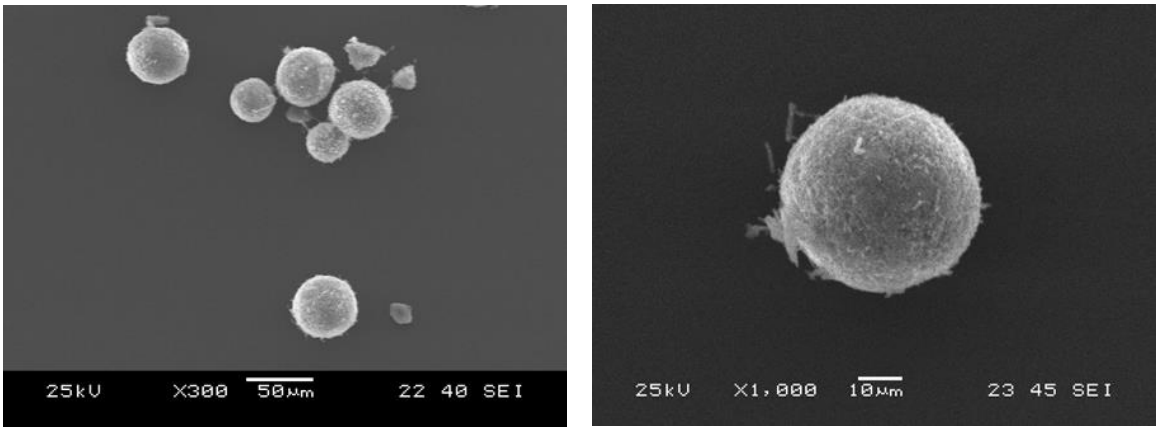

Figure 4.9: As-synthesised ferrierite SEM Images.

Table 4.2: EDX data of the acid site zeolites.

Zeolite	% Silicon	% Aluminium	Si/Al
ZSM-5	95.50 ± 0.17	4.50 ± 0.17	21
SSZ-13	95.32 ± 0.12	4.68 ± 0.12	20
Mordenite	91.01 ± 0.45	8.99 ± 0.45	10
Ferrierite	89.07 ± 0.47	10.93 ± 0.47	8

The EDX data for all zeolites is shown in table 4.2. The Si/Al ratios of ZSM-5 and SSZ-13 are 21 and 20 respectively, the highest ratios of the four zeolites. Ferrierite has a Si/Al ratio of 8, meaning it has the highest aluminium content of all the zeolites. Mordenite has a Si/Al ratio of 10, making it the second highest aluminium content.

4.4.1.3. Ammonia Temperature Programmed Desorption

The NH_3-TPD mass spectrometry data of the acid site zeolites is shown in figure 4.10. All plots show the characteristic double peak corresponding to low temperature (LT) and high temperature (HT) ammonia desorption.[7] It is generally thought that the low temperature desorption corresponds to physically adsorbed ammonia and therefore not directly related to the zeolite acidity. Longer purge times have been seen to reduce the intensity of the low temperature peak, due to a higher removal of physisorbed ammonia.[8] This may explain why the two larger pore zeolites, ferrierite and mordenite, have the greatest LT desorption peak, as they have a higher capacity for physisorbed molecules.

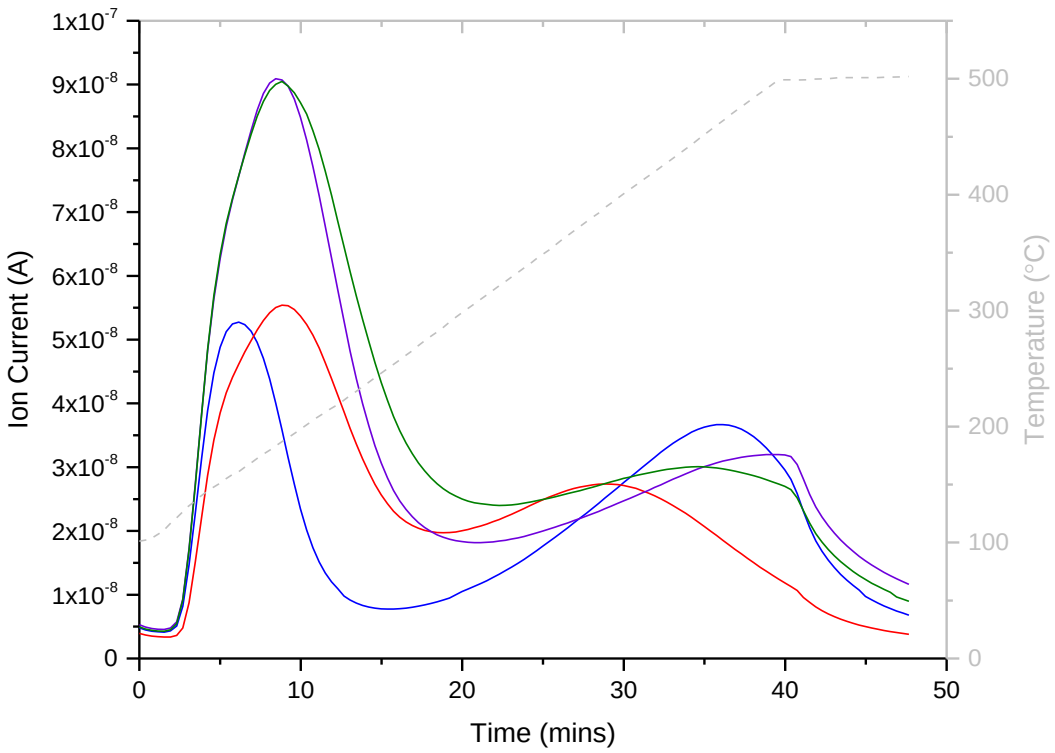

Figure 4.10: NH_3-TPD mass spectrometry plots of acid site SSZ-13 (blue), ZSM-5 (red), mordenite (purple) and ferrierite (green). The left-hand axis corresponds to the ion-current recorded by the mass spectrometer and is represented by the four coloured plots. The right-hand axis corresponds to temperature and is represented by the grey dashed line.

The HT peak is considered to be directly related to the acid strength and number of acid sites. The higher temperature of desorption is indicative of a stronger interaction between the acid site and the probe molecule, ammonia, and therefore a stronger acid strength[9]. The ion current obtained from the mass spectrometry is related to the number of ammonia ions detected. The higher the ion current suggests the greater number of ammonia molecules were adsorbed and therefore the higher number of acid sites present. Considering the maxima of the high temperature peaks (T_{max}), it is possible to identify the differences between the ion current and desorption temperature of the acid zeolites, figure 4.11. The T_{max} temperatures were taken as 389.0 °C for ZSM-5, 451.7 °C for ferrierite, 463.6 °C for SSZ-13 and 495.2 °C for mordenite.

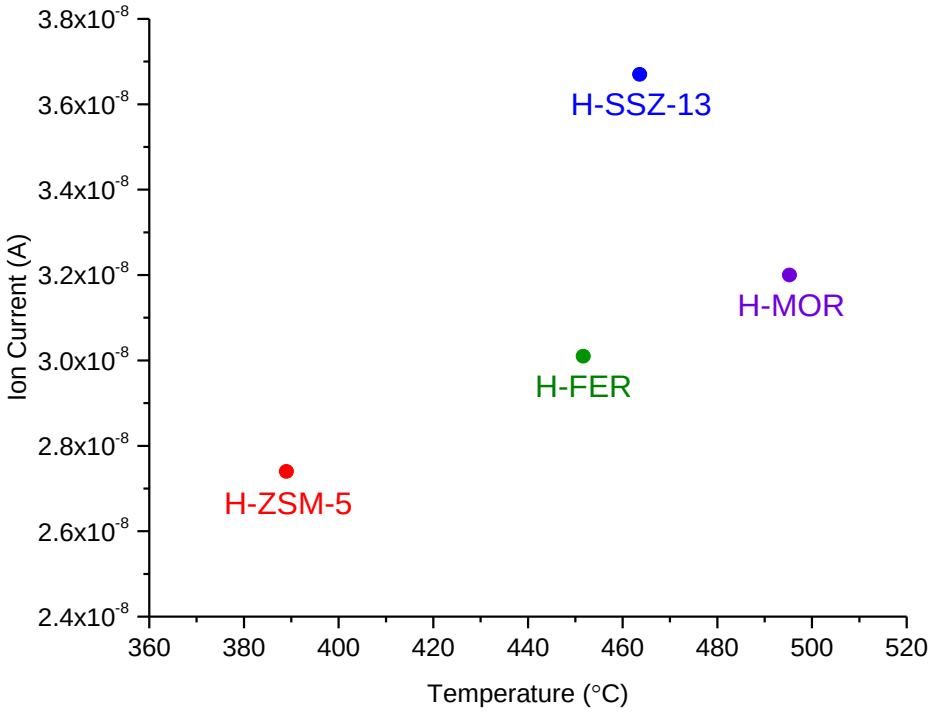

Figure 4.11: Ion current and temperature of the T_{max} of each acid site zeolite.

It is worth noting that the mordenite and ferrierite HT peaks contain a shoulder as the temperature plateaus at 500 °C, indicating that not all ammonia was removed. Ideally the temperature would have been taken higher to provide smooth curves for all the zeolites. This also lead to further issues calculating the number of acid sites. If possible, the HT peaks would have been integrated to quantify the number of sites, the shoulders however made it challenging to accurately fit a curve. The best option considered was taking the peak heights as an indication, this however leaves room for error with the measurements.

The ammonia desorption temperature increases in the order of H-ZSM-5, H-FER, H-SSZ-13 and H-MOR. This suggests that H-ZSM-5 has the weakest acid sites and H-MOR has the strongest. This has been observed previously with literature where there is around 100 °C difference between H-ZSM-5 and H-MOR ammonia desorption temperatures.[7,10] The data for ferrierite also matches well with previous literature values, with values of around 450 and 460 °C recorded.[11,12] Literature data for SSZ-13 appears inconsistent, with one source calculating T_{max} as 480 °C while another places it closer to 400 °C, therefore the data obtained by NH_3-TPD supports the higher T_{max}.[13,14]

The ion current results show that H-ZSM-5 has the lowest number of acid sites, identified by the lowest current of 2.75 x 10^{-8} A. This is followed by H-FER and H-MOR with 3.00 x 10^{-8} A and 3.25 x 10^{-8} A respectively. The greatest number of acid sites is from H-SSZ-13, with an ion current of 3.70 x 10^{-8} A.

There are a range of factors that can affect the Brønsted acidity of zeolites. The first involves the angle of the T-O-T bond, where the greater the bond angle allows for a stronger T-O bond and therefore a weaker O-H bond.[15] This is due to an increase in p-character of the O-H bond as the T-O-T bond angle increases, this increase in p-character decreases the bond strength.[16] A weaker O-H bond allows easier donation of the proton and is therefore a stronger acid. Due to the difficulty of differentiating between silicon and aluminium atoms in zeolites, pure silica zeolites will be considered when looking at bond angles.

A paper from Wragg et al. studied the structural difference between 35 different frameworks from literature, including the Si-O-Si bond angle, using structural tools like X-ray diffraction.[17] Three sets of crystallographic data were used for the Si-O-Si angle of the CHA framework (SSZ-13), the results for the average angles were 148.0 ± 2.0°, 146.8 ± 3.7° and 148.5 ±1.4°.[18–20] Similarly, three sets of data were studied for the FER framework, they showed Si-O-Si angles of 153.3 ± 8.2°, 152.6 ± 8.3° and 154.2 ± 6.3°.[20–22] Two sets of data were studied for the MFI framework (ZSM-5), with average angles of 156.0 ± 9.1° and 153.7 ± 10.4°.[23,24] The range of values for the MOR framework stretch from 138.7 ± 12.0° to 166.7 ± 4.0°.[25] Other literature sources however, claim a 180° T-O-T bond angle can be observed in the mordenite framework.[26] Considering this data, the weakest acid sites would come from SSZ-13 and the strongest from mordenite.

The second acid strength factor, concerns the aluminium distribution. Next nearest neighbours (NNN) refers to the T-atoms in the next coordination sphere to an aluminium atom. A higher number of aluminium atoms results in a lower acid strength.[27] This is due to the change in electronics with increasing aluminium atoms in NNN positions as aluminium has a lower electronegativity than silicon.[27,28] Again, it is difficult to differentiate between Si and Al atoms within the framework, therefore the structure will be taken as a whole and the Si/Al ratio considered. Looking at the Si/Al ratios, ferrierite has the highest number of aluminium atoms, this is followed by mordenite and then SSZ-13 and ZSM-5 which both have relatively low amounts of aluminium (Si/Al ~ 20). This would place ferrierite as the weakest acid and SSZ-13/ZSM-5 as the strongest.

The data collected by the NH_3-TPD does not correlate accurately with either of the above principles. The results of the NO production from the four acid site zeolites could perhaps cast more light on any possible trends relating to the acid sites.

4.4.2. Nitric Oxide Production

The NO production from sodium nitrite was studied on the NOA for all acid site zeolites in triplicate. Release profiles, showing NO concentration throughout the run, and production profiles, that show the total NO produced, were obtained. The runs were stopped once the nitric oxide concentration had returned to background levels, hence the varied length of time of the runs.

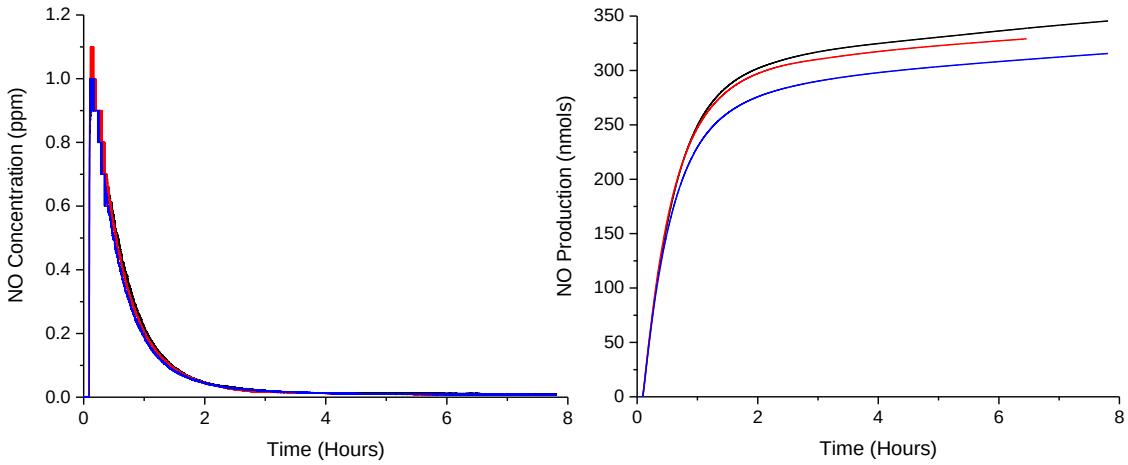

Figure 4.12: H-ZSM-5 triplicates release profile (left) and NO production (right).

H-ZSM-5, figure 4.12, showed a high initial concentration, spiking around 1 – 1.1 ppm of NO. The concentration dropped relatively quickly, with the majority of the NO produced within 3 hours. All three runs matched well, with the total NO produced from the runs around 300 nmols, corresponding to 24 % conversion of nitrite.

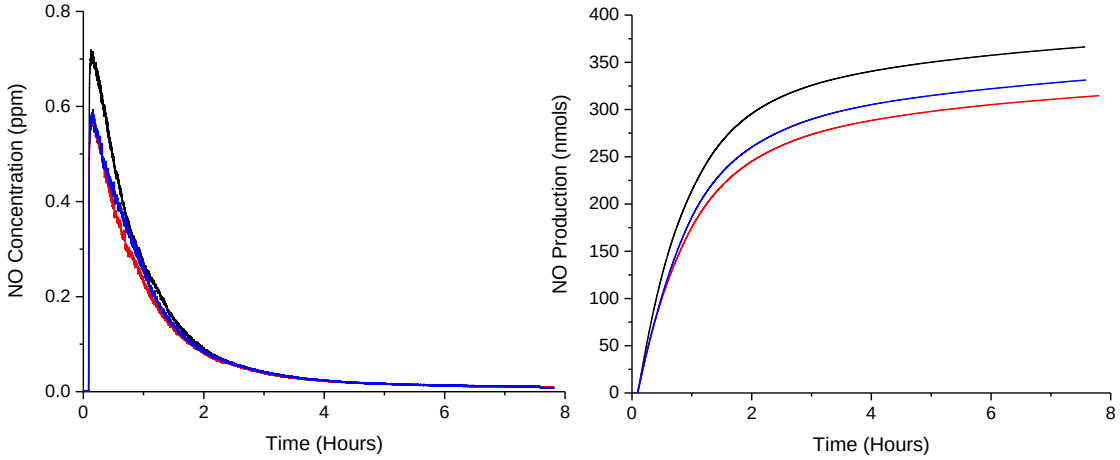

Figure 4.13: H-SSZ-13 triplicates release profile (left) and NO production (right).

H-SSZ-13, figure 4.13, shows initial NO concentration around 0.6 – 0.7 ppm, with production lasting around 6 hours. The total NO produced was also around 300 nmols (24 % conversion), like H-ZSM-5, but the production was at a lower concentration for a more sustained time period.

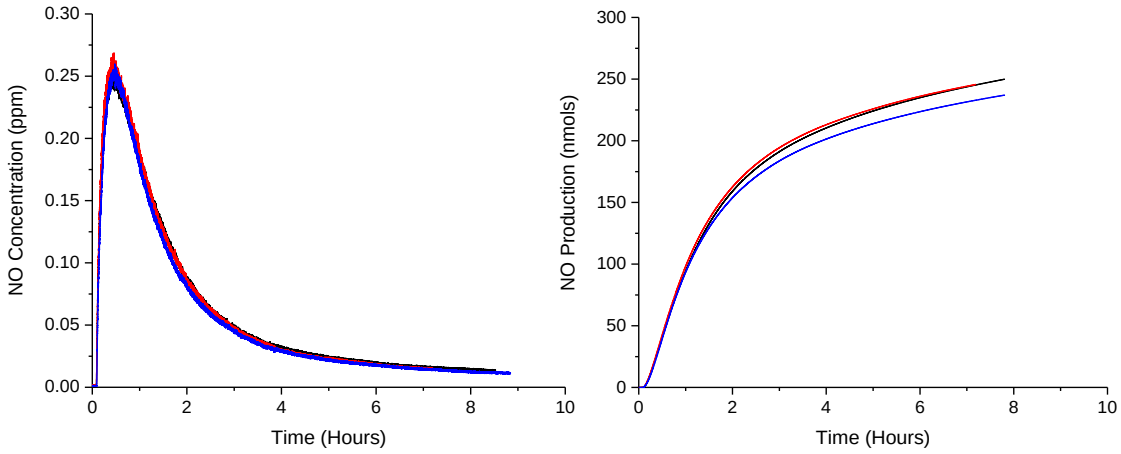

Figure 4.14: H-MOR triplicates release profile (left) and NO production (right).

H-MOR, figure 4.14, has a slightly different release profile shape than the previous samples, with a longer time period until the peak concentration of around 0.26 ppm. The

NO production lasted around 9 hours, significantly longer than any of the previous zeolites. The total NO produced was around 250 nmols, 20 % conversion of nitrite.

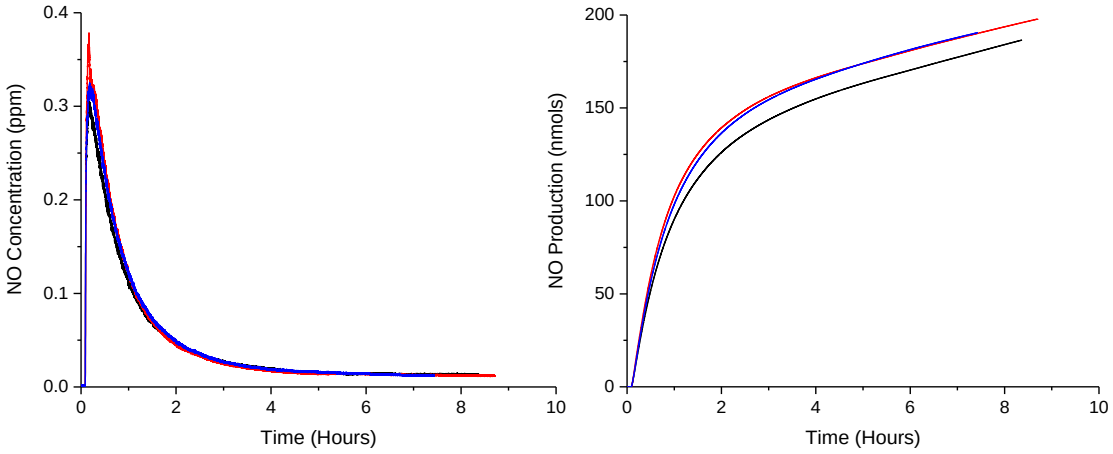

Figure 4.15: H-FER triplicates release profile (left) and NO production (right).

H-FER, figure 4.15, shows an initial NO concentration between 0.30 and 0.37 ppm, one of the triplicates (red) however, has a spike at the peak of the NO concentration which widens this range. The production lasts around 6 hours with 180 nmols of NO produced, corresponding to 14 % conversion, the lowest amount from all the acid site zeolites.

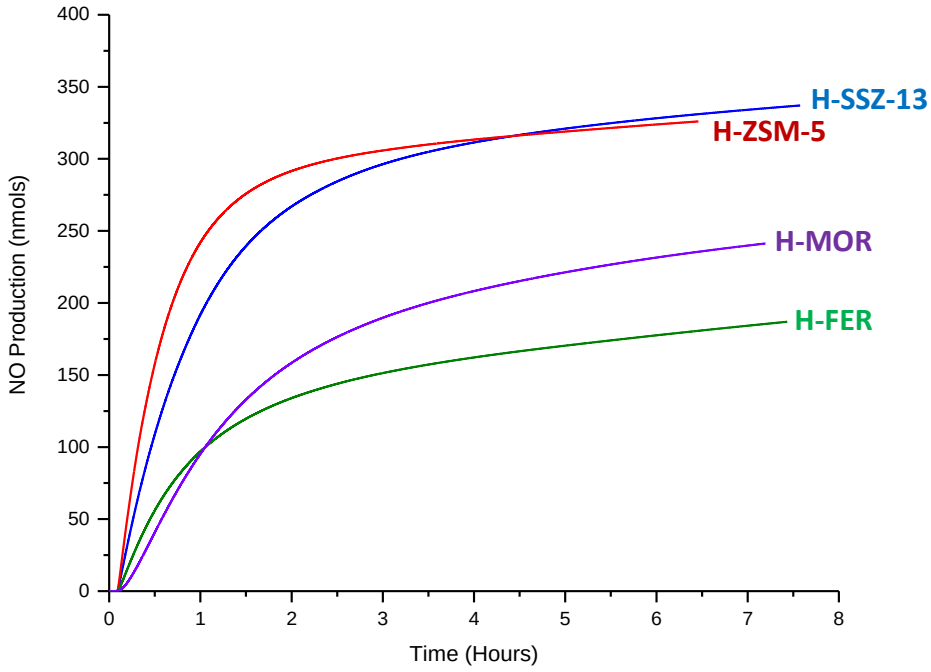

Figure 4.16: Comparison of average NO production of all acid site zeolites. SSZ-13 (blue), ZSM-5 (red), mordenite (purple) and ferrierite (green).

Figure 4.16 shows the average NO production from the triplicates of all the acid site zeolites. The results show H-SSZ-13 and H-ZSM-5 with the highest NO production, with 337 nmols and 326 nmols respectively. This is followed by H-MOR with 241 nmols and then H-FER with 187 nmols.

Comparing the results of the NH_3-TPD and the NO production, it is difficult to observe any trend between the acid strength and the catalysis. The weakest acid with the lowest number of acid sites, ZSM-5, shows one of the highest productions of NO, while mordenite that has the strongest acid sites shows the second lowest NO production. The substrate size may influence these results, due to the slightly larger size of the nitrite ion over the ammonium ion.[29,30] As discussed in section 1.1.4, mordenite and ferrierite contain channels which have a maximum diameter diffusion size of 1.57 Å and 1.56 Å respectively. This value is too small for a nitrite ion to diffuse, potentially limiting the accessibility of the acid sites and therefore resulting in a lower conversion of nitrite.

The varying local structures of the zeolites may also alter the ways in which the ammonia or nitrite molecules interact with active sites. Mordenite, for example, contains two distinct areas for cations to reside, the 12-membered channel and the smaller 8-membered channel and side pockets that runs next to it.[31] Differences in local structure, like that discussed with mordenite, may affect the rate and selectivity of the reaction due to size restraints of molecules or transition states.[16]

The zeolite ordering does follow the aluminium distribution however, with the low aluminium zeolites (SSZ-13 and ZSM-5) producing the highest amount of NO. This is consistent with the highest aluminium content zeolite (ferrierite) producing the lowest amount of NO.

4.4.3. Rates of Reaction

The rates of reaction were initially determined by use of the Avrami equation.[32] The equation is sometimes known as the Johnson-Mehl-Avrami-Kolmogoroff (JMAK) model and is commonly used to study phase transition kinetics.[33] At first, all plots from figure 4.16 were normalised between 0 and 1 on the y-axis to provide the extent of reaction, α. Equation 4.1 was then applied to the normalised curves to provide k and n. The Avrami exponent, n, can range between 1 and 4 and in most systems corresponds to nucleation and crystal growth mechanisms.[34] The overall rate constant, k, can be used to compare rates of reaction of the zeolites.

$$y = 1 - \exp(-kx^n) \tag{4.1}$$

The results of the fit are shown in figure 4.17 below and the corresponding k and n values presented in table 4.3. All Avrami plots throughout this thesis were produced with help from Susan Henkelis.

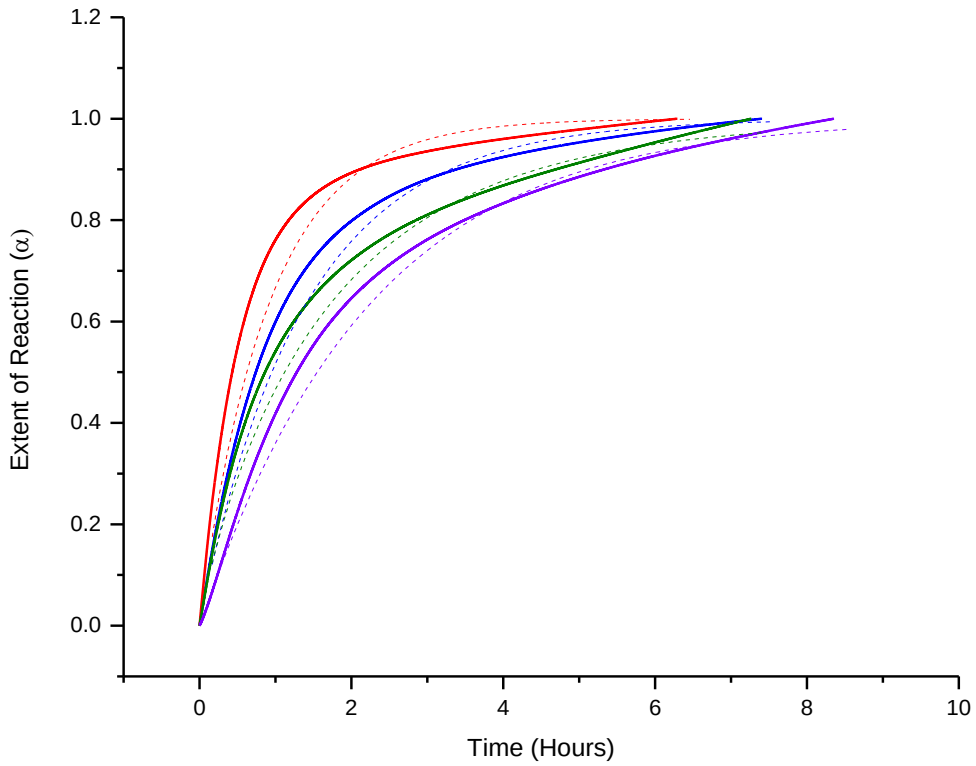

Figure 4.17: The Avrami fit (dashed line) of the normalised NO production (solid line) from the acid site zeolites. SSZ-13 (blue), ZSM-5 (red), mordenite (purple) and ferrierite (green).

Table 4.3: The k and n values derived from Figure 4.17.				
Zeolite	H-ZSM-5	H-SSZ-13	H-FER	H-MOR
n	0.97	0.97	0.87	1.00
k (hour^{-1})	1.10	0.72	0.59	0.45

The results show that n ≈ 1 for all the zeolites. Literature sources studying the release of ethylene gas from amorphous α-cyclodextrin and cold-water-soluble starch found that when n = 1 it corresponds to first-order kinetics.[35,36] This suggests that the reaction rate depends only on one reactants concentration. The poor match of the two plots however suggests that the mechanism may be too complex to fit by the Avrami equation. The rate increases in the order of mordenite < ferrierite < SSZ-13 < ZSM-5.

Since the Avrami fit does not match the lines as accurately as hoped, a second plot was also used to obtain n values. The Sharp-Hancock equation is shown in equation 4.2 and the graph was obtained by plotting ln (t-t_0) against ln(-ln(1-α)), figure 4.18, where α is the same extent of reaction that was used for the Avrami plot. The Sharp-Hancock plot should produce a straight line if the kinetics conform to the Avrami equation.[37] Any deviation to the straight line plot is indicative to a change in the NO production reaction mechanism.

$$\ln(-ln(1-\alpha)) = nlnk + nln(t-t_0) \tag{4.2}$$

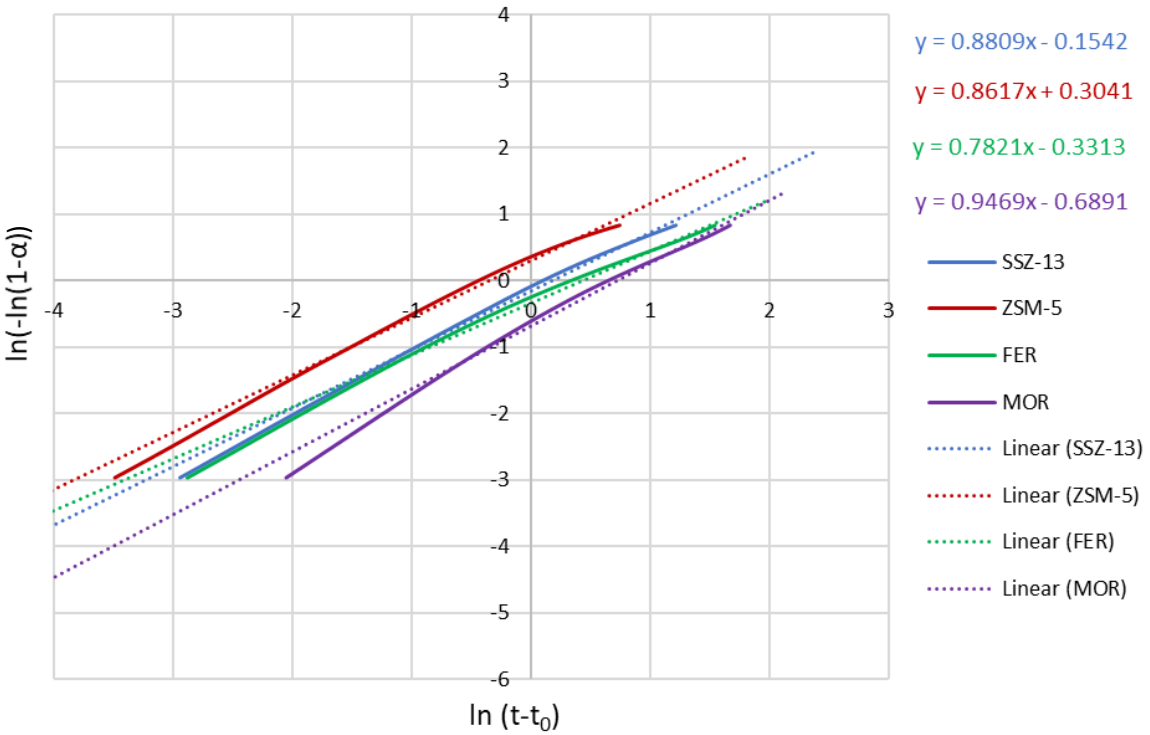

Figure 4.18: The Sharp-Hancock fit (dashed line) of the normalised NO production (solid line) from the acid site zeolites, SSZ-13 (blue), ZSM-5 (red), mordenite (purple) and ferrierite (green). The plotted values correspond to extent of reactions (α) between 5 and 90 %.[37] The equations of the linear trends are shown in the top right corner in the form of y = mx + c.

Table 4.4: The k and n values derived from the Sharp-Hancock plot in Figure 4.18.

Zeolite	H-ZSM-5	H-SSZ-13	H-FER	H-MOR
n	0.86	0.88	0.78	0.95
k (hour^{-1})	1.42	0.84	0.65	0.48

The k and n values were calculated by inserting the values from the y = mx + c equations, determined from the plot fit, into the same format as the Sharp-Hancock equation. The n values from the Sharp-Hancock plot, table 4.4, agree with the Avrami n values. This suggests that n = 1 values for all zeolites is a reasonable value. The slight deviation from the straight lines however, also suggest that the Avrami equation does not accurately fit the data.

The initial rates of the reaction can also be studied to help to identify further differences in the zeolites. Figure 4.19 shows the NO production in the first 15 minutes after the

sodium nitrite was injected. A linear fit was applied to each NO production and the rate of reaction in the first 15 minutes determined, table 4.5.

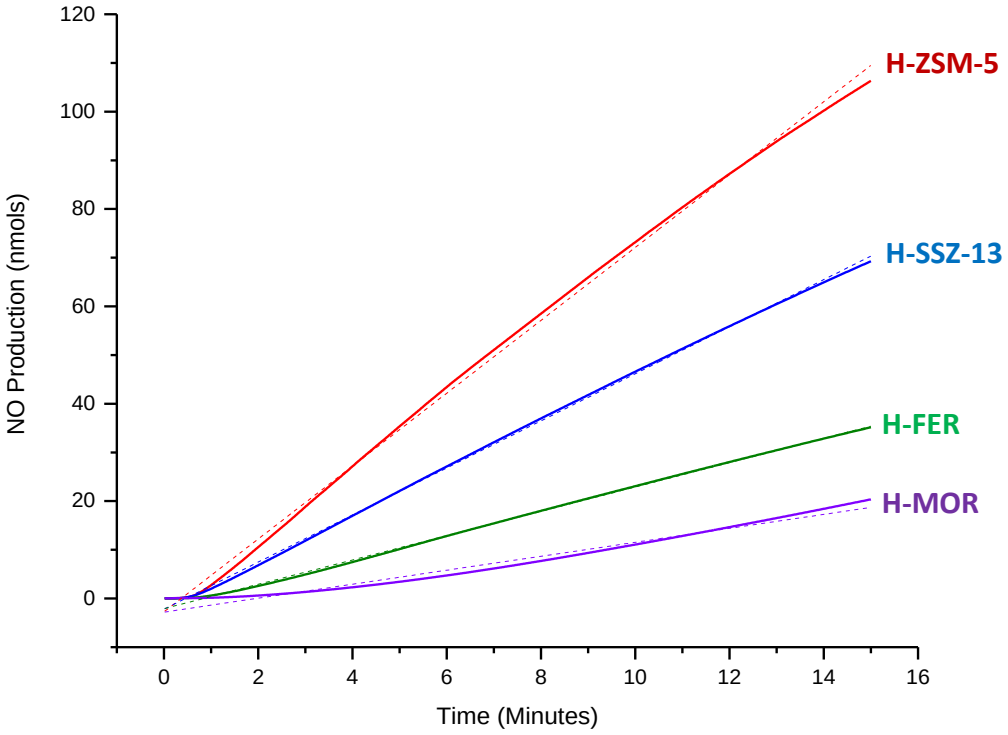

Figure 4.19: The NO production (solid) and linear fit (dashed) of the four acid site zeolites in the first 15 minutes after sodium nitrite injection. SSZ-13 (blue), ZSM-5 (red), mordenite (purple) and ferrierite (green).

Table 4.5: The gradients and rates derived from Figure 4.19.

Zeolite	H-ZSM-5	H-SSZ-13	H-FER	H-MOR
Gradient	7.483 ± 0.010	4.836 ± 0.004	2.499 ± 0.003	1.434 ± 0.008
Rate (nmol/min)	0.499	0.322	0.167	0.096

The results show the rate increasing in the order of mordenite, ferrierite, SSZ-13 and ZSM-5, the same order as the Avrami fit. This may be related to the channel dimensionality, with the two 2D channel systems, mordenite and ferrierite, having the lowest rate and the two 3D channel systems, SSZ-13 and ZSM-5, having the highest rate. The higher dimensionalities could allow faster access of the substrate to the active sites, resulting in faster NO production.

4.4.4. Lack of Regeneration

Due to the proposed biomedical applications, it is beneficial that the zeolites are able to regenerate the active site to allow a catalytic production and therefore a long-term NO production. Successive nitrite injections were performed with an acid site zeolite (H-SSZ-13) to observe if the initial amount of NO produced was sustained from a second injection.

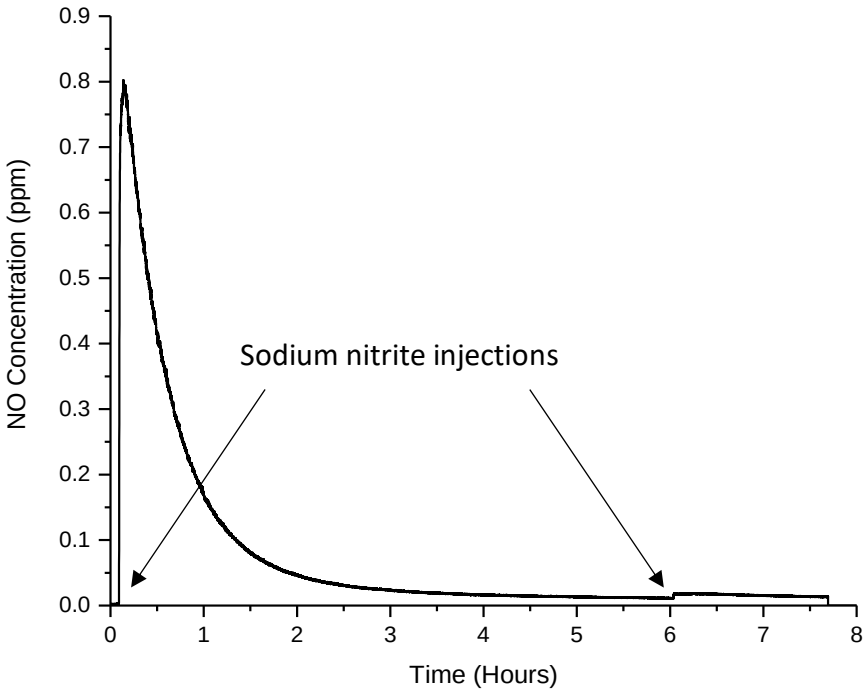

Figure 4.20: Release profile of H-SSZ-13 with two nitrite injections, one at the beginning of the run and a second six hours into the run.

The release profile, figure 4.20, shows that a second injection of substrate produced a considerably lower amount of NO than the first, 5 ppb of NO compared with 800 ppb. As initially highlighted in section 4.2, this suggests that the acid site has been consumed during the first reaction with nitrite and therefore removed the proton.

The lack of acid site regeneration inhibits the use of these zeolites within long term NO producing applications, such as stent coatings. They are, however, promising candidates for wound healing and antimicrobial applications. Acidified nitrite has been used rather extensively as a means to deliver NO to wounds or infections on the skin, this is commonly delivered by combining sodium nitrite and acid in aqueous creams.[38–40] Porous materials (MOFs and zeolites) have also been used to store and release NO for wound healing.[41] The

acid site zeolite catalysts may allow the ideal combination of the two different methods, with the capacity to store and release NO as well as catalytically produce it. This could provide a longer release of NO to enhance wound healing.

4.5. Conclusions

The acid forms of mordenite, ferrierite, ZSM-5 and SSZ-13 were prepared and studied as NO producing zeolite catalysts. The conversion of sodium nitrite to NO was greatest for SSZ-13 and ZSM-5, with 24 % and 20 % respectively. These two zeolites are classed as 3D zeolites, which may have helped the diffusion of the substrate to the active site locations. Furthermore, they have lower aluminium contents than mordenite and ferrierite, a factor which can increase acidity. SSZ-13 and ZSM-5 also had the highest rate of NO production, suggesting the substrate was interacting with the active sites quicker than the substrate with mordenite and ferrierite.

Interestingly, the NH_3-TPD data does not correlate directly to the NO production, this is potentially due to the slight difference in size of the ammonium and nitrite ions. Perhaps one of the most important findings, regarding the acid site zeolites, is the lack of regeneration after successive nitrite injections, with NO production limited to one substrate injection. This highlights that they may not be suitable for long term NO production and are more suited to short term NO production, such as wound healing and antimicrobial applications.

4.6. Future Work

The main issue that arose during this work, was the lack of correlation between NH_3-TPD results and NO production. Hence, it would be interesting to look at different properties of a zeolite that may affect the acidity, such as varying the Si/Al ratio. This would help to understand the influence of different factors on the quantity and strength of acid sites and how this affects the NO production. A second acid characterisation technique, such as infrared (IR) spectroscopy, may also help to understand the acid sites.

The consumption of the acid sites during the reaction is a big problem when considering long-term NO production. It would be interesting for future work to study methods of regenerating the acid sites to allow the zeolites to be recycled. This may be troublesome however, as the process to form the acid sites initially required a calcination. This is something that would not be possible when the target zeolite application is a biomedical application working at body temperatures.

4.7. References

1 R. Weller and M. J. Finnen, *Nitric Oxide*, 2006, **15**, 395–399.

2 R. Weller, R. J. Price, A. D. Ormerod, N. Benjamin and C. Leifert, *J. Appl. Microbiol.*, 2001, **90**, 648–652.

3 A. D. Ormerod, P. Copeland, I. Hay, A. Husain and S. W. B. Ewen, *J. Invest. Dermatol.*, 1999, **113**, 392–397.

4 J. A. Thomas and B. Ballantyne, *J. Am. Coll. Toxicol.*, 1992, **11**, 259–273.

5 H. Robson and K. P. Lillerud, in *Verified Syntheses of Zeolitic Materials*, Elsevier Science, Amsterdam, 2001, pp. 167–168.

6 H. Robson and K. P. Lillerud, in *Verified Syntheses of Zeolitic Materials*, Elsevier Science, Amsterdam, 2001, pp. 212–213.

7 M. Niwa and N. Katada, *Catal. Surv. from Japan 1*, 1997, **1**, 215–226.

8 L. Rodríguez-González, F. Hermes, M. Bertmer, E. Rodríguez-Castellón, A. Jiménez-López and U. Simon, *Appl. Catal. A Gen.*, 2007, **328**, 174–182.

9 V. Rakić and L. Damjanović, in *Calorimetry and Thermal Methods in Catalysis*, Springer Berlin Heidelberg, 2013, pp. 131–174.

10 F. Lónyi and J. Valyon, *Microporous Mesoporous Mater.*, 2001, **47**, 293–301.

11 H. Hu, M. Ke, K. Zhang, Q. Liu, P. Yu, Y. Liu, C. Li and W. Liu, *RSC Adv.*, 2017, **7**, 31535–31543.

12 P. Cañizares and A. Carrero, *Catal. Letters*, 2000, **64**, 239–246.

13 F. Gao, M. Kollár, R. K. Kukkadapu, N. M. Washton, Y. Wang, J. Szanyi and C. H. F. Peden, *Appl. Catal. B Environ.*, 2015, **164**, 407–419.

14 Q. Zhu, J. N. Kondo, T. Tatsumi, S. Inagaki, R. Ohnuma, Y. Kubota, Y. Shimodaira, H. Kobayashi and K. Domen, *J. Phys. Chem. C*, 2007, **111**, 5409–5415.

15 E. G. Derouane, J. C. Védrine, R. R. Pinto, P. M. Borges, L. Costa, M. Lemos, F. Lemos and F. R. Ribeiro, *Catal. Rev.*, 2013, **55**, 454–515.

16 N. Katada, K. Suzuki, T. Noda, G. Sastre and M. Niwa, *J. Phys. Chem. C*, 2009, **113**, 19208–19217.

17 D. S. Wragg, R. E. Morris and A. W. Burton, *Chem. Mater.*, 2008, **20**, 1561–1570.

18 P. A. Barrett, M. J. Díaz-Cabañas, M. A. Camblor and R. H. Jones, *J. Chem. Soc. Faraday Trans.*, 1998, **94**, 2475–2481.

19 M. J. Díaz-Cabañas and P. A. Barrett, *Chem. Commun.*, 1998, **0**, 1881–1882.

20 L. A. Villaescusa, I. Bull, P. S. Wheatley, P. Lightfoot and R. E. Morris, *J. Mater. Chem.*, 2003, **13**, 1978–1982.

21 S. J. Weigel, J. C. Gabriel, E. G. Puebla, A. M. Bravo, N. J. Henson, L. M. Bull and A. K. Cheetham, *J. Am. Chem. Soc.*, 1996, **118**, 2427–2435.

22 I. Bull, P. Lightfoot, L. A. Villaescusa, L. M. Bull, R. K. B. Gover, J. S. O. Evans and R. E. Morris, *J. Am. Chem. Soc.*, 2003, **125**, 4342–4349.

23 H. van Koningsveld, H. van Bekkum and J. C. Jansen, *Acta Crystallogr. Sect. B Struct. Sci.*, 1987, **43**, 127–132.

24 E. Aubert, F. Porcher, M. Souhassou, V. Petříček and C. Lecomte, *J. Phys. Chem. B*, 2002, **106**, 1110–1117.

25 P. Simoncic and T. Armbruster, *Am. Mineral.*, 2004, **89**, 421–431.

26 T. Demuth, J. Hafner, L. Benco and H. Toulhoat, *J. Phys. Chem. B*, 2000, **104**, 4593–4607.

27 J. Weitkamp and M. Hunger, in *Studies in Surface Science and Catalysis*, Elsevier, 2007, vol. 168, pp. 787–835.

28 K. Teraishi, *Microporous Mater.*, 1995, **5**, 233–244.

29 V. Sidey, *Acta Crystallogr. Sect. B*, 2016, **72**, 626–633.

30 L. A. Richards, A. I. Schäfer, B. S. Richards and B. Corry, *Small*, 2012, **8**, 1701–1709.

31 D. B. Lukyanov, T. Vazhnova, N. Cherkasov, J. L. Casci and J. J. Birtill, *J. Phys. Chem. C*, 2014, **118**, 23918–23929.

32 M. Avrami, *J. Chem. Phys.*, 1940, **8**, 212–224.

33 M. Fanfoni and M. Tomellini, *Phys. Rev. B*, 1996, **54**, 9828–9833.

34 Y. P. Khanna and T. J. Taylor, *Polym. Eng. Sci.*, 1988, **28**, 1042–1045.

35 B. T. Ho and B. R. Bhandari, *J. Agric. Food Chem.*, 2016, **64**, 3318–3323.

36 L. Shi, X. Fu, C. P. Tan, Q. Huang and B. Zhang, *J. Agric. Food Chem.*, 2017, **65**, 2189–2197.

37 A. Altree-Williams, A. Pring, Y. Ngothai and J. Brugger, *ACS Earth Sp. Chem.*, 2017, **1**, 89–100.

38 R. Weller, A. D. Ormerod, R. P. Hobson and N. J. Benjamin, *J. Am. Acad. Dermatol.*, 1998, **38**, 559–563.

39 A. D. Ormerod, A. A. J. Shah, H. Li, N. B. Benjamin, G. P. Ferguson and C. Leifert, *BMC Res. Notes*, 2011, **4**, 458.

40 R. Weller and M. J. Finnen, *Nitric Oxide - Biol. Chem.*, 2006, **15**, 395–399.

41 P. S. Wheatley, A. R. Butler, M. S. Crane, S. Fox, B. Xiao, A. G. Rossi, I. L. Megson and R. E. Morris, *J. Am. Chem. Soc.*, 2006, **128**, 502–509.

Chapter 5: Copper Site Zeolite Catalysts

5.1. Aim

This chapter will assess the potential of copper site zeolites to be used as catalysts for the production of nitric oxide (NO) for biomedical applications. Five zeolites will be looked at; mordenite, ferrierite, ZSM-5, SSZ-13 and UZM-4. As with the acid sites, the NO production from nitrite will be studied by the nitric oxide analyser (NOA). Since copper is held within the zeolite pores, leaching and toxicology studies will be performed to assess any potential risk for the use of these materials within the body.

5.2. Introduction

Copper zeolites are well known catalysts for a range of applications. One of the main areas that copper zeolites are used is the selective catalytic reduction (SCR) of NO_x gasses to nitrogen and water, a process known as deNO_x. While these reactions are generally performed at high temperatures, it has been found that room temperature reactions of nitrite with copper zeolites actually produced NO.[1,2] This mechanism can be used to exploit the numerous biological properties of NO for biomedical applications. One issue that had to be overcome, was the activation of the copper site. Since copper zeolites normally work at elevated temperatures, the active site is automatically reduced to the active Cu^+.[3] With the biological temperatures that these zeolites will be working at, a new method of reducing the copper was required. As the copper zeolites will be functioning within the body, a biologically available compound was considered to provide the required reduction of the copper active site.

5.2.1. Catalytic Cycle

To allow the regeneration of the copper sites, the biologically available amino acid cysteine was considered. Cysteine is present within the body from both the diet and the catabolism of methionine.[4] The aim of the catalytic cycle was for cysteine (RS-H) to reduce Cu^{2+} to Cu^+, resulting in the formation of an active copper species and an oxidised disulfide bridging cystine molecule (RS-SR), figure 5.1.

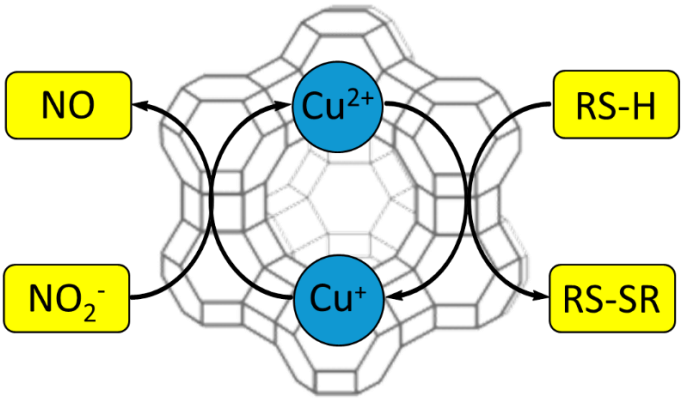

Figure 5.1: The proposed catalytic cycle of cysteine and nitrite interacting with the copper ions to produce nitric oxide.

The active Cu^{+} then reduces a molecule of nitrite to nitric oxide, resulting in the oxidation of Cu^{+} back to Cu^{2+}. The presence of cysteine and nitrite in the body would allow for a constant cycle with the copper zeolites. Furthermore, the fact that both compounds can be obtained through the diet indicates that any deficiencies that may affect the catalytic cycle, could be resolved by a change of diet.

5.3. Experimental

5.3.1. Materials

Materials used in the zeolite syntheses: Sodium hydroxide (pellets, Fisher Scientific), aluminium nitrate (nonahydrate, ≥98 %, Sigma Aldrich), Ludox AS-30 colloidal silica (30 wt. % suspension in water, Sigma Aldrich), aluminium hydroxide (reagent grade, Sigma Aldrich), tetraethylammonium hydroxide (35 w/w aqueous solution, Alfa Aesar), Ludox AS-40 colloidal silica (40 wt. % suspension in water, Sigma Aldrich), tetramethylammonium chloride (≥98 %, Sigma Aldrich), lithium chloride (≥98 %, Fluka).

Materials used in the single crystal ferrierite synthesis: Cab-O-Sil® (M-5, ACROS Organics), propylamine (99+ %, extra pure, ACROS Organics), pyridine (analytical, Fisher Scientific), HF/water (48 wt. % in H_2O, ≥99.99 % trace metals basis, Sigma Aldrich), sodium aluminate (technical, anhydrous, Al (Al_2O_3): 50 – 56 %, Na (Na_2O): 37 – 45 %, Sigma Aldrich).

5.3.2. Zeolite Synthesis

As discussed in section 4.3.1, the ZSM-5 and SSZ-13 samples were from Zeolyst and Chevron respectively. The ferrierite synthesis also followed the same procedure discussed previously.[5] Due to reasons discussed later within this chapter, single crystal ferrierite was also synthesised in an attempt to perform single crystal X-ray diffraction.

A different mordenite synthesis was performed compared to the acid site zeolites.[6] Water (23.17 g), sodium hydroxide (2.66 g, 0.067 mol) and aluminium nitrate (4.16 g, 0.011 mol) were stirred in the autoclave Teflon liner until dissolved. Ludox AS-30 colloidal silica (16.67 g, 0.278 mol) was added to the liner with high speed stirring to ensure complete mixing. The molar composition of the resulting gel was 12 Na_2O : 100 SiO_2 : 2 Al_2O_3 : 500 H_2O. The mixture was aged at room temperature for 20 hours before being placed in the oven at 175 °C for 5 days. The resulting crystals were recovered by vacuum filtration, washed with water and allowed to dry.

UZM-4 was synthesised following a literature protocol.[7] Aluminium hydroxide (1.89 g, 0.024 mol) was dissolved in 35 % tetraethylammonium hydroxide (32.64 g, 0.077 mol) with vigorous stirring. Water (8.28 g) and Ludox AS-40 colloidal silica (7.19 g, 0.048 mol) was added and the solution homogenised and then aged at 95 °C for 24 hours. Tetramethylammonium chloride (1.70 g, 0.016 mol) and lithium chloride (0.33 g, 0.008 mol) were dissolved in water (2.00 g) and added to 40 g of the aged gel. The resulting gel had a composition of 38 SiO_2 : 19 $Al(OH)_3$: 1400 H_2O : 62 TEAOH : 16 TMACl : 8 LiCl. The solution was homogenised for 2 hours and then transferred into an autoclave and placed into the oven at 125 °C for 3 days. The resulting crystals were recovered by vacuum filtration, washed with water and allowed to dry.

Single crystal ferrierite was synthesised with ranging Si/Al ratios. Half of the total Cab-O-Sil® (0.225 g, 0.004 mol), propylamine (1.68 mL, 0.020 mol) and pyridine (6.74 mL, 0.083 mol) were mixed together in a Teflon liner. The remainder of the Cab-O-Sil® (0.225 g, 0.004 mol) was added and stirred until dissolved. HF/water (228 µL, 0.006 mol) was added to the liner with stirring. In a beaker, sodium aluminate (0.048 g, 0.586 mmol) was dissolved in water (0.62 mL), this was added to the other solution and stirred for 2 – 3 hours. The resulting gel composition was 1.5 SiO_2 : 1.26 HF : 0.06 Al_2O_3 :

0.06 Na_2O : 4.1 $PrNH_2$: 8.4 H_2O : 16.2 pyr, corresponding to a Si/Al ratio of 12.5. The autoclave was placed into the 175 °C oven for 10 days, and the crystals collected by filtration.

The mass of sodium aluminate was altered to vary the Si/Al ratios of the synthesis. For a Si/Al ratio of 7.5, 82 mg (1 mmol) was used providing a composition of 1.5 SiO_2 : 1.26 HF : 0.10 Al_2O_3 : 0.10 Na_2O : 4.1 $PrNH_2$: 8.4 H_2O : 16.2 pyr. For a Si/Al ratio of 6.25, 98.4 mg (1.2 mmol) was used resulting in a composition of 1.5 SiO_2 : 1.26 HF : 0.12 Al_2O_3 : 0.12 Na_2O : 4.1 $PrNH_2$: 8.4 H_2O : 16.2 pyr. The lowest Si/Al ratio of 5 used 123 mg (1.5 mmol) of sodium aluminate which gives a synthesis gel composition of 1.5 SiO_2 : 1.26 HF : 0.15 Al_2O_3 : 0.15 Na_2O : 4.1 $PrNH_2$: 8.4 H_2O : 16.2 pyr.

5.3.3. Copper Site Formation

The copper sites were formed by copper ion exchange with a copper salt. The synthesised samples were calcined prior to ion exchange, to remove any organics within the pores. The calcinations were performed at 575 °C for 7 hours with a heating ramp of 1.5 °C/min. The UZM-4 sample could be directly ion exchanged due its highly porous nature.[7] The general procedure of the ion exchange comprised of refluxing the zeolite in a solution of copper (II) nitrate trihydrate (Sigma Aldrich, 0.3 M) at 95 °C for 24 hours, with a ratio of 10 mL of solution to 50 mg of zeolite. The zeolite was then filtered and washed with water to remove any residual copper. A colour change of white to blue provided a good indication of a successful copper ion exchange.

A different method was employed to ion exchange the ferrierite single crystals, in an attempt to minimise the crystal damage. The crystals were placed in a beaker with copper (II) acetate monohydrate (ACROS Organics, 0.3 M) and the solution stirred by an overhead stirrer. The stirring blades were placed above the bottom of the beaker to avoid any crystal grinding. The ion exchange took place over 8 days. The crystals were collected by vacuum filtration and washed with water. EDX measurements were used to determine the level of copper in each sample.

5.3.4. Catalytic Testing

The same NOA set-up as described in section 4.3.4 was used for the copper site catalytic tests. For the copper sites however, the sacrificial reductant cysteine was required and a smaller volume of nitrite was used. L-cysteine hydrochloride (BDH Chemicals, 0.05 M, 25 µL, 1.25 x 10^{-6} mols) was injected 5 minutes into the run, with the substrate, sodium nitrite (Alfa Aesar, 0.05 M, 5 µL, 2.5 x 10^{-7} mols), added 10 minutes later. The sample was run until the NO concentration returned to background levels. An excess of cysteine hydrochloride ensured that the reduction of the copper sites was never limiting the NO production from the nitrite.

A control run of the copper site catalysis can be found in figure A2 of the Appendix. The run was completed without any cysteine source to ensure that the sacrificial reductant was required for NO production.

A large-scale NO production was also performed with Cu-FER. This was in an attempt to prepare post-catalysis material for solid-state NMR. Cu-FER (200 mg) was placed in a round bottom flask with Milli-Q water (100 mL) and a stirrer bar. The flask was sealed with a septum. One large and one small needle were inserted through the septum, with the large needle reaching the solution and the short needle staying at the neck of the flask. Nitrogen gas was run through the large needle to bubble through the sample, while the short needle took any gas produced to the NOA.

The solution was degassed by nitrogen for 30 minutes prior to the run. D/L-cysteine (Sigma Aldrich, 0.05 M, 1 mL (injected as 4 x 250 µL), 5 x 10^{-5} mols) was injected 5 minutes into the run. Sodium nitrite (Alfa Aesar, 0.05 M, 0.2 mL, 1 x 10^{-5} mols) was injected twice during the run, first at 15 minutes and a second time at 10 hours 15 minutes.

5.3.5. Zeolite Toxicology

Zeolite toxicology studies were performed in collaboration with Dr Claudia Orellana at the Centre for Integrated Biology, Universidad Mayor, Santiago, Chile. I provided the five samples and Dr Orellana performed the cell viability assay.

The cytotoxicity of the copper zeolites was determined by measuring the cellular metabolic activity of human embryonic kidney cells (HEK 293) using an MTS reduction

assay, where MTS is (3-(4,5-dimethylthiazol-2-yl)-5-(3-carboxymethoxyphenyl)-2-(4-sulfophenyl)-2H-tetrazolium). The viability of HEK 293 cells was studied after 24 hour incubation with ranging concentrations of copper zeolites (0, 0.25, 0.50, 0.75 and 1.00 mg/mL). The viability values for the differing concentrations were normalised by the control value of untreated cells (cells incubated only with growth media and no zeolite).

The cytotoxicity activity was investigated using CellTiter 96® Aqueous Non-Radioactive Cell Proliferation Assay (Promega, UK). The day before the experiment, the cells were seeded in to a 96 well-plate at a density of 5 x 10^3 cells per well. Prior to the treatments, the cells were washed twice with PBS (phosphate-buffered saline). The different zeolite concentrations were dispersed in complete medium, then 100 µL were added to each well and incubated for 24 h at 37 °C with 5% CO_2. To measure the toxicity, the cells were washed extensively to remove the solids, the medium was replaced with 100 µL of fresh complete medium and 20 µL of 20 MTS:1 PMS (phenazine methosulfate) solution and the plate was incubated for 1 h and 15 min at 37 °C with 5% CO_2. The plates were then read by UV-Vis spectroscopy (Spectro Star^{Nano}, BMG Labtech) at 490 nm.

The complete medium used was Dulbecco's Modified Eagle's Medium (DMEM, with phenol red) supplemented with 10 % (v/v) Fetal Bovine Serum (FBS), 2 mM L-glutamine, 100 units/mL penicillin and 100 µg/mL streptomycin.

5.3.6. Copper Leaching

Copper leaching studies were run alongside the toxicology studies to identify any connection between the release of copper from the zeolite and the level of toxicity. Three different zeolite concentrations were placed in centrifuge tubes with 10 mL of Milli-Q water and incubated at 37 °C for four different time periods. The concentrations were 2.5, 5 and 10 mg/10 mL and the incubation periods were 1 hour, 4, 8 and 24 hours. All samples were run in triplicate, giving a total of 36 samples for each zeolite.

Once incubation was complete, the samples were removed and filtered through a syringe filter (Nylon, 0.2 µm, Fisher Scientific) to remove the zeolite. The initial set-up for the incubation was staggered by 5-minute intervals per triplicate to allow sufficient time for sample filtration. The resulting solutions were stored in centrifuge tubes and the copper leaching assessed by ICP-AES.

5.4. Results and Discussion

To aid the results and discussion section, a table summarising the previously discussed key features of the five zeolites is shown in table 5.1.

Table 5.1: Framework summaries of the five zeolites applied for copper catalysis.

Zeolite	Ring Sizes	Channel System	Diffusion Along the a, b and c Axes
ZSM-5	10, 6, 5 and 4	3D	4.70 Å, 4.46 Å, 4.46 Å
SSZ-13	8, 6 and 4	3D	3.72 Å, 3.72 Å, 3.72 Å
UZM-4	12, 8, 6 and 4	3D	3.51 Å, 3.51 Å, 6.01 Å
Mordenite	12, 8, 5 and 4	2D	1.57 Å, 2.95 Å, 6.45 Å
Ferrierite	10, 8, 6 and 5	2D	1.56 Å, 3.40 Å, 4.69 Å

5.4.1. Zeolite Characterisation

5.4.1.1 Powder X-Ray Diffraction

PXRD was used to determine the phase purity of the zeolites prior to copper ion-exchange. The PXRD patterns of the ZSM-5, SSZ-13 and ferrierite samples were shown in section 4.4.1.1 of the previous chapter. The resulting patterns of mordenite and UZM-4 are shown in figures 5.2 and 5.3 respectively.

The as-synthesised mordenite experimental pattern has a few additional peaks around the 24 – 25° region compared to the simulated pattern. It is possible that these peaks are visible due to differences in intensity compared to the simulated pattern. The other option is perhaps the presence of a slight impurity. Since the overall pattern matched well, the sample was taken to SEM to further analyse the phase purity.

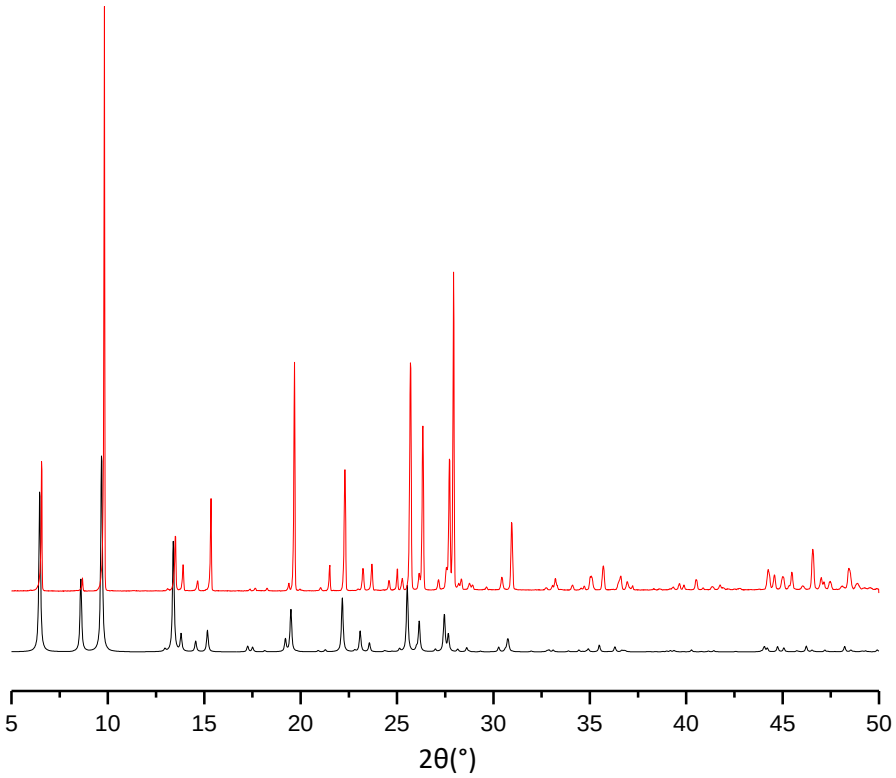

Figure 5.2: PXRD patterns of as-synthesised mordenite experimental (red) and simulated (black).

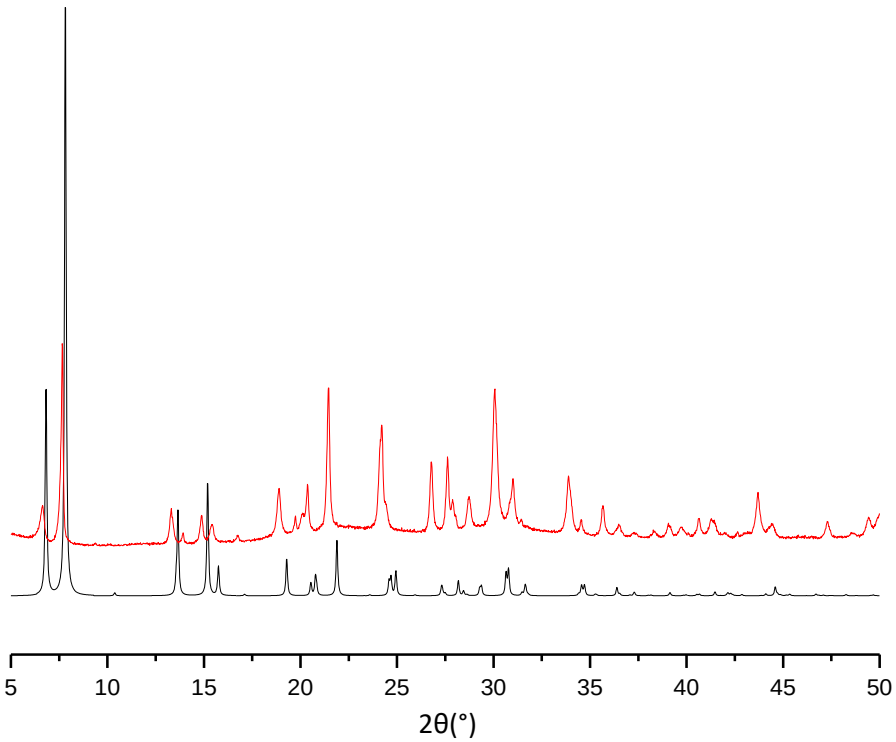

Figure 5.3: PXRD patterns of as-synthesised UZM-4 experimental (red) and simulated (black).

Looking at the UZM-4 results, the simulated peaks show a slight shift in comparison to the as-synthesised experimental peaks. As discussed later in this chapter, the UZM-4 sample has a high level of aluminium. The simulated comparison pattern is pure silica. The

inclusion of the larger aluminium atoms will increase the size of the unit cell and therefore the corresponding d-spacing. This increase in d-spacing will result in lower 2 theta values, hence the leftward shift of the experimental pattern. Aside from the slight shift, the peaks match relatively well, indicating a phase pure sample.

5.4.1.2. Scanning Electron Microscopy – Energy Dispersive X-Ray Spectroscopy

As with the acid site zeolites, once the phase purity had been determined by PXRD, a combination of SEM and EDX was used to study the morphology and size of the crystals and the Si/Al ratios of the zeolites. The SEM and EDX of the un-exchanged ZSM-5, SSZ-13 and powder ferrierite samples were shown in section 4.4.1.2.

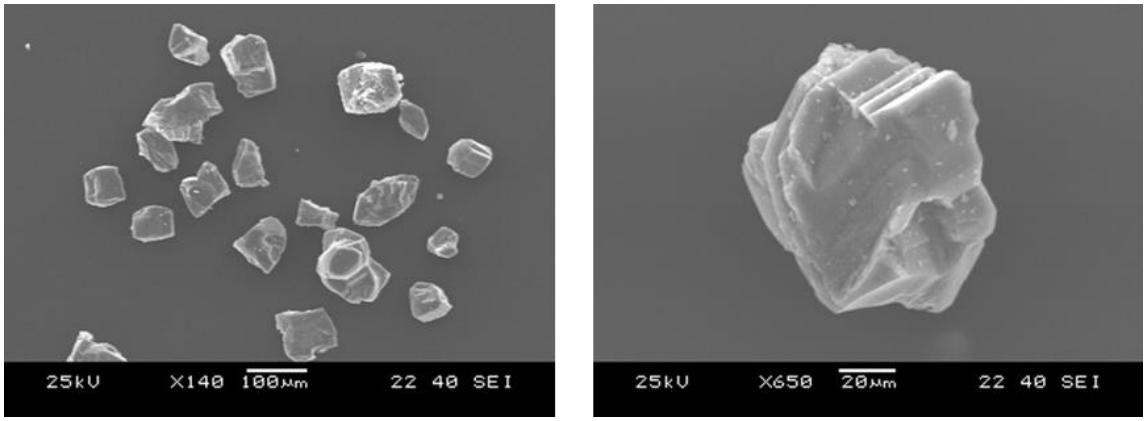

Figure 5.4: As-synthesised mordenite SEM images.

The SEM images of as-synthesised mordenite, figure 5.4, show relatively large, bulky, cubic-like crystals of size 50 – 100 µm. The homogeneity of the crystal shapes alludes towards a purely synthesised sample.

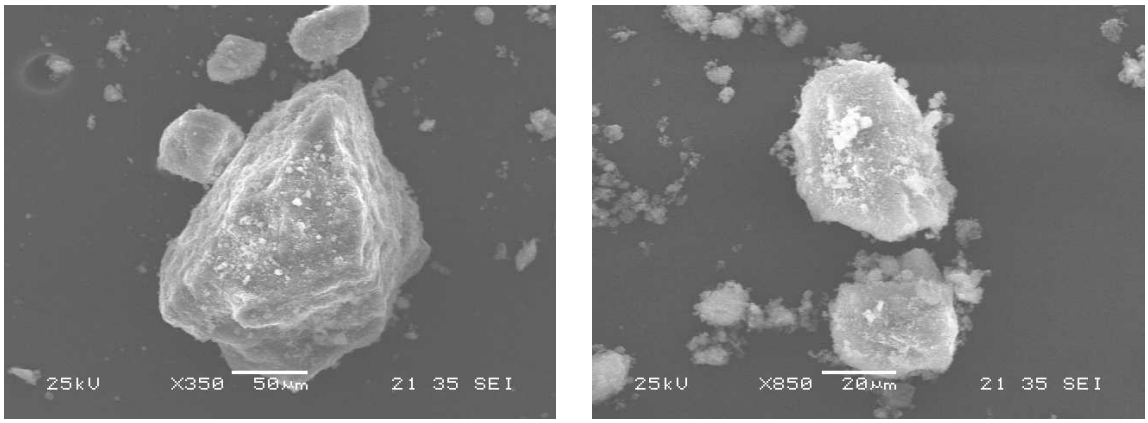

Figure 5.5: As-synthesised UZM-4 SEM images.

The SEM images of as-synthesised UZM-4, figure 5.5, show large crystals of around 30 – 100 µm with smaller crystals present. The crystals lack any obvious shape and are not homogenous in regard to size or morphology.

The EDX data for both of the newly-synthesised zeolites is shown in table 5.2. The data shows a Si/Al ratio of ~6 for mordenite, making it slightly higher in aluminium than the mordenite used for the acid site catalysis. The Si/Al ratio for UZM-4 is ~2, the highest level of aluminium out of all five zeolites.

Table 5.2: EDX data of the acid site zeolites.

Zeolite	% Silicon	% Aluminium	Si/Al Ratio
Mordenite	20.7 ± 2.4	3.6 ± 0.4	6
UZM-4	16.1 ± 2.7	7.8 ± 1.1	2

Once the samples had been ion-exchanged with copper, further EDX measurements were taken to determine the levels of copper in each sample. Table 5.3 shows the Cu/Al ratios of the five copper zeolites. All samples were exchanged until the Cu/Al ratio was around 0.4 – 0.5. Since the copper is inserted as Cu^{2+}, the highest possible Cu/Al ratio is 0.5, this is in relation to the 1- charge contribution from each aluminium atom.

Table 5.3: EDX data of the powder Cu-zeolites with the resulting Cu/Al ratio.

Zeolite	% Copper	% Aluminium	Cu/Al Ratio
Cu-SSZ-13	0.6 ± 0.2	1.4 ± 0.1	0.43
Cu-ZSM-5	0.5 ± 0.2	1.1 ± 0.3	0.47
Cu-UZM-4	4.0 ± 2.1	7.8 ± 1.1	0.51
Cu-MOR	1.9 ± 0.6	3.6 ± 0.7	0.52
Cu-FER	1.5 ± 0.6	3.1 ± 0.6	0.48

The SEM images of the single crystal ferrierite samples are shown in figure 5.6. The crystals show a decrease in size with an increase in synthesis gel aluminium content, from ~150 µm with a Si/Al ratio of 12.5 to ~ 30 µm with a Si/Al ratio of 5. All crystals are cubic, but with an observed increase in roundness as the aluminium content increases. The EDX data, table 5.4, shows the recorded Si/Al ratios of the single crystals.

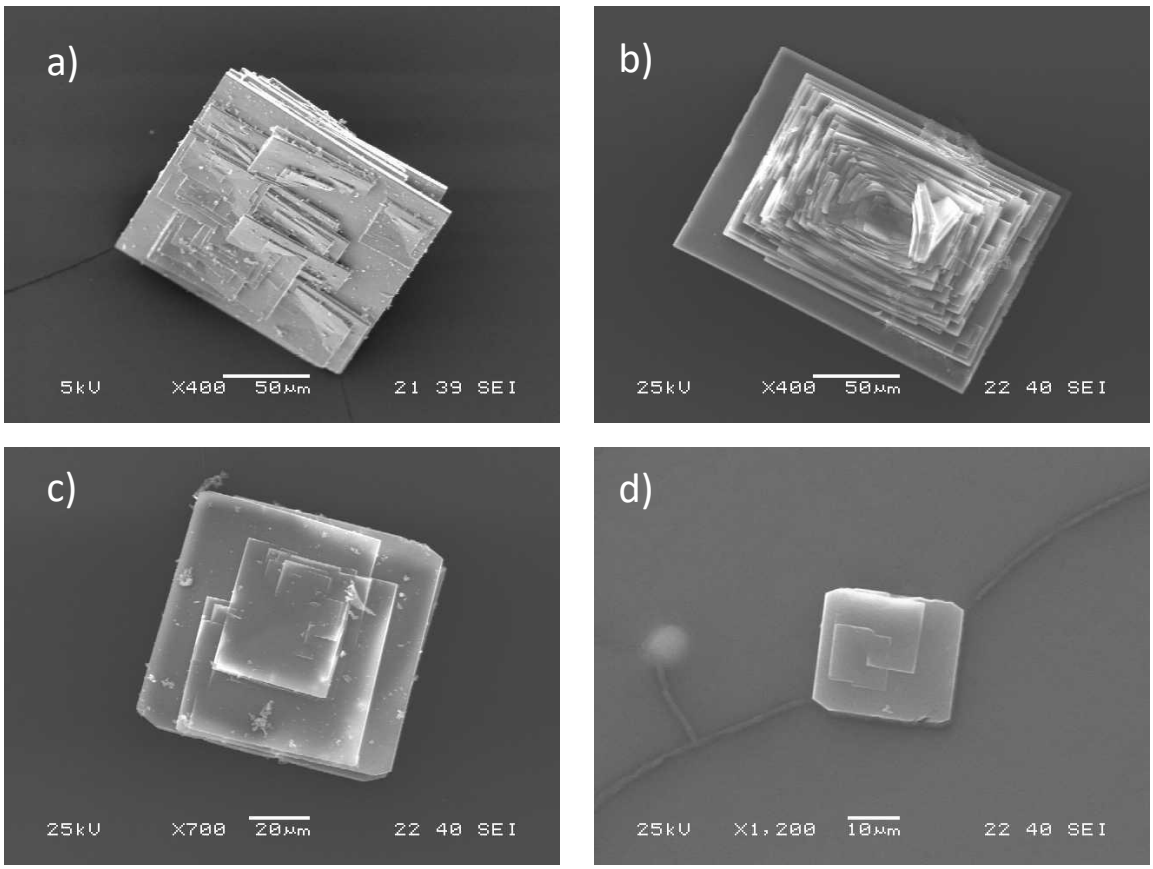

Figure 5.6: SEM images of ferrierite single crystals with varying synthesis gel Si/Al ratios; a) 12.5, b) 7.5, c) 6.25 and d) 5.

Table 5.4: EDX data of single crystal ferrierite with ranging Si/Al ratios.

Synthesis Gel Si/Al Ratio	% Silicon	% Aluminium	Crystal Si/Al Ratio
12.5	97.5 ± 0.2	2.6 ± 0.2	38
7.5	96.6 ± 0.3	3.5 ± 0.3	28
6.25	96.2 ± 0.3	3.83 ± 0.3	25
5	95.6 ± 0.6	4.5 ± 0.6	21

The crystal Si/Al ratios are significantly higher than the synthesis gel ratios, suggesting that aluminium incorporation into single crystal ferrierite is not favourable. The Al content does increase slightly as the synthesis gel Al composition increases. The reduced crystal size with the highest Al incorporation (Si/Al of 21) suggests that the synthesis may be reaching the limit, as further Al incorporation would make crystals that are too small for single crystal X-ray diffraction.

Two of the single crystal ferrierite samples were copper ion-exchanged, with the EDX results shown in table 5.5. Both copper exchanges result in slight over-exchange of the copper, but this may have been residual copper crystals in the sample from the concentrated copper solution used during the exchange process. Furthermore, the high levels of standard deviation suggest that the true Cu/Al ratio could be closer to 0.5. Once a sufficient level of copper had been incorporated into the zeolites, they were assessed by single crystal X-ray diffraction in an attempt to locate the copper positions.

Table 5.5: EDX data of the single crystal ferrierite Cu/Al ratios.

Single Crystal Si/Al	% Copper	% Aluminium	Cu/Al Ratio
38	2.1 ± 1.7	3.4 ± 1.7	0.62
21	3.4 ± 1.5	4.5 ± 0.6	0.75

5.4.2. Nitric Oxide Production

The NO production from sodium nitrite was studied three times on the NOA for all copper site zeolites. Release profiles, showing NO concentration throughout the run, and production profiles, which show the total NO produced, were obtained. Due to the quick NO production from some zeolites, a second nitrite injection was performed as part of the same run. The two peaks were separated to obtain the NO concentration and production from each substrate injection.

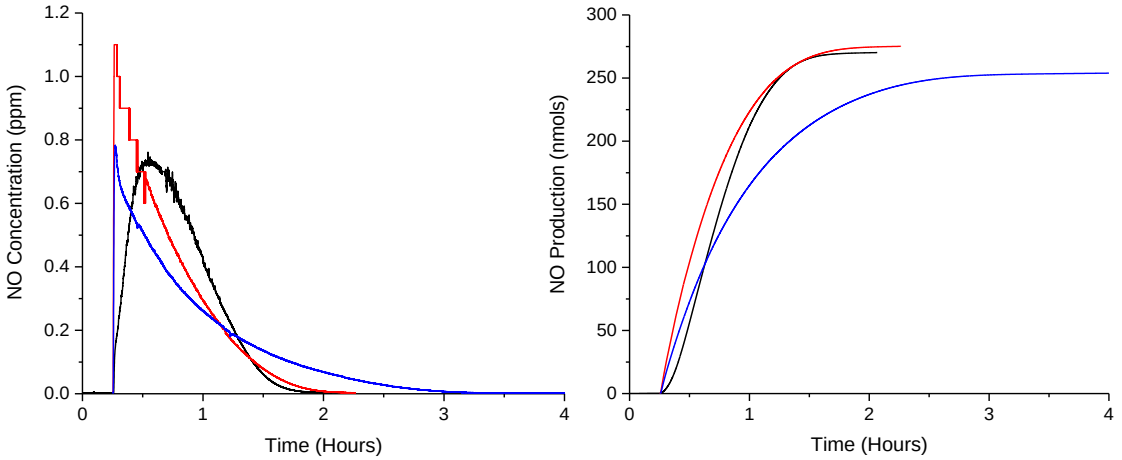

Figure 5.7: Cu-ZSM-5 release profiles (left) and NO production (right), where the red and blue runs are from initial substrate injections and the black run is from a second injection.

Cu-ZSM-5, figure 5.7, shows a range of NO release profiles with varying rates and NO production time. The run in black was a second substrate injection in a run, which may explain the different peak shape from the blue and red runs which were first substrate injections in a run. The NO production is rather consistent for all three, with an average of around 250 nmols. The length of time that NO production occurs varies slightly, with runs complete within 2 – 3 hours.

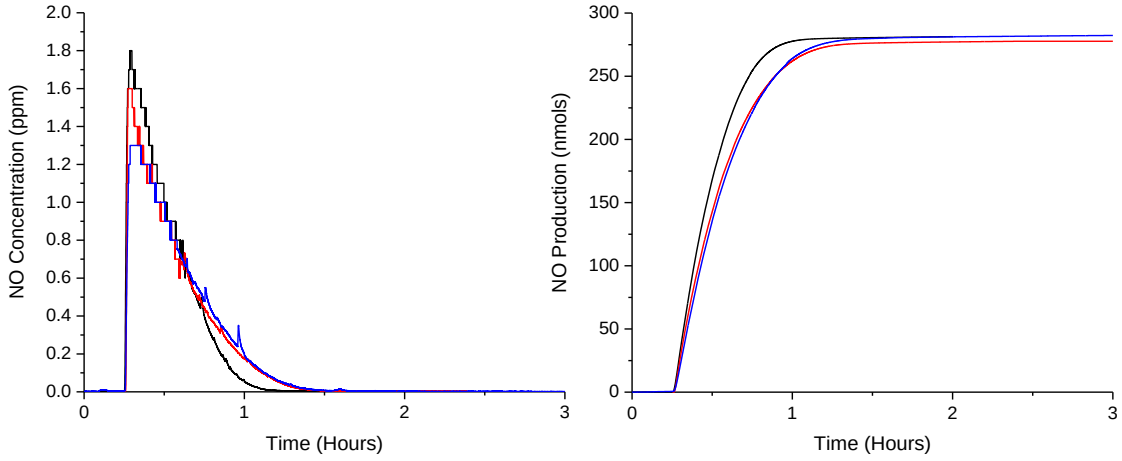

Figure 5.8: Cu-SSZ-13 triplicates release profile (left) and NO production (right).

Cu-SSZ-13, figure 5.8, shows three very similar release profiles and corresponding NO production. There is a quick production time of only 1 – 1.5 hours, with total NO production around 250 nmols, the same as Cu-ZSM-5.

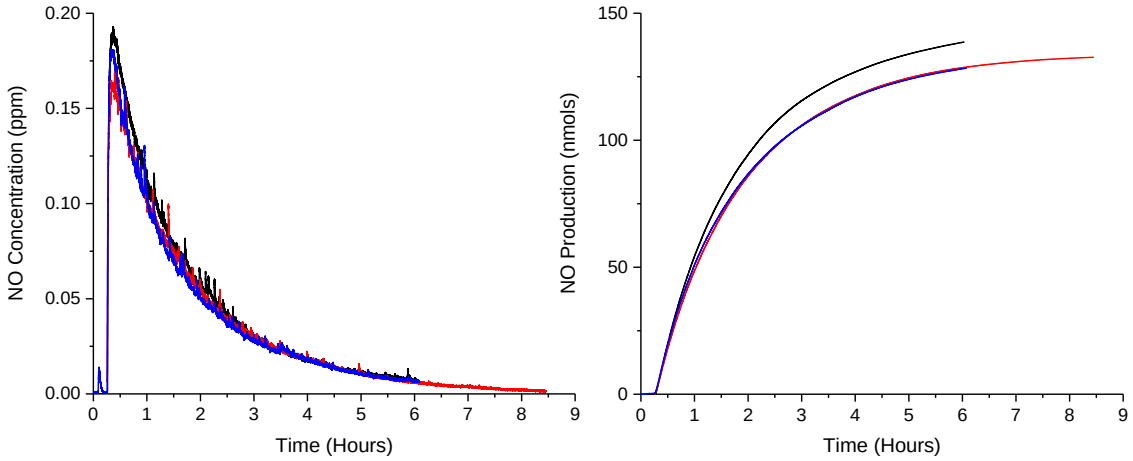

Figure 5.9: Cu-MOR triplicates release profile (left) and NO production (right).

Cu-MOR, figure 5.9, again shows very similar results between the three runs. The NO concentration is much less than the Cu-ZSM-5 and Cu-SSZ-13 results, with a peak concentration of 0.20 ppm obtained, the production however is significantly longer at 8 – 9 hours. The total NO production is around 130 nmols.

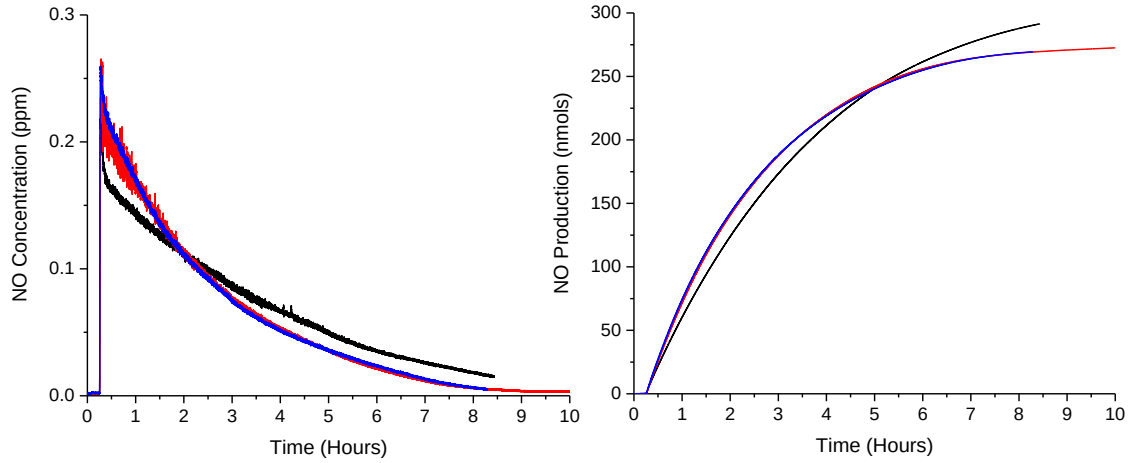

Figure 5.10: Cu-UZM-4 triplicates release profile (left) and NO production (right).

Cu-UZM-4, figure 5.10, shows slight variation in the three runs. The NO concentration peaks around 0.27 ppm with a long production time of up to 10 hours, the longest of any of the copper zeolites. The total NO production is around 250 nmols, the same as Cu-SSZ-13 and Cu-ZSM-5.

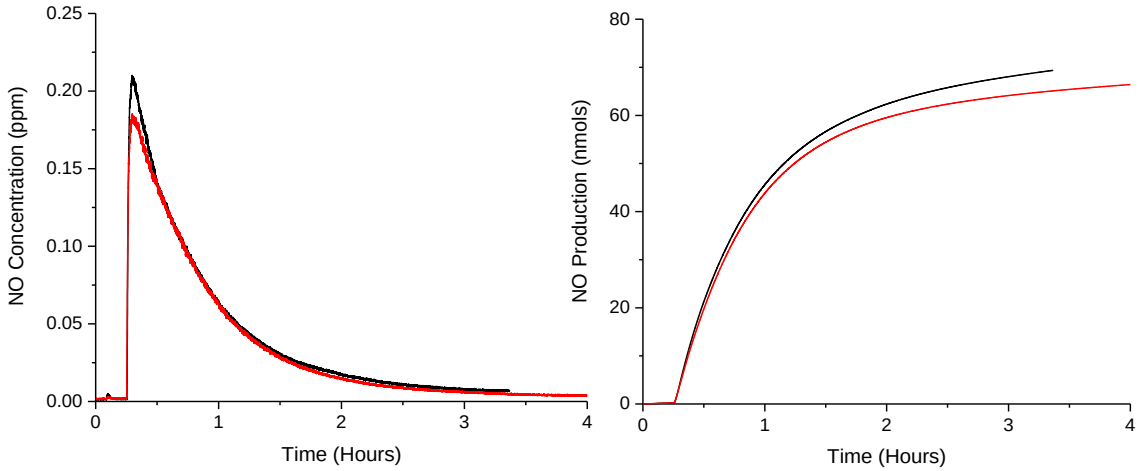

Figure 5.11: Cu-FER duplicate release profile (left) and NO production (right).

The Cu-FER data, figure 5.11, is only presented in duplicate due to numerous runs presenting abnormal release profile shapes, that are discussed later in section 5.4.2.1. Only two of the many runs completed produced "classic" release profiles as shown by the duplicates. This should still give a good indication of the potential of Cu-FER for NO production. The NO concentration is similar to that of Cu-MOR and Cu-UZM-4 but has a shorter production time of 3 – 4 hours. This results in a lowered total production of around 60 – 70 nmol, the lowest of all the copper zeolites.

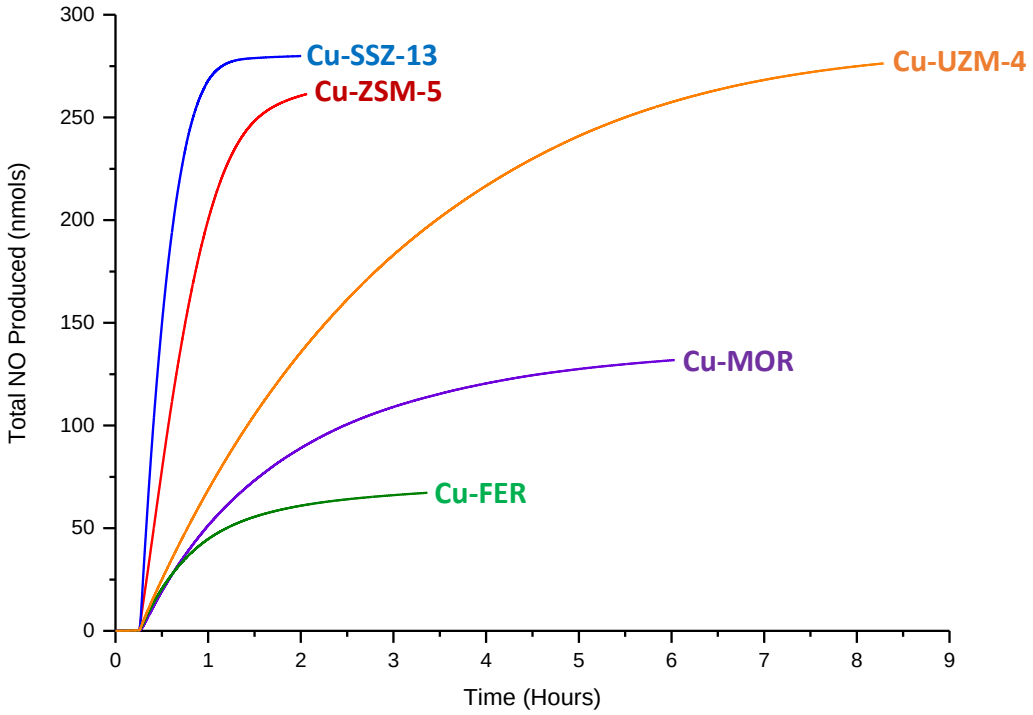

Figure 5.12: Comparison of NO production of all copper site zeolites. SSZ-13 (blue), ZSM-5 (red), UZM-4 (orange), mordenite (purple) and ferrierite (green).

Figure 5.12 displays the average NO production of all the copper site zeolites. The highest NO production was from Cu-SSZ-13, Cu-UZM-4 and Cu-ZSM-5 with 280, 276 and 261 nmols respectively. This was followed by Cu-MOR with 132 nmols and lastly, Cu-FER with 67 nmols. 100 % conversion of sodium nitrite to NO corresponds to 250 nmols, meaning that some of the zeolites produced over 100 % conversion. The reason for this may be due to human error when preparing a 0.05 M solution of sodium nitrite or when adding 5 µL of this by microsyringe.

The three zeolites with the highest NO production, SSZ-13, ZSM-5 and UZM-4, all have 3D channel systems, which may be a considerable factor for the catalytic activity. The two 2D zeolites, mordenite and ferrierite, show a significantly lower NO production, suggesting that the active sites may not be as accessible as those in the 3D channel system zeolites. A trend is also apparent regarding the zeolite pore size. The two large pore zeolites, mordenite and UZM-4, have a longer NO production time than the other zeolites. The large pores may allow the substrate to pass over the active site without interacting with it, whereas the smaller pored zeolites will direct the substrate to the active site. This is highlighted by Cu-SSZ-13 which has the smallest pores of all the zeolites but the quickest NO production, with the production plateauing after 1 – 1.5 hours. Cu-ZSM-5 and Cu-FER have the next largest pore sizes and further confirm this trend with increasing NO production time.

One issue which arose late into the project was the identification of NO being produced from the reaction between sodium nitrite and cysteine hydrochloride alone, as shown in figure 5.13. The reason for cysteine hydrochloride being used in the first place, was due to its much higher solubility than D/L-cysteine. Unfortunately, the acidity of the cysteine was not considered until completion of the NO studies. There is now a slight difficulty in deciphering whether NO production is resultant from the copper sites or if there has been a contribution from the acidity of the hydrochloride.

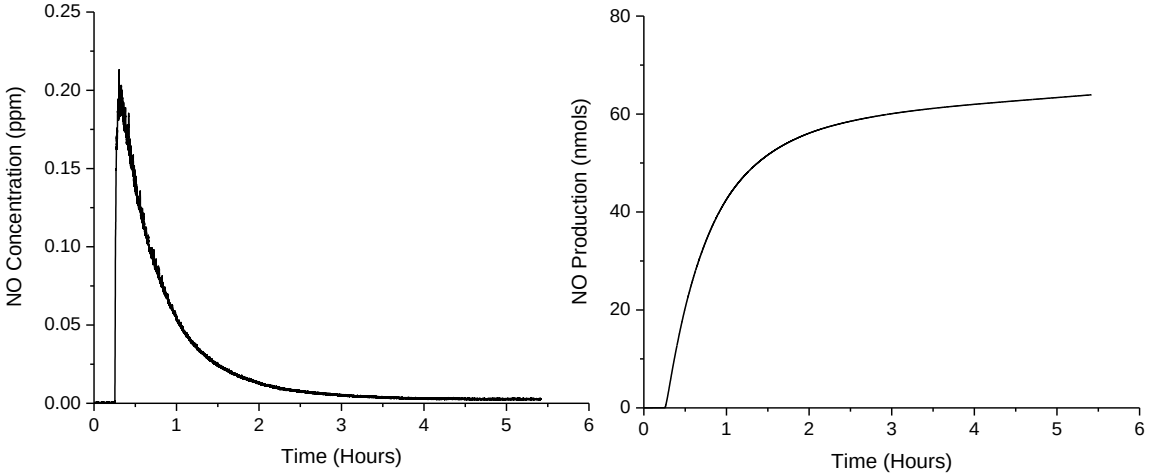

Figure 5.13: NO release profile (left) and total production (right) from the reaction between sodium nitrite and cysteine hydrochloride.

According to figure 5.13, the maximum NO production from cysteine hydrochloride with 5 µL of sodium nitrite would be 64 nmol after the NO concentration returned to the background levels, therefore it is possible to back calculate the minimum NO production from the copper sites, table 5.6. Although it is not an ideal method, the calculation provides a good indication of the minimum contribution from the copper sites.

Table 5.6: NO production considering the 64 nmol contribution from the reaction between sodium nitrite and cysteine hydrochloride.

Zeolite	Total NO Production (nmols)	NO Production Subtracting Contribution from Acidity (nmols)	% Conversion
Cu-ZSM-5	261	197	79
Cu-SSZ-13	280	216	86
Cu-MOR	132	68	27
Cu-UZM-4	276	212	85
Cu-FER	67	3	1

The results show that ZSM-5, UZM-4 and SSZ-13 still have a good level of conversion with around 80+ % of nitrite converted to NO. The MOR conversion was relatively poor with only 27 % of nitrite converted. The most interesting result is from Cu-FER, where the

results suggest that the total activity may have come from the cysteine acidity. However, as discussed in the next section, ferrierite may have a greater activity than was initially indicated.

5.4.3. Ferrierite Anomalies

As mentioned previously, Cu-FER produced unpredicted release profiles that showed drastic changes in NO concentration throughout the run. An example of these runs is shown in figure 5.14 where a much greater concentration of NO was produced upon a second nitrite injection.

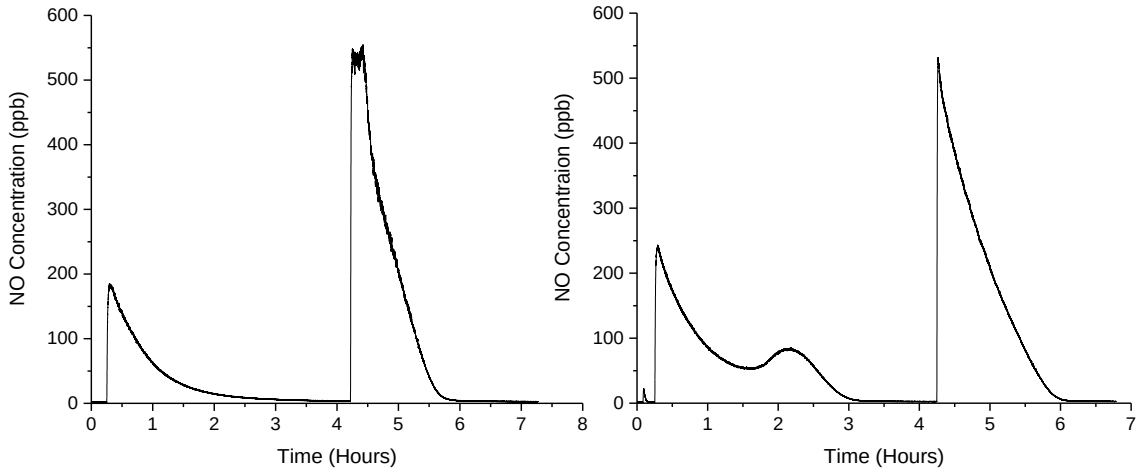

Figure 5.14: The unexpected shapes of the Cu-FER nitric oxide release profiles.

Different ferrierite batches were tested and they all showed the same result, ruling out a batch anomaly. After the initial studies presented unusual results, a more extensive run with multiple substrate injections was performed to try to further understand the results.

The result of four sodium nitrite injections is shown in figure 5.15. The first peak, around 15 minutes, corresponds to 85 nmols and has a standard looking release profile. The second peak, around 2 hours 15 minutes, shows a higher initial concentration that begins to decrease but then spikes for a second time around 45 minutes later. The total NO production from this peak is 201 nmols, over double the production from the initial peak. The third and fourth peaks, at 4 hours 25 minutes and 6 hours 25 minutes, both show release profiles that are similar to the first peak but at a much higher concentration. The total production from the third and fourth peaks is 220 and 223 nmols respectively.

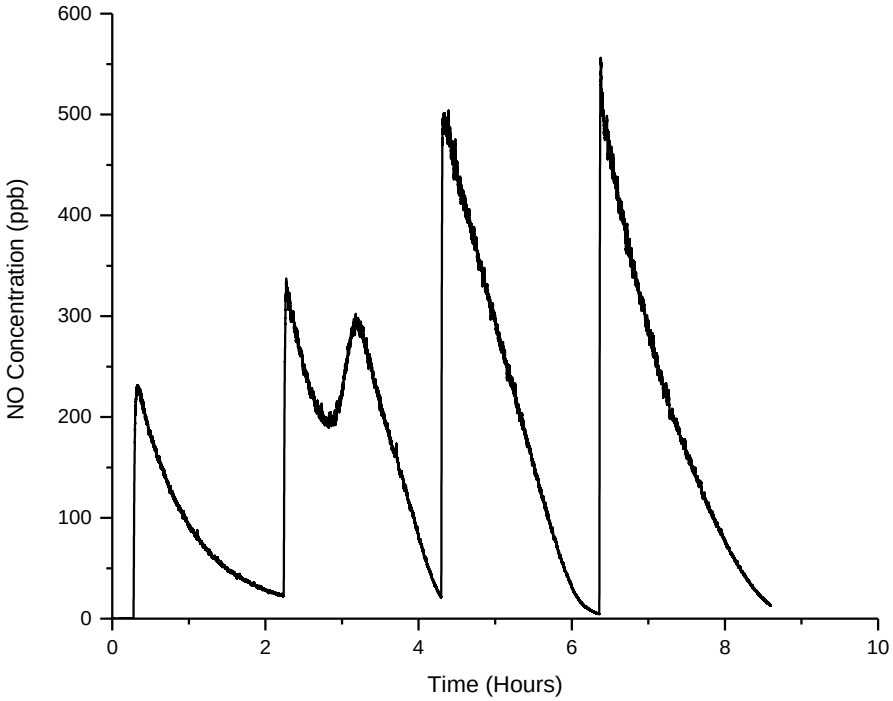

Figure 5.15: Release profile of Cu-FER with four sodium nitrite injections to study the changing NO concentrations.

The results suggest that there may be a change occurring that enhances the catalytic activity of the Cu-FER. The changing profile shape during the second peak and the subsequent sustained increase in NO production for the third and fourth peaks suggests that there may be a change in zeolite structure or a change in copper location.

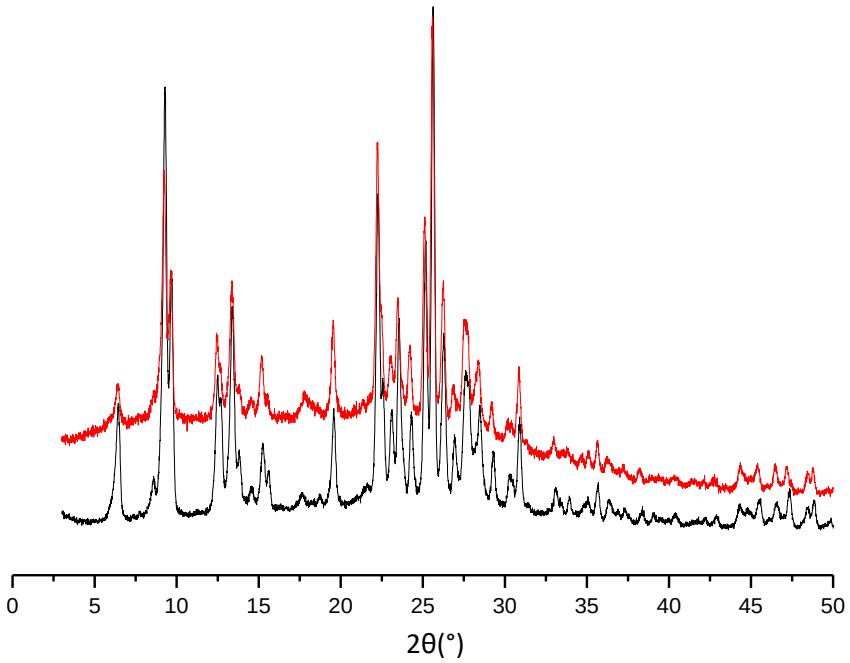

Figure 5.16: PXRD comparison of pre-catalysis (black) and post-catalysis (red) Cu-FER.

The initial property considered was a change in zeolite structure. Samples of Cu-FER, both before and after catalysis, were taken to Diamond Light Source for powder X-ray diffraction. The resulting patterns, figure 5.16, showed no significant change in ferrierite structure, indicating that a change in structure had not affected the catalytic activity.

The second property considered was a change in copper location. This is much harder to examine due to the potential disorder of the copper within the pores, as well as the relatively low levels of copper across the structure as a whole. After limited success of Rietveld refinement of the synchrotron data, single crystal diffraction was considered. The aim of the study was to be able to locate the copper by X-ray diffraction, perform the catalysis, and then locate the copper positions again and observe if there was any movement. Single crystal aluminosilicate ferrierite was synthesised with varying Si/Al ratios, as discussed in section 5.3.1.

Unfortunately, out of the two copper ferrierite crystals studied, with Si/Al ratios of 38 and 21, neither showed a definite presence of copper within the pores. This suggests that the copper was not ordered enough to provide electron density that could be assigned as a copper ion. The structure produced from the Si/Al ratio of 21 diffraction pattern is shown in figure 5.17 and confirms the ferrierite framework. Due to such small differences between the electron count of aluminium and silicon, the T-atoms could not be distinguished as one or the other, hence the lack of different T-atoms in the generated structure.

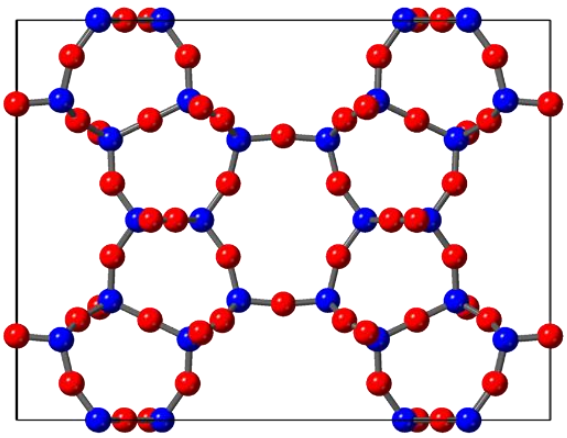

Figure 5.17: The resulting crystal structure of Cu-FER (Si/Al = 21) from single crystal X-ray diffraction, where blue is silicon/aluminium, red is oxygen and the grey box represents the unit cell.

Due to unsuccessful attempts at locating the copper ions by single crystal diffraction, the next method considered to identify any change in copper location, was solid-state NMR. A large-scale catalysis run was completed to prepare material for NMR studies. The results are shown in figure 5.18 where sodium nitrite was injected at 15 minutes and at 10 hours 15 minutes. The first injection showed an increase of NO concentration to 1 ppm which began to increase again after 3 hours, reaching up to 3.5 ppm. The second injection produced a much higher concentration of NO, reaching 6 ppm.

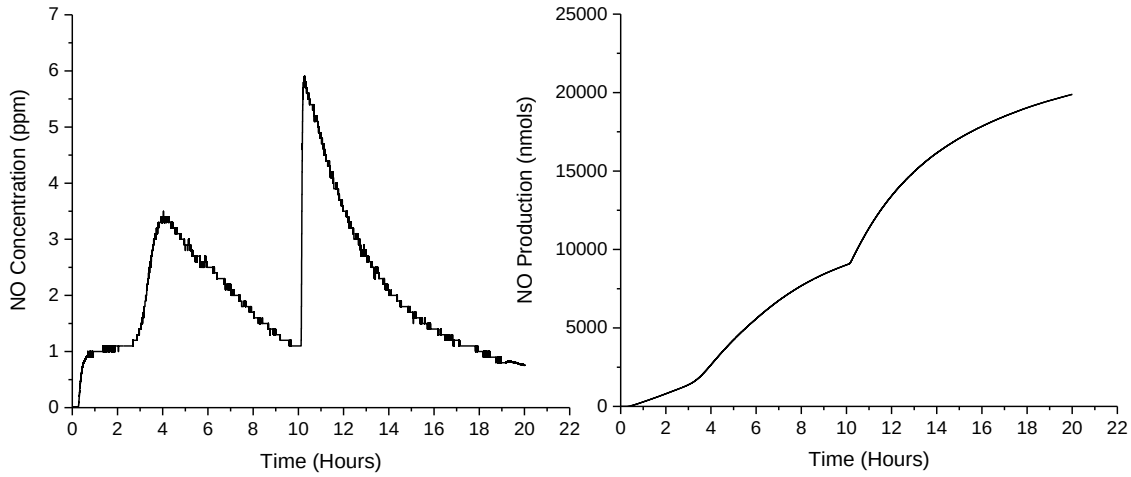

Figure 5.18: Large scale Cu-FER catalysis for solid state NMR.

The ferrierite was collected by filtration after the catalysis. A batch of pre and post-catalysis Cu-FER samples were studied by solid-state NMR by Dr Daniel Dawson. ^{27}Al and ^{29}Si variable-temperature MAS NMR spectra were recorded to observe any change in the sample before and after catalysis.

The ^{27}Al NMR spectra, figure 5.19, shows little change of the structure with varying temperature. The two samples show no major differences, apart from the presence of a slight peak around 0 ppm with the post-catalysis sample. This peak is most likely from six-coordinate aluminium, potentially suggesting that the catalytic process has caused minor dealumination, resulting in extra-framework aluminium.[8]

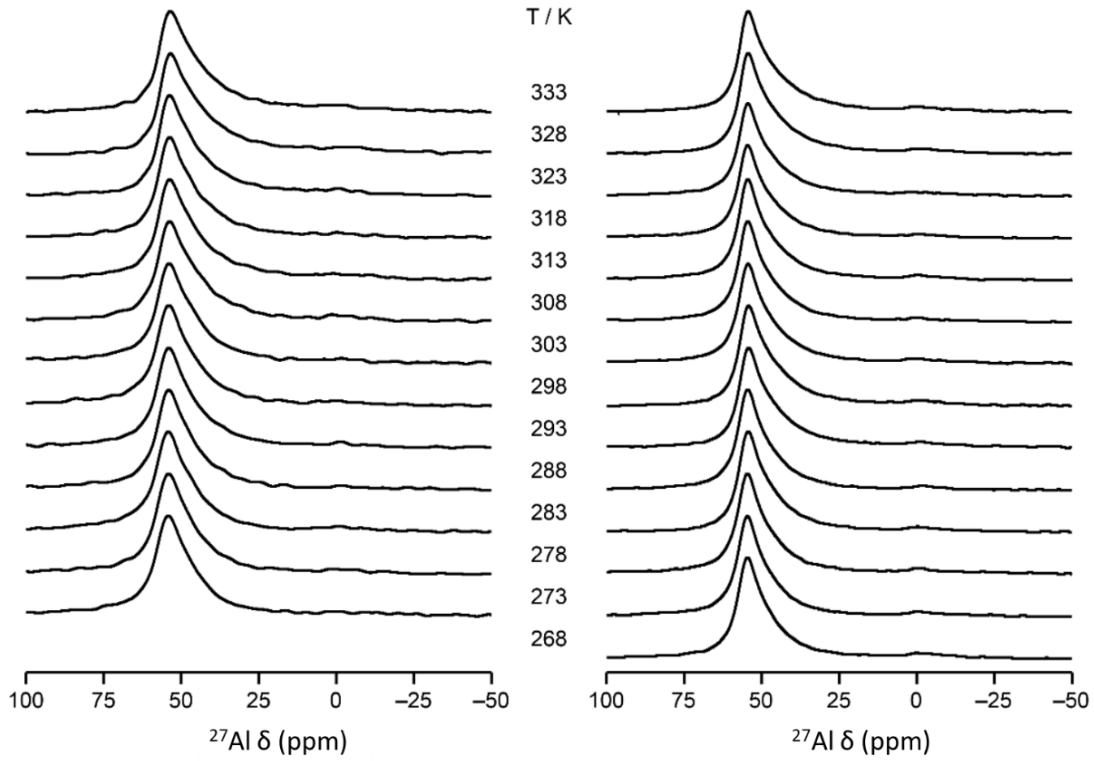

Figure 5.19: Variable-temperature ^{27}Al (14.1 T, 37.5 kHz MAS) NMR spectra of Cu-FER before (left) and after (right) catalysis.

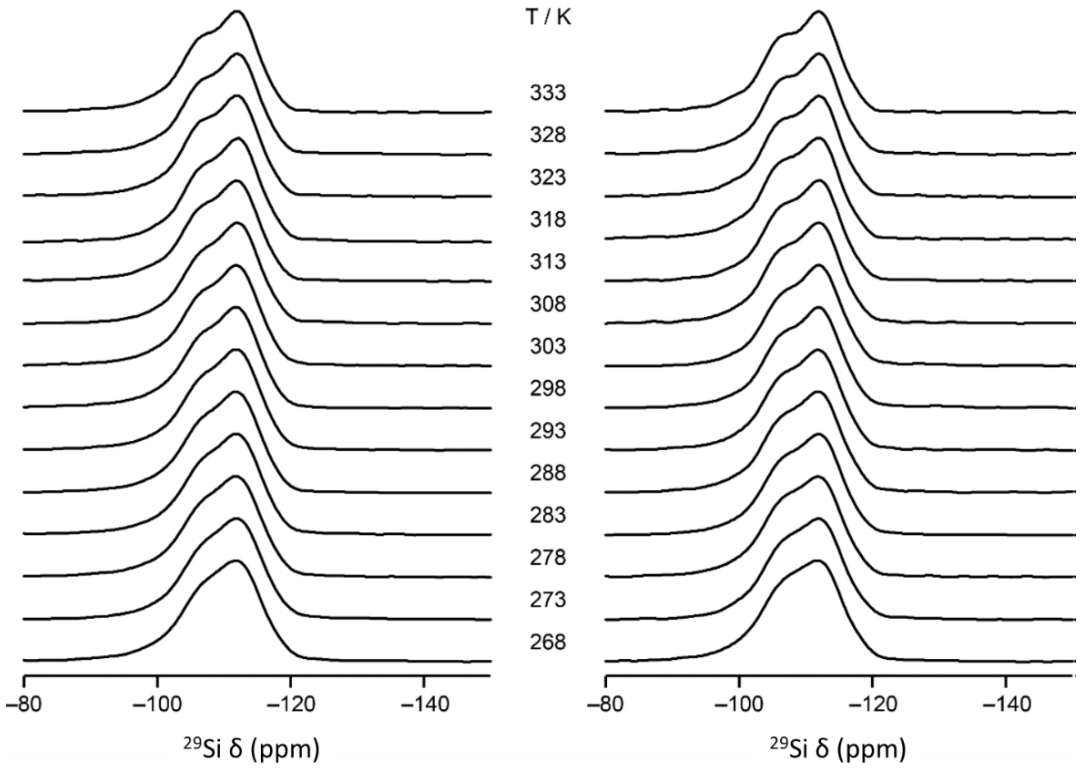

Figure 5.20: Variable-temperature ^{29}Si (14.1 T, 37.5 kHz MAS) NMR spectra of Cu-FER before (left) and after (right) catalysis.

The ^{29}Si NMR spectra, figure 5.20, shows peaks around 106 and 112 ppm in both samples. These most likely correspond to $Si(OSi)_3(OAl)_1$ and $Si(OSi)_4$, respectively.[9] As with the ^{27}Al spectra, there is no significant change in the structure with varied temperature.

A breakdown of the peak positions and widths can be seen in figure 5.21 (a) and (b), corresponding to pre and post-catalysis. The main difference between the two samples, is the narrowing of the 106 ppm peak post-catalysis. The fact that the pre-catalysis peak around 106 ppm, corresponding to $Si(OSi)_3(OAl)_1$, has a greater width than the 112 ppm peak could be explained by the localisation of Cu^{2+} close to the aluminium. Any small differences from the locations of copper atoms would result in broader peaks. While the line width of the peak around 112 ppm stays the same both before and after catalysis, the 106 ppm peak decreases in width post-catalysis. This could indicate either a small loss in Cu^{2+} or a more uniform distribution of the Cu^{2+} throughout the sample.

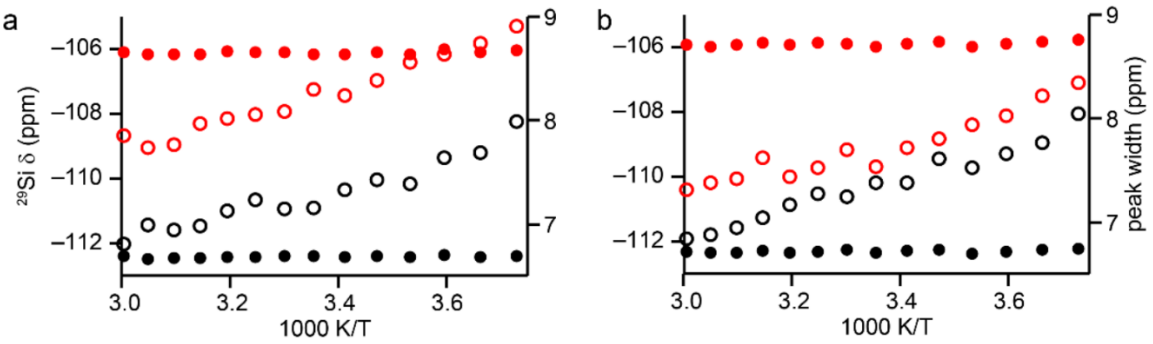

Figure 5.21: Plots of the ^{29}Si peak positions (left axis, filled points) and peak width (right axis, open points) as a function of temperature, where red and black correspond to the two peaks, (a) is the pre-catalysis sample and (b) is the post-catalysis sample.

The change in catalytic activity could be related to this alteration of Cu^{2+} distribution. Even though it is difficult to know the specifics of the copper location at this stage, it looks likely that there are some small changes when comparing the Cu-FER pre and post-catalysis. While the NMR results are not conclusive enough on their own, additional techniques could be used to further probe this theory of copper movement. The possibility of *in situ* solid-state NMR may be an option, something that has been completed with zeolites previously.[10]

Despite the reasons behind the altered NO production remaining slightly uncertain, it does indicate a greater potential for Cu-FER as a NO-producing catalyst than initially thought. Returning to the catalytic tests, the greater NO production from Cu-FER observed from latter nitrite injections, around 200 nmols, can be plotted against the averages of the other zeolites. As seen in figure 5.22, this places the NO production from Cu-FER above Cu-MOR and below Cu-ZSM-5, Cu-UZM-4 and Cu-SSZ-13.

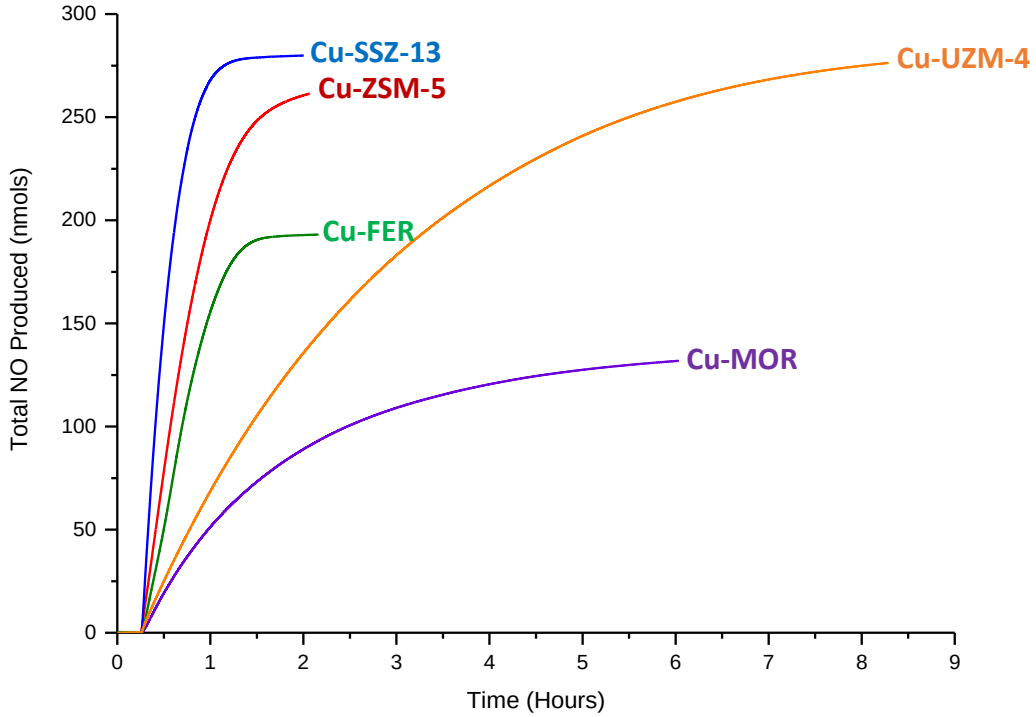

Figure 5.22: Comparison of NO production of all copper site zeolites considering the larger Cu-FER production. SSZ-13 (blue), ZSM-5 (red), UZM-4 (orange), mordenite (purple) and ferrierite (green).

The fact that Cu-FER may have a higher NO production than Cu-MOR could be due to the channel systems. While MOR is classed as a 2D zeolite by the IZA, it is closer to a 1D system due to the lower volume of diffusion along the b axis. As discussed previously, this suggests that active site accessibility could be related to channel systems which may be the factor influencing the total NO production.

5.4.4. Copper Site Recyclability

The recyclability of the copper site zeolites was assessed by multiple nitrite injections. The results of three nitrite injections with Cu-SSZ-13 can be seen in figure 5.23.

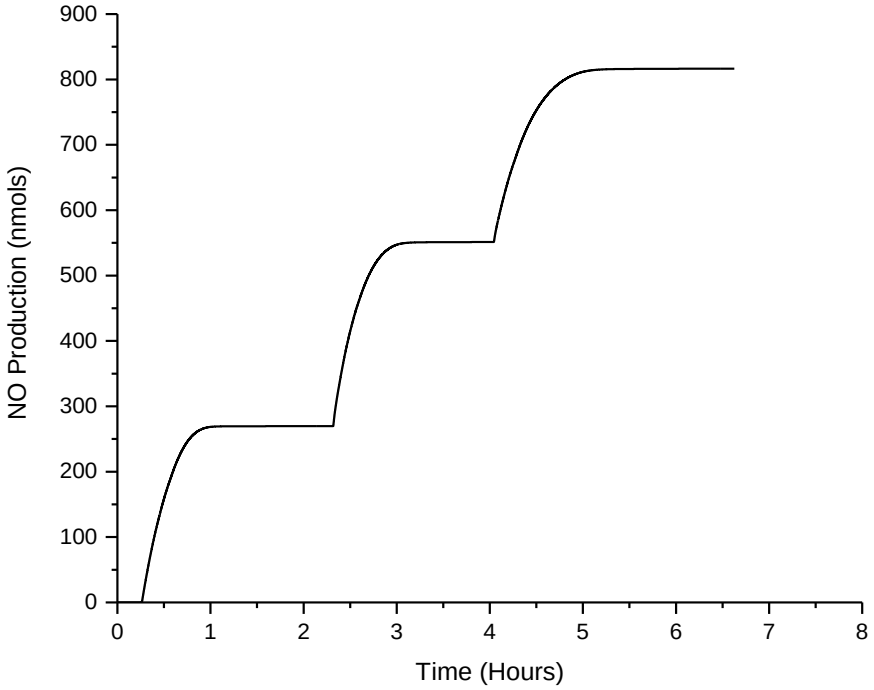

Figure 5.23: The NO production of Cu-SSZ-13 with three nitrite injections. The injections were performed around 15 minutes, 2 hours 15 minutes and 4 hours 15 minutes.

The results show sustained activity of the copper site zeolites, with all injections producing between 265 and 282 nmols of NO. This suggests that the copper sites are successfully being regenerated through the use of cysteine as a sacrificial reductant. This indicates that the copper zeolites would be suitable for long-term NO production applications.

5.4.5. Rates of Reaction

As with the acid sites, section 4.4.3, the rates of reaction for the zeolites can be determined. Again, both the Avrami and the Sharp-Hancock equations were applied to the data from figure 5.22 normalised between 0 and 1, known as α. The Avrami plots and the derived n and k values are shown in figure 5.24 and table 5.7 respectively.

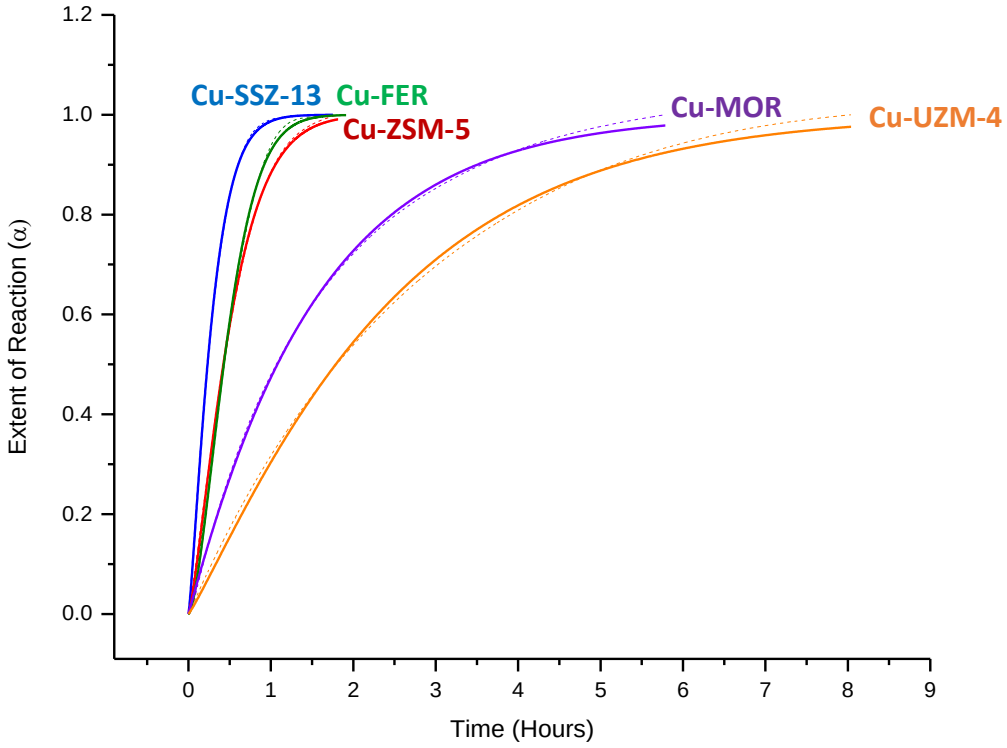

Figure 5.24: The Avrami fit (dashed line) of the normalised NO production (solid line) from the copper site zeolites. SSZ-13 (blue), ZSM-5 (red), mordenite (purple), ferrierite (green) and UZM-4 (orange).

Table 5.7: The k and n values derived from the Avrami plot in Figure 5.23.

Zeolite	Cu-ZSM-5	Cu-SSZ-13	Cu-FER	Cu-MOR	Cu-UZM-4
n	1.32	1.25	1.58	1.02	1.12
k (h^{-1})	1.70	3.22	1.84	0.65	0.40

Compared to the acid sites, the Avrami fit matches much better for the copper sites, as shown by the similarity between the dashed and solid lines. The n values obtained are all above 1. As discussed with the acid sites, this indicates a first order reaction.[11] The rate increases in the order of UZM-4, MOR, ZSM-5, FER and SSZ-13, which follows the length of time for the total NO production.

The Sharp-Hancock plot is shown in figure 5.25. The plot of $\ln(t-t_0)$ against $\ln(-\ln(1-\alpha))$, with an extent of reaction between 5 and 90 %, generated straight lines that allowed the linear equation to be determined. The k and n values could then be calculated by substituting this equation into the Sharp-Hancock equation, table 5.8.

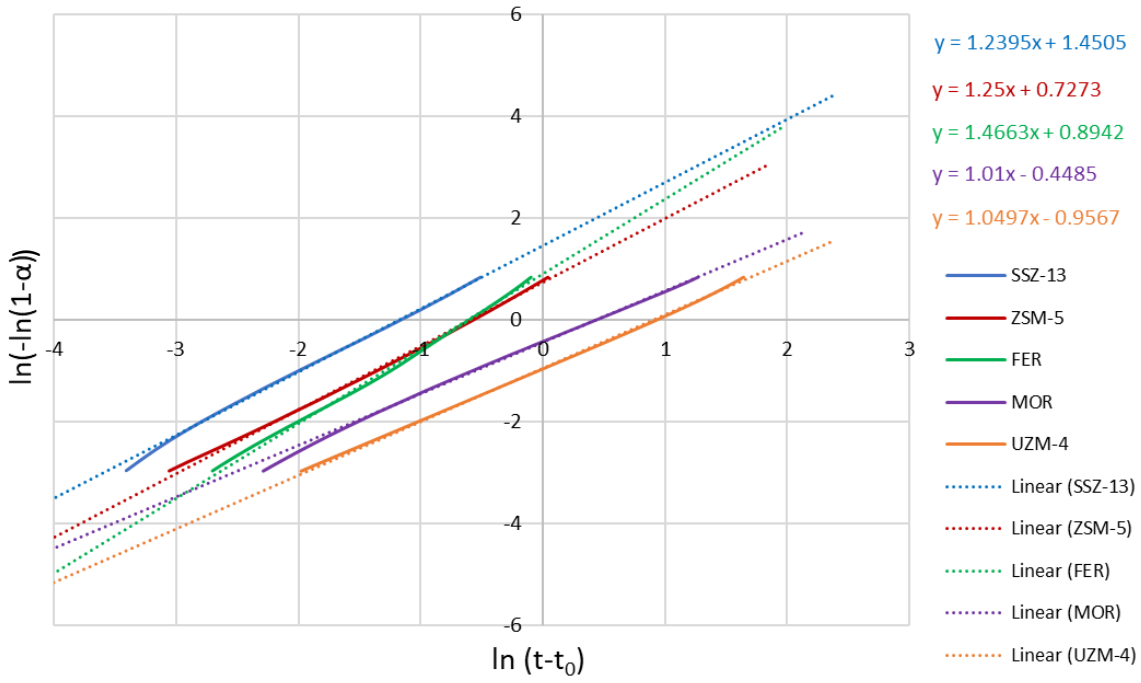

Figure 5.25: The Sharp-Hancock fit (dashed line) of the normalised NO production (solid line) from the copper site zeolites. SSZ-13 (blue), ZSM-5 (red), mordenite (purple), ferrierite (green) and UZM-4 (orange). The plotted values correspond to extent of reactions (α) between 5 and 90 %.[12] The equation of the linear trend is shown in the top right in the form of y = mx + c.

Table 5.8: The k and n values derived from the Sharp-Hancock plot in Figure 5.24.

Zeolite	Cu-ZSM-5	Cu-SSZ-13	Cu-FER	Cu-MOR	Cu-UZM-4
n	1.24	1.25	1.47	1.01	1.05
k (h^{-1})	1.79	3.22	1.84	0.64	0.40

The k and n values obtained from the two plots are very similar, indicating reasonable values. This confirms that the NO production proceeds through a first order reaction.

The improved fit of the copper sites compared to the acid sites could suggest a difference of mechanism between the two active sites. The fact that the copper active sites are regenerated could indicate a similar mechanism for NO production throughout. The consumption of the acid sites however, may alter the mechanism as the reaction proceeds. This could explain the difference in the fit of the plots.

5.4.6. Zeolite Toxicology

Data from toxicology studies identifies any decrease in HEK 293 cell viability in comparison to normalised cell growth. A drop below 80 % of cell viability was deemed a negative impact on cell growth and therefore cytotoxic.

Considering the results, an initial area of interest concerns the increase in cell viability (over 100 %) with some of the lower concentrations of zeolites (SSZ-13, MOR and FER). A viability greater than 100 % is most likely due to the zeolites contributing in some way to the activity of the cells, for example a component in the zeolites that the cells are using to produce amino acids. Previous studies of copper nitrate with HeLa cells, Appendix figure A4, does not suggest that the presence of copper can aid cell growth, therefore ruling out the copper presence. Further studies would be required however to determine the exact cause. As the zeolite concentrations increase there is a negative effect that exceeds the positive influence on the cell growth, hence the drop in cell viability.

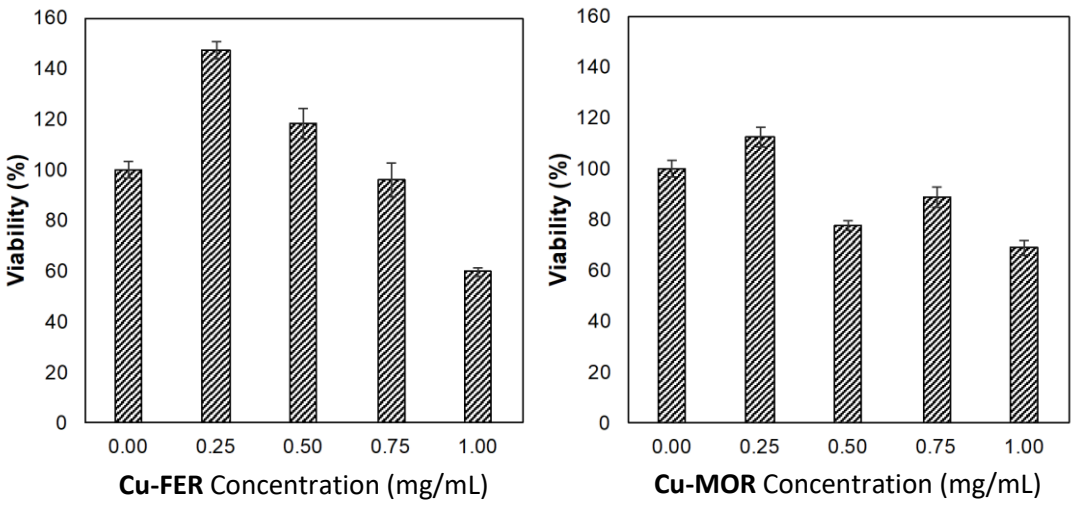

Figure 5.26: Cell viability of ranging zeolite concentrations for Cu-FER (left) and Cu-MOR (right).

Starting from 0.25 mg/mL, Cu-FER shows a gradual decrease in cell viability with each increase in zeolite concentration, figure 5.26 (left). The cell viability stays above 95 % for all concentrations except 1 mg/mL, which drops to 60 %. This shows that Cu-FER is biocompatible at most concentrations. Cu-MOR, figure 5.26 (right) has a relatively good level of biocompatibility with none of the concentrations dropping much below 80 % cell viability. Interestingly, an increase in zeolite concentration does not relate directly to viability, with 0.50, 0.75 and 1 mg/mL all sitting within a 10 % viability window.

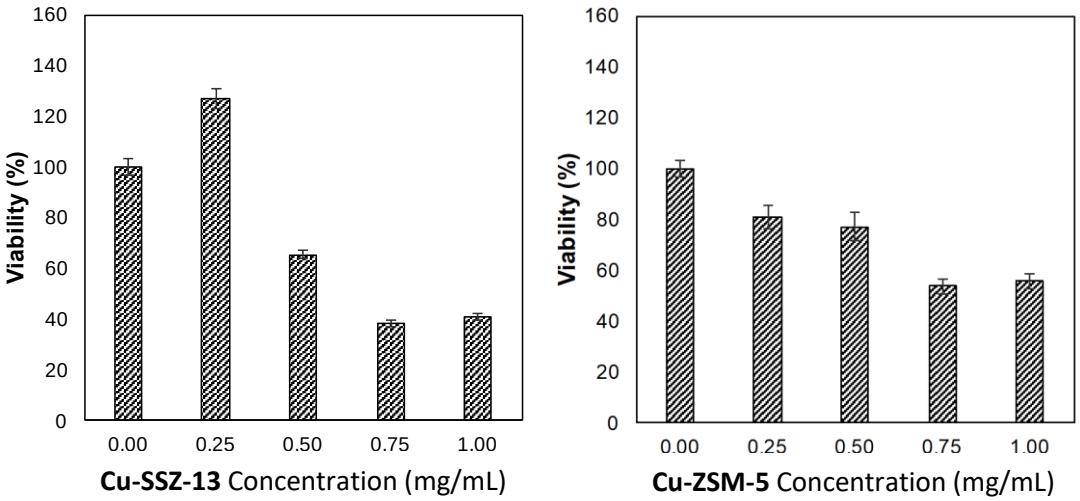

Figure 5.27: Cell viability of ranging zeolite concentrations for Cu-SSZ-13 (left) and Cu-ZSM-5 (right).

Cu-SSZ-13, figure 5.27 (left), has a decrease in viability from 0.25 to 0.75 mg/mL, where the viability then plateaus around 40 % for 0.75 and 1 mg/mL. The increasing drop in cell viability, indicates that Cu-SSZ-13 is not biocompatible at higher concentrations. Cu-ZSM-5, figure 5.27 (right), has a more gradual decrease in cell viability which again plateaus around 0.75 mg/mL at 50/60 %. 0.25 and 0.50 mg/mL both have a cell viability around 80 %, implying biocompatibility at these lower zeolite concentrations. The results suggest that both Cu-SSZ-13 and Cu-ZSM-5 would only be suitable for biomedical applications at lower zeolite concentrations, as higher concentrations would cause risk of cell damage.

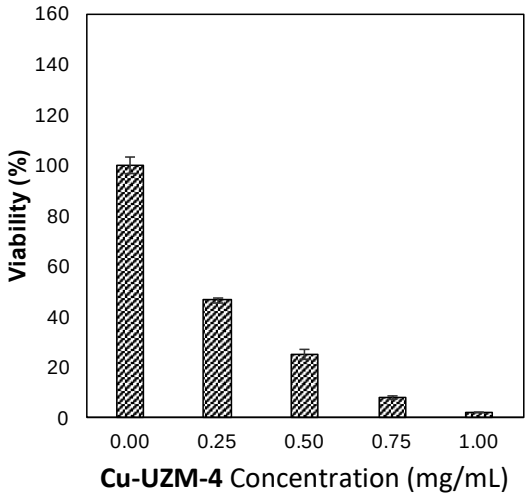

Figure 5.28: Cell viability of ranging zeolite concentrations for Cu-UZM-4.

The decrease in cell viability for Cu-UZM-4, figure 5.28, is more extreme than any of the other zeolites. The initial increase from 0 to 0.25 mg/mL shows a 50 % drop in cell viability. There is then a 10 – 20 % drop in viability with each increase in concentration, resulting in a cell viability close to 0 % for 1 mg/mL, signifying death of the majority of the cells.

The significantly higher toxicity of Cu-UZM-4 could possibly be due to the higher copper levels of the zeolite, that is directly related to the higher levels of aluminium. The toxic affect may be a result of the copper leaching from the pores and interacting with the HEK 293 cells. Leaching studies of the toxicology samples were performed to examine any trend between copper leaching and toxic effects.

5.4.7. Copper Leaching

The copper leaching was performed using three of the same concentrations as the toxicology data, with 0.25, 0.5 and 1 mg/mL performed in 10 mL of Milli-Q water requiring zeolite masses of 2.5, 5 and 10 mg. The leaching data is presented in two forms. First, as the concentration of copper detected by ICP-AES, quoted as ppm measurements. Secondly, the determined copper concentrations have been further calculated as the % of total copper from each zeolite, meaning that no leaching would equal 0 % and full copper leaching would equal 100 %. The total copper in each zeolite was determined from the aluminium content calculated from EDX and was related to the mass of zeolite; 2.5, 5 or 10 mg. The calculated maximum possible copper concentration for each zeolite and mass is shown in table 5.9.

Table 5.9: Maximum possible concentration of copper for each zeolite and mass if all copper was leached into solution.

	Mass (mg)		
Zeolite	**2.5**	**5**	**10**
Cu-FER	23 ppm	47 ppm	93 ppm
Cu-MOR	17 ppm	34 ppm	68 ppm
Cu-SSZ-13	6 ppm	12 ppm	23 ppm
Cu-ZSM-5	6 ppm	13 ppm	25 ppm
Cu-UZM-4	53 ppm	105 ppm	210 ppm

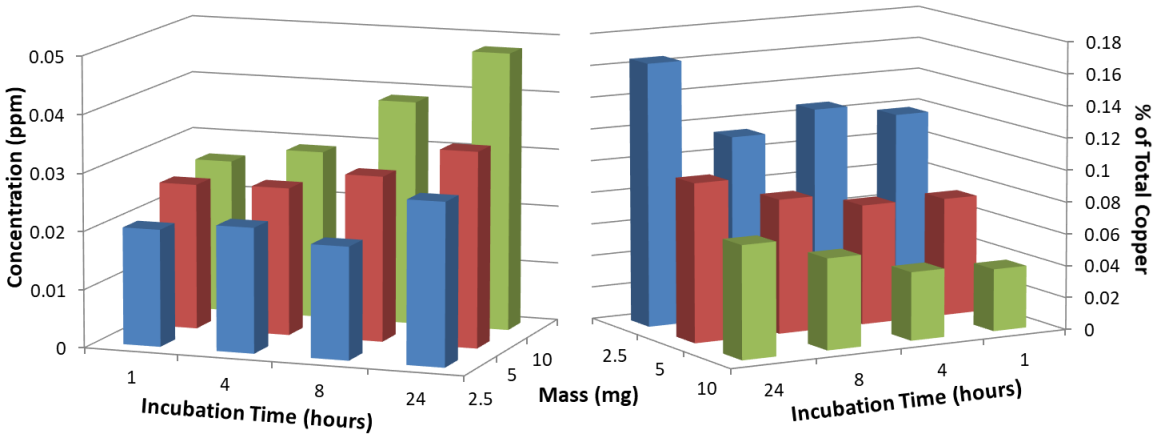

Figure 5.29: Copper leaching results of Cu-MOR showing the copper concentrations determined by ICP-AES (left) and the % of total copper leached from the zeolite (right).

The concentration of copper leached from Cu-MOR, figure 5.29, increases with increasing zeolite mass. This is also the general trend with the increasing incubation time, with 24 hours showing the greatest leaching for each mass. As expected, the greatest leached copper concentrations came from 10 mg of zeolite incubated for 24 hours. Perhaps unexpectedly, the greatest percentage of total copper came from 2.5 mg incubated for 24 hours, corresponding to 0.16 %. Overall, the concentration of leached copper from Cu-MOR is the lowest of all the zeolites studied, Cu-MOR also has the lowest % of total copper leached. This may help to explain the low toxicity of Cu-MOR determined by the toxicology studies.

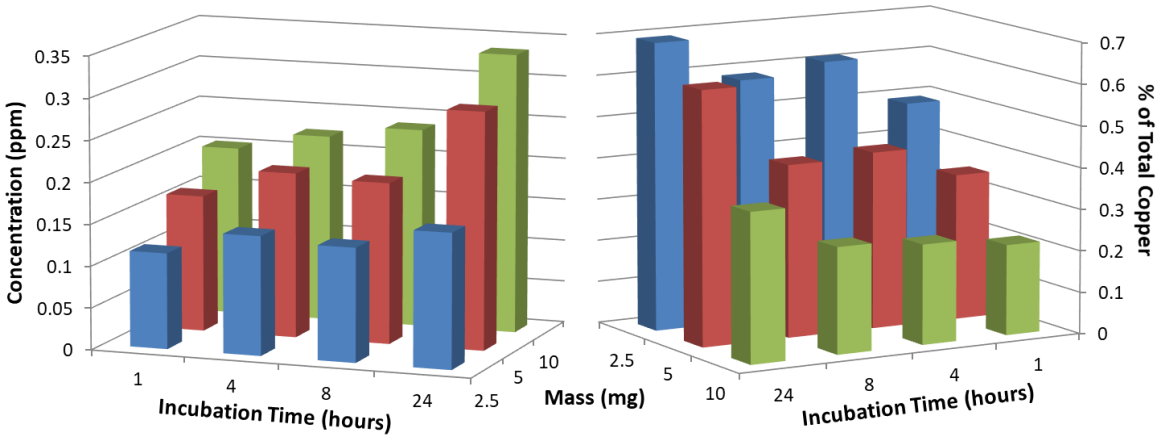

Figure 5.30: Copper leaching results of Cu-FER showing the copper concentrations determined by ICP-AES (left) and the % of total copper leached from the zeolite (right).

The Cu-FER leaching, figure 5.30, shows a general increase in copper concentration with increasing incubation time and increasing mass, but with a few exceptions, such as 5 mg with 8 hours incubation. The highest concentration of copper observed was 0.33 ppm from 10 mg with 24 hours of incubation. Again, the greatest total % of copper came from 2.5 mg incubated for 24 hours, corresponding to 0.69 %. Considering the same incubation period as the toxicology studies, 24 hours, the leaching trend looks to follow that of the toxicology data where 0.5 and 1 mg/mL are closer in values than that of 0.25 mg/mL.

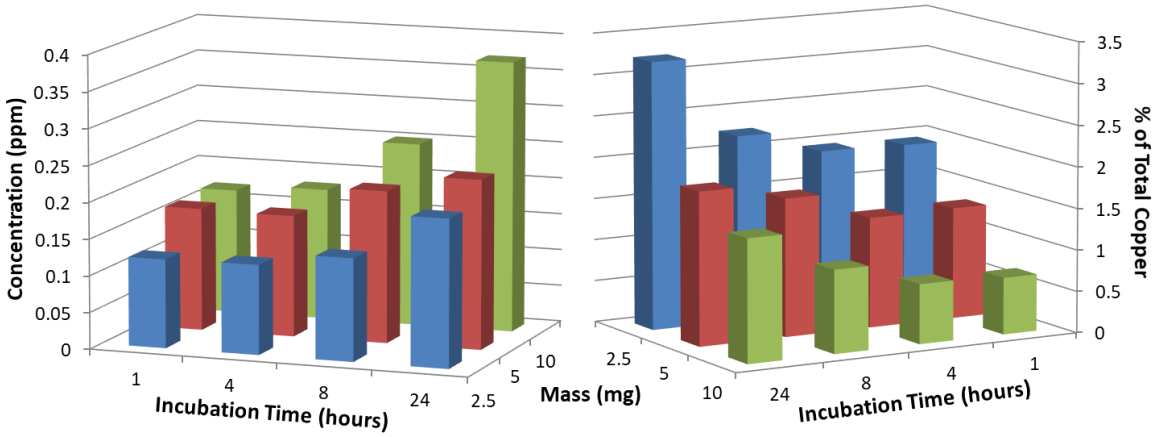

Figure 5.31: Copper leaching results of Cu-ZSM-5 showing the copper concentrations determined by ICP-AES (left) and the % of total copper leached from the zeolite (right).

The results from the Cu-ZSM-5 leaching, figure 5.31, again shows a general increase in copper concentration with increasing mass and incubation time. The highest copper concentration observed is 0.37 ppm and the greatest % of total copper is 3.23 %. Considering the leached copper ppm values are similar to that of Cu-FER, the toxicology data showed that the Cu-ZSM-5 sample has a greater toxic effect than Cu-FER. This is perhaps due to the cells also interacting with copper ions within the pores and not just with copper that has leached from the sample. The 3D nature of ZSM-5 may allow greater access for cells than the 2D ferrierite.

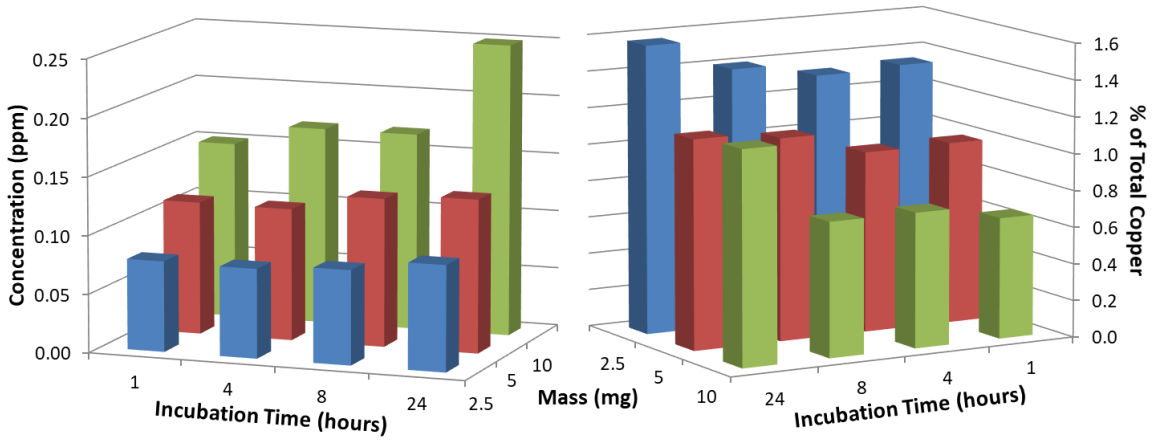

Figure 5.32: Copper leaching results of Cu-SSZ-13 showing the copper concentrations determined by ICP-AES (left) and the % of total copper leached from the zeolite (right).

The Cu-SSZ-13 leaching results, figure 5.32, follow the same trend as the previous zeolites. The highest copper concentration is 0.25 ppm and the greatest % of total copper is 1.57 %. As with Cu-ZSM-5, the toxicology data suggest relatively toxic effects from the Cu-SSZ-13 even though the copper leaching is less than Cu-FER. This is likely due to similar reasoning as Cu-ZSM-5, where the cells could access the extra-framework copper due to the 3D channel systems of SSZ-13.

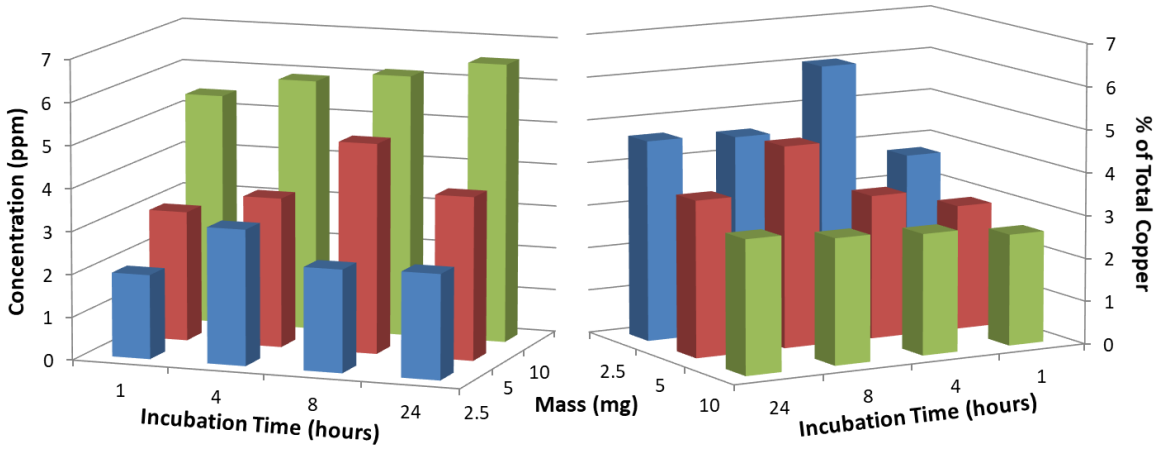

Figure 5.33: Copper leaching results of Cu-UZM-4 showing the copper concentrations determined by ICP-AES (left) and the % of total copper leached from the zeolite (right).

The copper concentrations from Cu-UZM-4, figure 5.33, were significantly higher than any of the other zeolites, with the highest concentration of copper leached at 6.56 ppm. The greatest % of total copper was also higher than the rest of the zeolites, at 6 %, but this time resulting from 2.5 mg incubated for 4 hours. There is a significantly higher copper content in UZM-4 than any of the other zeolites, which may be related to the high copper leaching concentrations. This also agrees with the toxicology studies that show a drastic decrease in cell viability with increasing zeolite concentration.

Considering the toxicology and copper leaching data, it is apparent that there is a trend relating increased copper leaching to increased toxicity. This is most evident with Cu-UZM-4 which has the highest toxicity and the greatest copper leaching. There may be other factors that determine the toxicity, one being the ability of the cells to access the copper within the pores. This is highlighted by greater toxicity from the 3D zeolites compared to the 2D zeolites. In view of the obtained data, the zeolite that showed the most positive results is Cu-MOR due to the low toxicity and low levels of copper leaching. The majority of the other zeolites may only be suitable depending upon the concentration required for the application, with the levels of toxicity generally increasing with an increase in zeolite concentration.

Interestingly, the majority of data sets show the greatest % of total copper coming from 2.5 mg of zeolite, with decreasing percentages with increasing masses. This may be due to the ion-exchange equilibrium, where the copper leached into solution will eventually move into the zeolite pores once again. Using Milli-Q water as the solution means that there will be no other ions to balance the charge of the zeolite after the loss of copper, therefore the copper leached is likely to re-exchange into the zeolite to balance the charge. It may be that the equilibrium is reached quicker with the higher masses of zeolite, resulting in lower amounts of copper released into the surrounding solution.

Another factor to consider when discussing the toxicology and leaching is the affect that incorporation of the zeolite powders into a polymer may have, as this is the set-up that the zeolites will most likely be used as in the biomedical applications. It is likely that a second barrier may help to prevent as much copper leaching from the sample, as well as prevent cells from accessing the zeolite pores as easily. The incorporation of zeolites into polymers is discussed in depth in chapter 6.

5.5. Conclusions

The results show that SSZ-13, ZSM-5 and UZM-4 produce the greatest amounts of NO. This suggests that the copper active sites are more accessible, which may be related to the 3D classification of the zeolites. The lower dimensionality zeolites, mordenite and ferrierite, had lower levels of NO production, further indicating that active site accessibility may play a role in catalytic activity. The pore sizes of the zeolites also appear to play a role in the NO production, with the large pore zeolites, mordenite and UZM-4, having the longest length of time for production. Likewise, SSZ-13 with the smallest pores had the shortest production time.

The reasons behind the interesting Cu-FER NO production has been thoroughly explored by a range of methods. Whilst a change in framework structure was ruled out by synchrotron PXRD data, further methods looked into any change in copper location within the pores. Single crystal samples of Cu-FER could not locate enough electron density within the pores that could be assigned to a copper atom. This was most likely due to the levels of copper being too low within the sample or a high level of copper disorder. Solid-state NMR data comparing Cu-FER pre and post-catalysis provided a slight breakthrough. Post-catalysis line narrowing of the $Si(OSi)_3(OAl)_1$ peak suggests that there may have been a loss or a movement of the copper. The relatively low leaching of copper from Cu-FER helps to disregard the possibility of solution copper contributing to NO production. Especially since other zeolites with similar levels of leaching did not show a change in NO production with multiple substrate injections. This would suggest that there has been a slight movement of copper location post-catalysis, which may help to explain the change in NO production during catalysis.

The toxicology and leaching studies revealed a connection between the amount of copper leached from the pores and the toxicity of the zeolites. This was most apparent by UZM-4, where the highest concentrations of copper were leached and the most toxic response against HEK 293 cells was observed. While UZM-4 performed well in the catalytic tests, this high toxicity unfortunately suggests it would not be suitable for use within the body.

Considering all the results from this chapter, it would seem that mordenite may be the best candidate for NO production from a stent coating. This is due to the low levels of both copper leaching and toxicity and the NO production from nitrite. Ferrierite is also a possible candidate based on the low toxicity, however the current lack of complete understanding of the increasing NO production would make it a less desirable option.

5.6. Future Work

The copper locations of the zeolites most likely play a large role in a range of the results seen in this chapter. The locations may influence the NO production by their accessibility, as well as the potential release by leaching and the subsequent toxicology from this release. While many literature sources have studied the copper locations of most of these zeolites by a range of techniques, there are still a lot of discrepancies. Ideally, the copper locations would have been studied for each copper zeolite within this chapter, to have a better understanding of how it behaves. As was seen with the study of the ferrierite copper location however, it is not an easy task to find potentially disordered extra-framework copper in a zeolite framework.

The solid-state NMR results provided a lead for the changing NO production of Cu-FER. To further probe the potential movement of copper within the zeolite, new methods of characterisation will be required. One area that may be of interest are *in situ* studies that could potentially capture any movement during the catalysis.

The toxicology and leaching data provided some extremely useful information on how the zeolites may behave within the body. The two techniques were used to identify if there was any connection between copper release and cell death. One factor which was not possible to keep constant however, was the medium that the samples were run in. The complex medium of the toxicology data was not possible to apply to the ICP-AES system for analysing the leaching data, therefore the leaching studies were performed in water. It would be useful to find a way to study and analyse the leaching behaviour of the copper zeolites in medium that more closely represents the biological system.

As was briefly mentioned, the incorporation of the zeolites in the polymer may help to reduce any leaching or toxic affect. Since the zeolites would be used within the body as part of a polymer, the behaviour of the zeolite/polymer film may provide a better idea of

toxicity levels. It may also act as a barrier that prevents copper from leaching as easily, resulting in higher concentrations of zeolites producing acceptable levels of response. Therefore, there would not be such a limitation on the zeolites that could be used.

5.7. References

1 A. K. Boës, B. Xiao, I. L. Megson and R. E. Morris, *Top. Catal.*, 2009, **52**, 35–41.

2 A. K. Boës, P. S. Wheatley, B. Xiao, I. L. Megson and R. E. Morris, *Chem. Commun.*, 2008, **0**, 6146–6148.

3 F. X. Llabrés i Xamena, P. Fisicaro, G. Berlier, A. Zecchina, G. T. Palomino, C. Prestipino, S. Bordiga, E. Giamello and C. Lamberti, *J. Phys. Chem. B*, 2003, **107**, 7036–7044.

4 G. Courtney-Martin and P. B. Pencharz, in *The Molecular Nutrition of Amino Acids and Proteins*, Academic Press, Boston, 2016, pp. 265–286.

5 H. Robson and K. P. Lillerud, in *Verified Syntheses of Zeolitic Materials*, Elsevier Science, Amsterdam, 2001, pp. 167–168.

6 H. M. Aly, M. E. Moustafa and E. A. Abdelrahman, *Adv. Powder Technol.*, 2012, **23**, 757–760.

7 C. S. Blackwell, R. W. Broach, M. G. Gatter, J. S. Holmgren, D.-Y. Jan, G. J. Lewis, B. J. Mezza, T. M. Mezza, M. a. Miller, J. G. Moscoso, R. L. Patton, L. M. Rohde, M. W. Schoonover, W. Sinkler, B. A. Wilson and S. T. Wilson, *Angew. Chemie Int. Ed.*, 2003, **42**, 1737–1740.

8 S. Li, A. Zheng, Y. Su, H. Fang, W. Shen, Z. Yu, L. Chen and F. Deng, *Phys. Chem. Chem. Phys.*, 2010, **12**, 3895.

9 E. Lippmaa, M. Maegi, A. Samoson, M. Tarmak and G. Engelhardt, *J. Am. Chem. Soc.*, 1981, **103**, 4992–4996.

10 G. P. M. Bignami, D. M. Dawson, V. R. Seymour, P. S. Wheatley, R. E. Morris and S. E. Ashbrook, *J. Am. Chem. Soc.*, 2017, **139**, 5140–5148.

11 L. Shi, X. Fu, C. P. Tan, Q. Huang and B. Zhang, *J. Agric. Food Chem.*, 2017, **65**, 2189–

2197.

12 A. Altree-Williams, A. Pring, Y. Ngothai and J. Brugger, *ACS Earth Sp. Chem.*, 2017, **1**, 89–100.

Chapter 6: Copper Site Zeolite Applications

6.1. Aim

Chapter 5 showcased the nitric oxide (NO) production capabilities of the copper zeolite powders. This chapter looks to apply these zeolite catalysts in further steps towards the desired biomedical applications. All five copper zeolites will first be studied in a flow set-up to understand the NO production with a constant substrate stream, a set-up which more closely mimics how the zeolite would behave within the artery. Secondly, the zeolites will be incorporated into polymer films, which could be one method to bind the zeolite powder to a metal stent, to understand any change in NO production compared to the free powders alone. These studies will be performed on the NOA.

6.2. Introduction

In chapter 5, the potential of the copper zeolite powders was explored. Whilst we have a good understanding of the zeolite powders in a closed, stationary system, this is not the best representation of the environment that the copper zeolites would be working within the body. Therefore, a flow system equipped with NO specific electrodes was designed and assembled that would allow the copper zeolite to remain stationary while the substrates flowed over the catalyst at a steady rate. Cysteine and nitrite are present within blood plasma at levels of 230 – 280 µmol/L and 0.1 – 0.5 µmol/L respectively.[1–3] The increased level of cysteine is mimicked in the flow studies with concentrations of 41.27 mmol/L for cysteine and 14.49 mmol/L for nitrite in the stock solution. While these values are considerably higher than physiological concentrations, it provides clear results from the measurements that can then be scaled down to biological levels as required.

The incorporation of zeolites into polymers is well studied, with applications including toxin removal, fuel cells and carbon dioxide capture.[4–6] A concern with this work, is the use of the larger cysteine molecule that may have diffusion issues with some of the polymers. The solubility of the polymers also needs to be considered, with water-stable zeolite/polymer films being a must for the proposed biomedical applications.

6.3. Experimental

6.3.1. Materials

Materials used in the zeolite syntheses: Sodium hydroxide (pellets, Fisher Scientific), tetrapropylammonium hydroxide (40 wt% solution, Sigma Aldrich), silicic acid (powder, -100 mesh, Sigma Aldrich) and sodium aluminate (technical, anhydrous, Al (Al_2O_3): 50 – 56 %, Na (Na_2O): 37 – 45 %, Sigma Aldrich).

The flow set-up used L-cysteine (98+ %, ACROS Organics) and sodium nitrite (Alfa Aesar). The syringe filters that supported the Cu-zeolites were polyethersulfone (PES) membrane, 0.2 μm filters from Fisher Scientific. The materials used in the polymer syntheses were polyurethane (pellets, MDI-polyester/polyether polyurethane, Sigma Aldrich), polyvinylchloride (pellets, Sigma Aldrich), dioctyl sebacate (Sigma Aldrich) and tetrahydrofuran (THF, >99.5 %, Fisher Scientific). The three PIM samples, PIM-1, EA-TB(Me) and EA-TB(H_2), were kindly provided by Prof. Neil McKeown at The University of Edinburgh. The polymer NOA catalytic tests used the same sodium nitrite source as the flow studies and D/L-cysteine (Sigma Aldrich).

6.3.2. Zeolite Synthesis

As opposed to the Zeolyst NH_4-ZSM-5 that was used in previous chapters, the work in this chapter used a synthesised batch of ZSM-5 due to limited Zeolyst sample.[7] The seed gel was prepared by dissolving sodium hydroxide (0.39 g, 9.75 mmol) and tetrapropylammonium hydroxide (1.67 g with 1.67 g distilled water to make 20 wt%, 3.28 mmol) in distilled water (20.29 g). This was followed by the addition of silicic acid (4.54 g, 0.076 mol) in portions. This was then stirred for one hour before aging at 100 °C for 16 hours.

The synthesis gel was formed by the mixing of distilled water (24.79 g), sodium hydroxide (0.25 g, 6.23 mmol) and sodium aluminate (0.29 g, 3.54 mmol), followed by the addition of silicic acid (3.23 g, 0.054 mol) in portions. This was stirred for 1 hour before the addition of 1.43 g of the seed gel, providing a batch composition of 3.25 Na_2O : Al_2O_3 : 30 SiO_2 : 800 H_2O : 0.1 TPAOH. The resulting mixture was stirred for an hour and placed into a 180 °C oven for 40 hours. The resulting crystals were recovered by vacuum filtration, washed with water and allowed to dry at room temperature.

Mordenite, UZM-4 and ferrierite were all prepared using the same syntheses as discussed in chapter 5. The H-SSZ-13 zeolite was from the same batch that was obtained from Chevron. All calcinations and copper ion-exchanges were performed in the same way as discussed in section 5.3.3.

6.3.3. APOLLO Flow System

The APOLLO electrode flow set-up was used to study the NO production of the zeolites. The short flow runs (1.5 – 2 hours) used ~250 mL of stock solution that was prepared in a 500 mL batch by dissolving L-cysteine (2.5 g, 0.021 mol) and sodium nitrite (0.5 g, 7.246 mmol) in Milli-Q water (500 mL). The longer flow runs (6 – 7 hours) required 2 L of stock solution that was prepared in 2 x 1 L volumetric flasks with each containing L-cysteine (5 g, 0.041 mol) and sodium nitrite (1 g, 0.014 mol) dissolved in Milli-Q water (1 L). This provided solutions with concentrations of 41.27 mmol/L for cysteine and 14.49 mmol/L for nitrite. Once dissolved, the solution was degassed with nitrogen for 30 minutes. During this time, the Cu-zeolite (15 mg) was dispersed in a syringe filter and connected to the APOLLO flow set up with the tubing set to by-pass the zeolite.

The stock solution was placed in the large round bottom flask and the flow rate set at 5 mL/min for the short runs and 4 – 5 mL/min for the long runs. A flow of nitrogen was applied to the substrate, to both reduce any oxygen that could react with the produced NO and to apply a pressure to the system, allowing the substrate to flow. The stock solution was run through the tubing for around 5 minutes at the beginning of the run to allow the current of the two electrodes to settle. The electrodes were then zeroed and the stopcocks opened to allow the stock solution to pass over the zeolite. The current from the electrodes was recorded throughout the run. The run was completed when all the stock solution had passed through the system, which resulted in a slight variation in the length of time of the runs.

The total change in current was determined by calculating the difference between the two electrodes, this was then converted to NO concentration using the calibration curve, section 3.2. A slight alteration to the set-up was used for the long runs of SSZ-13, mordenite and ZSM-5, this was due to a broken electrode. Only one electrode was used, which was placed after the zeolite-packed filter, this was the electrode that was normally

situated before the filter. Therefore, any change in current was determined by one electrode only and not a difference between the two electrodes. While not an ideal set-up, it was seen previously that the electrode placed before the zeolite showed little deviation from 0 pA once zeroed, therefore monitoring the second electrode only should provide reliable data.

A control flow run was performed with no zeolite held within the filter, figure A4 in the Appendix. This was to ensure that any NO production observed was attributed to the copper zeolites.

6.3.4. Polymer Incorporation

A range of polymers were studied with various zeolites and zeolite loadings. The incorporation was generally performed by use of an overheard stirrer to dissolve the polymer in the solvent (THF) overnight, the zeolite was then added either directly or as a slurry. The direct addition was the addition of the ground zeolite directly to the dissolved polymer. The slurry was formed by reserving a portion of the solvent to grind with the zeolite prior to addition to the dissolved polymer. After addition, the zeolite was stirred with the overhead stirrer for 30 minutes before the polymer film was cast onto a glass plate and left to slowly dry under a desiccator lid to limit any air bubble formation upon drying. Once dried, the film was carefully peeled from the glass plate and stored in sealed bags. The range of zeolite/polymer films synthesised with polyurethane, the first polymer studied, are shown in table 6.1 below. A range of different zeolite loadings were prepared in an attempt to understand the optimal loading for NO production.

Table 6.1: The compositions of the various polyurethane films.

Zeolite	Zeolite Mass (g)	Polyurethane Mass (g)	THF Mass (g)	Zeolite Loading (wt%)	Direct or Slurry?
Cu-ZSM-5	0.5	5	45	9	Direct
Cu-ZSM-5	0.55	5	45	10	Slurry
Cu-UZM-4	0.5	2	18	20	Slurry
Cu-MOR	0.8	1.2	10.8	40	Slurry

A zeolite film using polyvinylchloride was also prepared following a similar procedure from literature based on MOF/polymer films.[8] The use of a plasticiser, dioctyl sebacate (DOS) in this case, was used to soften the usually rigid polyvinylchloride to allow for a flexible film. The method was similar to that of the polyurethane polymers, with the PVC (1.30 g) and DOS (0.43 g) being dissolved by overhead stirring in THF (11.7 g) overnight. Cu-UZM-4 (0.19 g) was added as a slurry to the dissolved polymer the following morning, stirred to incorporate, and the film cast. This provided a 10 wt% UZM-4/PVC film.

Three polymers of intrinsic microporosity (PIMs) were studied: PIM-1, EA-TB(Me) and EA-TB(H_2). Due to the slightly brittle nature of PIMs, the zeolite/PIM films were coated onto stainless steel clips which acted as a "stent model". This was in an attempt to prevent them from breaking during the catalytic tests. The mass of the stainless steel clips was recorded prior to the film coating, to allow a calculation of the mass of polymer film on the clip. For all samples, zeolite (25 mg) was ground with THF (1 g) and added to a sample vial with stirring. The desired PIM (0.1 g) was added to the sample vial and the stirring continued until the PIM had fully dissolved, providing a 20 wt% zeolite sample. The stainless steel clip was then dipped into the zeolite/PIM solution for a couple of minutes and hung under a desiccator lid to dry. The mass of polymer film was calculated from the initial clip mass and the clip dipped for a second time if required, with the target of 50 mg of polymer film corresponding to 10 mg of zeolite.

6.3.5. Polymer Catalytic Testing

The polyurethane and polyvinylchloride films and the PIM-coated clips were tested for NO production on the NOA. The polymer films were cut to provide the desired mass, while the clips were used as prepared. The polymer was placed in a vial with Milli-Q water (2.6 mL) and sealed with a cap. The polyurethane and polyvinylchloride films tended to be wrapped around the inside of the vial to prevent them from floating in the water. The solution was degassed with nitrogen for 10 minutes prior to the start of the run. D/L-cysteine (0.05 M, 25 µL, 1.25 x 10^{-6} mols) was injected 5 minutes into the run, with the substrate, sodium nitrite (0.05 M, 25 µL, 1.25 x 10^{-6} mols), added 10 minutes later and the sample run until the NO concentration returned to background levels.

6.4. Results and Discussion

To aid the results and discussion section, a table summarising the previously discussed key features of the five zeolites is shown below, table 6.2.

Table 6.2: Framework summaries of the five zeolites applied for copper catalysis.

Zeolite	Ring Sizes	Channel System	Diffusion Along the a, b and c Axes
ZSM-5	10, 6, 5 and 4	3D	4.70 Å, 4.46 Å, 4.46 Å
SSZ-13	8, 6 and 4	3D	3.72 Å, 3.72 Å, 3.72 Å
UZM-4	12, 8, 6 and 4	3D	3.51 Å, 3.51 Å, 6.01 Å
Mordenite	12, 8, 5 and 4	2D	1.57 Å, 2.95 Å, 6.45 Å
Ferrierite	10, 8, 6 and 5	2D	1.56 Å, 3.40 Å, 4.69 Å

6.4.1. Zeolite Characterisation

6.4.1.1. Powder X-Ray Diffraction

The newly synthesised batches of mordenite, UZM-4 and ferrierite were characterised by PXRD, with all batches matching well with the corresponding previous patterns in section 5.4.1.1, indicating pure samples. The SSZ-13 was the same batch as has been used previously, therefore further PXRD characterisation was not required.

The newly-synthesised ZSM-5 was compared to the Zeolyst sample used in chapter 5 to determine the purity. The results, figure 6.1, reveal a rather good peak match between the industrial and synthesised samples, with no obvious differences, indicating a similar level of phase purity.

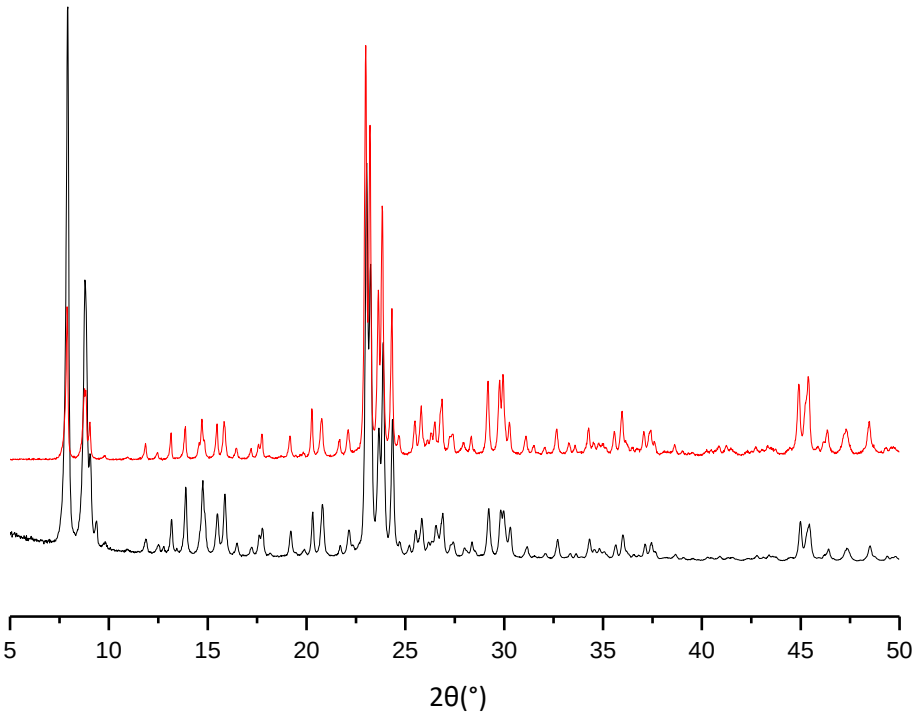

Figure 6.1: PXRD patterns of as-synthesised ZSM-5 experimental (red) and Zeolyst NH_4-ZSM-5 (black).

6.4.1.2. Scanning Electron Microscopy – Energy Dispersive X-Ray Spectroscopy

The SEM images of the as-synthesised ZSM-5 powder are shown in figure 6.2 below. The crystals are small and spherical, with a diameter of around 10 µm. Some of the crystals don't appear to be fully formed, with some crystals connected to each other and large amounts of agglomeration, suggesting that a slightly longer synthesis may be beneficial.

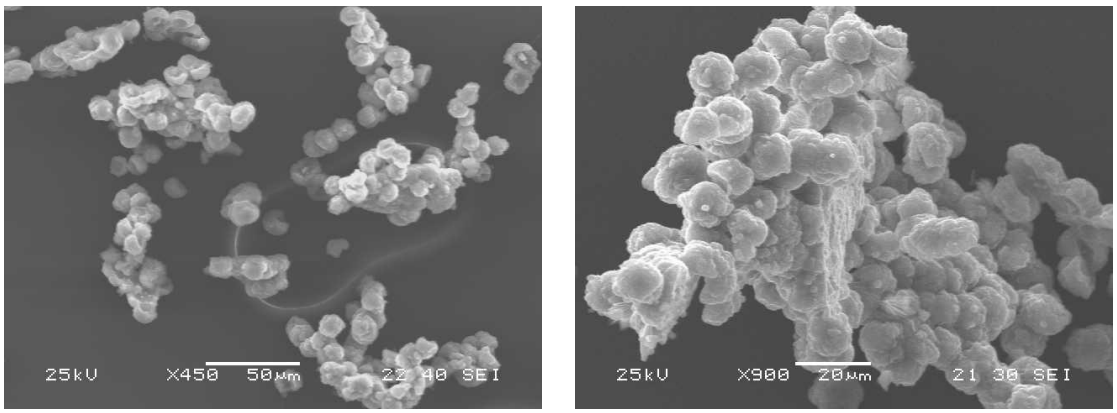

Figure 6.2: As-synthesised ZSM-5 SEM images.

Although all samples in this chapter came from the same zeolite batches, a range of ion-exchanged samples were used throughout the flow and polymer studies. A summary of the sample compositions can be seen in table 6.3. All compositions were determined by EDX and the error calculated by standard deviation of a range of measurements. While

the majority measured the presence of Si, Al and Cu only, one measurement (SR2_12_CH68) included oxygen, therefore it does not total to 100 %. Small differences between Si/Al ratios of the same zeolite (e.g. UZM-4) are due to rounding of the average EDX values.

Table 6.3: Copper zeolite compositions for flow and polymer studies.

Sample	Zeolite	% Silicon	% Aluminium	% Copper	Si/Al	Cu/Al
Flow Study Samples						
SR2_135	UZM-4	63.8 ± 2.2	24.8 ± 1.0	11.4 ± 1.4	3	0.46
SR2_140	FER	85.9 ± 2.4	9.7 ± 1.4	4.3 ± 1.4	9	0.45
SR2_141	SSZ-13	92.9 ± 0.2	4.9 ± 0.2	2.2 ± 0.2	19	0.44
SR2_151	ZSM-5	91.6 ± 1.5	5.2 ± 1.1	3.1 ± 0.7	18	0.60
SR2_155_MOR	MOR	82.4 ± 1.1	11.7 ± 0.44	6.0 ± 0.9	7	0.51
SR2_155_ZSM-5*	ZSM-5	91.5 ± 1.1	5.2 ± 0.5	3.3 ± 1.0	18	0.64
Polyurethane Samples						
SR2_83	ZSM-5	92.7 ± 0.2	5.0 ± 0.1	2.3 ± 0.1	18	0.46
SR2_93	UZM-4	64.2 ± 1.2	24.7 ± 0.4	11.1 ± 0.9	3	0.45
Polyvinylchloride Sample						
SR2_12_CH68	UZM-4	16.4 ± 1.5	7.8 ± 0.7	3.3 ± 0.5	2	0.43
PIM Samples						
SR2_135	UZM-4	63.8 ± 2.2	24.8 ± 1.0	11.4 ± 1.4	3	0.46
SR2_140	FER	85.9 ± 2.4	9.7 ± 1.4	4.3 ± 1.4	9	0.45
SR2_141	SSZ-13	92.9 ± 0.2	4.9 ± 0.2	2.2 ± 0.2	19	0.44
SR2_143	ZSM-5	91.3 ± 1.0	5.2 ± 0.3	3.5 ± 0.8	17	0.67
SR2_131	MOR	82.9 ± 1.3	11.3 ± 0.3	5.8 ± 1.2	7	0.51

*A different sample of ZSM-5 was used for the long flow studies (SR2_155_ZSM-5) compared to the initial and recycled flow studies (SR2_151). Although not ideal, this was due to limited amount of SR2_151. The ZSM-5 was from the same synthesis batch but a different batch of ion-exchanged sample.

6.4.2. Zeolite Catalysis in Flow

6.4.2.1. Initial Studies

All copper zeolites were studied on the flow system in triplicate with the runs complete when all stock solution had passed through the system. The triplicate results are presented as the NO concentration produced which was calculated from the difference of current between the two electrodes. Although a constant flow rate of 5 mL/min was targeted, air bubbles or changes in pressure were difficult to avoid and the flow rate varied slightly throughout the runs. This resulted in ranging length of times for the runs, from around 1.5 – 2.2 hours. Sudden changes in NO concentration were generally caused by air bubbles located at the tip of electrode preventing adequate contact with the solution. The air bubbles were removed by increasing the flow rate momentarily until they were flushed out of the system, the rate was then returned to 5 mL/min. Any drastic alterations in current, and therefore NO concentration, contributed by an air bubble was removed from the averages to prevent inaccurate data.

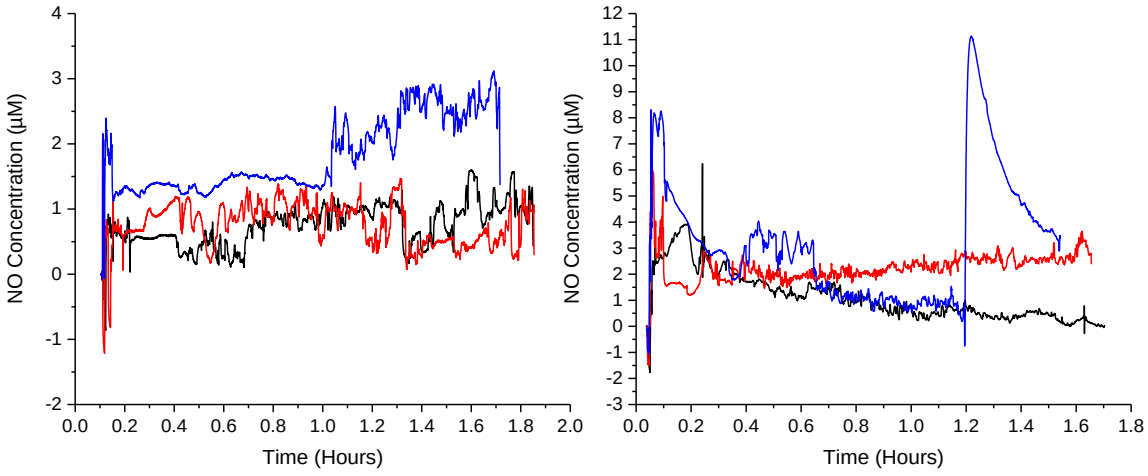

Figure 6.3: Triplicate nitric oxide flow studies of Cu-ZSM-5 (left) and Cu-SSZ-13 (right).

The results of the Cu-ZSM-5 flow studies, figure 6.3 (left), shows two runs (black and red) with very similar NO concentrations, ranging between 0 and 1.5 µM. The third run (blue) shows a slightly greater NO concentration that ranges between 1 and 3 µM, with the higher concentrations obtained towards the end of the run.

The Cu-SSZ-13 results, figure 6.3 (right), show a high initial concentration for the blue run, spiking around 8 µM, that slowly decreases over the following hour, before spiking for a second time at 1.2 hours reaching 11 µM. The second spike was caused by the clearance of an air bubble and showed elevated NO concentrations for the remainder of the run. This increase due to the air bubble has been removed from the average calculation. The red run showed a consistent concentration of 2 – 3 µM throughout, while the black line slowly decreased during the 1.7 hours, finishing around 0 µM.

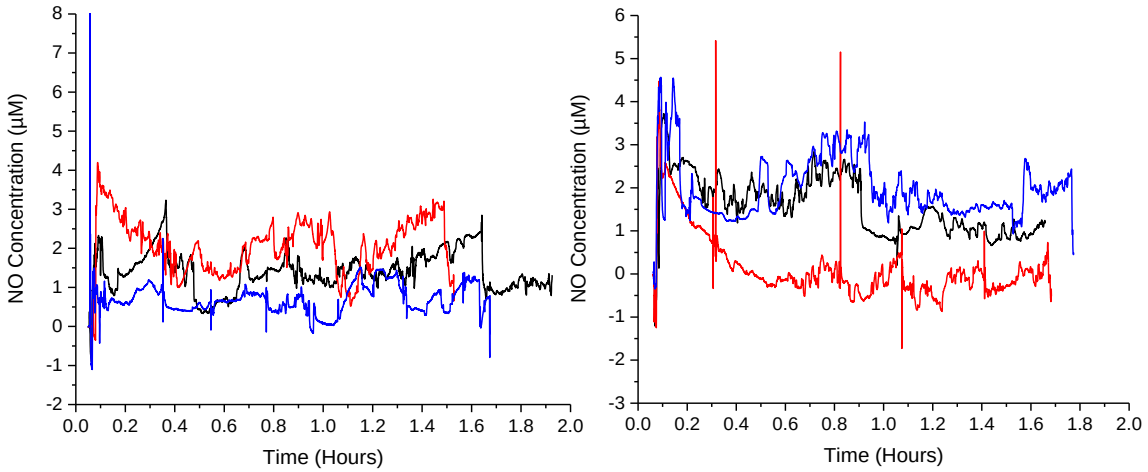

Figure 6.4: Triplicate nitric oxide flow studies of Cu-MOR (left) and Cu-FER (right).

The Cu-MOR results, figure 6.4 (left), show NO concentration between 0 and 4 µM. All runs are fairly similar, with the blue run showing the lowest concentration and the red run showing the highest. There is quite a big difference in the time, with the shortest run taking 1.5 hours and the longest taking 2 hours.

The Cu-FER flow results, figure 6.4 (right), show similar NO concentrations for the black and blue runs, with 1 – 4 µM of NO produced. The red run shows a lowered NO concentration, with the second half of the run producing around 0 µM of NO. All three runs lasted for a similar amount of time of around 1.7 hours.

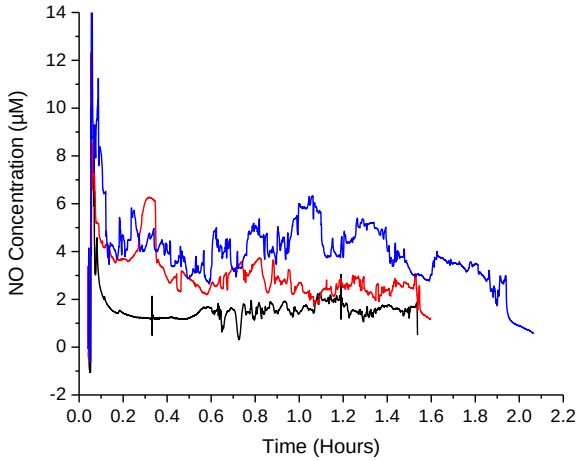

Figure 6.5: Triplicate nitric oxide flow studies of Cu-UZM-4.

The blue run of Cu-UZM-4, figure 6.5, shows the highest and longest NO production out of the triplicates. The NO concentration sits between 3 and 6 µM and the run lasts around 2 hours, suggesting a slower actual flow rate than the other two runs. The black and red runs have similar NO concentrations, between 1 and 4 µM, and similar lengths of time for the runs around 1.6 hours.

The triplicates for the majority of the zeolites showed a large amount of deviation, suggesting the flow studies are not very reproducible. They do however, show promise that all the Cu-zeolites produce NO in a flow set-up. The average of the triplicates can help to suggest which zeolites may perform best in this set-up, but are only being used as an indication at this stage.

The averages shown in figure 6.6 show that all copper zeolites produce NO between 0.5 and 4 µM for the whole of the 1.6 – 1.8 hour runs. Cu-UZM-4 has the highest NO concentration for the majority of the run, with the other four zeolites showing similar concentrations throughout. As with the Cu-zeolite NOA results discussed in section 5.4.2, UZM-4 is a large pore, 3D zeolite; two factors that may aid the interaction of the nitrite with the active copper sites. The main difference between the previous NOA catalytic tests and the flow system is the movement of the substrate. The small pore zeolites SSZ-13 and ZSM-5 that performed equally as well as UZM-4 in the NOA tests in chapter 5, may not be performing as well in these tests due to the limited time interacting with the substrates. This limited exposure could possibly be affecting the diffusion of the substrate into the small pores.

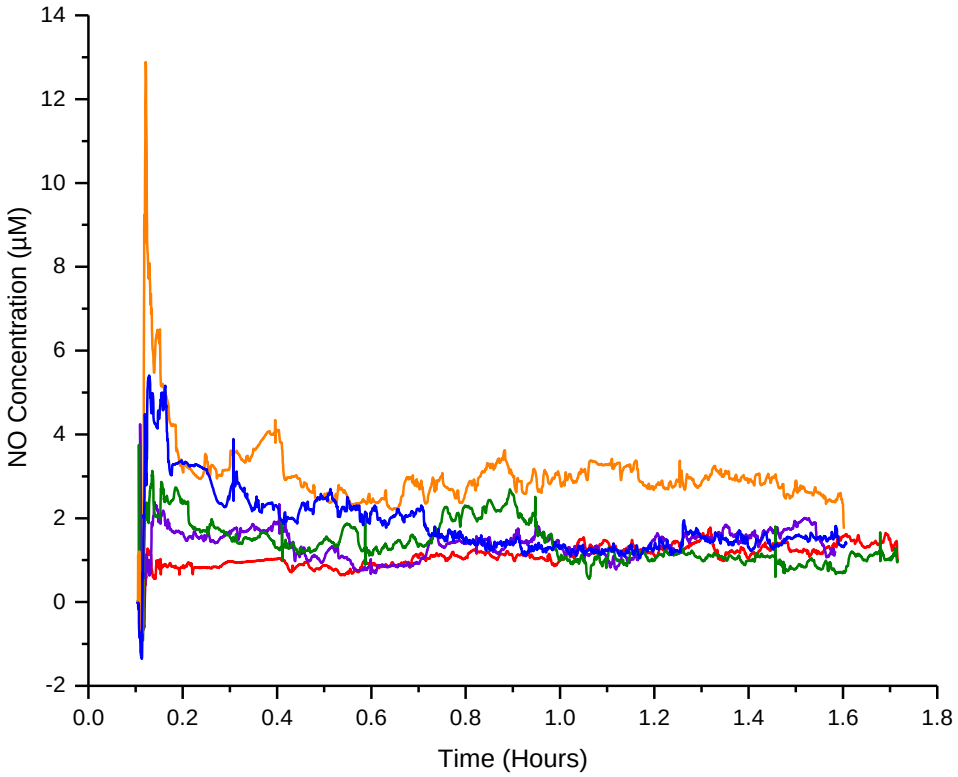

Figure 6.6: Average NO concentration of each copper zeolite from the initial flow studies. SSZ-13 (blue), ZSM-5 (red), UZM-4 (orange), mordenite (purple) and ferrierite (green).

A comparison of the observed NO concentrations to biological concentrations allows an understanding of the therapeutic potential of these zeolites. Free NO plasma concentrations have been determined as 3.4 ± 0.58 nM, considerably lower than the values that have been obtained with the flow studies.[9] A second literature source considered the wide range of physiological NO concentrations in vivo that have been reported.[10] The study placed the concentration range between 100 pM and 5 nM, but states that NO concentrations into the low picomolar range could still elicit biological responses. The reported values are significantly lower than the experimental values obtained. This is a promising sign however, since the substrate concentrations used were increased by a factor of 10 – 10000 compared to the biological concentrations, in an attempt to aid the recording of the results due to the equipment sensitivity. Comparing the experimental flow concentrations to the physiological range quoted, there is also a difference of around 1000 for the values. This indicates that biologically relevant concentrations of NO could be produced with the Cu-zeolites when supplied with biological concentrations of cysteine and nitrite.

6.4.2.2. Recyclability

All zeolite-packed filters were allowed to dry before being studied on the flow rig for a second time, to assess the recyclability of the samples. The procedure was the exact same as the initial studies. Only duplicate results could be obtained for SSZ-13 and ferrierite due to the blockage of one of the filters preventing the flow of stock solution.

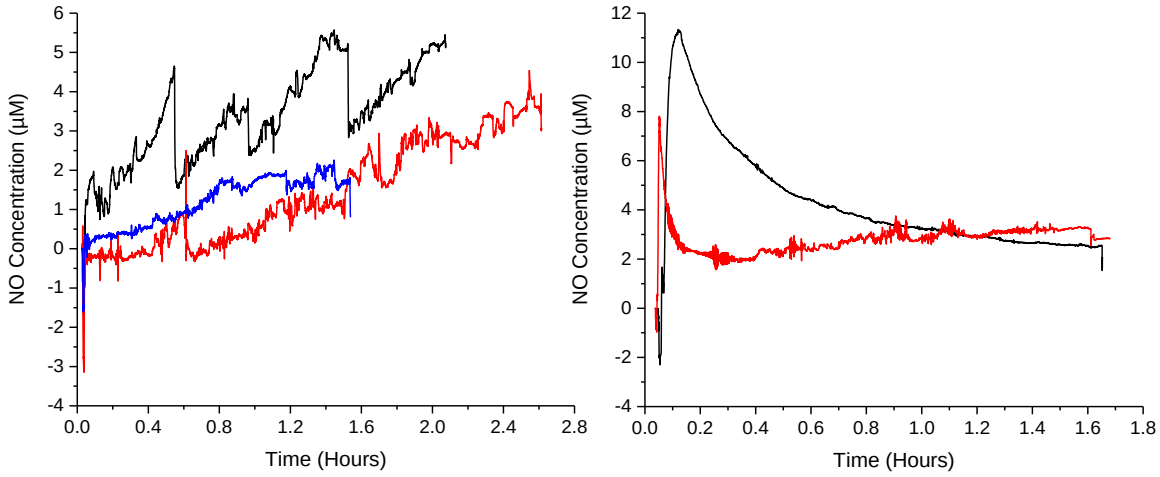

Figure 6.7: Triplicate nitric oxide recycled flow studies of Cu-ZSM-5 (left) and duplicate results of recycled Cu-SSZ-13 (right).

The results of the recycled Cu-ZSM-5, figure 6.7 (left), showed increasing NO concentrations throughout the run for all the triplicates. The length of the runs varied quite drastically, with the quickest being around 1.6 hours and the longest around 2.7 hours, over one hour difference. This is due to a couple of the filters being partially blocked and therefore reducing the rate at which the stock solution can pass through the system. On comparison to the initial Cu-ZSM-5 studies, the NO concentrations of the recycled samples are slightly higher, reaching a maximum of 5.5 µM.

The recycled Cu-SSZ-13, figure 6.7 (right), showed two very different trends, with the red run initially peaking at 8 µM and then quickly settling between 2 and 4 µM, while the black run peaked at 11 µM and slowly decreased during the rest of the run. The two runs lasted a similar time of 1.7 hours. On comparison to the initial flow data, the recycled red run is very similar to the initial red run, while the recycled black run shows a considerably higher concentration than what was observed previously.

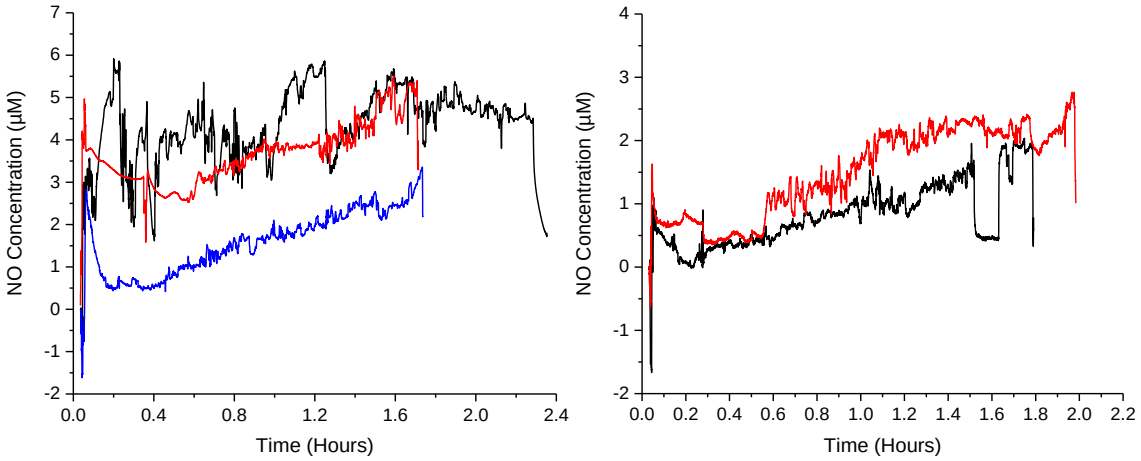

Figure 6.8: Triplicate nitric oxide recycled flow studies of Cu-MOR (left) and duplicate results of recycled Cu-FER (right).

The results of the recycled Cu-MOR triplicates, figure 6.8 (left), revealed a wider span of NO concentrations in comparison to the initial studies, with a range of 0.5 to 6 µM. The black recycled run lasted over 0.5 hours longer than the other two runs, again this was due to a slightly blocked filter and therefore slower flow rate.

The Cu-FER recycled duplicates, figure 6.8 (right), are similar to each other, with both runs slowly increasing in NO concentration over time. The values are also similar to the initial studies where the triplicates ranged between 0 and 3 µM.

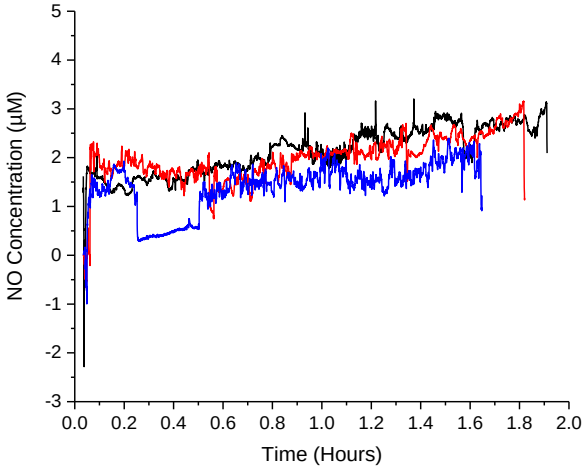

Figure 6.9: Triplicate nitric oxide recycled flow studies of Cu-UZM-4.

The results of the recycled UZM-4, figure 6.9, show rather similar triplicates, with the only exception being the concentration drop of the blue run around 0.25 hours. All three produced between 1 and 3 µM of NO between 1.6 and 2 hours of run time.

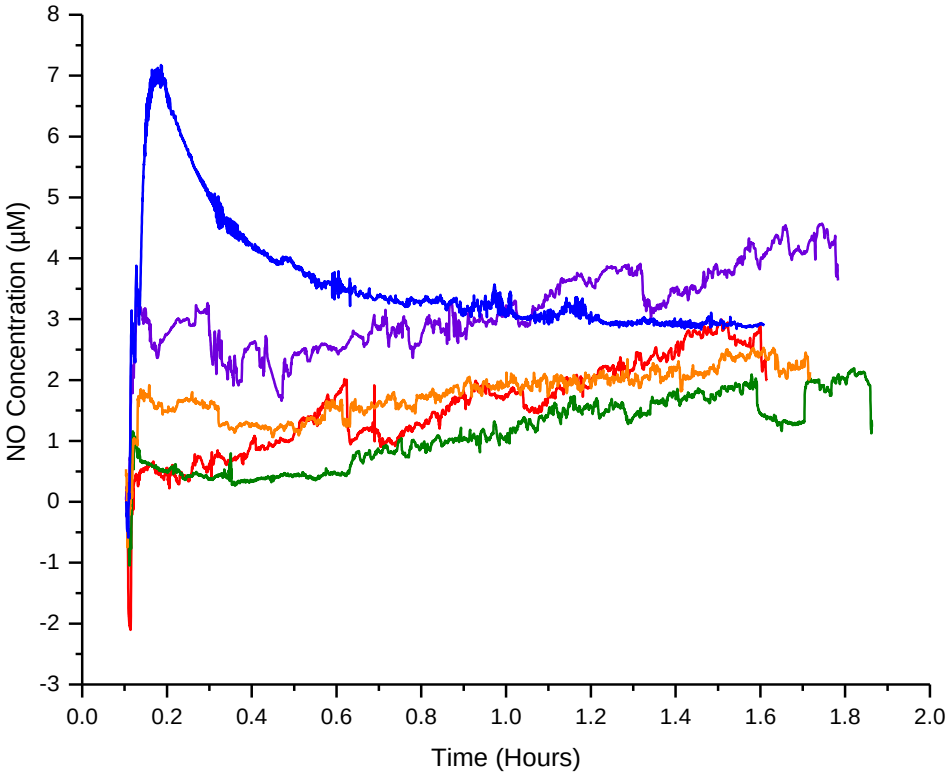

Figure 6.10: Average NO concentration of each copper zeolite from the recycled flow studies. SSZ-13 (blue), ZSM-5 (red), UZM-4 (orange), mordenite (purple) and ferrierite (green).

The average NO concentration of each recycled duplicate/triplicate is shown in figure 6.10. The highest NO concentration is 7 µM which comes from Cu-SSZ-13, however this is largely skewed by one of the duplicate runs and therefore not a fair assumption. Cu-MOR also has a relatively high level of NO produced, ranging between 2 and 4.5 µM. The lowest NO concentrations were produced from Cu-FER with a range of 0 to 2 µM.

Comparing the initial averages and the recycled averages, there is a similar range of NO concentrations produced, with the recycled zeolites sitting mainly between 0.5 and 5 µM. There is quite a difference in the ordering of the zeolites from the initial study results, as well as a larger dispersion between the zeolite measurements. The factors most likely to be affected by the recycling, would be loss of the copper sites due to copper leaching or due to pore blockages from the substrate. The reduction in NO concentration from UZM-4 could be due to the high level of leaching that was observed in section 5.4.4, resulting in subsequent loss of active sites after the initial flow studies.

6.4.2.3. Longer Flow Studies

The positive results of the initial and recycled samples led to the study of the copper zeolites over longer time periods, achieved by an increase in stock solution volume and decrease in flow rate. As mentioned in section 6.3.3, a different set-up was used for the long runs of SSZ-13, mordenite and ZSM-5 due to a broken electrode, where the electrode that normally monitored the current before the catalyst was moved to after the catalyst.

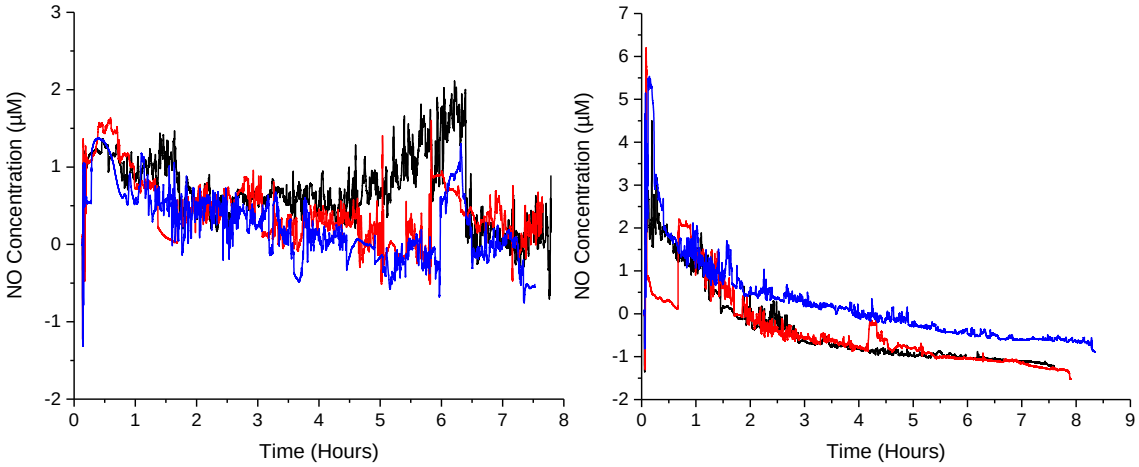

Figure 6.11: Triplicate nitric oxide long flow studies of Cu-ZSM-5 (left) and Cu-SSZ-13 (right).

All three triplicates of Cu-ZSM-5, figure 6.11 (left), are similar in the NO concentration produced and the length of run around 7 – 8 hours. The runs veer towards 0 µM after the first couple of hours and stay around this mark for the majority of the run. The black run is an exception to this as the concentration increases between 4 and 6.5 hours before dropping back down to the 0 µM mark.

The Cu-SSZ-13 triplicates, figure 6.11 (right), all follow a similar trend with decreasing NO concentration throughout the runs. The NO concentration drops below 0 µM after around 2 hours for the red and black runs and 4 – 5 hours for the blue run. This indicates that the Cu-SSZ-13 does not perform well under the longer flow conditions.

The Cu-MOR longer flow studies, figure 6.12 (left), range between -1.5 and 1.5 µM and last between 7 and 8 hours. The red run remains above 0 µM throughout the run, whereas the other two runs drop below 0 µM after a couple of hours.

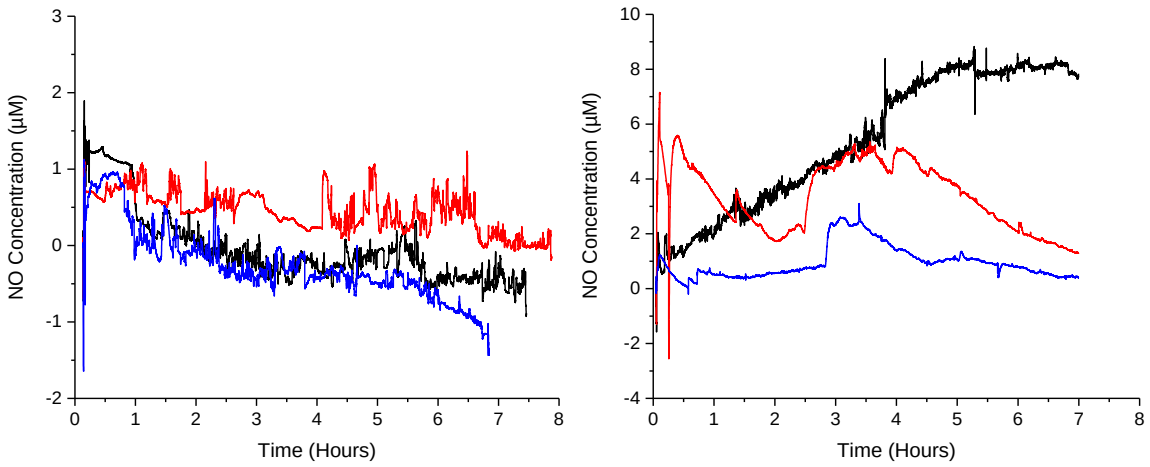

Figure 6.12: Triplicate nitric oxide long flow studies of Cu-MOR (left) and Cu-FER (right).

The triplicates of the long runs of Cu-FER, figure 6.12 (right), varied quite significantly. The blue run had the lowest NO concentration, which remained around 0 µM for the majority of the run. This was followed by the red run that ranged between 1 and 6 µM over the 7-hour period. The black run gradually increased from 1 µM to 8 µM over the 7-hour run, the highest NO concentrations for Cu-FER.

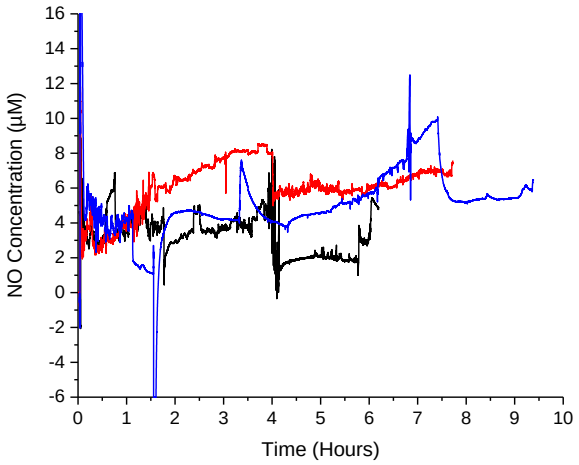

Figure 6.13: Triplicate nitric oxide long flow studies of Cu-UZM-4.

The long flow results of Cu-UZM-4, figure 6.13, are rather shaky for all three runs. The blue run went "off-scale" twice, the first at the very beginning and the second around 1.5 hours, hence the lines disappearing momentarily from the graph. These points were removed when calculating the average NO production as the changes resulted from air bubbles at one of the electrodes. The NO concentration of this run varied between 2 and 10 µM during the 9.5 hour period. The black run was much shorter than the other runs,

lasting around 6.5 hours, suggesting the flow rate was quicker than the other two. The red run was the most consistent of all three with a gradual NO concentration increase for the first 4 hours, followed by 4 hours settled around 6 µM.

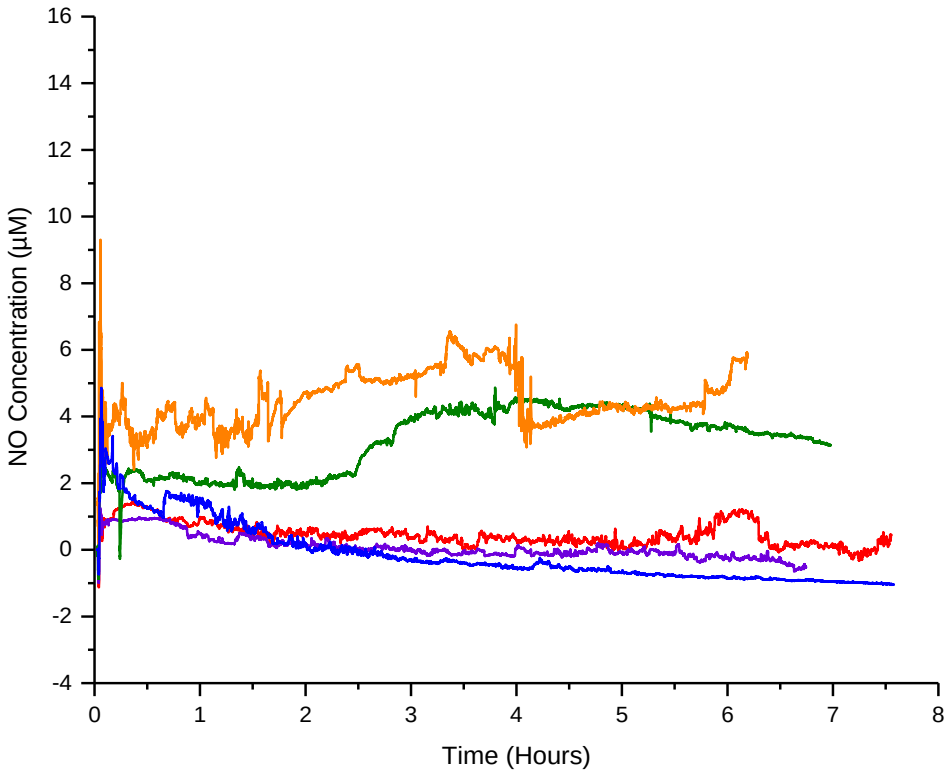

Figure 6.14: Average NO concentration of each copper zeolite from the long flow studies. SSZ-13 (blue), ZSM-5 (red), UZM-4 (orange), mordenite (purple) and ferrierite (green).

The averages of the longer flow studies, figure 6.14, reveal that the new method that used just one electrode showed much lower NO concentrations than the two-electrode method. This may be due to the current being taken from one electrode only and not being able to calculate any overall change current before and after the zeolite catalyst. Ideally, all zeolites would have been assessed by the same method to fairly compare the longer flow studies. Out of the Cu-UZM-4 and the Cu-FER averages, Cu-UZM-4 performs best, with the average NO concentration between 3 and 6 µM. Of the Cu-SSZ-13, Cu-MOR and Cu-ZSM-5 averages, Cu-ZSM-5 performs best by maintaining around 1 µM of NO throughout and Cu-SSZ-13 the worst with a decreasing NO concentration that drops below 0 µM within 2 hours.

While the initial and recycled flow studies provide a good indication that the copper zeolites would be active in a flowing substrate, the varying results of the longer flow studies suggest that there may be a limitation. Unfortunately, the three zeolites assessed by the one-electrode set-up were the three that showed limited NO production over a prolonged period. This therefore leaves a slight doubt over where the issue lies, if it was the set-up or the lack of activity from the zeolites. The results also potentially highlight a further issue that even with frequent calibrations, there may still be differences in sensitivity with different electrodes. Lastly, the presence of air bubbles became a great inconvenience during some runs, greatly altering some of the results. Thankfully we can rule out these sudden changes in concentration in a biological system as air bubbles would no longer be a factor. Overall, while this work has greatly helped to observe the zeolite potentials for a moving substrate system, there are still experimental factors that need to be overcome.

The results as they stand would suggest that the zeolites may not be suitable for long term applications, such as a stent, but could be suited to short term NO production. While the flow studies have provided a good insight into the functioning of the zeolites in a setting more closely related to an artery, in vivo studies would still provide a much more accurate representation of the zeolites biological functions. Previous studies of antithrombotic effects of platelet cells and blood flow levels of topically applied creams are two examples of studies that could help increase the understanding of the Cu-zeolites suitability for biological applications.[11,12]

6.4.3. Polymer Incorporation

6.4.3.1. Polyurethane Polymer Films

The first polyurethane film was prepared by direct addition of the ground zeolite to the dissolved polymer. The resultant film, figure 6.15 (left), was grainy in texture and speckled in appearance. The synthesis was repeated with a slight alteration of the zeolite mass to provide a 10 wt% loading, rather than the 9 wt% that was obtained with the first method. On this occasion, the zeolite was added to the dissolved polymer as a slurry. The resultant film, figure 6.15 (right), was smooth in texture and homogenous in appearance, suggesting greater dispersion of the zeolite.

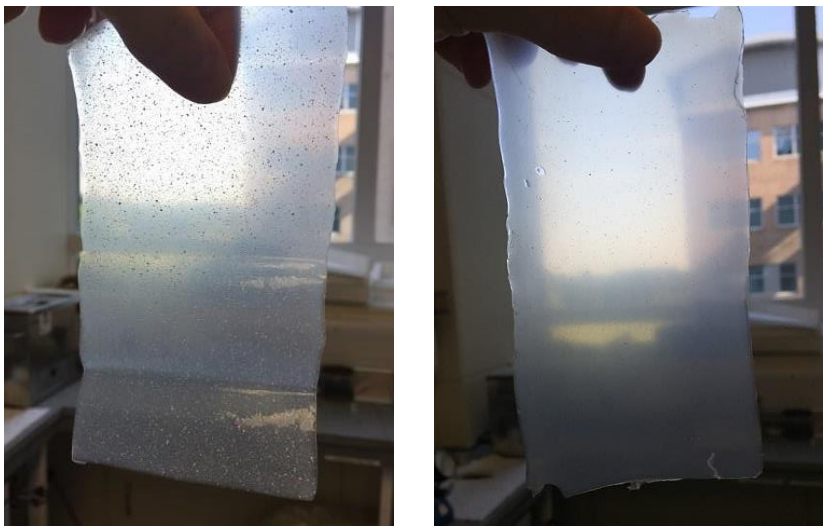

Figure 6.15: Polymer films of polyurethane with direct zeolite incorporation (left) and zeolite addition as a slurry (right).

The dispersity of the zeolite in the homogeneous film was supported by SEM imaging performed by Simon Vornholt. The SEM images, figure 6.16, initially revealed good dispersion of the zeolite on the surface of the film, represented by small bumps on the polymer surface. The cross-section removal by a focused ion beam allowed an understanding of the dispersion in the depth of the polymer film and confirmed that the zeolite had not settled on the surface of the film. Zeolite particles and small agglomerates can be seen in the polymer cross-section, indicating dispersion throughout the whole of the polymer film. With the zeolite slurry addition producing well dispersed zeolite in the polymer films, this process was taken forward as the preferred zeolite addition method.

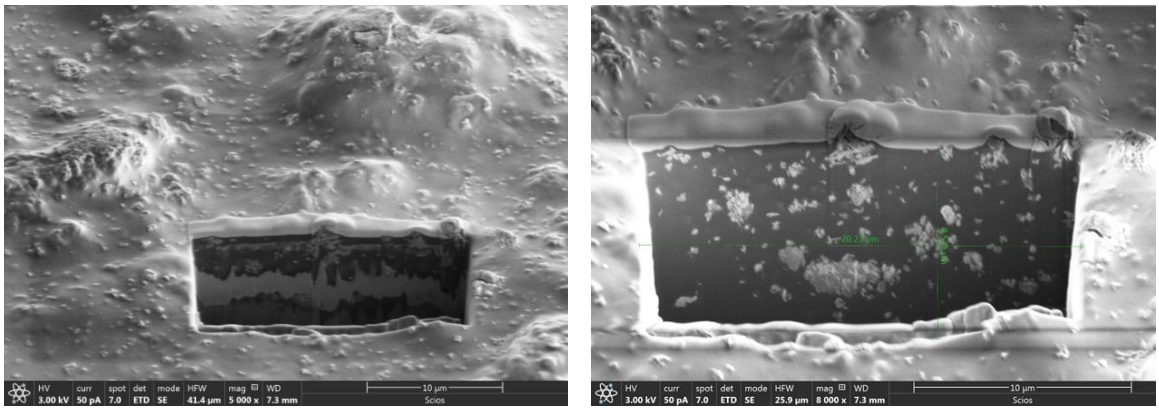

Figure 6.16: SEM images of the polymer film was a cross section removed (left) and magnified image of the cross section (right).

The nitric oxide production of the initial zeolite/polyurethane films was assessed using the NOA. A range of zeolites and zeolite masses were used in an attempt to observe the NO production, as discussed in table 6.1 in section 6.3.4. The data for two of the samples can be seen in figures 6.17 and 6.18.

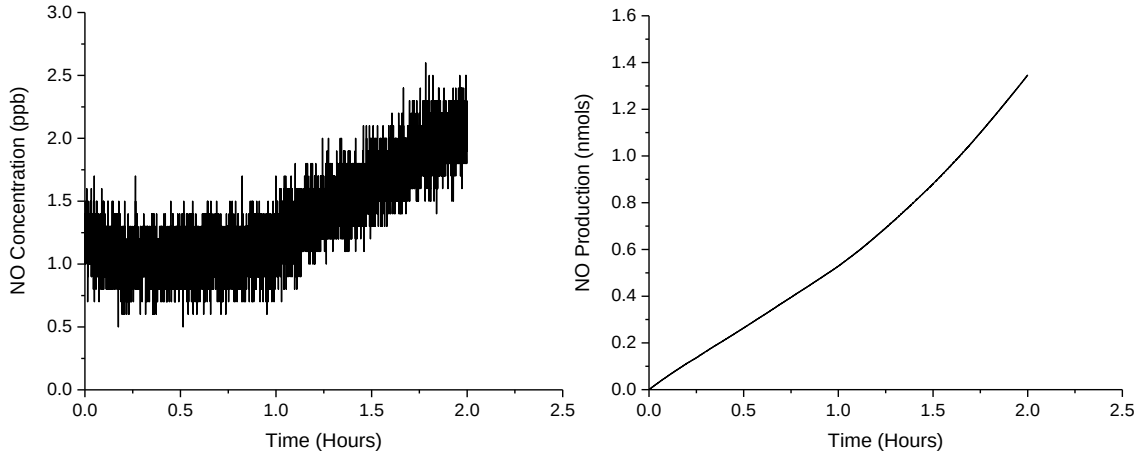

Figure 6.17: ZSM-5/polyurethane film release profile and NO production.

The 10 wt% ZSM-5 sample is shown in figure 6.17, with NO concentrations of 1 – 2 ppb obtained and a NO production of 1.4 nmols. These are similar values to what you would expect from the background levels of the NOA that sit somewhere between 0 and 5 ppb.

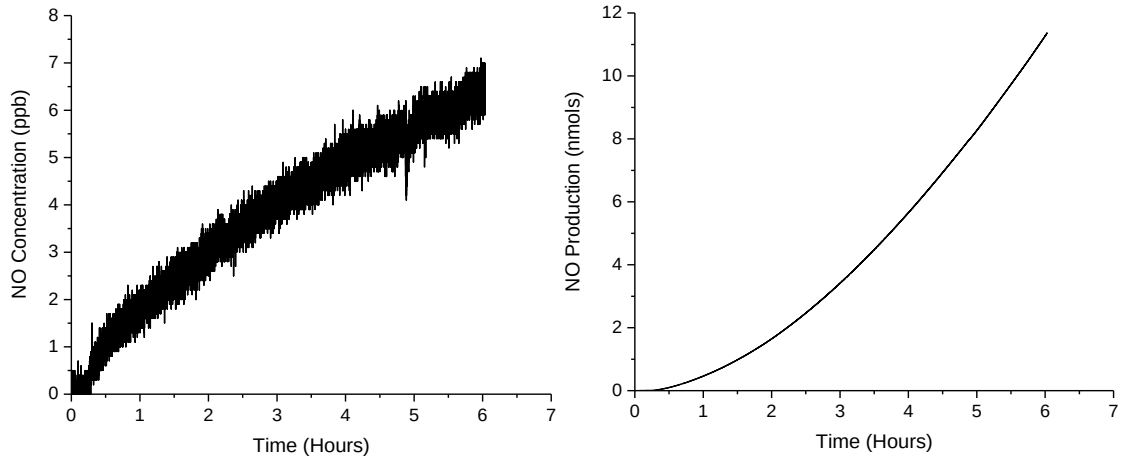

Figure 6.18: UZM-4/polyurethane film release profile and NO production.

The 20 wt% UZM-4 sample in figure 6.18 shows slightly more promise than the previous sample, with NO concentration reaching 7 ppb and a total production of 12 nmols. This, however, is after 6 hours, indicating a very slow NO production. Overall, the NO production from the zeolite/polyurethane films was very low. Therefore, it was considered that the best route may be to explore different polymers.

6.4.3.2. Polyvinylchloride Films

The polyvinylchloride/dioctyl sebacate film was considered after the limited NO production from the polyurethane films. The cast zeolite/PVC film was less flexible than the PU films, even with the plasticiser addition. The NO production was assessed in the same way by use of the NOA.

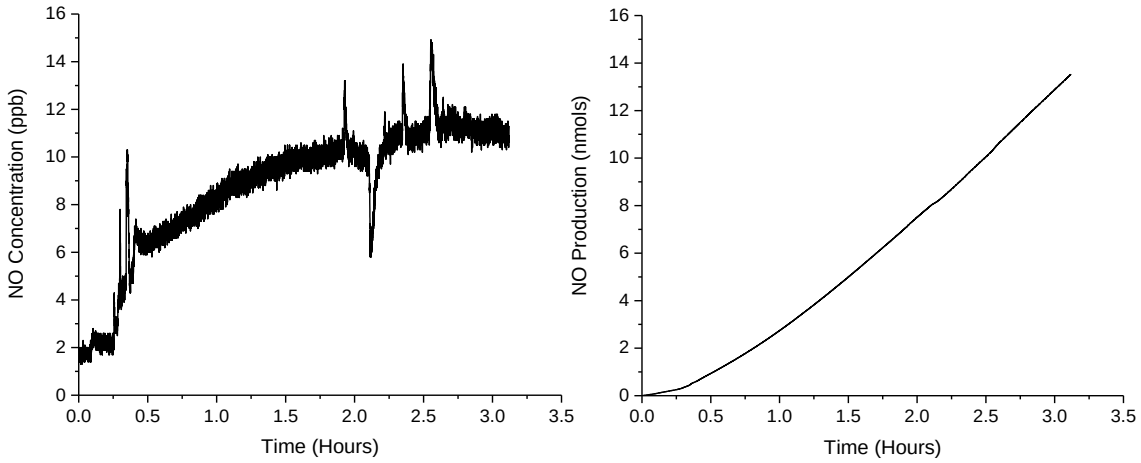

Figure 6.19: UZM-4/polyvinylchloride film release profile and NO production.

The NO production can be seen in figure 6.19, where concentrations of 10 -12 ppb and a total production of 14 nmols were obtained. While these values are greater than those from the polyurethane films, they are still rather low.

The decrease in NO production from the zeolite powders (chapter 5) to the zeolite/PVC polymer films suggest that the polymer may be preventing access to the copper active sites. Polyurethane and polyvinylchloride are both relatively flexible polymers and therefore tend to pack tightly together in a polymer film. The lack of NO production suggests that the substrate molecules may be failing to reach the active sites, especially since the sacrificial reductant, cysteine, is a relatively large molecule. To probe this theory, a new type of polymer was considered. Polymers of intrinsic microporosity (PIMs) contain intermolecular voids that make them an ideal candidate to study the effect of copper site accessibility.

6.4.3.3. Polymers of Intrinsic Microporosity (PIMs)

Three types of PIM were used to make films with each of the five copper zeolites, they were PIM-1, EA-TB(Me) and EA-TB(H_2). The attempts at coating the stainless steel clip with EA-TB(H_2) proved troublesome due to the powdery nature of the PIM. The zeolite/polymer film was too fragile and therefore easily crumbled off the clip, for this reason, only the PIM-1 and EA-TB(Me) PIMs were used for zeolite incorporation and subsequent NO testing. An example of a zeolite/PIM coated stainless steel clip is shown in figure 6.20.

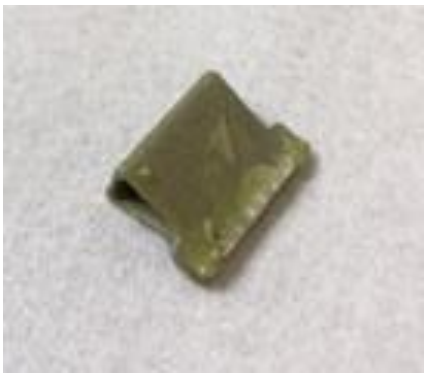

Figure 6.20: Stainless steel clip acting as a "stent model", with a zeolite/PIM coating.

Table 6.4 provides the masses of each of the zeolite/PIM clip coatings, where 20 wt% of zeolite was used in each case. Due to the dipping nature of the clip coatings, it was near impossible to provide the exact same zeolite/PIM covering on each clip, therefore difference measurements were used to determine the mass of coating on the clip. The most important measurement was the mass of zeolite in the film, which was calculated by 20 wt% of the film mass.

Once all the clips were prepared, the NO production was assessed by the NOA. The catalytic tests were run three times where the same coated clip was washed with Milli-Q water and dried in between each run. The PIM-1 results are shown first, followed by the EA-TB(Me) results. The order of the three runs follows black as the first run, red as the second run and blue as the third.

Table 6.4: The polymer and zeolite masses of the final PIM films coated on the "stent model".					
Initial Clip Mass (mg)	**Polymer**	**Zeolite**	**Coated Mass (mg)**	**Film Mass (mg)**	**Zeolite Mass (mg)**
762	PIM-1	UZM-4	810	48	9.6
730	EA-TB(Me)	UZM-4	779	49	9.8
772	PIM-1	FER	849	77	15.4
738	EA-TB(Me)	FER	793	55	11
799	PIM-1	ZSM-5	860	61	12.2
750	EA-TB(Me)	ZSM-5	796	46	9.2
799	PIM-1	MOR	862	63	12.6
759	EA-TB(Me)	MOR	813	54	10.8
750	PIM-1	SSZ-13	815	65	13
744	EA-TB(Me)	SSZ-13	798	54	10.8

The ZSM-5/PIM-1 results, figure 6.21, show NO concentration peaking between 7 and 11 ppb, a relatively low concentration of NO. This provides 20 – 35 nmols over the 8 – 10 hour runs. The three runs runs are similar, suggesting reproducibility.

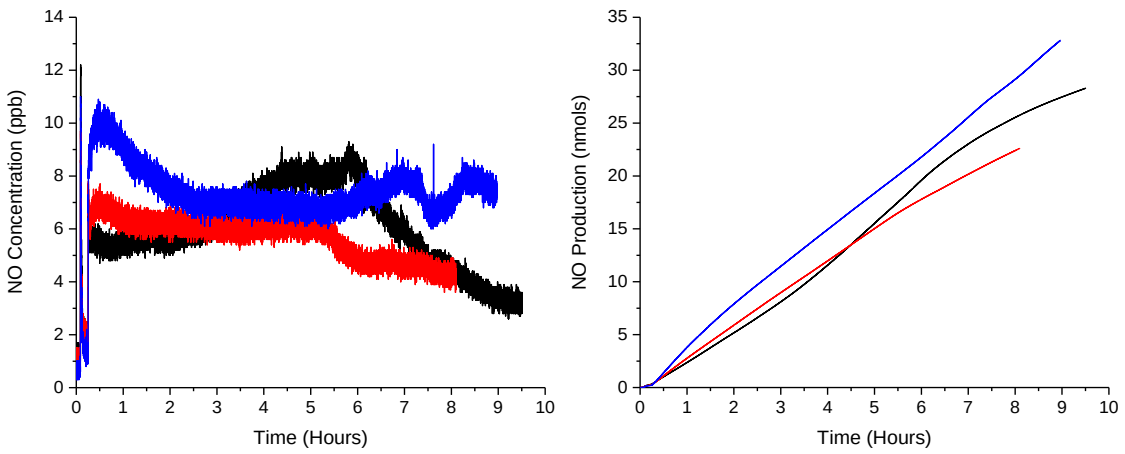

Figure 6.21: ZSM-5/PIM-1 coated clip initial run (black), 1st recycling (red) and 2nd recycling (blue) release profiles and NO production.

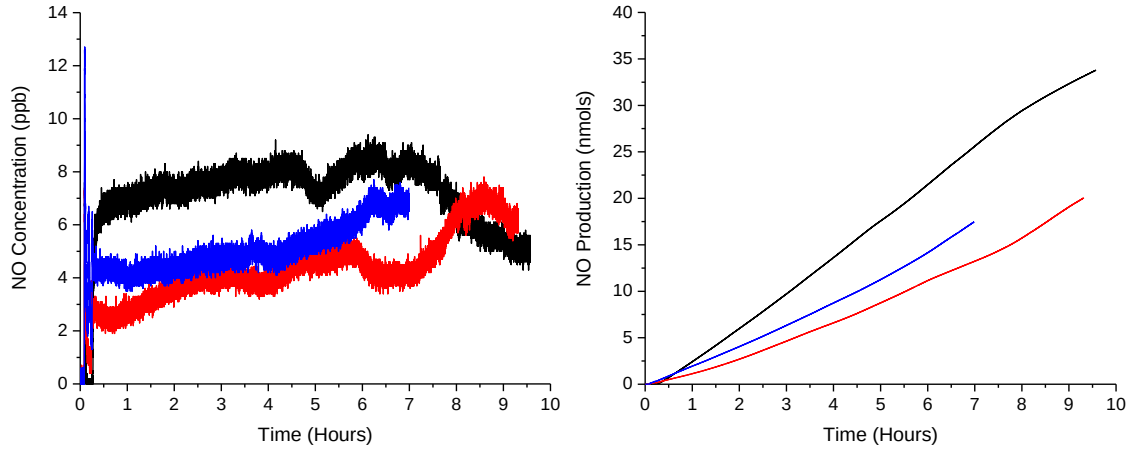

Figure 6.22: SSZ-13/PIM-1 coated clip initial run (black), 1st recycling (red) and 2nd recycling (blue) release profiles and NO production.

The SSZ-13/PIM-1 runs, figure 6.22, produced peak NO concentrations between 6 and 9 ppb, again very low values. The total production for the 7 – 10 hour runs was between 15 and 30 nmols. The three runs vary slightly, with the black initial run performing best.

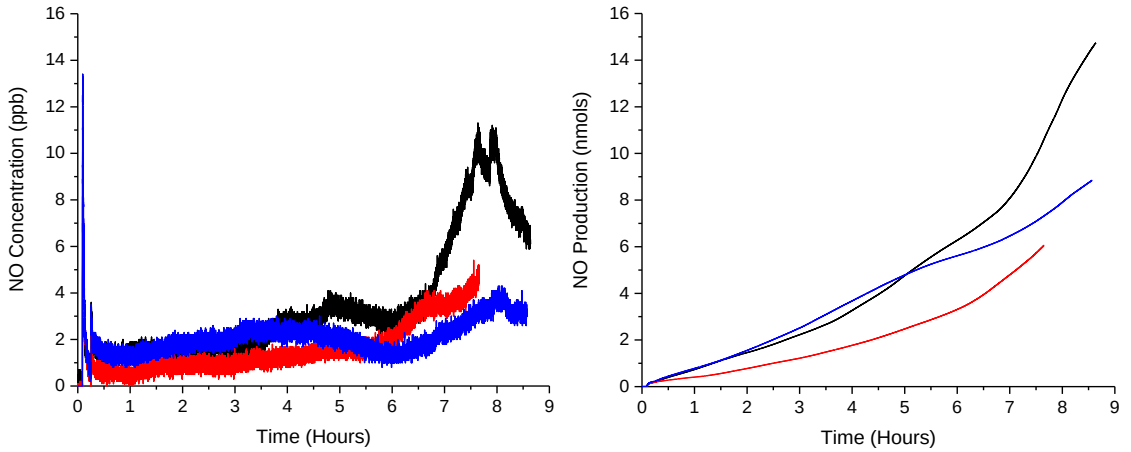

Figure 6.23: MOR/PIM-1 coated clip initial run (black), 1st recycling (red) and 2nd recycling (blue) release profiles and NO production.

The NO concentration values for MOR/PIM-1 are very low, figure 6.23, suggesting that there is perhaps no NO production from the polymer film. There is a spike in concentration for the black run around 7 hours into the run, this is most likely due to the needle of the NOA set-up being knocked and causing a spike.

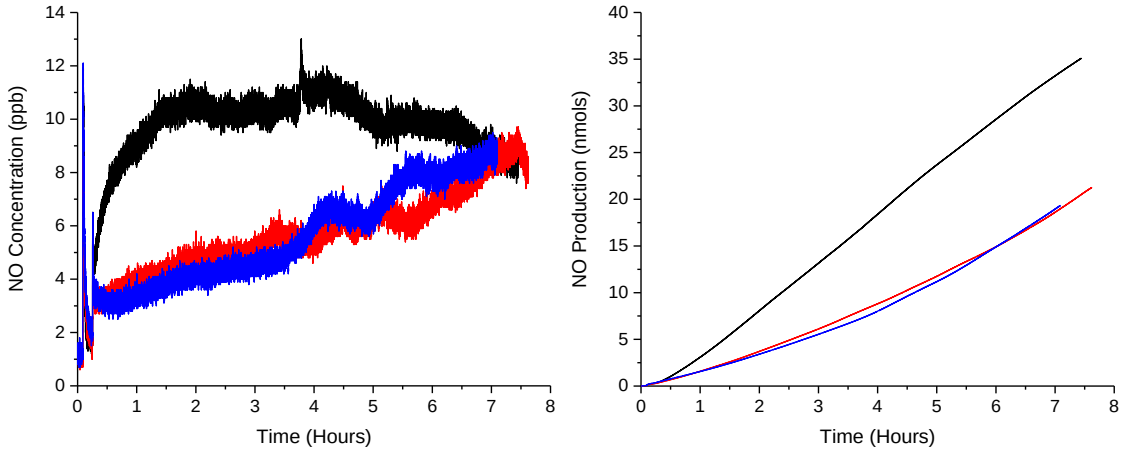

Figure 6.24: FER/PIM-1 coated clip initial run (black), 1st recycling (red) and 2nd recycling (blue) release profiles and NO production.

The three runs for FER, figure 6.24, show the black run with NO concentration around 10 – 12 ppb and a total production of 35 nmols, but the red and blue runs with NO concentrations increasing from 3 to 9 ppb and a total production of 20 nmols.

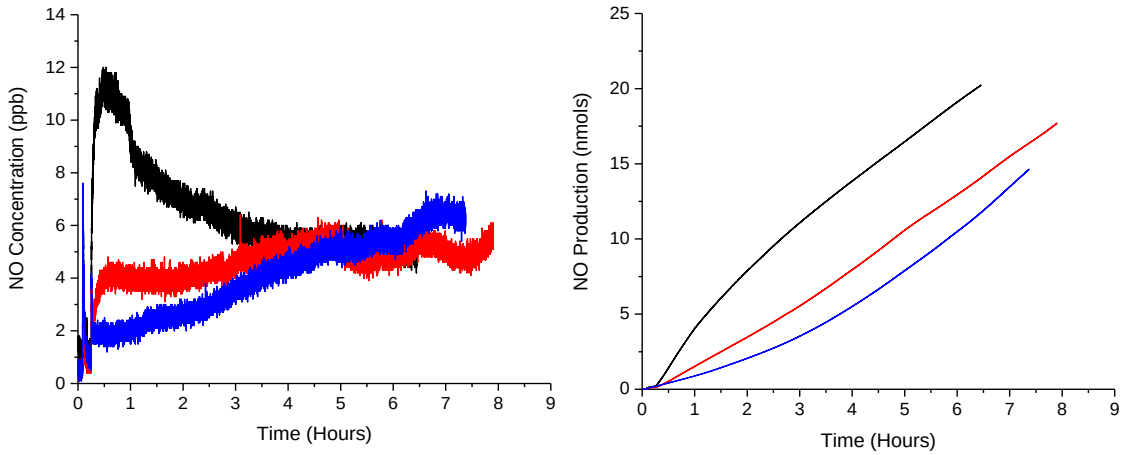

Figure 6.25: UZM-4/PIM-1 coated clip initial run (black), 1st recycling (red) and 2nd recycling (blue) release profiles and NO production.

The black run of UZM-4/PIM-1, figure 6.25, has a peak concentration around 12 ppb, which decreases over time, giving a total production of 20 nmols. The red and blue run are similar to each other, with NO concentrations of 2 – 6 ppb and total productions of 18 and 14 nmols respectively.

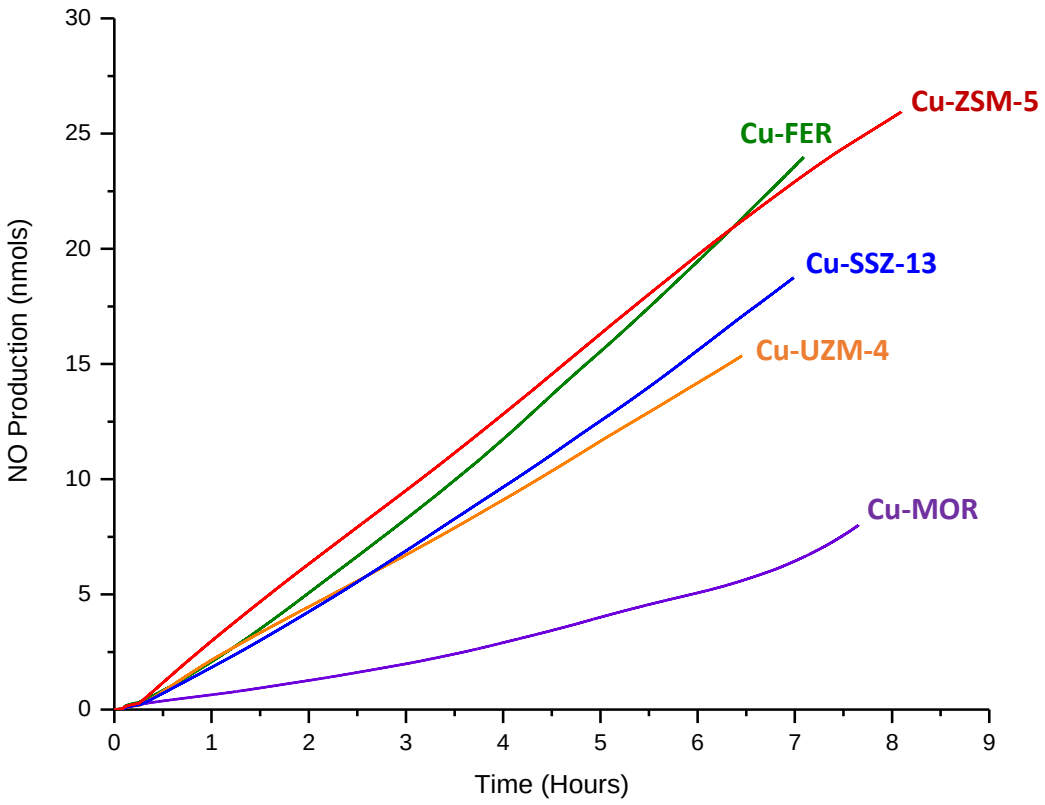

Figure 6.26: Comparison of average NO production of all PIM-1 coated clips. SSZ-13 (blue), ZSM-5 (red), UZM-4 (orange), mordenite (purple) and ferrierite (green).

The averages of the three runs for the PIM-1 coated clips, figure 6.26, placed mordenite as the lowest NO production, followed by SSZ-13 and UZM-4, and lastly ZSM-5 and ferrierite as the highest NO production. An issue with the PIM-1 data, is that a lot of the runs produced low levels of NO, which are similar to that of the background levels of the NOA. Therefore, it is difficult to separate contributions from the zeolite/PIM-1 film and the background. For that reason, the data for the PIM-1 films may contain a large degree of error.

The EA-TB(Me) films generally performed a lot better than the PIM-1 films, with the NO concentration and production data for the three runs presented hereafter.

The ZSM-5/EA-TB(Me) coated clip, figure 6.27, produced a peak of 70 ppb in NO concentration and a total production of 130 nmols on the first run. This, however, was not continued with the second and third runs, with the NO concentration and production dropping drastically, producing 65 and 35 nmols respectively.

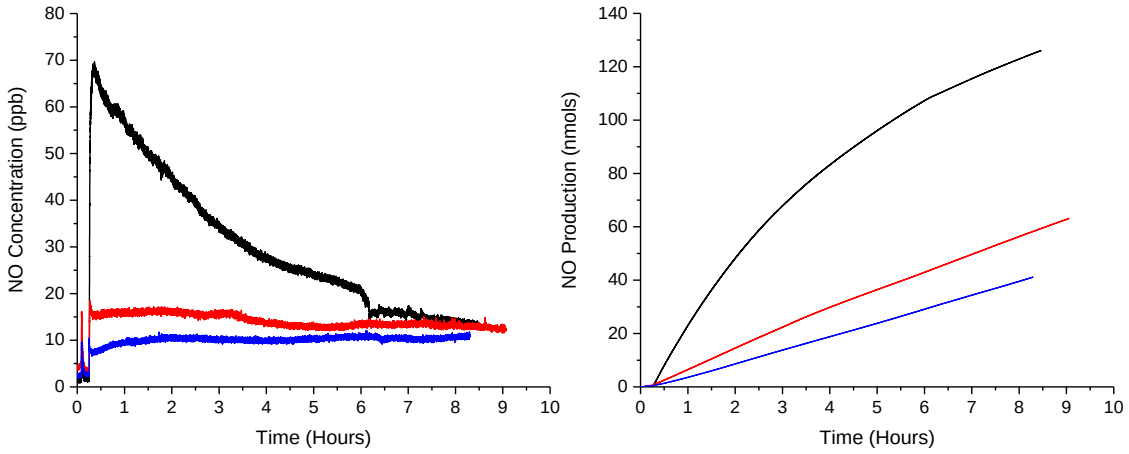

Figure 6.27: ZSM-5/EA-TB(Me) coated clip initial run (black), 1st recycling (red) and 2nd recycling (blue) release profiles and NO production.

One possibility for the reduced production after the initial run, could be the blocking of some of the EA-TB(Me) intermolecular voids by cystine. Cystine is the disulphide molecule formed by the oxidation of cysteine, that will form during the first run. The cystine molecules may be trapped within the PIM and therefore not removed when the sample is washed with water in between runs, due to its low solubility in water.[13]

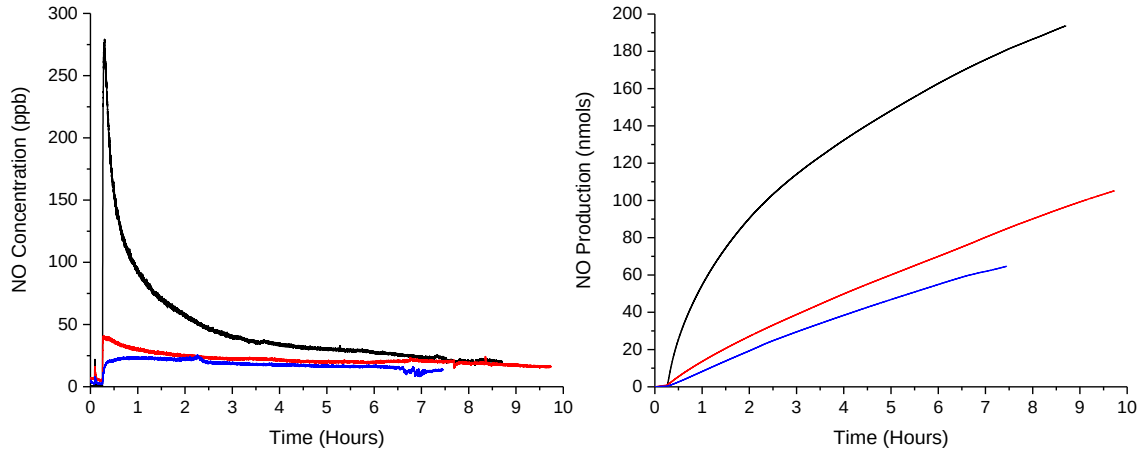

Figure 6.28: SSZ-13/EA-TB(Me) coated clip initial run (black), 1st recycling (red) and 2nd recycling (blue) release profiles and NO production.

The SSZ-13/EA-TB(Me) data, figure 6.28, shows the same drop in NO production as ZSM-5/EA-TB(Me), with the second and third runs producing considerably less NO than the first. The first run peaked around 280 ppb and produced a total of 190 nmols in the 8.5 hour run, a greater amount than the ZSM-5 sample. The second and third runs produced around 100 and 60 nmols of NO respectively.

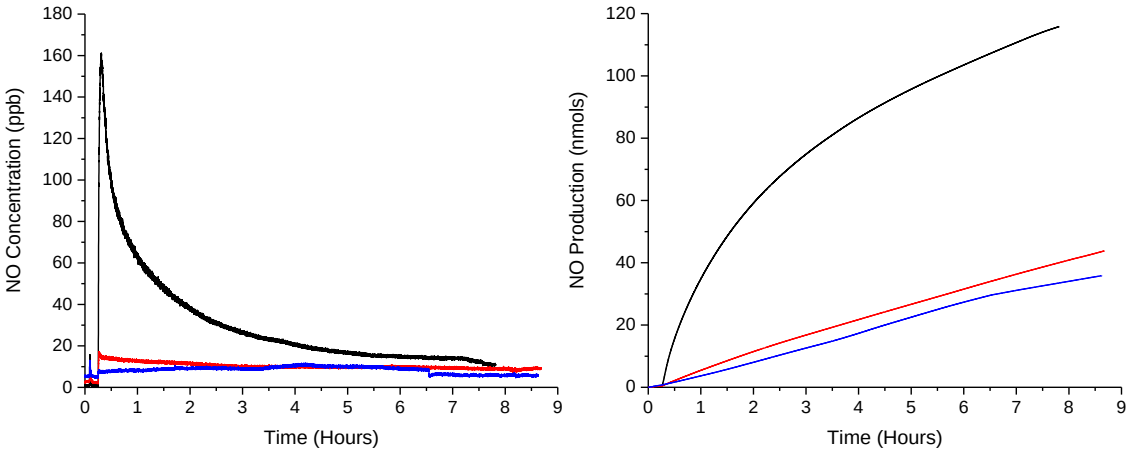

Figure 6.29: MOR/EA-TB(Me) coated clip initial run (black), 1st recycling (red) and 2nd recycling (blue) release profiles and NO production.

The NO production difference between the first and the second two runs is again observed with MOR/EA-TB(Me), figure 6.29. There is a significant drop from 115 nmols of NO to 30 – 40 nmols. The mordenite production from the first run is the lowest of all the zeolite/EA-TB(Me) films first run on the NOA.

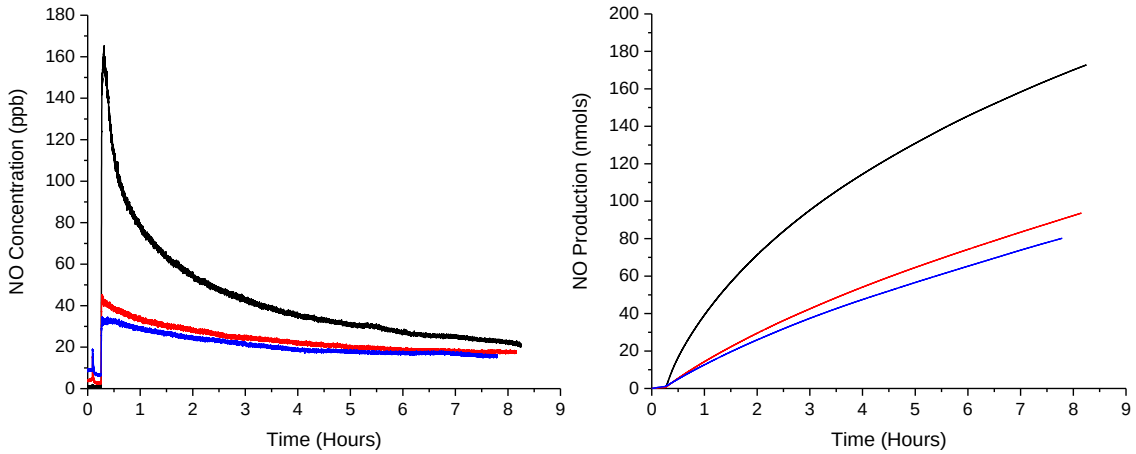

Figure 6.30: FER/EA-TB(Me) coated clip initial run (black), 1st recycling (red) and 2nd recycling (blue) release profiles and NO production.

The FER/EA-TB(Me) data, figure 6.30, has a NO concentration peak of 160 ppb for the first run and a NO production corresponding to 180 nmol in the 8.5 hour period. Again, the second and third runs are significantly lowered. The Cu-FER performs surprisingly well considering the relatively low initial NO production from the powder Cu-FER studies in chapter 5.

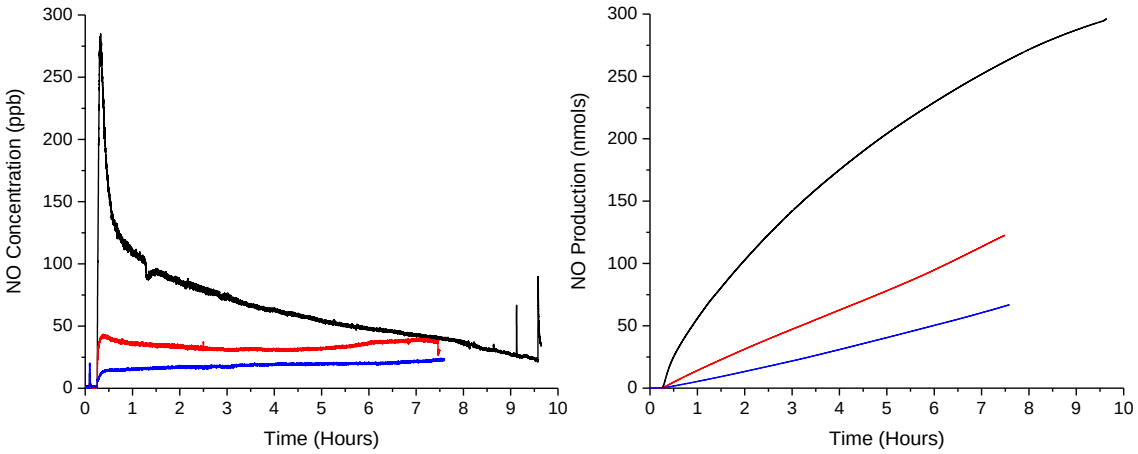

Figure 6.31: UZM-4/EA-TB(Me) coated clip initial run (black), 1st recycling (red) and 2nd recycling (blue) release profiles and NO production.

As expected, the UZM-4 data also shows the change in NO production after the first run, figure 6.31, therefore completing this observation for all five of the zeolite/EA-TB(Me) films. The first run of the UZM-4/EA-TB(Me) polymer produced a maximum NO concentration of 280 ppb and a total production of nearly 300 nmols during the 10-hour run, the highest of all the zeolite/EA-TB(Me) films. There appears to be a reasonable difference between the second and third run also, with around 120 nmols and 50 nmols produced respectively, suggesting further void blocking may be occurring.

The average NO production of the three runs for the zeolite/EA-TB(Me) films is presented in figure 6.32. The results placed UZM-4 with the highest NO production, followed by SSZ-13 and ferrierite with similar levels of NO and lastly ZSM-5 and mordenite.

Since the mass of zeolite in each PIM film varies slightly, the nmols of NO/mg of zeolite were calculated to allow for a fair comparison of the different activities. Table 6.5 provides the nmols/mg for each of the runs and the average of these values for both the PIM-1 films and the EA-TB(Me) films.

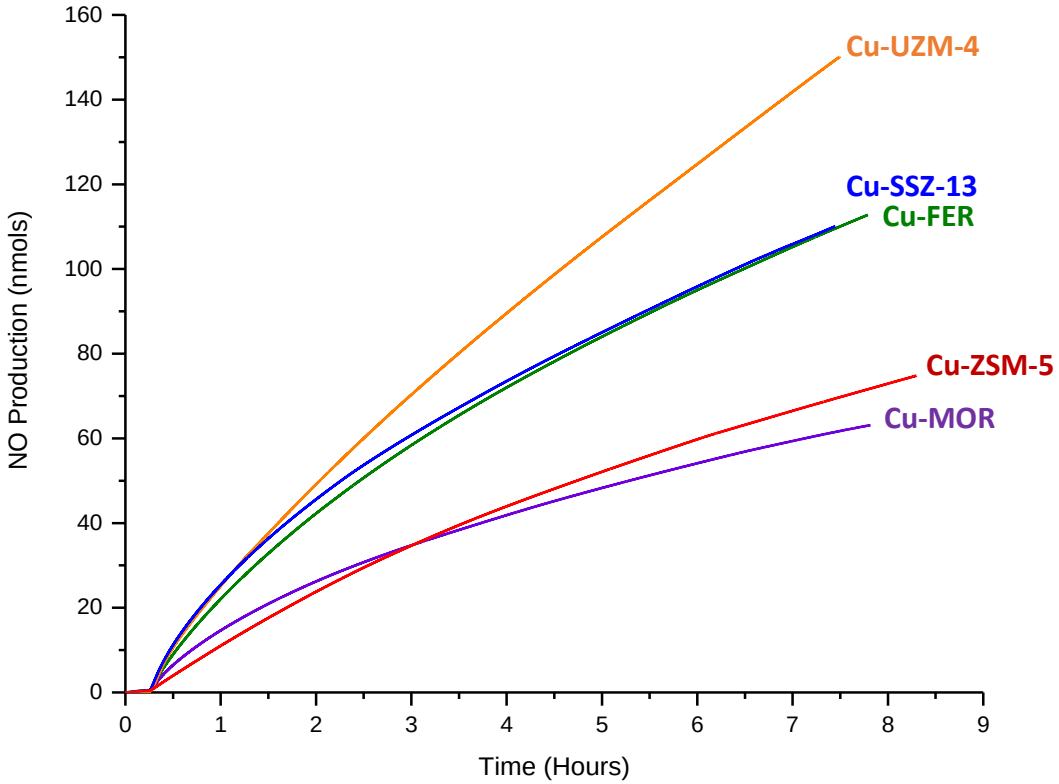

Figure 6.32: Comparison of average NO production of all EA-TB(Me) coated clips. SSZ-13 (blue), ZSM-5 (red), UZM-4 (orange), mordenite (purple) and ferrierite (green).

For all of the zeolites, the EA-TB(Me) film produced a higher amount of NO than the PIM-1 film counterpart. This is likely an effect of the greater surface area of the EA-TB PIM than PIM-1, with values of 1028 and 780 m^2g^{-1} respectively.[14,15] The permeability of the PIMs will also play a large role, with the permeability of N_2 measuring 525 – 580 Barrer for EA-TB and 252 Barrer for PIM-1, this increased permeability will allow greater access for the substrates and the subsequent release of produced NO.[14,16,17]

The ordering of the zeolites varies slightly between the two different PIMs. The PIM-1 ordering, from lowest to highest production is: MOR, FER, SSZ-13=UZM-4 and ZSM-5, whereas for EA-TB(Me), the ordering is: MOR, ZSM-5, FER, SSZ-13 and UZM-4. The main difference comes from ZSM-5 which has the highest production with PIM-1 and second lowest with EA-TB(Me).

Table 6.5: The nmols of NO/mg of zeolite for each of the zeolite/PIM film NO runs.				
Sample	**nmols/mg Run 1**	**nmols/mg Run 2**	**nmols/mg Run 3**	**nmols/mg Average**
PIM-1/UZM-4	2.11	1.84	1.53	1.83
EA-TB(Me)/ UZM-4	30.2	12.5	6.83	16.51
PIM-1/FER	2.28	1.38	1.26	1.64
EA-TB(Me)/FER	15.7	8.51	7.29	10.5
PIM-1/ZSM-5	2.32	1.85	2.69	2.29
EA-TB(Me)/ZSM-5	13.7	6.86	4.48	8.35
PIM-1/MOR	1.17	0.48	0.7	0.78
EA-TB(Me)/MOR	10.7	4.06	3.32	6.03
PIM-1/SSZ-13	2.6	1.54	1.34	1.83
EA-TB(Me)/SSZ-13	17.9	9.74	5.99	11.21

The general orders are similar to the NO production from the zeolite powders that were observed in chapter 5, with MOR having a low production and UZM-4 and SSZ-13 having a high production. The high NO production from SSZ-13 and UZM-4 is likely related to the 3D nature of the framework allowing greater substrate access to the active sites. This is similar reasoning for the low NO production from MOR which has a 2D framework and therefore limited access to the copper sites. The slight difference of the Cu-ZSM-5 is most likely due to the fact that the Zeolyst ZSM-5 was used in chapter 5, whereas in this chapter, synthesised ZSM-5 has been used. The industrial process will be well executed to produce well-defined zeolite crystals, but the small-scale lab synthesis may contain defects. Further analytical techniques, such as N_2 adsorption, may be useful to confirm this theory, but it would explain the high level of NO production from Cu-ZSM-5 in the powders but lower levels from the EA-TB (Me) polymer films.

6.5. Conclusions

The flow studies highlighted the potential for the copper zeolites to produce a steady rate of NO in a therapeutic range. The obtained NO concentrations (0.5 – 5 µM) were considerably higher than physiological concentrations (100 pM – 5 nM), but this difference also coincided with the increased concentrations of the substrate in the flow studies. This suggests that the biological concentrations of substrate would produce NO in the desired biological range.

UZM-4 showed the highest levels of NO production with the initial studies, perhaps resulting from the large pores and 3D channel system allowing high accessibility for the substrate to the active sites. The recycled samples showed a rather different result with SSZ-13 and MOR producing the highest levels. The data from SSZ-13 however, was only performed in duplicate and produced two very different results, suggesting a high degree of error from the results. Whilst the change in zeolite performance may be due to copper leaching or blocking effects, it does raise awareness that the electrode set-up may not be as reliable as the NOA used in chapter 5. This is further backed-up by the lack of reproducibility from some of the triplicates.

The main positive from the initial and recycled flow studies was the continuous NO production from all five copper zeolites. The longer flow studies encountered some issues due to broken equipment, with three of the five Cu-zeolites tested by a one-electrode system as opposed to two. This change in system had an impact on the results, with Cu-FER and Cu-UZM-4, the two zeolites run on the two-electrode system, producing the best results. Consequently, it is hard to contribute the poor performances of the other three zeolites; Cu-MOR, Cu-ZSM-5 and Cu-SSZ-13, to the zeolite activities or to the experimental set-up. Considering the reasonable performance of all three zeolites in the initial and recycled studies it is more indicative of a set-up issue altering the performances in the long flow studies as opposed to a lack of activity.

Considering the polymer studies, a successful zeolite slurry incorporation method was determined that was used across the range of zeolites. While polyurethane, polyvinylchloride and PIM-1 all produced rather low NO concentrations, and EA-TB(H_2) proved to not be compatible for film coatings, EA-TB(Me) showed initial promise with high

NO concentrations. Recycling of the EA-TB(Me) films revealed a decrease in activity that may be due to blocked polymer voids, while not ideal, the NO production was still significantly higher than any other polymer that was assessed. This places EA-TB(Me) as the current best candidate for the polymer support.

The zeolite ordering remained similar to that of the Cu-zeolite powders in chapter 5, with the 3D channel system zeolites generally performing better than the 2D channel systems. The main outlier came from ZSM-5, this was assigned to the fact that a different ZSM-5 source was used in this chapter. Overall, the UZM-4/EA-TB(Me) polymer film performed best as a NO producing catalyst.

6.6. Future Work

The flow studies and polymer incorporation are both rather preliminary results. With a replacement electrode, it would be useful to perform long flow runs of SSZ-13, mordenite and ZSM-5 with the two-electrode set-up as opposed to just one-electrode, this would allow a more accurate comparison of the zeolites. Variation of the stock solution concentrations would also be of interest, to reduce the cysteine and nitrite levels to be closer to biological values and observe the difference in NO concentration.

The possible blockage of the EA-TB(Me) film with the cystine molecule would be of great interest to study further. The use of N_2 adsorption measurements before and after catalysis may help to understand any pore blockages that are limiting access to the zeolite. A range of zeolite loadings would also be of interest, to observe the optimal loading for NO production. Lastly, polymer incorporation with the Zeolyst ZSM-5 would help to understand any difference between the industrially prepared and lab-synthesised ZSM-5.

6.7. References

1 Y. Ozkan, E. Ozkan and B. Simsek, *Int. J. Cardiol.*, 2002, **82**, 269–277.

2 B. De Chiara, V. Sedda, M. Parolini, J. Campolo, R. De Maria, R. Caruso, G. Pizzi, O. Disoteo, C. Dellanoce, A. R. Corno, G. Cighetti and O. Parodi, *Sci. World J.*, 2012, **2012**, 1–7.

3 J. O. Lundberg and E. Weitzberg, *Arterioscler. Thromb. Vasc. Biol.*, 2005, **25**, 915–

922.

4 K. Namekawa, M. Tokoro Schreiber, T. Aoyagi and M. Ebara, *Biomater. Sci.*, 2014, **2**, 674–679.

5 B. Libby, W. H. Smyrl and E. L. Cussler, *AIChE J.*, 2003, **49**, 991–1001.

6 K. Ramasubramanian, M. A. Severance, P. K. Dutta and W. S. W. Ho, *J. Colloid Interface Sci.*, 2015, **452**, 203—214.

7 H. Robson and K. P. Lillerud, in *Verified Syntheses of Zeolitic Materials*, Elsevier Science, Amsterdam, 2001, pp. 198–200.

8 M. J. Neufeld, B. R. Ware, A. Lutzke, S. R. Khetani and M. M. Reynolds, *ACS Appl. Mater. Interfaces*, 2016, **8**, 19343–19352.

9 J. S. Stamler, O. Jaraki, J. Osborne, D. I. Simon, J. Keaney, J. Vita, D. Singel, C. R. Valeri and J. Loscalzo, *Proc. Natl. Acad. Sci.*, 1992, **89**, 7674–7677.

10 C. N. Hall and J. Garthwaite, *Nitric Oxide*, 2009, **21**, 92–103.

11 P. S. Wheatley, A. R. Butler, M. S. Crane, S. Fox, B. Xiao, A. G. Rossi, I. L. Megson and R. E. Morris, *J. Am. Chem. Soc.*, 2006, **128**, 502–509.

12 M. Mowbray, X. Tan, P. S. Wheatley, R. E. Morris and R. B. Weller, *J. Invest. Dermatol.*, 2008, **128**, 352–360.

13 M. Grieff and D. A. Bushinsky, in *Nutritional Management of Renal Disease*, Academic Press, 2013, pp. 699–709.

14 M. Carta, R. Malpass-Evans, M. Croad, Y. Rogan, J. C. Jansen, P. Bernardo, F. Bazzarelli and N. B. McKeown, *Science*, 2013, **339**, 303–307.

15 M. Carta, K. J. Msayib, P. M. Budd and N. B. McKeown, *Org. Lett.*, 2008, **10**, 2641–2643.

16 M. Carta, M. Croad, R. Malpass-Evans, J. C. Jansen, P. Bernardo, G. Clarizia, K. Friess, M. Lanč and N. B. McKeown, *Adv. Mater.*, **26**, 3526–3531.

17 P. Li, T. S. Chung and D. R. Paul, *J. Memb. Sci.*, 2013, **432**, 50–57.

Chapter 7: ADORable Catalysts

7.1. Aim

In this thesis so far, a range of aluminosilicates have been studied for nitric oxide (NO) production. In this chapter, a new family of zeolites is explored. The series of zeolites produced from the ADOR process of UTL gives a range of zeolites with similar layers but differing connecting units. The connecting units alter the size of the zeolite pores and generate a series of structures with varying ring sizes. This chapter aims to explore the use of these zeolites for catalysis to understand how the changing ring size influences the NO production.

7.2. Introduction

The general concept of the ADOR process was introduced in section 1.1.5. In this chapter, the focus will be based on the synthesis of Al-UTL and three daughter zeolites, Al-IPC-2, Al-IPC-4 and Al-IPC-6.

The first part of this project looked into the synthesis of Al-UTL, which is somewhat troublesome due to the small pH range that the Al-UTL forms.[1] The ideal pH range for the successful synthesis is 11.3 – 12, with lower values producing amorphous material and higher values forming an STF impurity. Furthermore, the aluminium content of the synthesis gel also affects the resulting UTL purity. An increase of aluminium past 1.5 mol % leads to a resulting mixture of STF and UTL, concentrations much past 2 mol % produce amorphous material. To add to this, the SDA required for the synthesis is different to that used for Ge-UTL, with 6,10-dimethyl-5-azoniaspiro[4,5]decane required for Ge-UTL and 7-ethyl-6-azoniaspiro[5.5]undecane required for Al-UTL.

The second part of the project looked at applying the ADOR process to form a series of isoreticular zeolites for catalysis. The production of three aluminated daughter zeolites will provide an insight into the effect of pore size of the catalysts on the NO production. The four zeolites studied, including the parent Al-UTL, are shown in figure 7.1 in the pure silica forms to understand the differing pore sizes down the series.

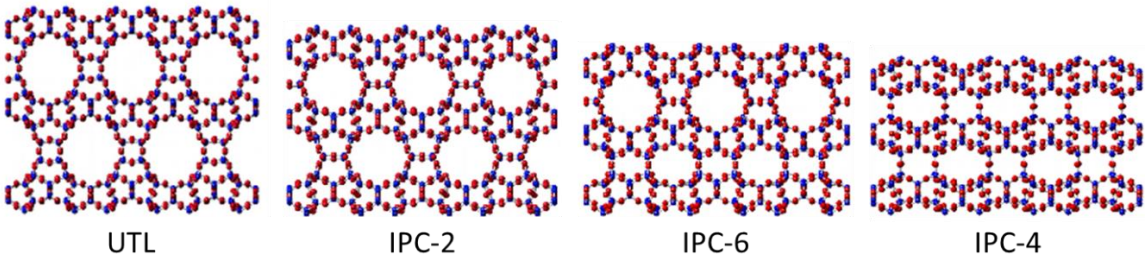

Figure 7.1: The four zeolites to be synthesised within this chapter that will allow the study on the effect of ring size on the NO production.[2]

The size of the UTL 14 and 12 rings are 9.5 x 7.1 Å and 8.5 x 5.5 Å respectively, the largest of the ADOR series studied. This is followed by IPC-2 with 12 rings of 6.6 x 6.2 Å and 10 rings of 5.4 x 5.3 Å. The second smallest rings come from IPC-6 with 12 and 10 rings the same size as IPC-2, as well as 10 and 8 rings of 5.8 x 3.8 Å and 4.5 x 3.6 Å respectively. The smallest rings are from IPC-4 with 10 and 8 rings of 5.8 x 3.8 Å and 4.5 x 3.6 Å also.

7.3. Experimental

7.3.1. Materials

The materials used for the SDA syntheses: 1,5-dibromopentane (97%, Sigma Aldrich), 1,4-dibromobutane (99 %, Sigma Aldrich), (2R,6S)-2,6-dimethylpiperidine (Sigma Aldrich), 2-ethylpiperidine (95 % Fluorochem), potassium carbonate (Fisher Scientific), acetonitrile (Fisher Scientific), ion-exchange resin (Ambersep® 900 hydroxide form, Sigma Aldrich) and diethylether (Sigma Aldrich).

Materials used in zeolite syntheses: Aluminium hydroxide (reagent grade, Sigma Aldrich), germanium dioxide (Alfa Aesar), Cab-O-Sil® (M-5, ACROS Organics), hydrochloric acid (Concentrated (dilutions performed as required), Fisher Scientific), aluminium nitrate nonahydrate (BDH Chemicals), octylamine (99 %, Sigma Aldrich) and acetic acid (100 %, VWR), diethoxydimethylsilane (ACROS Organics).

7.3.2. ADOR Process of Al-UTL

Two projects were completed that looked at the incorporation of aluminium into the ADOR process. The first was through the synthesis of Al-UTL that could be directly disassembled into Al-containing daughter zeolites. It was hoped that these ranging pore sizes of Al-containing zeolites could be used for catalytic NO production.

7.3.2.1. Synthesis of SDA for Al-UTL

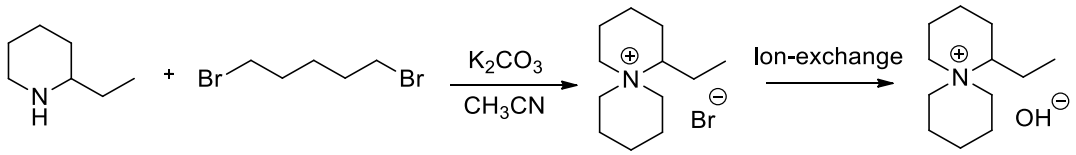

Scheme 7.1: The synthetic route to form 7-ethyl-6-azoniaspiro[5.5]undecane from 1,5-dibromopentane and 2-ethylpiperidine.

To synthesise Al-UTL, the SDA 7-ethyl-6-azoniaspiro[5.5]undecane was required, scheme 7.1. The synthesis was performed by adding 1,5-dibromopentane (25.6 mL, 188 mmol) dropwise to a solution of 2-ethylpiperidine (25 mL, 188 mmol), potassium carbonate (27.64 g, 200 mmol) and acetonitrile (120 mL). The solution was heated under reflux at 82 °C for three hours. Once cooled, the solution was filtered for potassium carbonate removal and the solvent reduced by rotary evaporation. Diethyl ether was added in portions to the solution to precipitate the SDA salt. The product was collected by filtration, washed with diethyl ether and dried in air. Once dry, a yield was calculated and NMR prepared in D_2O.

The prepared salt was in the bromide form, but the hydroxide salt was required for the zeolite synthesis. Ion-exchange resin was used to exchange the bromide ion to the hydroxide ion. The SDA was dissolved in distilled water (~ 270 mL) and stirred with ion-exchange resin (35 g), where the resin was changed daily for 10 days. A simple test using silver nitrate was performed to determine that the ion-exchange was complete. The resulting SDA solution was then titrated against hydrochloric acid (0.1 M) to determine the concentration.

7.3.2.2. Synthesis of Al-UTL

Two batches of Al-UTL were prepared.[1] The first dissolved aluminium hydroxide (0.029 g, 0.037 mmol) in the SDA solution (10.70 mL, 0.897 M, 9.60 mmol) and water (2.26 mL) with stirring. Germanium dioxide (1.002 g, 9.58 mmol) was added to the solution and stirred for 30 minutes, followed by the addition of Cab-O-Sil® (1.134 g, 1.89 mmol). Once a homogenous solution was obtained, it was split between two autoclaves. The pH of each was adjusted using concentrated hydrochloric acid, with sample (1) at pH 11.71 and sample (2) at pH 11.31. The two autoclaves were placed in the oven at 175 °C for 20 days.

Upon removal, the synthesis at pH 11.71 showed large rectangular crystals under the microscope, whereas the synthesis at pH 11.31 showed small poorly defined crystals, therefore it was placed back into the oven for a further 3 days.

The synthesis was repeated with a higher amount of aluminium within the synthesis gel. In this case, 0.044 g (0.056 mmol) of aluminium hydroxide was dissolved in the SDA solution. The other chemicals and masses all remained the same. Again, the solution was split between two autoclaves and the pH adjusted, with sample (3) measuring 12.01 and sample (4) measuring 11.04. The autoclaves were placed in the oven at 175 °C for the longer time of 28 days.

In both syntheses, the products were collected by filtration, washed with water and dried. PXRD patterns were recorded to determine the purity.

7.3.2.3. Disassembly of Al-UTL

The first step in the disassembly of Al-UTL was a calcination to remove the organic SDA from the pores. The samples were calcined at 575 °C for 7 hours, with a heating ramp of 1 °C/min. PXRD was used to confirm successful calcination.

The hydrolysis was performed by placing calcined Al-UTL (0.35 g) in hydrochloric acid (0.1 M, 50 mL) and heating under reflux at 95 °C overnight. The sample was collected by filtration and dried. PXRD was used to confirm successful hydrolysis.

7.3.3. Aluminium Incorporation During the ADOR Process

The second project considered the addition of aluminium during the ADOR process, focussing on the organisation step.[3] This was to generate a series of aluminated-daughter zeolites. To be able to compare the Al-daughter zeolites with a UTL sample, Al-UTL was synthesised once again. This time, however, a different approach was considered where synthesised Ge-UTL was converted to Al-UTL by an aluminium salt. To do this, a batch of Ge-UTL was first prepared.[4] This part of the project was completed in collaboration with Rachel Doyle as part of her 4th year research project. The majority of the following syntheses were performed by Rachel.

7.3.3.1. Synthesis of SDA for UTL

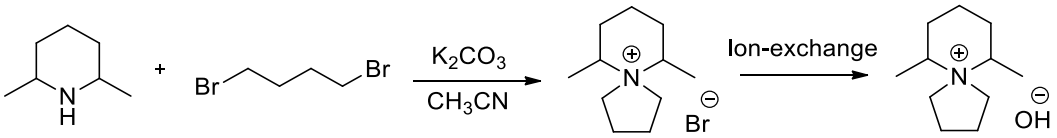

Scheme 7.2: The synthetic route to form 6,10-dimethyl-5-azoniaspiro[4,5]decane from 1,4-dibromobutane and 2,6-dimethylpiperidine.

The synthesis for the Ge-UTL SDA was extremely similar to that of the Al-UTL SDA. In the case of Ge-UTL, the SDA required was 6,10-dimethyl-5-azoniaspiro[4,5]decane, scheme 7.2. 1,4-dibromobutane (30.63 mL, 142 mmol) was added dropwise to a solution of 2,6-dimethylpiperidine (16.07 g, 142 mmol), potassium carbonate (19.63 g, 170.4 mmol) and acetonitrile (100 mL). The solution was heated under reflux at 95 °C for 16 hours. The remaining work-up and ion-exchange procedure was the same as that in section 7.3.2.1.

7.3.3.2. Synthesis of Ge-UTL

Cab-O-Sil® (0.61 g, 10 mmol) was added to a stirring solution of germanium dioxide (0.52 g, 5 mmol) and SDA solution (0.541 M, 11.30 mL, 6 mmol). Concentrated hydrochloric acid was added to adjust the pH within the range of 9.5 – 11.5. The resulting gel was transferred to an autoclave and heated at 175 °C for 7 – 10 days. The product was collected by filtration, washed with water and dried.

The synthesised UTL was calcined under the same conditions as the Al-UTL in section 7.3.2.3 to remove the SDA from within the pores. All subsequent calcinations in this section were performed under the same conditions.

7.3.3.3. Conversion of Ge-UTL to Al-UTL

Calcined UTL (0.2 g) and aluminium nitrate solution (1 M, 20 mL) were stirred together for 20 minutes, prior to addition to an autoclave. The autoclave was heated at 175 °C for 24 hours. The product was then collected by filtration and stirred with dilute hydrochloric acid (0.01 M, 10 mL) for 10 minutes to remove any extra-framework aluminium. The washed product was collected by filtration, washed with water and dried.

7.3.3.4. Synthesis of Al-IPC-1P from Ge-UTL

Calcined Ge-UTL (0.5 g), acetic acid (1 M, 75 mL) and aluminium nitrate solution (1 M, 50 mL) were heated under reflux at 90 °C for 16 hours. The product was collected by filtration.

7.3.3.5. Synthesis of Al-IPC-2

Al-IPC-1P (0.354 g), nitric acid (1 M, 3.54 g) and diethoxydimethylsilane (0.071 g, 0.48 mmol) were heated in an autoclave at 175 °C for 16 hours. The product was collected by filtration, washed with distilled water and calcined.

7.3.3.6. Synthesis of Al-IPC-4

Al-IPC-1P (0.304 g) was stirred in hydrochloric acid (**0.1 M**, 25 mL) for 10 minutes and filtered. It was then stirred with octylamine (10 mL, 60.5 mmol) at 60 °C for 16 hours. The resulting product was collected by filtration and calcined.

Al-IPC-4 was also produced with a slight variation to this method, relating to the hydrochloric acid concentration. A second batch of Al-IPC-1P (0.294 g) was stirred in hydrochloric acid (**0.01 M**, 20 mL) for 10 minutes. The following steps were the same as the previously discussed method.

7.3.3.7. Synthesis of Al-IPC-6

Calcined Ge-UTL (0.247 g), acetic acid (1 M, 37.5 mL) and aluminium nitrate (1.6 M, 25 mL) were heated under reflux at 90 °C for 16 hours. The resulting Al-IPC-1P was collected by filtration. This product was then heated with octylamine (10 mL, 60.5 mmol) at 60 °C for 16 hours. The solid was collected by filtration and calcined.

7.3.4. Acid Site Formation

Acid sites were formed in the Al-containing zeolites by a simple ion-exchange procedure followed by a calcination. The procedure is discussed in section 4.3.3 in chapter 4.

7.3.5. Catalytic Testing

The catalytic NO production was assessed by the nitric oxide analyser (NOA). The procedure is the same as that in section 4.3.4 in chapter 4.

7.4. Results and Discussion

7.4.1. ADOR Process of Al-UTL

The first step in preparing the Al-UTL was the synthesis of the SDA. Solution-state NMR confirmed that the product obtained was that of 7-ethyl-6-azoniaspiro[5.5]undecane.

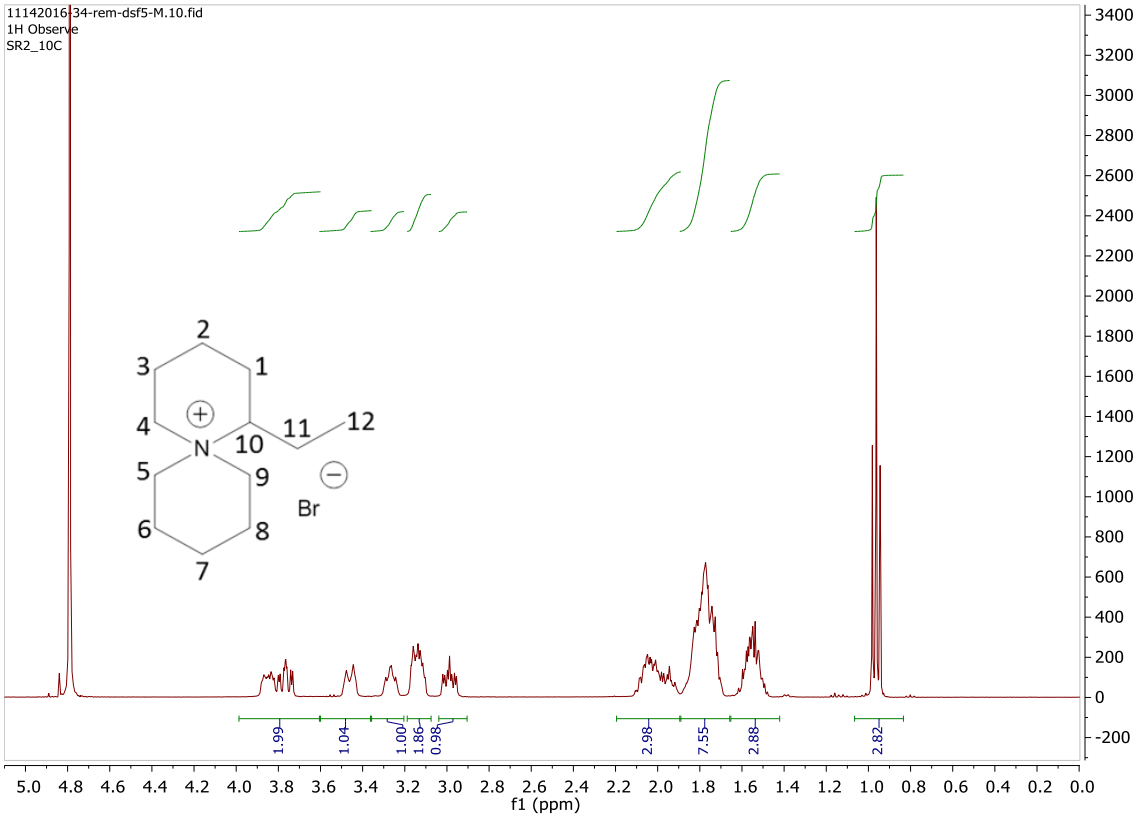

Figure 7.2: NMR spectrum of 7-ethyl-6-azoniaspiro[5.5]undecane.

^{1}H NMR (400 MHz, Deuterium Oxide) δ 3.94 – 3.66 (m, H_4), 3.46 (d, *J* = 13.2 Hz, H_{10}), 3.35 – 3.21 (m, H_9), 3.20 – 3.08 (m, H_5), 2.99 (ddd, *J* = 13.1, 8.8, 3.7 Hz, H_1), 2.19 – 1.90 (m, H_2), 1.90 – 1.67 (m, H_3, H_6, H_8 and H_{11}), 1.64 – 1.46 (m, H_7), 0.96 (t, *J* = 7.4 Hz, H_{12}).

The mass of SDA obtained was 32.97 g, providing a 67 % yield. The yield calculation is shown below:

$$Theoretical\ Yield = 188\ mmol\ \times 262.5\ gmol^{-1}$$

$$= 49.35\ g$$

$$Yield = \frac{32.97\ g}{49.35\ g} \times 100$$

$$= 66.8\ \%$$

Table 7.1: A summary of the synthesis conditions for the four batches of Al-UTL.		
Sample	**High or low Al?**	**pH**
1	Low (0.037 mmol)	11.71
2	Low (0.037 mmol)	11.31
3	High (0.056 mmol)	12.01
4	High (0.056 mmol)	11.04

The four batches of synthesised Al-UTL were assessed by PXRD, SEM and EDX. The samples and synthesis conditions are summarised in table 7.1. The PXRD patterns of the four products are compared with UTL in figure 7.3. A lack of crystallinity was observed from sample 3, with limited peaks and the presence of broader peaks. Samples 2 and 4, the low pH syntheses, showed the highest level of crystallinity amongst the samples, with peaks that matched well to the simulated UTL.

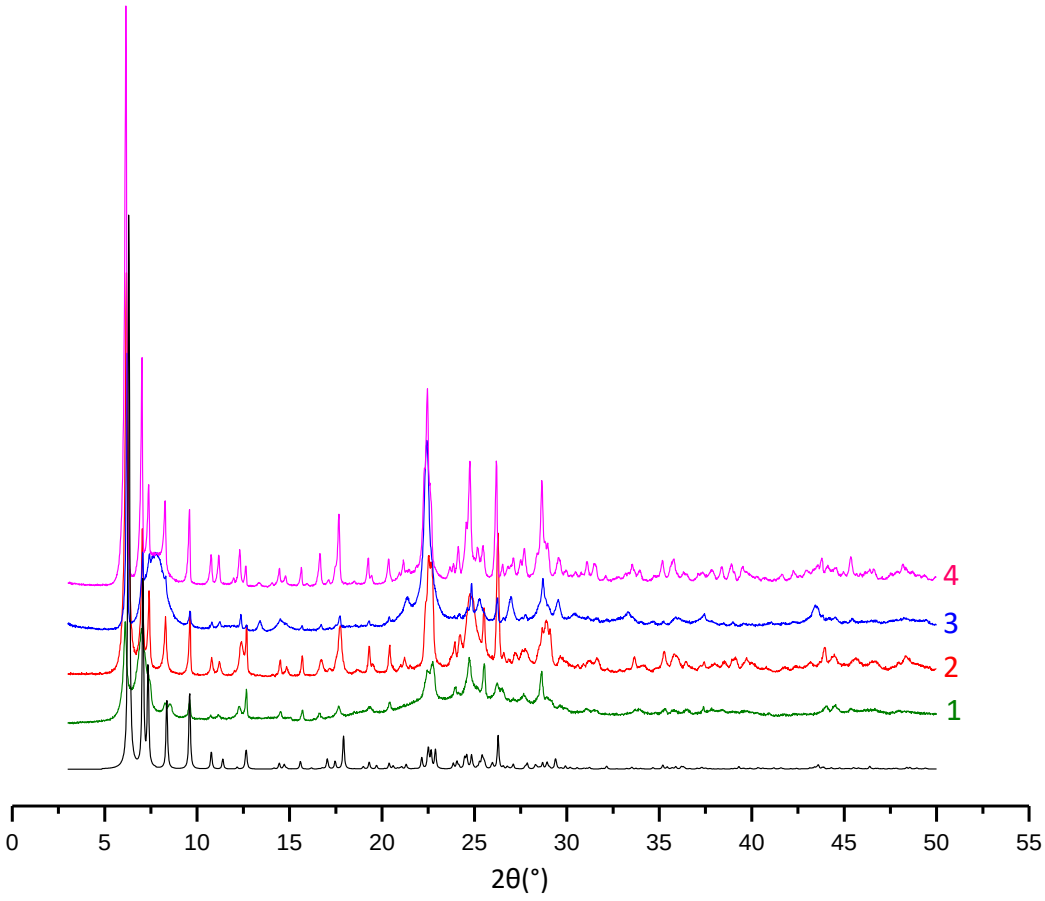

Figure 7.3: The PXRD patterns of the calcined Al-UTL samples compared with simulated UTL (black).

The SEM images of the two low aluminium syntheses are shown in figure 7.4. The high pH crystals (left) show a tombstone morphology with small crystals on the surface. Employing pin point EDX measurements, it was possible to determine the high aluminium content of the surface crystals. To remove the small crystals, the sample was sonicated and decanted. The low pH crystals (right) show a rounded tombstone morphology with no obvious presence of small surface crystals.

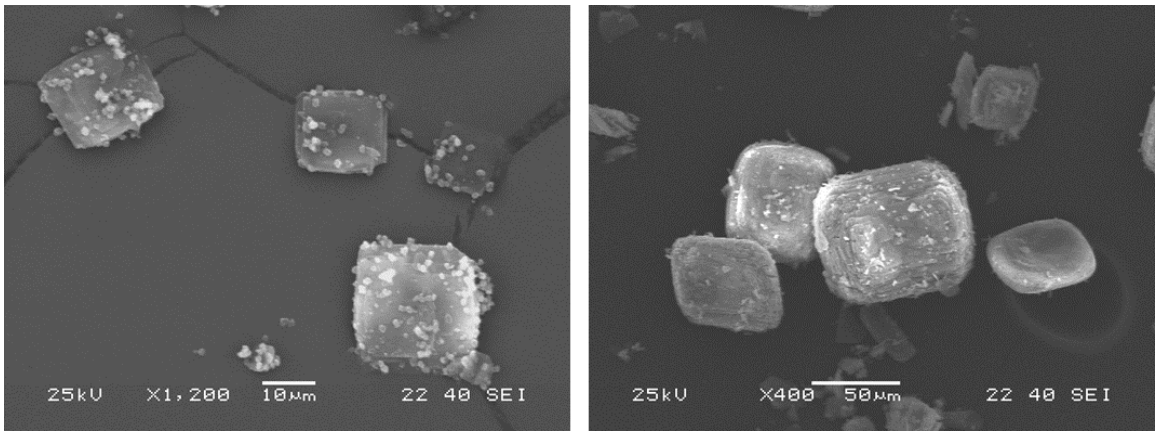

Figure 7.4: SEM images of Al-UTL samples 1 (left) and 2 (right).

The SEM images of the high aluminium syntheses, figure 7.5, show amorphous material produced from the high pH synthesis (left). The powdery material lacked any defined shape. The low pH synthesis (right) produced thin tombstone shapes with a lot of smaller crystals present. As with the small crystals observed previously, it was concluded by EDX measurements that the crystals were aluminium-containing.

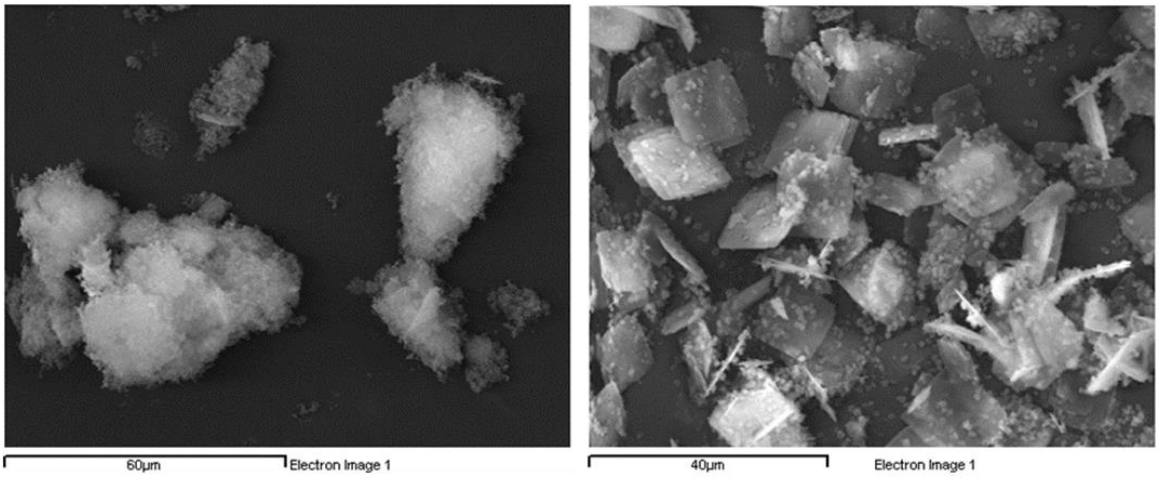

Figure 7.5: SEM images of Al-UTL samples 3 (left) and 4 (right).

EDX measurements were performed on the as-synthesised samples to determine the silicon, aluminium and germanium content, table 7.2. All samples contained aluminium, confirming the incorporation of aluminium either into or onto the UTL framework. The sonicated sample showed a dramatic decrease in aluminium, confirming that the small crystals observed by SEM had been removed and were aluminium-containing.

Table 7.2: EDX data of the four synthesised Al-UTL samples.

Sample	% Silicon	% Germanium	% Aluminium	Si/Al	Si/Ge
1	17.7 ± 5.1	3.5 ± 1.2	0.6 ± 0.3	29	5
1 (sonicated)	24.1 ± 3.2	5.4 ± 0.4	0.2 ± 0.1	113	4
2	27.4 ± 2.9	4.9 ± 0.5	0.6 ± 0.3	49	6
3	17.7 ± 2.9	2.1 ± 0.1	0.7 ± 0.1	25	8
4	19.1 ± 1.8	4.1 ± 0.3	0.4 ± 0.1	47	5

Considering the three methods of characterisation, it would appear that the low aluminium and low pH synthesis, sample 2, produced the best Al-UTL sample. A high crystallinity was observed by PXRD and the EDX data showed a reasonable level of aluminium at 0.6 %. The most interesting characterisation came from the SEM, with the low aluminium and low pH synthesis the only one that produced tombstone crystals without the obvious presence of smaller aluminium crystals. This suggests that the aluminium was incorporated into the framework as opposed to crystallising on the surface. The rounding of the crystals also suggests a higher presence of aluminium, as was previously observed with the single-crystal ferrierite in section 5.4.1.2.

Despite the differences in crystallinity and Si/Al ratios, all four zeolites were hydrolysed. The hydrolysis products were determined by PXRD, figure 7.6. The patterns showed the expected low angle peak around 8° which correlates to high d-spacing. This d-spacing is caused by the space between the layered IPC-1P material, suggesting all Al-UTL samples were successfully hydrolysed. The remainder of the PXRD pattern for the majority of the samples showed a lack of peaks compared to the simulated IPC-1P. This suggests that the layered material has been damaged during the hydrolysis procedure.

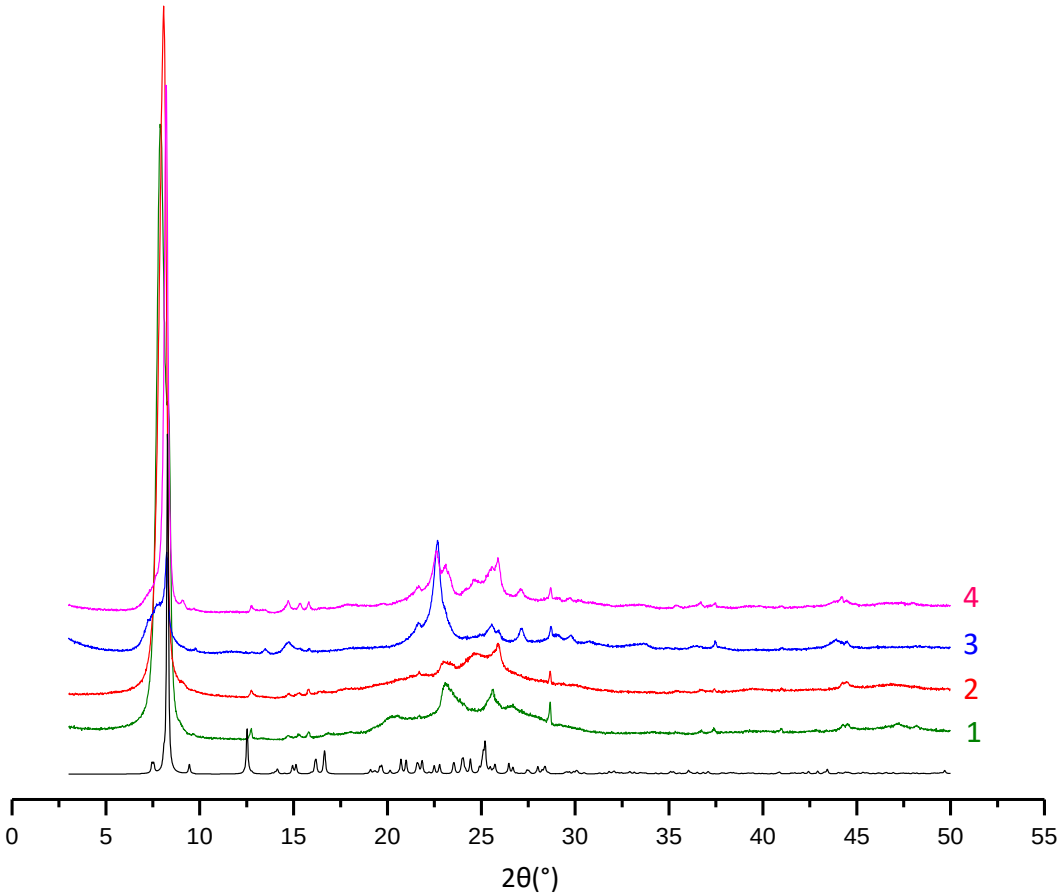

Figure 7.6: The PXRD patterns of the hydrolysed Al-UTL samples compared with simulated IPC-1P (black).

Once hydrolysed, the samples were studied by EDX once again to further confirm successful hydrolysis by the loss of germanium. The results of all four zeolites, table 7.3, show not only the expected loss of germanium, but also a loss of aluminium. All four zeolites show extremely high Si/Al ratios, indicating a very low level of aluminium remaining within the disassembled layers.

Table 7.3: EDX data of the four Al-IPC-1P samples post-hydrolysis.

Sample	% Silicon	% Germanium	% Aluminium	Si/Al	Si/Ge
1 (sonicated)	21.3 ± 1.9	0.5 ± 0.0	0	0	39
2	26 ± 3.0	0.3 ± 0.0	0.1 ± 0.0	344	77
3	22.2 ± 2.7	0.8 ± 0.2	0.1 ± 0.0	156	29
4	19.3 ± 2.8	0.68 ± 0.1	0.1 ± 0.1	361	28

This suggests that the aluminium incorporated into the UTL during the synthesis is either removed during the hydrolysis, similar to the loss of germanium, or the sample is dealuminated by the hydrolysis conditions. The first possibility would suggest that aluminium has been incorporated into the double four rings and has then been removed by the hydrolysis. The second possibility suggests that the acidic hydrolysis conditions have resulted in dealumination of the sample.

It is widely accepted that zeolites can be dealuminated under acidic conditions but there does seem to be a difference of opinion on how extreme the levels of dealumination are for differing concentrations of acid. Some studies observe framework vacancies and resultant increase in Brønsted activity from acid dealumination.[5,6] Other literature studies, however, have found that the level of dealumination can be very low and acid concentrations above 1 M are required to see any considerable changes in the aluminium content of the framework.[7,8] It is considered that extra-framework aluminium can be removed by acid washing with acid concentrations between 0.001 and 1 M.[9]

The lack of crystallinity remaining in the layered materials would suggest that they may have defects caused by aluminium removal. This would suggest that the acid hydrolysis has removed aluminium present within the framework. The removal of aluminium from samples 1 and 4 is most-likely an acid clean-up of the extra-framework aluminium that could be observed on the surface of the crystals by SEM. It is likely that extra-framework aluminium was also present within the pores. It is the decrease in aluminium from sample 2 that would suggest that framework dealumination has occurred. The sample didn't contain any obvious surface aluminium, suggesting the aluminium had been incorporated within the framework.

The low levels of aluminium in the layered IPC-1P materials indicate that the reassembled daughter zeolites would also have very low levels of aluminium. This would result in low ion-exchange capacity that would not be beneficial for catalytic testing. While the Al-UTL synthesis has been successful, unfortunately the loss of aluminium during the hydrolysis step limits the use of these materials for catalysis. Instead, a second method for incorporating aluminium during the ADOR process will be considered.

7.4.2. Conversion of UTL to Al-UTL

The Al-UTL synthesis in the second project looked at a different way to insert aluminium into UTL. This required the synthesis of Ge-UTL. The SDA, 6,10-dimethyl-5-azoniaspiro[4,5]decane bromide, was prepared and confirmed by solution-state NMR, figure 7.7.

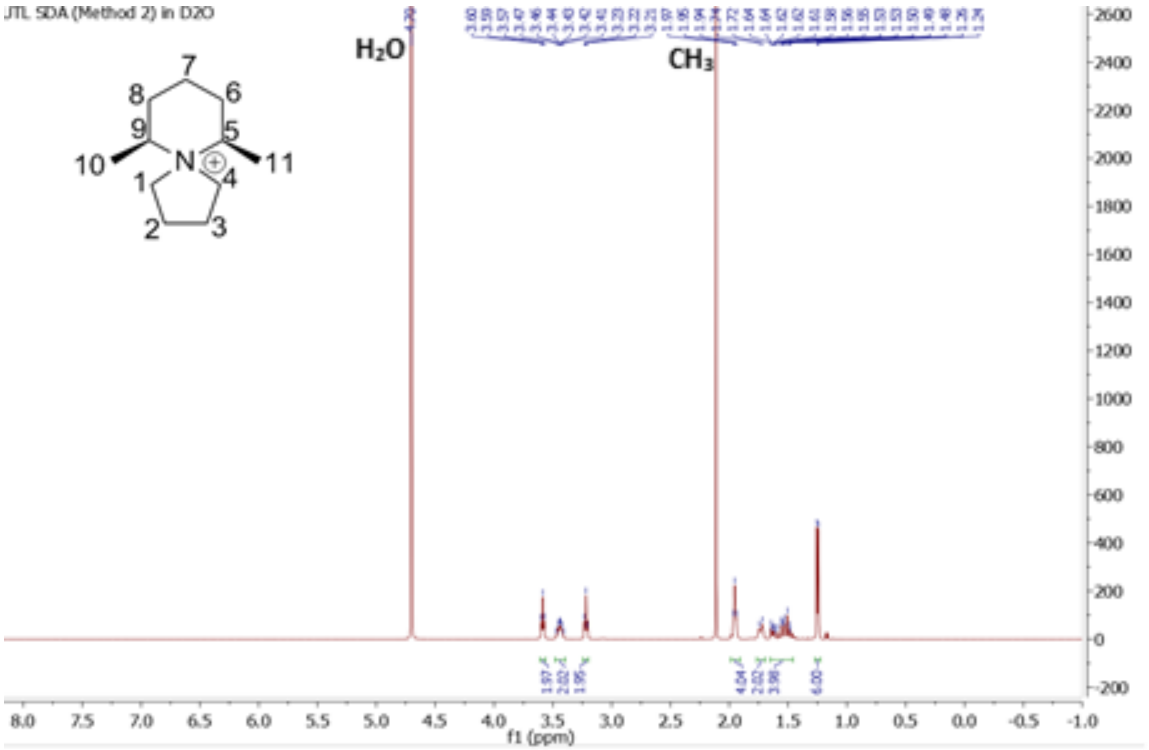

Figure 7.7: NMR spectrum of 6,10-dimethyl-5-azoniaspiro[4,5]decane bromide.

^{1}H NMR (500 MHz, Deuterium Oxide) δ_H 3.41 (dt, *J* = 5 and 180 Hz, H_1 and H_4), 3.47-3.41 (m, H_5 and H_9), 1.95 (t, *J* = 10 Hz, H_2 and H_3), 1.73 (d, *J* = 10 Hz), 1.64-1.48 (m, H_6 and H_8) and 1.25 (d, *J* = 10.0 Hz, H_{10} and H_{11}).

The mass of SDA obtained was 28.17 g, providing an 80 % yield. The yield calculation is shown below:

$$Theoretical\ Yield = 142\ mmol\ \times 248.5\ gmol^{-1}$$

$$= 35.29\ g$$

$$Yield = \frac{28.17\ g}{35.29\ g} \times 100$$

$$= 79.8\ \%$$

Once the SDA was obtained, a batch of UTL was prepared, calcined and characterised by PXRD. The UTL was then treated with a concentrated aluminium solution in an autoclave in an attempt to insert the aluminium within the framework. The synthesised Ge-UTL and subsequent Al-UTL PXRD patterns are shown in figure 7.8.

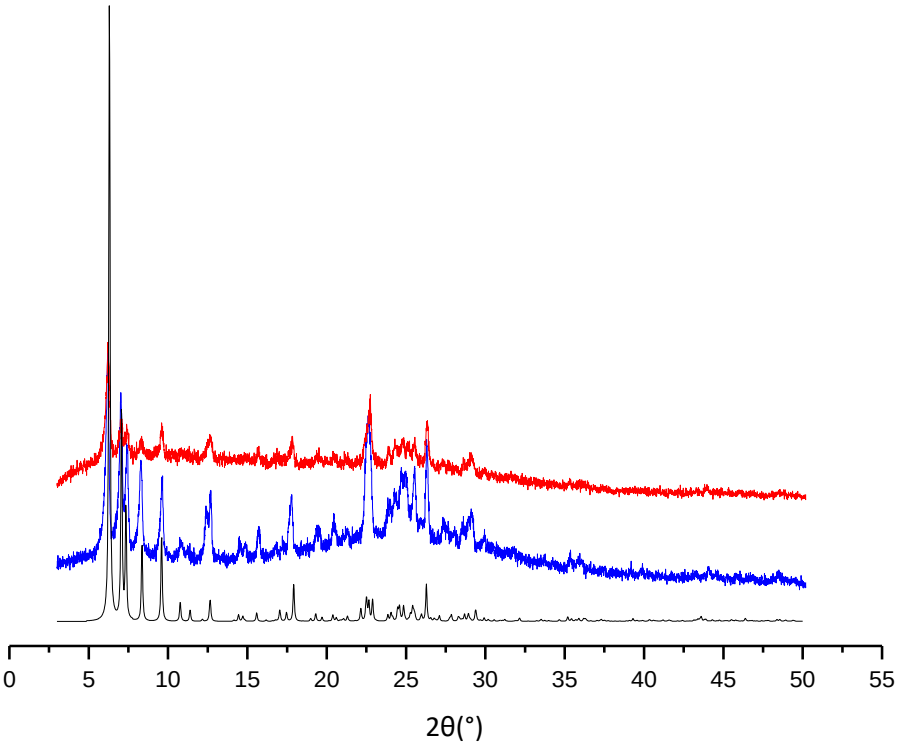

Figure 7.8: PXRD patterns of simulated UTL (black), synthesised Ge-UTL (blue) and Al-UTL converted from the synthesised Ge-UTL (red).

The synthesised Ge-UTL matched relatively well with the simulated UTL pattern. The Al-UTL showed some loss in crystallinity, seen by the loss of some peaks. This is most likely due to the harsh conditions of the alumination, as well as the aluminium incorporation disturbing the framework.

SEM images, figure 7.9, confirmed the classic tombstone shapes of the Ge-UTL crystals. EDX measurements were also recorded of the initial UTL and the post-aluminium treatment UTL, table 7.4.

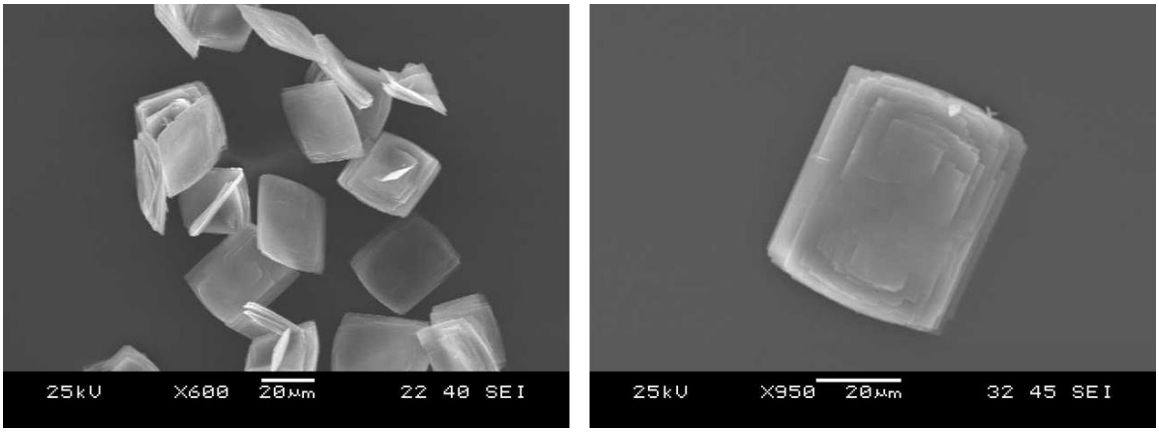

Figure 7.9: SEM images of the synthesised Ge-UTL crystals.

The EDX results, table 7.4, showed not only an increase in aluminium for Al-UTL, but there was also a surprising decrease in germanium. This suggests that the procedure for aluminium incorporation hydrolysed the Ge-O bonds, removing the majority of the germanium from the framework. This indicates that the aluminium may have replaced some of the germanium in the connecting d4r. The replacement of the hydrolytically unstable Ge-O bonds with Si-O-Al bonds would generate a more stable structure. This therefore removes the possibility of the Al-UTL undergoing the ADOR process, meaning that it is not possible to generate aluminated daughter zeolites from this Al-UTL.

Table 7.4: EDX data of the initial UTL and the aluminium-incorporated UTL.

Sample	% Silicon	% Germanium	% Aluminium	Si/Al	Si/Ge
UTL	17.1 ± 2.1	4.5 ± 0.4	-	-	3.8
Al-UTL	24.9 ± 3.5	0.3 ± 0.0	1.98 ± 0.2	13	83

7.5. Acid Site ADOR Series

After the synthesis of non-ADORable Al-UTL, the next challenge was the formation of aluminated ADOR products through the ADOR process of Ge-UTL. The aluminated daughter zeolites formed by aluminium addition during the organisation step were assessed by PXRD and compared to simulated patterns to determine their success.

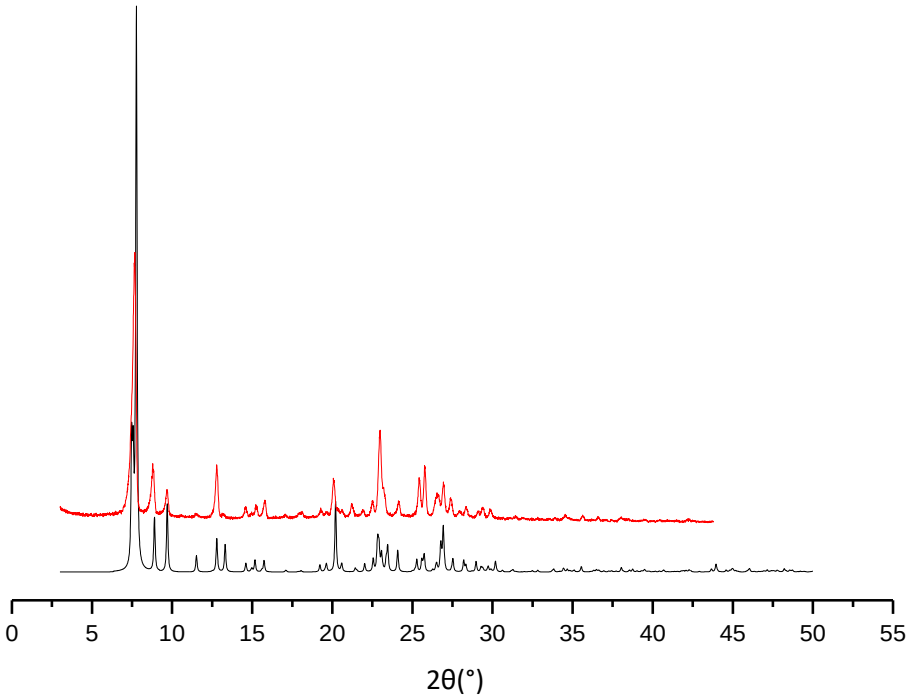

Figure 7.10: PXRD patterns of Al-IPC-2 experimental (red) and simulated (black).

Although the Al-IPC-2 data only ran until 45 °, it is still possible to see the high number of matching peaks with the simulated sample, figure 7.10. This similarity confirms the synthesis of IPC-2 from the hydrolysed Ge-UTL.

The two Al-IPC-4 samples showed matching peaks to the simulated patterns, figure 7.11, indicating the synthesis of IPC-4 from both methods. The slightly broader and less-intense peaks suggest some damage to the sample during the process.

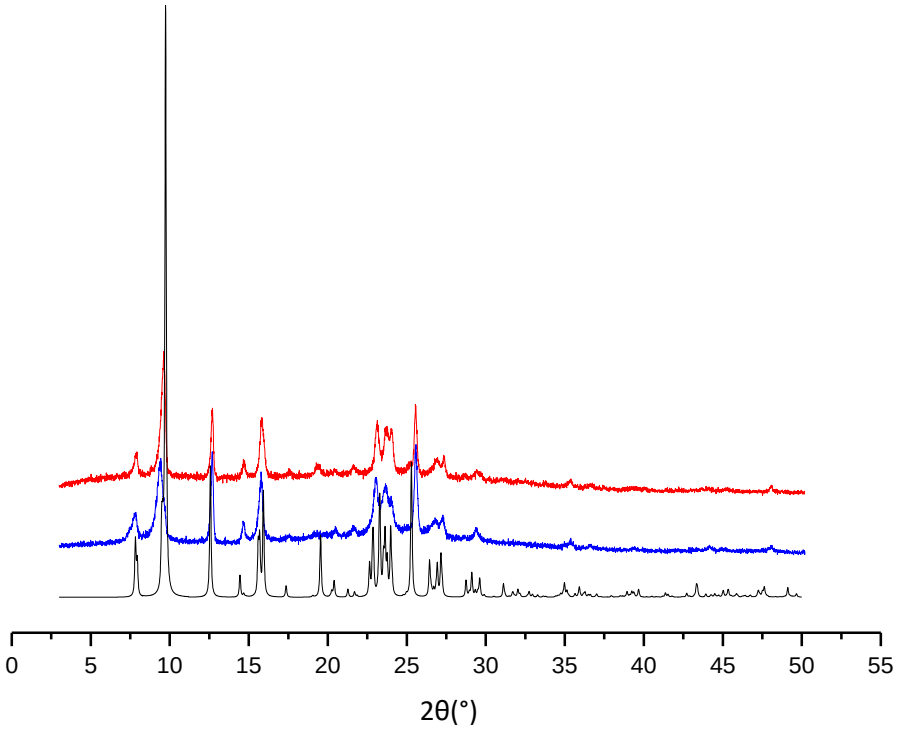

Figure 7.11: PXRD patterns of Al-IPC-4 washed with 0.1 M hydrochloric acid (red), Al-IPC-4 washed with 0.01 M hydrochloric acid (blue) and simulated IPC-4 (black).

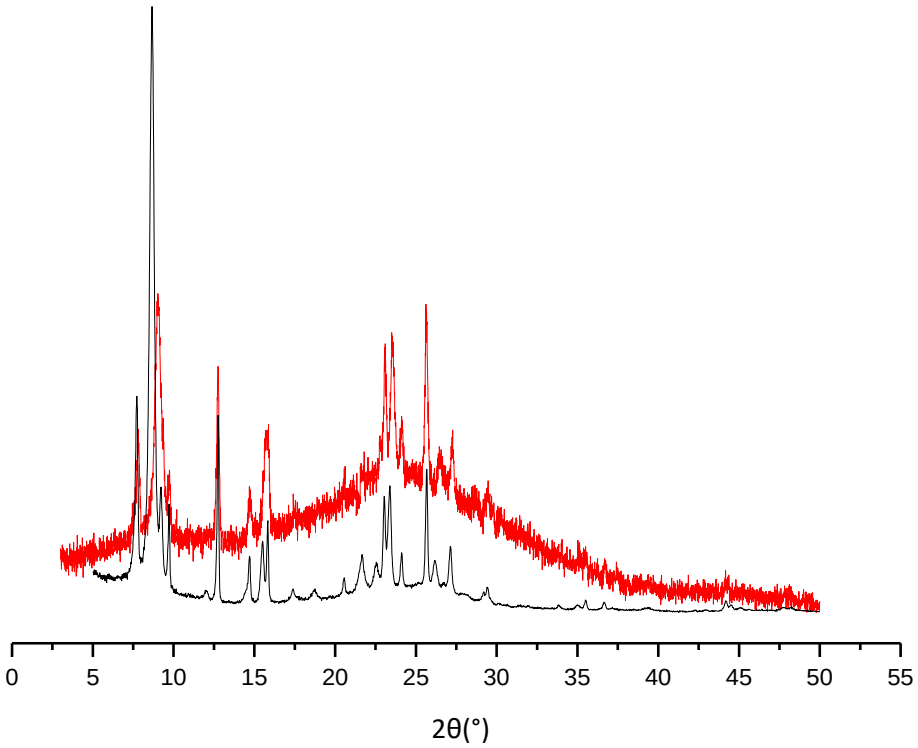

Figure 7.12: PXRD patterns of Al-IPC-6 (red) and a previously synthesised reference (black).

The PXRD pattern of the synthesised IPC-6 was compared to a previously synthesised reference, figure 7.12. Although the Al-IPC-6 pattern is relatively noisy, it is still possible to see the matching peaks compared to the reference pattern. While the Al-IPC-6 material was not as crystalline as desired, the peak similarity confirmed the successful preparation of the material.

The EDX data of the four newly formed zeolites, table 7.5, confirmed the inclusion of aluminium within the structures. An interesting result was observed from the two different Al-IPC-4 syntheses, with aluminium levels of 0.3 and 1 %, quite a significant difference. The main difference between the two samples is the different hydrochloric acid concentrations used in the washing of the Al-IPC-1P in the synthesis of the samples.

Table 7.5: EDX data of the four aluminated daughter zeolites.

Sample	% Silicon	% Germanium	% Aluminium	Si/Al	Si/Ge
Al-IPC-2	25.6 ± 1.0	0.3 ± 0.0	0.5 ± 0.1	52	98
Al-IPC-4 (0.1 M)	23.9 ± 4.0	0.4 ± 0.0	0.3 ± 0.0	80	60
Al-IPC-4 (0.01 M)	31.6 ± 5.9	0.5 ± 0.2	1.0 ± 0.1	32	63
Al-IPC-6	20.8 ± 1.5	0.8 ± 0.2	0.7 ± 0.2	30	26

As discussed previously, generally acid concentrations below 1 M result in extra-framework dealumination, as opposed to framework. Therefore, the concentrations of 0.1 M and 0.01 M are not likely to remove framework aluminium. However, the Al-IPC-1P structure is a layered material that was aluminated during the disassembly. It could be that the aluminium introduced into the layered material is not strictly “framework” and therefore more susceptible to acid dealumination. In this case the differing strengths of acid may have had a greater impact on the aluminium levels of the layered material. This could explain the lower aluminium content, 0.3 %, for the Al-IPC-4 sample prepared from stronger acid concentrations.

7.5.1. Nitric Oxide Production

The Al-UTL formed from the insertion of aluminium into UTL was ion-exchanged to form acid sites and analysed for NO production on the NOA. The series of daughter zeolites formed from Ge-UTL were also ion-exchanged and assessed on the NOA, these were the two Al-IPC-4 samples, Al-IPC-2 and Al-IPC-6. All samples were studied in triplicate, with the exception of Al-IPC-4 (1 % Al) that was run in duplicate due to limited sample. All results are presented as both the release profile (NO concentrations) and the total NO production.

A condensed version of table 1.1 from section 1.1.5 may help to understand the catalytic activity from the zeolites. The table summarises the connection between the newly assembled layers and the sizes of the rings formed by these connections. The range of ring sizes formed from the ADOR process allows a study of the effect of zeolite ring size on the NO production from nitrite. Unfortunately, the quantity and strength of acid sites of the samples were not characterised during this project. Due to the same acid site formation procedure for all samples it is assumed that the level of ion-exchange will be similar across all samples.

Table 1.1 (condensed): The new zeolites formed from the ADOR process of UTL, including the layer connections and the ring size of the newly formed rings. The ring sizes of UTL correspond to the two rings that will be altered during the ADOR process.

Zeolite	Layer Connection	Ring Size
UTL	d4r	14 and 12
IPC-2	s4r	12 and 10
IPC-4	direct oxygen	10 and 8
IPC-6	s4r and oxygen	12, 10 and 10, 8

7.5.1.1. Al-UTL

The NO release profiles of Al-UTL, figure 7.13 (left), show initial NO concentrations between 0.2 and 0.3 ppm after the nitrite injection. The NO is then produced for around 9 hours, before the NO levels return to background concentrations.

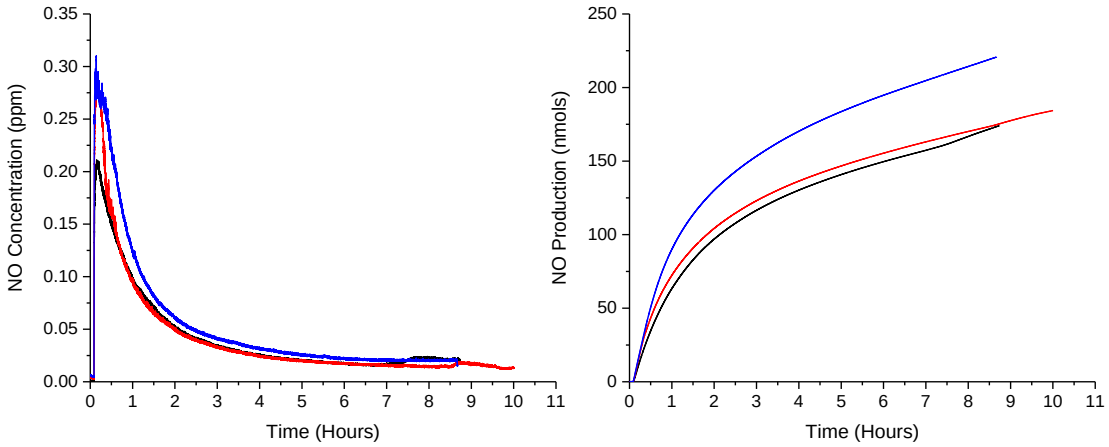

Figure 7.13: Al-UTL triplicate release profile (left) and NO production (right).

The NO production, figure 7.13 (right), reveals the black and red runs produce similar levels of NO, around 175 nmols. The blue run has a higher level of NO produced, with a total of around 225 nmols produced during the run.

7.5.1.2. Al-IPC-2

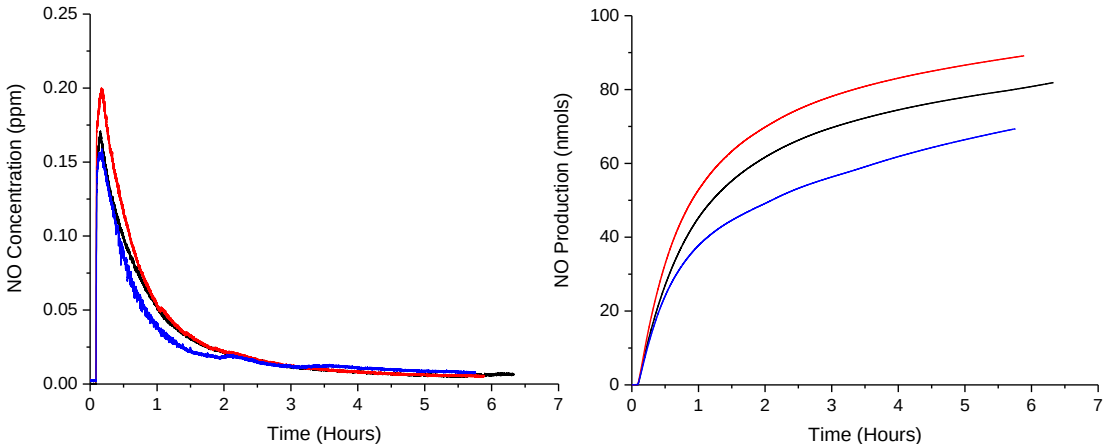

Figure 7.14: Al-IPC-2 triplicate NO release profile (left) and NO production (right).

The Al-IPC-2 NO release profiles, figure 7.14 (left), show an initial NO concentration between 0.16 and 0.20 ppm for the triplicate runs. The runs last around 6 hours until the NO levels return to the background values. Both the NO concentrations and the length of the runs are lower than the Al-UTL sample. The total NO produced from the triplicate runs, figure 7.14 (right), show values between 65 and 90 nmols.

7.5.1.3. Al-IPC-4

The two Al-IPC-4 samples were studied on the NOA. The first was the sample with 0.3 % aluminium (0.1 M HCl washing). The release profile results, figure 7.15 (left), show NO concentrations between 55 and 85 ppb, considerably lower than the Al-UTL and Al-IPC-2 samples. The NO production for the triplicates, figure 7.15 (right), is 41, 50 and 57 nmols.

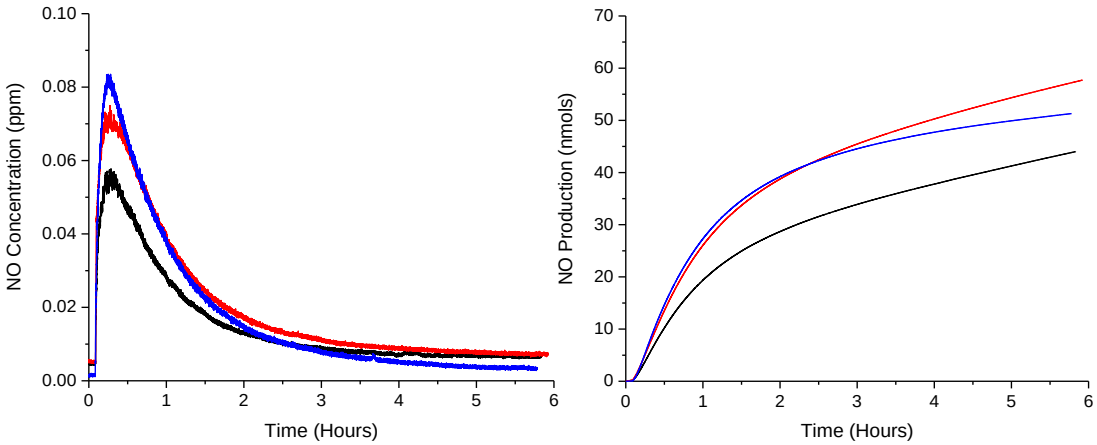

Figure 7.15: Al-IPC-4 (0.3 % Al) triplicate NO release profile (left) and NO production (right).

The results of the NOA catalytic tests of the Al-IPC-4 sample with 1 % aluminium (0.01 M HCl washing) are shown in figure 7.16. The duplicate release profiles produced peak NO concentrations of 49 – 59 ppb. The NO production lasted around 6 – 7 hours before returning to background levels. A similar amount of NO was produced from the two runs, both providing an overall production of 50 – 60 nmols.

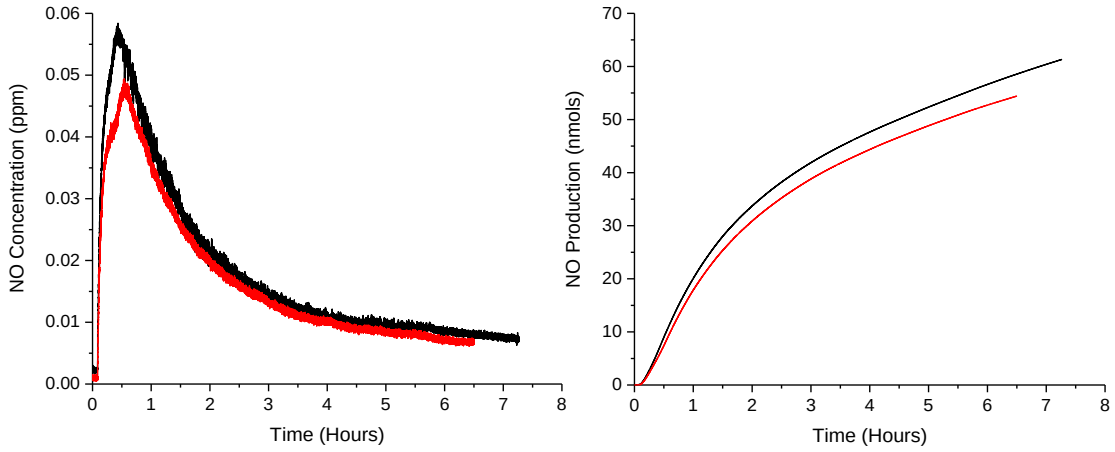

Figure 7.16: Al-IPC-4 (1 % Al) duplicate NO release profile (left) and NO production (right).

Comparing the data of the two different Al-IPC-4 samples, it would appear that the aluminium content doesn't have a huge impact on the NO production from nitrite. The two samples produced similar levels of NO, suggesting that the pore size has a greater influence on the level of the production than the aluminium content.

7.5.1.4. Al-IPC-6

The NO production from Al-IPC-6 is shown in figure 7.17. The three runs all produced similar results, with peak NO concentrations between 0.13 and 0.17 ppm. The runs were recorded for 7 hours, with NO levels returning to background concentrations after 6 – 7 hours. The total NO produced is between 72 and 78 nmols, similar levels to Al-IPC-2.

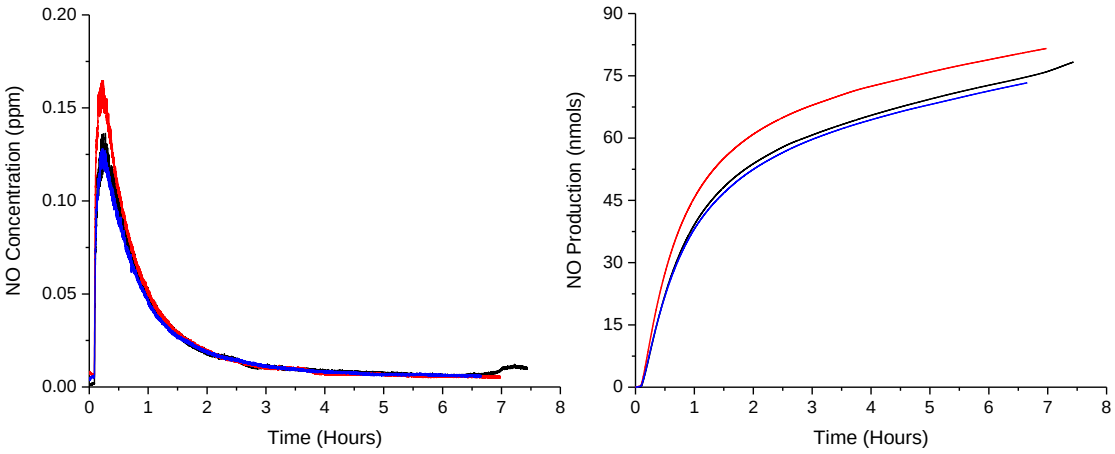

Figure 7.17: Al-IPC-6 triplicate NO release profile (left) and NO production (right).

The average NO production for each sample is presented in figure 7.18. The results show the considerably highest production from Al-UTL, followed by similar levels of production from Al-IPC-2 and Al-IPC-6, followed by the two Al-UTL-4 samples with the lowest levels of NO. This ordering follows the order of the ring sizes, with the large 14 and 12 rings of Al-UTL having the highest NO production and the smallest 10 and 8 rings of Al-IPC-4 producing the lowest. The 12 and 10 rings of Al-IPC-2 produce slightly more NO than the alternating 12/10 rings and 10/8 rings of Al-IPC-6.

The findings indicate that the larger ring sizes of the ADOR series increase the NO production. This is most likely due to an increase in accessibility to the active acid sites or the increased diffusion from the larger rings.

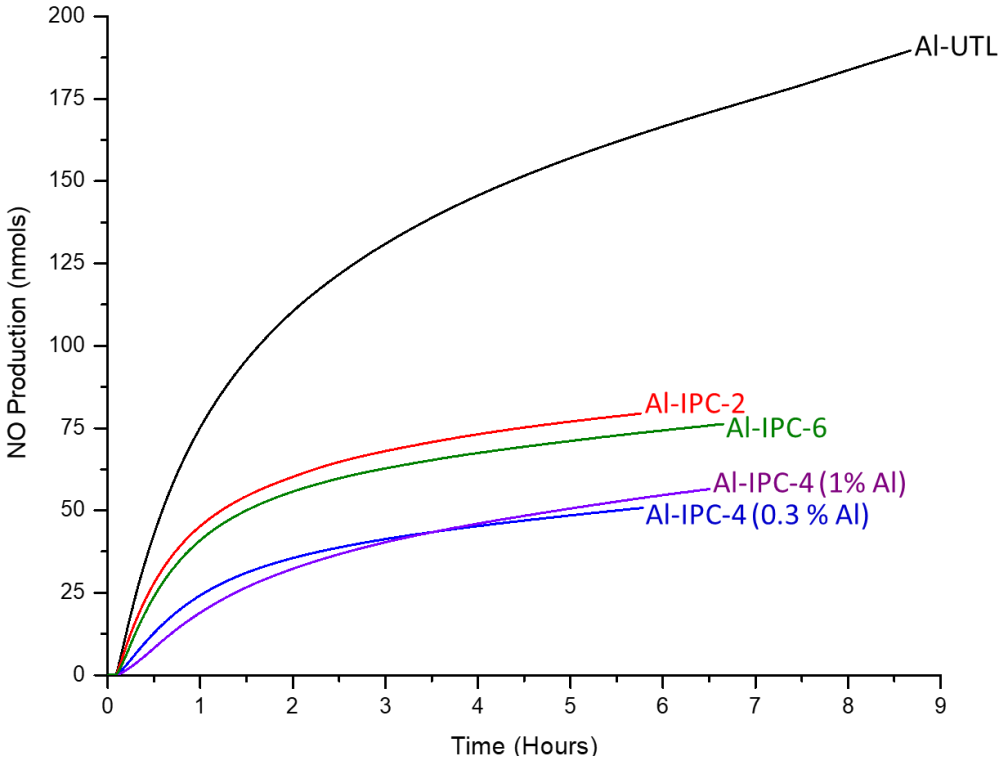

Figure 7.18: Comparison of NO production of all aluminated ADOR zeolites. Al-UTL (black), Al-IPC-2 (red), Al-IPC-6 (green), Al-IPC-4 (0.3 % Al) (blue) and Al-IPC-4 (1 % Al) (purple).

Unfortunately, as with the acid site zeolites in chapter four, the ADOR zeolites are not recyclable when it comes to NO production. A second injection of nitrite once the initial NO production was complete, showed minimal NO production. This is likely due to the consumption of the proton from the acid site during the reaction.

7.5.2. Rates of Reaction

As with chapters 4 and 5, the rates of reaction can be determined by the Avrami and the Sharp-Hancock equation. The plot of time against extent of reaction, α, is shown in figure 7.19. As with the acid site zeolites in chapter 4, the Avrami fit does not match the plotted data as well as hoped. This further suggests that the mechanism of the acid sites is different to the copper sites mechanism. The obtained k and n values from the plot are shown in table 7.6.

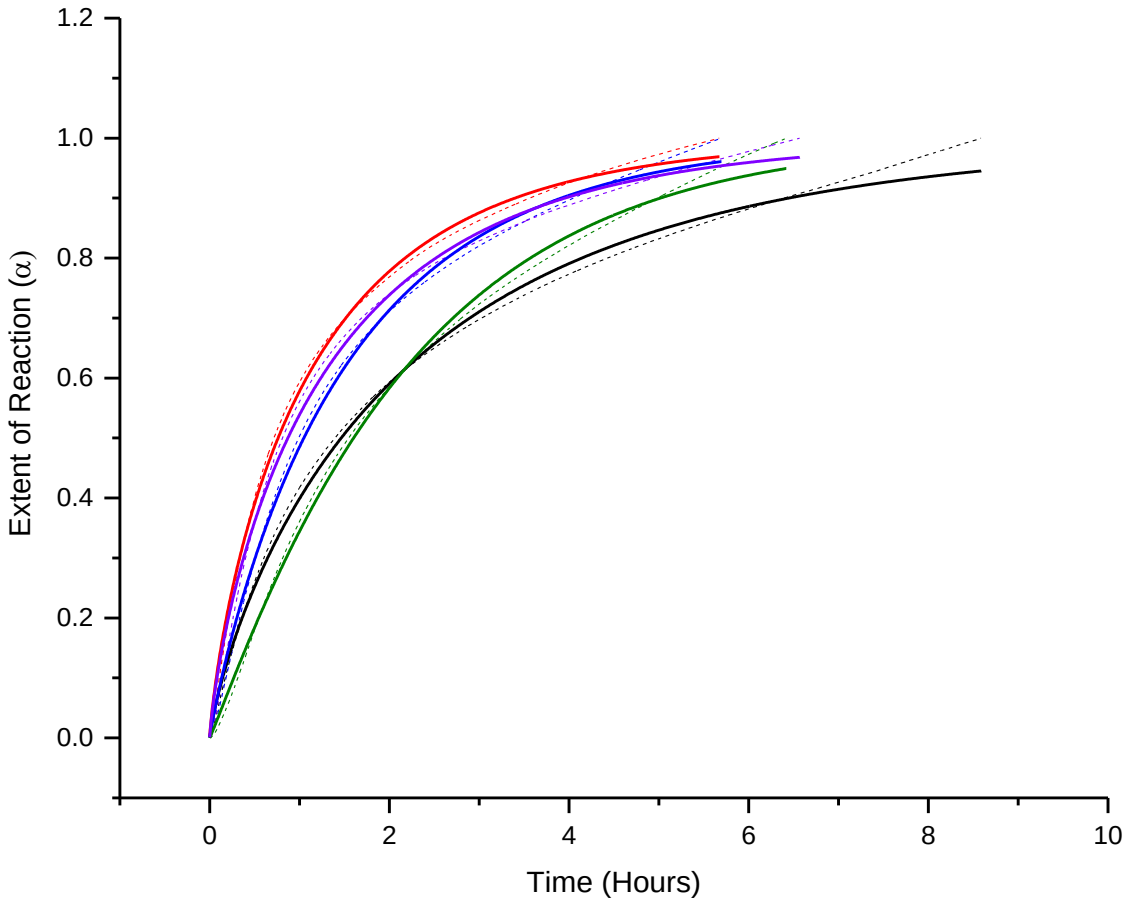

Figure 7.19: The Avrami fit (dashed lines) of the normalised NO production (solid lines) from the acid site ADOR zeolites. Al-UTL (black), Al-IPC-2 (red), Al-IPC-4 (0.3 % Al, blue), Al-IPC-4 (1 % Al, green) and Al-IPC-6 (purple).

Table 7.6: The k and n values derived from the Avrami plot in Figure 7.19.

Zeolite	Al-UTL	Al-IPC-2	Al-IPC-4 (0.3 % Al)	Al-IPC-4 (1 % Al)	Al-IPC-6
n	0.81	0.80	0.91	1.05	0.79
k (h^{-1})	0.43	0.83	0.64	0.44	0.72

The n values range between 0.80 and 1.05, sitting in the region that signifies a first order reaction. Interestingly, the n values are lower for the larger ringed zeolites. This suggests that the NO production from the larger ringed zeolites is closer to a diffusive mechanism than the other zeolites.[10] The k values increase in the order of Al-UTL < Al-IPC-4 (1 % Al) < Al-IPC-4 (0.3 % Al) < Al-IPC-6 < Al-IPC-2.

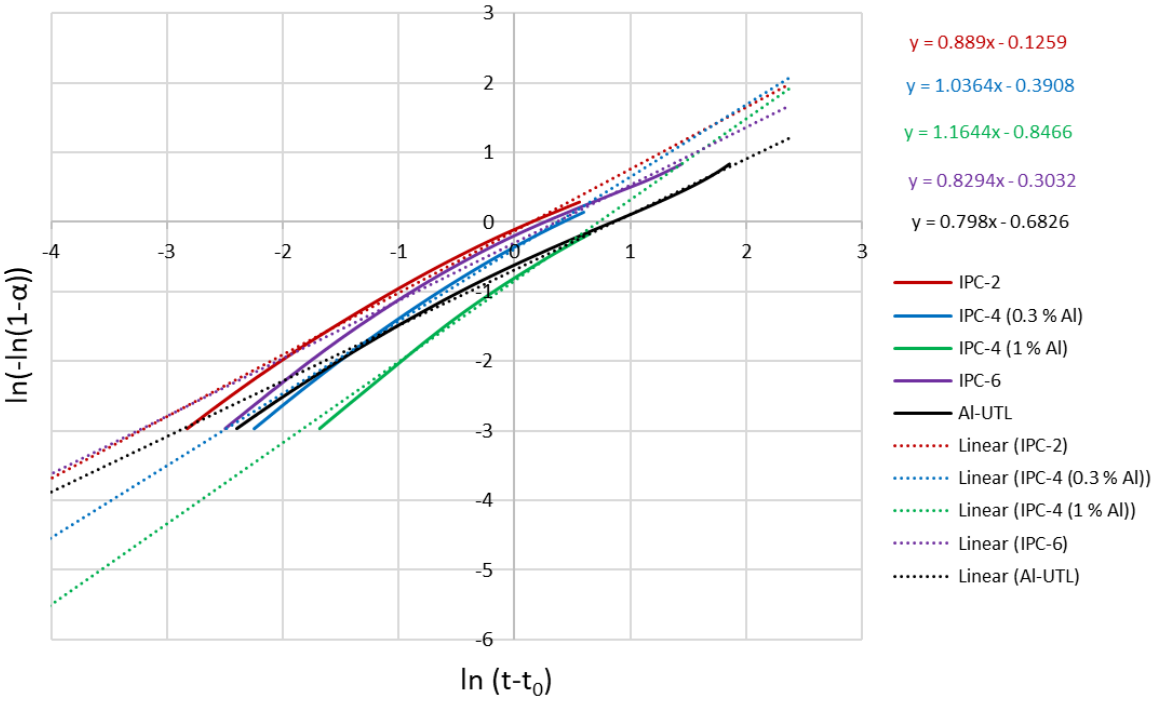

Figure 7.20: The Sharp-Hancock fit (dashed line) of the normalised NO production (solid line) from the acid site ADOR zeolites. Al-UTL (black), Al-IPC-2 (red), Al-IPC-4 (0.3 % Al) (blue), Al-IPC-4 (1 % Al) (green) and Al-IPC-6 (purple). The plotted values correspond to extent of reactions (α) between 5 and 90 %.[11]

The Sharp-Hancock data, figure 7.20, reveals slight curves in the plotted lines, which can indicate a change in reaction mechanism. The ordering of the n values are similar to the Avrami ordering, but the values themselves are quite different, table 7.7. Again, the lower n values of Al-UTL, Al-IPC-2 and Al-IPC-6 may suggest a diffusive mechanism, indicating that the diffusion of the substrate to the active site plays a role in the reaction kinetics.

Table 7.7: The k and n values derived from the Sharp-Hancock plot in Figure 7.20.

Zeolite	Al-UTL	Al-IPC-2	Al-IPC-4 (0.3 % Al)	Al-IPC-4 (1 % Al)	Al-IPC-6
n	0.80	0.89	1.04	1.16	0.83
k (h^{-1})	0.43	0.87	0.69	0.48	0.69

7.6. Conclusions

The first attempt to produce a series of aluminated ADOR products was not successful. Four Al-UTL syntheses were performed with a range of pH values and aluminium content. Three of the syntheses produced UTL with a reasonable level of aluminium, 0.4 – 0.6 %. Imaging by SEM, however, revealed the presence of small spherical crystals on the surface of the UTL for two of the samples. EDX revealed a high aluminium content of these spherical crystals. Subsequent sonication of one of the samples removed the presence of the small spherical crystals and ultimately reduced the aluminium content of the sample, confirming the small crystals had been rich in aluminium. The successful incorporation of aluminium by one of the samples suggests that a low pH and a low aluminium synthesis gel content favour incorporation of aluminium into the zeolite framework.

All samples were hydrolysed in acidic conditions, with the resulting PXRD patterns confirming the formation of a layered material in all cases. EDX data revealed that not only had the germanium been removed from the UTL d4r, but the majority of the aluminium had also been removed. This was considered to be due to the removal of extra-framework aluminium as well as some framework dealumination, as observed by the loss of crystallinity of the layered material. The loss of aluminium drew the project to an end as the reassembled zeolites would be lacking the catalytically-important aluminium.

The second project looked at aluminating the ADOR process at the disassembly/organisation step. An initial Al-UTL sample was prepared by exposing a sample of Ge-UTL to a high concentration of aluminium nitrate in an autoclave. The production of Al-UTL was determined to be successful by PXRD and EDX.

The Ge-UTL was then hydrolysed in the presence of aluminium nitrate to form Al-IPC-1P. The Al-IPC-1P was organised and reassembled to produce Al-IPC-2, Al-IPC-4 and Al-IPC-6. Al-IPC-4 was produced via two slightly different methods, resulting in different aluminium levels between the samples. All samples, including the Al-UTL, were ion-exchanged and calcined to prepare acid sites for NO production catalysis.

The NO production showed an interesting trend relating to the zeolite ring size. The highest NO production came from Al-UTL, the largest ring sizes of the series, the lowest

NO production came from the two Al-IPC-4 zeolites, the smallest ring sizes. Assuming the channel systems of the series are the same, due to their isoreticular nature, it would be a fair assumption to say that the pore sizes of the ADOR series have the greatest influence on the catalytic nature. An observation that was also made with ADOR catalysts for toluene alkylation reactions in literature.[3]

The project also allowed an interesting insight into how the different aluminium levels affect the NO production. The two samples with aluminium levels of 0.3 and 1 % showed similar NO production, both producing around 50 nmols. This indicates that the overriding NO production influence came from the ring sizes as opposed to the aluminium levels. This is most likely due to the fact that the higher number of acid sites, formed from the higher level of aluminium, can weaken the strength of the acid sites. Assuming that the strength of the acid site plays a role in the NO production, the weakened strength may decrease the NO production.

Overall, this chapter provided an insight into the relationship between ring size and NO production. While the ADOR zeolites did not perform as well as those in chapter 4, the varying size of rings formed from different layer connections provided an understanding into the impact on NO production.

7.7. Future Work

While the results from the chapter demonstrated a good correlation between pore size and NO production, further characterisation of the samples would be beneficial. A method of studying the acid site strengths could help to decipher how much of a role, if any, they play in the amount of NO produced. As opposed to the ranging zeolites studied by NH_3-TPD in chapter 4, in this chapter the isoreticular series of zeolites limits other factors that may affect NO production. Either the same NH_3-TPD method or an alternative probe molecule, such as pyridine, may be useful.

The results from chapter 5 showed that the copper sites have a greater activity than the acid sites. Therefore, incorporation of copper ions into the ADOR zeolites, and the subsequent catalytic NO production, would be of interest to observe if the ring size trend is still present.

7.8. References

1 M. V. Shamzhy, O. V. Shvets, M. V. Opanasenko, P. S. Yaremov, L. G. Sarkisyan, P. Chlubná, A. Zukal, V. R. Marthala, M. Hartmann and J. Čejka, *J. Mater. Chem.*, 2012, **22**, 15793–15803.

2 S. A. Morris, G. P. M. Bignami, Y. Tian, M. Navarro, D. S. Firth, J. Čejka, P. S. Wheatley, D. M. Dawson, W. A. Slawinski, D. S. Wragg, R. E. Morris and S. E. Ashbrook, *Nat. Chem.*, 2017, **9**, 1012–1018.

3 N. Žilková, P. Eliášová, S. Al-Khattaf, R. E. Morris, M. Mazur and J. Čejka, *Catal. Today*, 2016, **277**, 55–60.

4 O. V. Shvets, N. Kasian, A. Zukal, J. Pinkas and J. Čejka, *Chem. Mater.*, 2010, **22**, 3482–3495.

5 Z. Yan, D. Ma, J. Zhuang, X. Liu, X. Liu, X. Han, X. Bao, F. Chang, L. Xu and Z. Liu, *J. Mol. Catal. A Chem.*, 2003, **194**, 153–167.

6 E. F. T. Lee and L. V. C. Rees, *J. Chem. Soc. Faraday Trans. 1 Phys. Chem. Condens. Phases*, 1987, **83**, 1531.

7 D. M. Roberge, H. Hausmann and W. F. Hölderich, *Phys. Chem. Chem. Phys.*, 2002, **4**, 3128–3135.

8 P. J. Kooyman, P. van der Waal and H. van Bekkum, *Zeolites*, 1997, **18**, 50–53.

9 A. W. O'Donovan, C. T. O'Connor and K. R. Koch, *Microporous Mater.*, 1995, **5**, 185–202.

10 H. Shiga, H. Yoshii, T. Nishiyama, T. Furuta, P. Forssele, K. Poutanen and P. Linko, *Dry. Technol.*, 2001, **19**, 1385–1395.

11 A. Altree-Williams, A. Pring, Y. Ngothai and J. Brugger, *ACS Earth Sp. Chem.*, 2017, **1**, 89–100.

Chapter 8: Conclusions and Future Work

The overall aim of this thesis was to assess the potential for zeolite catalysts to be used within biomedical applications for nitric oxide (NO) production. The main application that the thesis considered was the use of NO-producing materials as a component of a stent coating to help prevent stent thrombosis. An overall of nine different frameworks were studied, including ADOR zeolites, with either acid or copper active sites.

Chapter 4 considered the conversion of nitrite to nitric oxide from acid site mordenite, ferrierite, ZSM-5 and SSZ-13. The results showed SSZ-13 and ZSM-5 to produce the highest amounts of NO, followed by mordenite and then ferrierite. No obvious comparison could be found between the number and strength of the acid sites and the amount of NO produced, which suggested that the framework structures play a large role in the level of production. SSZ-13 and ZSM-5 are both classed as 3D zeolites, which may allow greater access to the active sites by the substrate and a resultant higher production of NO. Perhaps one of the main findings of this work, was the lack of regeneration of the acid sites. This is considered due to the consumption of the acid site during the reaction, however post-catalysis NH_3-TPD comparisons would help to confirm this theory. This finding rendered the acid site zeolites as poor candidates for long term NO production applications. Therefore, no further studies were performed.

Chapters 5 and 6 focussed on copper site mordenite, ferrierite, ZSM-5, SSZ-13 and UZM-4. Nitric oxide catalytic tests were performed in the same way as the acid sites, as well as further studies that considered copper leaching, toxicology of HEK 293 cells, NO production from a flow system and polymer incorporation.

The catalytic studies of the copper sites required a sacrificial reductant to reduce the Cu^{2+} to Cu^{+}. The amino acid cysteine was employed with good success, with catalyst recyclability observed. The L-cysteine hydrochloride initially used however, was later found to produce NO from the reaction with sodium nitrite. In hindsight, this reaction is most likely a result of the acidic hydrochloride reacting with the sodium nitrite in a similar reaction that was observed with the acid site zeolites. Therefore, the cysteine source was changed to D/L-cysteine later in the project to remove the unnecessary acidity. This

change of cysteine source successfully removed any NO production that was not attributed to the reaction between the zeolite and nitrite.

The NOA copper catalysis showed the highest NO production from ZSM-5, SSZ-13 and UZM-4. As with the acid sites, it was the zeolites with the higher channel systems that performed best. This suggests that it may be a combination of the substrate diffusion and the active site accessibility that governs the level of NO production. A further trend was observed that showed the larger pored zeolites, such as mordenite and UZM-4 having the most prolonged NO production. This may be due to the small pore zeolites directing the substrate towards the active sites, resulting in a quick production of NO, whereas the large pores allow the substrate to move through the channels without interacting, slowing down the process.

One of the areas of most interest arose from the Cu-FER NO production. Multiple nitrite injections revealed an interesting increase in NO production, suggesting a change in the material was enhancing the catalytic ability. While powder and single crystal X-ray diffraction confirmed no change in the ferrierite framework, it was the solid-state NMR results that indicated an interesting movement of the copper ions within the pores. The narrowing of ^{29}Si spectral lines after catalysis suggested that the copper may be more dispersed than before catalysis, suggesting a movement had taken place. It may be that the dispersion places the copper into more accessible locations within the zeolite framework, resulting in more nitrite being catalytically converted to nitric oxide. The other option may be an initial clustering of copper that was separated during catalysis, resulting in more copper sites to interact with the nitrite. Future *in situ* studies of the catalytic process may be able to identify any movement of the copper as it happens.

The leaching and toxicology studies of the copper site zeolites were essential in understanding any potential risks of using copper within the body. Similar concentrations of zeolites were used in both studies to be able to observe any correlation between the leached copper and the toxic impact on HEK 293 cells. The results showed that UZM-4 had the highest levels of copper leaching, as well as the highest toxicity, suggesting that the copper may be the source of toxicity from the zeolites. There was no obvious reason for UZM-4 to have the highest copper leaching, except from the fact that it contained the most copper to begin with. Unfortunately, there are no studies on the copper location of

Cu-UZM-4, as it could be that the location or coordination of some copper sites are more easily removed than others, resulting in higher levels of leaching. Further studies into the factors affecting leaching would be beneficial.

Copper site catalysis was also performed in flow, in an attempt to understand how the zeolites would behave in a set-up that mimics blood flow. Each zeolite was secured in place and the stock solution, containing cysteine and nitrite, flowed over it at a constant rate. The NO produced was monitored by NO-specific electrodes. Initial studies with around 2 hours of substrate flow were performed, as well as recycled samples for a similar time period and longer flow studies with an increased amount of stock solution that lasted around 7 – 8 hours.

The flow studies showed that the zeolites were capable of producing steady rate NO production for prolonged periods of time. Furthermore, the NO concentrations obtained were on a similar level to biologically active levels of NO when biological substrate concentrations are considered. The performance of individual zeolites however is hard to determine due to varied results. This is due to the experimental set-up, where air bubbles and slight changes in flow rate appeared to affect the reading from the electrodes.

The incorporation of the copper site zeolites into polymer films showed varied success when it came to the catalytic tests. Initial studies with polyurethane and polyvinylchloride showed significantly reduced NO production in comparison to the free powders. This may be due to a problem with diffusion of the cysteine and/or nitrite to the zeolite within the polymer films. To probe this theory, PIMs were used for the polymer films instead, where it was hoped that the larger voids would reduce diffusion limitations. PIM EA-TB(Me) proved a promising candidate, with the highest levels of NO production from any of the polymer films. One issue that arose however, was the reduction of NO production with EA-TB(Me) recycling. This reduction may be due to PIM void blocking by the dimer formed from the oxidation of cysteine to cystine. One way to further probe this theory could be by the use of adsorption measurements to observe any reduction that could be attributed to the presence of cystine within the polymer voids.

All factors considered from the copper site zeolites, the best candidate for NO production from a stent coating is mordenite. The main reason for this is the low leaching and toxicology data obtained, perhaps the second most important factor after NO production. Although it shows the lowest levels of NO production, the low and steady production may actually be beneficial for use within the body as it could help to prevent spikes in NO concentration that may be toxic. Unfortunately, the more catalytically active zeolites showed an increased toxicity. This toxicology however, may be reduced upon inclusion of the zeolites into polymer films. If so, this would allow a wider range of zeolites to be considered as a component of the stent coating.

A further area that may need to be explored is the accessibility of the cysteine to the copper sites. Cysteine is a large molecule in comparison to some of the zeolite channels and therefore may have limited accessibility at times. While this thesis has understood that the presence of cysteine is essential for the NO production, further studies into the interactions between copper and cysteine would be beneficial. This could involve the use of smaller reducing agents that may have better diffusion to the active sites.

Chapter 7 considered different zeolites to those studied previously, with the use of the ADOR process to form a series of isoreticular aluminium-containing zeolites for catalysis. The acid site series of zeolites, Al-IPC-2, 4 and 6, were used to explore the relationship between ring size and NO production. Results showed a correlation between the ring size of the zeolites and the NO production, with Al-UTL the largest NO production and Al-IPC-4 the smallest. As has been observed with the acid and copper sites, it would appear that a combination of substrate diffusion and active site accessibility plays a role in the level of NO production.

The rates of reaction were determined for the acid, copper and ADOR zeolites. In all cases, the Avrami and the Sharp-Hancock equations were applied to obtain an understanding of the reaction mechanism. The data from the copper zeolites fitted well with both plots, with n values suggesting a first order reaction. The two acid-based zeolites, chapters 4 and 7, did not fit the Avrami plot as well, suggesting a more complex reaction mechanism may be occurring. It may be that the observed consumption of the acid sites alters the reaction mechanism during the catalysis. One possibility could be that as more acid sites are consumed during the reaction, the mechanism becomes more diffusion driven, with less active sites present for the substrate to react with. Further studies into the mechanism would aid the understanding of how the reactions are proceeding.

Focussing on the proposed application, this thesis has shown that catalytic NO production is possible from copper site zeolites. Efforts have been taken to focus on studies that will help to develop these zeolites as materials for stent coatings, including toxicology studies and polymer incorporation. While there are still many steps required before the zeolites could be used in a stent coating, this thesis has underlined the behaviour of a group of zeolites that could be prime candidates to prevent stent thrombosis.

Appendix

A range of control measurements were recorded to ensure that there were no secondary reactions going on alongside the zeolite catalysis.

The first concerned the acid sites, where a sample of water only was run on the NOA under the same conditions as the acid site zeolites. No zeolite was present for the NOA run. The results showed a small increase in NO concentration initially, up to 12 ppb, that returned to low levels after 10 minutes. This indicates that any NO produced from the acid site zeolites with nitrite is from the reaction with the acid of the zeolite.

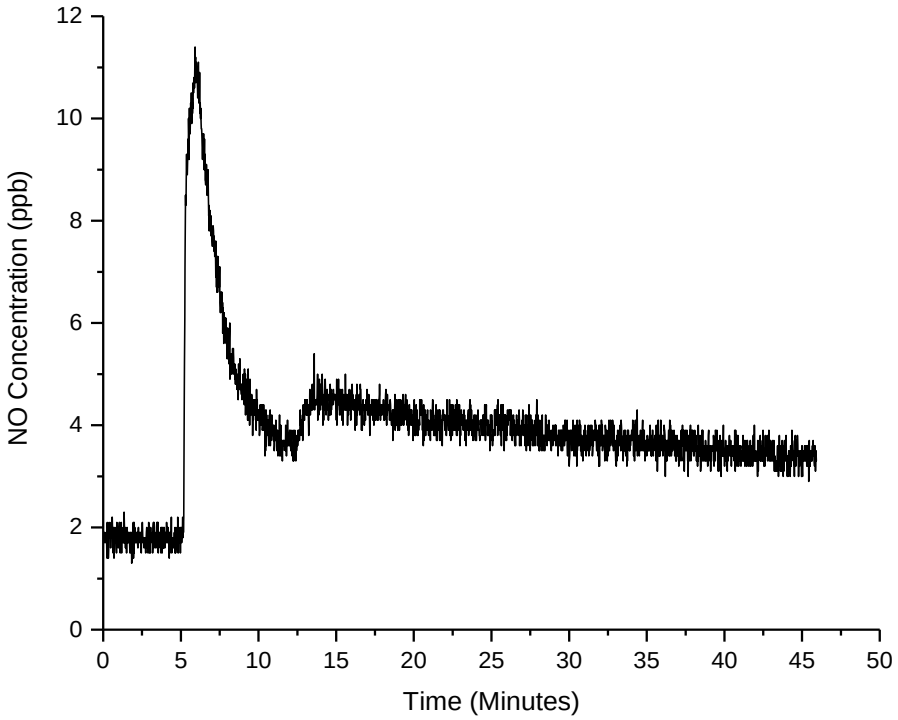

Figure A1: The NO concentration from 2.6 mL of water with sodium nitrite (0.05 M, 250 µL) injected after 5 minutes. This was to assess the importance of the acid site zeolite in catalysis.

The second control measurement concerned the use of cysteine as a sacrificial reductant. The reaction of Cu-UZM-4 with sodium nitrite was performed with no cysteine present. This was to assess the importance and impact from the sacrificial reductant. The results showed no nitric oxide production, highlighting the very important role of copper reduction by the cysteine.

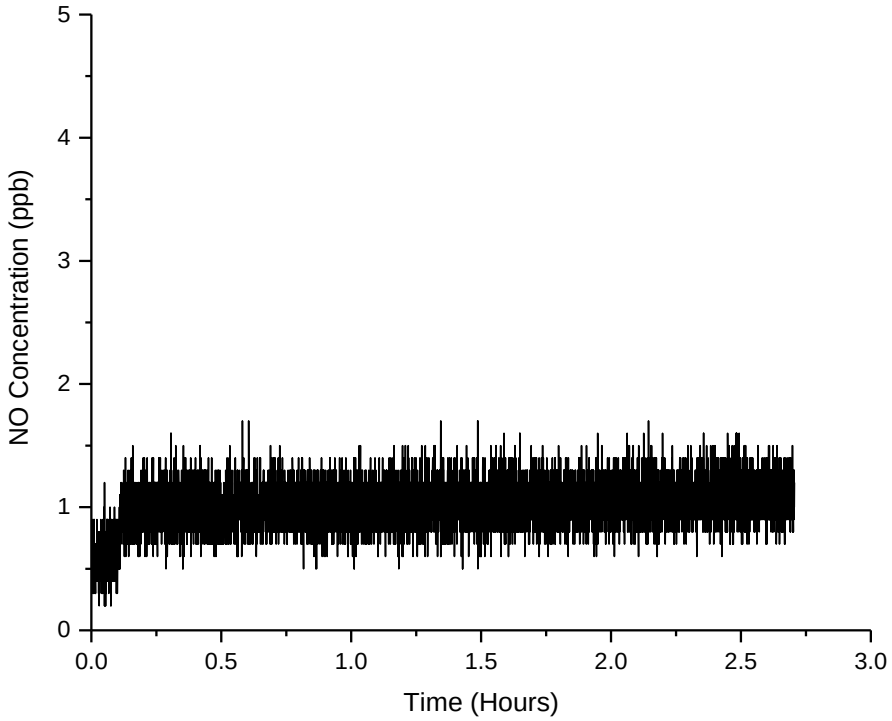

Figure A2: The NO concentration from 5 mg of Cu-UZM-4 in 2.6 mL of water with sodium nitrite (0.05 M, 5 µL) injected after 5 minutes. This was to assess the importance of the sacrificial reductant, cysteine, for the copper zeolite catalysis.

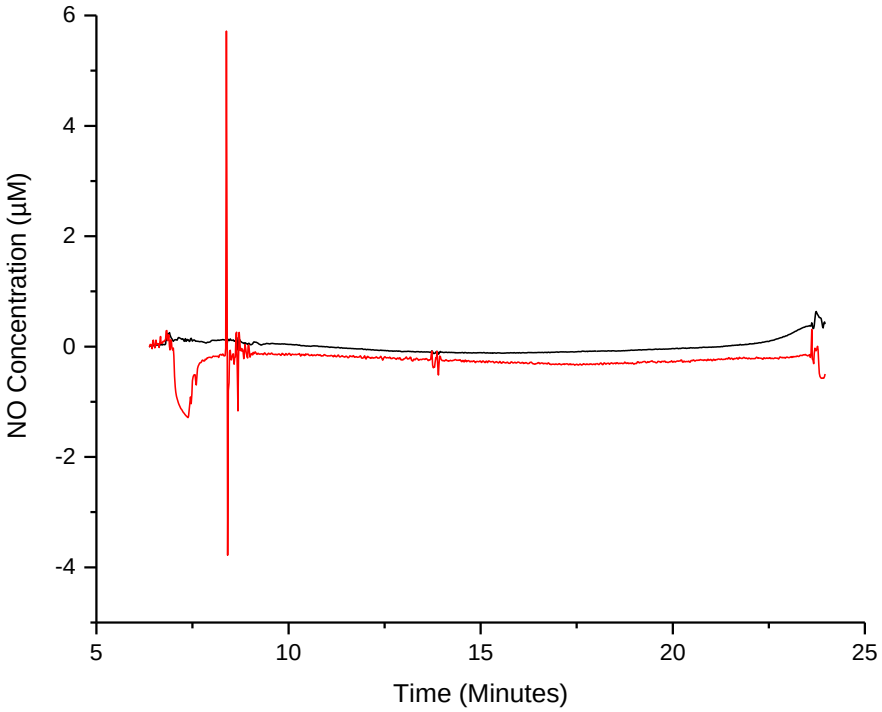

Figure A3: The NO concentrations before (black) and after (red) the empty syringe filter. This was to assess any influence from the syringe filter on the NO production.

The final NO control measurement concerns the APOLLO flow system. To ensure that there was no component of the syringe filter that affected the NO production, a flow run was completed with no zeolite loaded into the filter. The results showed no major differences between the two electrodes, indicating no contribution from the syringe filter to the NO production. The reference also did highlight the slight fluctuation of NO concentrations that were observed frequently during chapter 6.

Lastly, measurements of the effect of copper nitrate against HeLa cell toxicity were recorded to understand the toxicity of copper. Although the data presented in chapter 5 studies the viability against HEK 293 cells, the toxic effect of copper on the HeLa cells may help to understand the copper toxicity. The results show a drastic decrease in cell viability with the increase of copper nitrate concentration from 0.05 to 0.10 mg/mL. This suggests that small differences in copper concentrations can greatly impact on the cell viability, indicating that a high level of toxicity arises from copper.

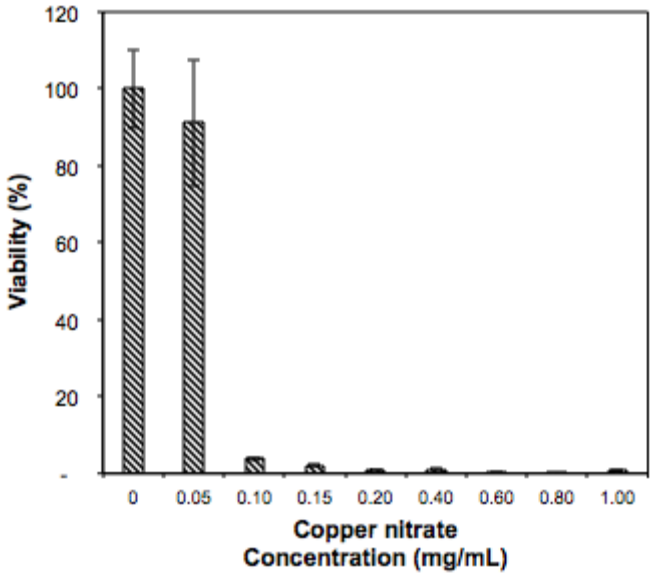

Figure A4: The viability of HeLa cells with increasing concentrations of copper nitrate.